

AD-A038 667

AIR FORCE AERO PROPULSION LAB WRIGHT-PATTERSON AFB OHIO
THE EFFECT OF TURBULENCE ON LASER BEAM QUALITY.(U)
NOV 76 R B RIVIR

F/G 20/5

UNCLASSIFIED

AFAPL-TR-76-94

NL

1 OF 3
AD
A038667



AD A 038667

AFAPL-TR-76-94

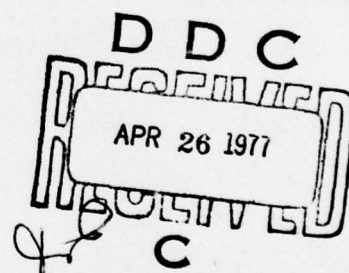
AB-815
J
(13)

THE EFFECT OF TURBULENCE ON LASER BEAM QUALITY

RAMJET TECHNOLOGY BRANCH
RAMJET ENGINE DIVISION

NOVEMBER 1976

TECHNICAL REPORT AFAPL-TR-76-94
FINAL REPORT FOR PERIOD MARCH 1973 to AUGUST 1976



Approved for public release; distribution unlimited

AD No. _____
DDC FILE COPY

AIR FORCE AERO PROPULSION LABORATORY
AIR FORCE WRIGHT AERONAUTICAL LABORATORIES
AIR FORCE SYSTEMS COMMAND
WRIGHT-PATTERSON AIR FORCE BASE, OHIO 45433

NOTICE

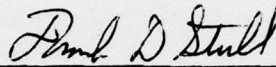
When Government drawings, specifications, or other data are used for any purpose other than in connection with a definitely related Government procurement operation, the United States Government thereby incurs no responsibility nor any obligation whatsoever; and the fact that the government may have formulated, furnished, or in any way supplied the said drawings, specifications, or other data, is not to be regarded by implication or otherwise as in any manner licensing the holder or any other person or corporation, or conveying any rights or permission to manufacture, use, or sell any patented invention that may in any way be related thereto.

This report has been reviewed by the Information Office (ASD/OIP), and is releasable to the National Technical Information Service (NTIS). At NTIS it will be available to the general public, including foreign nations.

This technical report has been reviewed and is approved for publication.

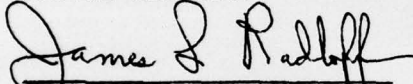


RICHARD B. RIVIR
Project Engineer/AFAPL



FRANK D. STULL
Chief, Ramjet Technology Branch
Ramjet Engine Division

FOR THE COMMANDER



JAMES L. RADLOFF, Major USAF
Chief, Components Branch
Turbine Engine Division

Copies of this report should not be returned unless return is required by security considerations, contractual obligations, or notice on a specific document.

UNCLASSIFIED

SECURITY CLASSIFICATION OF THIS PAGE (When Data Entered)

| REPORT DOCUMENTATION PAGE | | READ INSTRUCTIONS BEFORE COMPLETING FORM |
|--|--|---|
| 1. REPORT NUMBER AFAPL-TR-76-94 | 2. GOVT ACCESSION NO. | 3. RECIPIENT'S CATALOG NUMBER rept. |
| 4. TITLE (and Subtitle) THE EFFECT OF TURBULENCE ON LASER BEAM QUALITY. | 5. TYPE OF REPORT & PERIOD COVERED FINAL MARCH 73 - AUGUST 76 | |
| 7. AUTHOR(s) RICHARD B. RIVIR | 8. CONTRACT OR GRANT NUMBER(s) N/A | |
| 9. PERFORMING ORGANIZATION NAME AND ADDRESS AIR FORCE AERO PROPULSION LABORATORY WRIGHT-PATTERSON AFB, OHIO 45433 | 10. PROGRAM ELEMENT, PROJECT, TASK AREA & WORK UNIT NUMBERS Element 62203F, Task 14 Project 3012 Work Unit 04 | |
| 11. CONTROLLING OFFICE NAME AND ADDRESS AIR FORCE AERO PROPULSION LABORATORY WRIGHT-PATTERSON AFB, OHIO 45433 | 12. REPORT DATE November 1976 | |
| 14. MONITORING AGENCY NAME & ADDRESS (if different from Controlling Office) AIR FORCE AERO PROPULSION LABORATORY WRIGHT-PATTERSON AFB, OHIO 45433 | 13. NUMBER OF PAGES 196 | |
| 15. SECURITY CLASS. (of this report) UNCLASSIFIED | | 15a. DECLASSIFICATION/DOWNGRADING SCHEDULE |
| 16. DISTRIBUTION STATEMENT (of this Report) 12221p APPROVED FOR PUBLIC RELEASE: DISTRIBUTION UNLIMITED | | |
| 17. DISTRIBUTION STATEMENT (of the abstract entered in Block 20, if different from Report) APPROVED FOR PUBLIC RELEASE: DISTRIBUTION UNLIMITED | | |
| 18. SUPPLEMENTARY NOTES | | |
| 19. KEY WORDS (Continue on reverse side if necessary and identify by block number) LASER BEAM SPREAD, FOCUSED BEAM, TURBULENCE, TURBULENCE SCALES | | |
| 20. ABSTRACT (Continue on reverse side if necessary and identify by block number) Helium Neon and Helium Cadmium Laser Beams were propagated through a turbulent medium and the Mean Laser Beam Intensity and Power Profiles were measured in the Focal Plane. The parameter's effect of ranges of the ratios of integral and micro scales of turbulence to laser beam diameter and ranges of turbulence intensities which are typical of laser cavities are reported. The experimental measurements are compared with analytical predictions of Chernov and Sutton showing that the uncertainty in predicting laser beam spread in the presence of random fluctuations has been reduced by a factor of at least 2. | | |

011570

AB

FOREWORD

This report contains the results of a dissertation which was prepared for the Aeronautical and Astronomical Engineering Department of Ohio State University. The effort was supported by the Laser Aerodynamics Branch, the Components Branch, and the Interim Compressor Research Facility Group of the Air Force Aero Propulsion Laboratory, Air Force Systems Command, Wright-Patterson AFB, Ohio, under Project 3012, Task 14, and Work Unit 04. The effects of integral scale, micro scale, and intensity of turbulence on a laser beam which has propagated through the turbulent medium, as measured in the focal plane of the laser beam, are reported. The Geometric ranges of Turbulence and laser beam parameters were investigated which are typical of laser cavities. The effort was conducted by Richard B. Rivir during the period of March 1973 to August 1976.

| | |
|---------------|---------------------------------|
| APR 1977 | |
| RTS | |
| DAE | |
| UNCLASSIFIED | |
| JUSTIFICATION | |
| BY | DISTRIBUTION/AVAILABILITY CODES |
| DA | PRIC. AND/OR SPECIAL |
| A | |

TABLE OF CONTENTS

| Chapter | Page |
|--|------|
| I. INTRODUCTION | 1 |
| II. DEFINITION OF THE PROBLEM | 7 |
| Examples of Laser Cavity Flows | 7 |
| Examples of Correlation of Experiment with Theory and Comparison of Similar Theories | 11 |
| Statement of the Problem | 14 |
| Selection of Experimental Parameters and Their Ranges | 14 |
| Scope of the Investigation | 23 |
| III. APPARATUS AND INSTRUMENTATION | 24 |
| Schematic of the Experimental Apparatus | 24 |
| Wind Tunnel | 26 |
| Vortex Generators | 28 |
| Anemometer System | 30 |
| Optical Components | 31 |
| Optical Benches | 31 |
| Laser Sources | 31 |
| Light Pipe | 32 |
| Beam Diagnostics | 33 |
| Correlator | 34 |

TABLE OF CONTENTS (Cont'd)

| Chapter | Page |
|--|------|
| IV. EXPERIMENTAL MEASUREMENT AND PARAMETER CALCULATION PROCEDURES | 37 |
| Flow Property Measurement | 39 |
| Tunnel Profile Calculations for Mean Temperature, Mean Velocity, Mean Index of Refraction, RMS Temperature, RMS Velocity, RMS Index of Refraction, T_u , T_T , and T_n | 65 |
| Determination of Integral Scale and Microscale of Turbulence from Correlation Functions | 67 |
| Laser Beam Power Measurement and Calculation | 78 |
| Detector Calibration and Frequency Response | 78 |
| The Selection of the Scanning Aperture Size at the Focal Spot | 81 |
| The Calculation of Integral Laser Power | 83 |
| V. EXPERIMENTAL RESULTS | 95 |
| Summary | 95 |
| Mean and Turbulent Tunnel Profiles | 97 |
| Effects of Convection | 97 |
| Variations of Fluid Properties Along the Tunnel Axis | 103 |
| Variations of Fluid Properties Along the Tunnel Axis with the Non-Dimensional Heat Addition Parameters | 111 |

TABLE OF CONTENTS (Concl'd)

| Chapter | Page |
|--|------|
| Laser Beam Spread Measurements | 126 |
| Distribution of Beam Spread | 130 |
| The Reduction of Centerline Intensity | 175 |
| The Effect of $\langle \Delta \eta \rangle^2$ on Centerline Intensity | 175 |
| The Effect of the Diameter of the Beam/ Λ_T Ratio on Beam Spread | 189 |
| VI. CONCLUSIONS | 191 |
| VII. RECOMMENDATIONS | 196 |
| LIST OF REFERENCES | 197 |

LIST OF ILLUSTRATIONS

| <u>Figure</u> | <u>Page</u> |
|--|-------------|
| 1. Simulated Cold Flow of a Proposed Injection Technique for an EDL. | 8 |
| 2. Simulated GDL Cold Flow Courtesy, Dr. Shine, AFIT Aero-Mechanical Engineering Department | 8 |
| 3. Greenbaum's Comparison of Required Initial Beam Radii Given Maximum Allowable Focal Spot Diameter | 13 |
| 4. Beam Diameter Scaling | 17 |
| 5. Laser Cavity Scales of Turbulence | 19 |
| 6. Reynolds Number and Turbulence Scale Capability of the 23 cm AFIT Tunnel. | 21 |
| 7. Path Length Limitations for Geometric Optics or the Neglect of Diffractive Effects | 22 |
| 8. Identification of Apparatus and Instrumentation | 25 |
| 9. AFIT 23 cm Tunnel with 50 Milliwatt Helium Cadmium Laser | 26 |
| 10. Schematic | 27 |
| 11. Traverse Mechanisms | 35 |
| 12. Frequency Response of Probe 8712, Wire No. 1, Horizontal Time Scale 5×10^{-6} Seconds/Division, Constant Temperature - OH = 1.5 | 43 |
| 13. Schematic of Frequency Response Measurement | 44 |
| 14. Frequency Response of Probe 8712, Wire No. 2, Horizontal Time Scale 2×10^{-3} Seconds/Division, Constant Current Mode - OH = 1.15, Chopper Blade with Four Slots | 45 |

| <u>Figure</u> | <u>Page</u> |
|---|-------------|
| 15. Frequency Amplitude for Probe 8712, Wire No. 2, 200, 400, and 600 Hertz Temperature Pulse. | 46 |
| 16. Frequency Amplitude for Probe 8712, Wire No. 2, 800, 1000, and 1200 Hertz Temperature Pulse. | 47 |
| 17. Temperature Frequency Response of Probe 8712 with IR Industries Model 830 Chopper - Multiple Pulse | 48 |
| 18. Temperature Frequency Response of Probe 8712 with Four-Slotted Blade Chopper - Single Pulse. | 49 |
| 19. Temperature Frequency Response of Probe 8712 for Single Pulse | 51 |
| 20. Reynolds Number Dependence of the Temperature Wire, Probe 8712 | 53 |
| 21. Calibration of Temperature Wire, Probe 8712. | 55 |
| 22. Velocity Calibration of Probe 8712 | 57 |
| 23. Velocity Calibration of Probe 8712 with Least Squares Fit of the Data. | 58 |
| 24. T_u for Probe 8712 at a Fluid Temperature of 23°C | 61 |
| 25. Schematic of Graphical Computation of V_m for Large Values of T_u | 62 |
| 26. Top View of Tunnel Illustrating Horizontal Traverse Locations for .64 cm Perforation Diameter T_u Generator. . | 64 |
| 27. End View of Tunnel Illustrating Correlation Stations and Traverse Region | 64 |
| 28. Schematic of Longitudinal and Lateral Correlation Functions from Hinze | 68 |
| 29. Parabolic Definition of the Microscale of Turbulence . . . | 71 |
| 30. The Scales of Turbulence from the "Two/Thirds Law" | 74 |

| <u>Figure</u> | <u>Page</u> |
|---|-------------|
| 31. Autocorrelation of Velocity - Single Scale of Turbulence | 77 |
| 32. Autocorrelation of Temperature - Two Scales of Turbulence. | 77 |
| 33. Autocorrelation of Velocity - Multiple Scales of Turbulence. | 77 |
| 34. Power Meter Frequency Response. | 79 |
| 35. Power Meter Amplitude Frequency Response. | 80 |
| 36. Comparison of Focal Plane Aperture Intensity Tracking . . . | 82 |
| 37. 14.03 mm Diameter He Cd Laser Beam Traverse at an L/D _p Station of 28, Medium Heat | 85 |
| 38. 14.03 mm Diameter He Cd Laser Beam Traverse at an L/D _p Station of 28, Zero Heat | 85 |
| 39. Integral Laser Power, Zero Heat | 87 |
| 40. Integral Laser Power, Medium Heat | 88 |
| 41. Integral Laser Power, Zero Heat | 90 |
| 42. Integral Laser Power, Low Heat. | 91 |
| 43. Integral Laser Power, Medium Heat | 92 |
| 44. Integral Laser Power, High Heat | 93 |
| 45. Horizontal Tunnel Traverse, L/D _p = 45, Zero Heat. | 98 |
| 46. Horizontal Tunnel Traverse, L/D _p = 45, Low Heat | 99 |
| 47. Horizontal Tunnel Traverse, L/D _p = 34.5, Medium Heat. . . . | 100 |
| 48. Horizontal Tunnel Traverse, L/D _p = 28, High Heat. | 101 |
| 49. Vertical Tunnel Traverse, L/D _p = 34.5, High Heat. | 102 |

| <u>Figure</u> | <u>Page</u> |
|---|-------------|
| 50. Temperature Fluctuations. | 104 |
| 51. Temperature Turbulence Intensity. | 105 |
| 52. Index of Refraction Turbulence Intensity. | 106 |
| 53. Axial Tunnel Variation of T_u | 109 |
| 54. Axial Tunnel Variation of the Integral Turbulence Scale of Temperature | 110 |
| 55. $\langle \Delta \eta \rangle$ versus KQ/U at $L/D_p = 28$, Turbulence Generator B . . | 113 |
| 56. $\langle \Delta \eta \rangle$ versus KQ/U at $L/D_p = 34.5$, Turbulence Generator B . | 114 |
| 57. $\langle \Delta \eta \rangle$ versus KQ/U at $L/D_p = 45$, Turbulence Generator B . . | 115 |
| 58. $\langle \Delta \eta \rangle$ at $L/D_p = 45$ for Low, Medium and High Heat Addition, $U^p = .99\text{m/sec}$ to 1.16 m/sec | 116 |
| 59. $\langle \Delta \eta \rangle$ versus KQ/U at $L/D_p = 14$, Turbulence Generator A . . | 117 |
| 60. Centerline Variation of T_u at $L/D_p = 28$, Turbulence Generator B. | 118 |
| 61. Centerline Variation of T_u at $L/D_p = 34.5$, Turbulence Generator B. | 119 |
| 62. Centerline Variation of T_u at $L/D_p = 45$, Turbulence Generator B. | 120 |
| 63. Centerline Variation of T_u at $L/D_p = 14$, Turbulence Generator A. | 122 |
| 64. Centerline Value of the Integral Temperature Scale of Turbulence, $L/D_p = 28$, Turbulence Generator B | 123 |
| 65. Centerline Value of the Integral Temperature Scale of Turbulence, $L/D_p = 34.5$, Turbulence Generator B | 124 |
| 66. Centerline Value of the Integral Temperature Scale of Turbulence, $L/D_p = 45$, Turbulence Generator B | 125 |

| <u>Figure</u> | <u>Page</u> |
|--|-------------|
| 67. Centerline Value of the Micro Temperature Scale of Turbulence, $L/D_p = 28$, Turbulence Generator B | 127 |
| 68. Centerline Value of the Micro Temperature Scale of Turbulence, $L/D_p = 34.5$, Turbulence Generator B | 128 |
| 69. Centerline Value of the Micro Temperature Scale of Turbulence, $L/D_p = 45$, Turbulence Generator B | 129 |
| 70. Comparison of Gaussian Profiles Normalized to Differing Radial Values of Integral Power | 132 |
| 71. Comparison of a Turbulent Half-Width Power Profile to a Gaussian Half-Width Power Profile. | 134 |
| 72. Sutton's 3-D Turbulence Approximation for Beam Spread at the $.5 P_0$ Point of the Distribution. | 135 |
| 73. Half Power Point Variation of Focal Spot Size, He Cd, $L/D_p = 28$, $D = 50$ mm | 137 |
| 74. Half Power Point Variation of Focal Spot Size, He Cd, $L/D_p = 45$, $D = 30.58$ mm. | 138 |
| 75. Half Power Point Variation of Focal Spot Size, He Cd, $L/D_p = 28$, $D = 50$ mm | 141 |
| 76. Half Power Point Variation of Focal Spot Size, He Cd, $L/D_p = 28$, $D = 30.58$ mm. | 142 |
| 77. Half Power Point Variation of Focal Spot Size, He Cd, $L/D_p = 28$, $D = 14.03$ mm. | 143 |
| 78. Half Power Point Variation of Focal Spot Size, He Cd, $L/D_p = 28$, $D = 1.5$ mm. | 144 |
| 79. Half Power Point Variation of Focal Spot Size, He Cd, $L/D_p = 34.5$, $D = 50$ mm | 145 |
| 80. Half Power Point Variation of Focal Spot Size, He Cd, $L/D_p = 34.5$, $D = 30.58$ mm. | 146 |

| <u>Figure</u> | <u>Page</u> |
|---|-------------|
| 81. Half Power Point Variation of Focal Spot Size, He Cd, $L/D_p = 34.5$, $D = 14.03$ mm | 147 |
| 82. Half Power Point Variation of Focal Spot Size, He Cd, $L/D_p = 45$, $D = 50$ mm. | 148 |
| 83. Half Power Point Variation of Focal Spot Size, He Cd, $L/D_p = 45$, $D = 30.58$ mm | 149 |
| 84. Half Power Point Variation of Focal Spot Size, He Cd, $L/D_p = 45$, $D = 14.03$ mm | 150 |
| 85. Half Power Point Variation of Focal Spot Size, He Cd, $L/D_p = 45$, $D = 1.5$ mm | 151 |
| 86. Half Power Point Variation of Focal Spot Size, He Ne, $L/D_p = 28$, $D = 50$ mm. | 152 |
| 87. Half Power Point Variation of Focal Spot Size, He Ne, $L/D_p = 28$, $D = 26$ mm. | 153 |
| 88. Half Power Point Variation of Focal Spot Size, He Ne, $L/D_p = 28$, $D = 14.03$ mm | 154 |
| 89. Half Power Point Variation of Focal Spot Size, He Ne, $L/D_p = 28$, $D = 26$ mm. | 155 |
| 90. Half Power Point Variation of Focal Spot Size, He Ne, $L/D_p = 28$, $D = 26$ mm. | 156 |
| 91. Half Power Point Variation of Focal Spot Size, He Cd, $L/D_p = 28$, $D = 30.58$ mm | 157 |
| 92. Half Power Point Variation of Focal Spot Size, He Ne, $L/D_p = 14$, $D = 50$ mm. | 161 |
| 93. Half Power Point Variation for the Chernov-Sutton Calculation, He Cd, $L/D_p = 28$, $D = 50$ mm | 162 |
| 94. Half Power Point Variation for the Chernov-Sutton Calculation, He Cd, $L/D_p = 28$, $D = 30.58$ mm. | 163 |

| <u>Figure</u> | <u>Page</u> |
|--|-------------|
| 95. Half Power Point Variation for the Chernov-Sutton Calculation, He Cd, $L/D_p = 28$, $D = 14.03$ mm | 164 |
| 96. Half Power Point Variation for the Chernov-Sutton Calculation, He Cd, $L/D_p = 34.5$, $D = 50$ mm. | 165 |
| 97. Half Power Point Variation for the Chernov-Sutton Calculation, He Cd, $L/D_p = 34.5$, $D = 30.58$ mm | 166 |
| 98. Half Power Point Variation for the Chernov-Sutton Calculation, He Cd, $L/D_p = 34.5$, $D = 14.03$ mm | 167 |
| 99. Half Power Point Variation for the Chernov-Sutton Calculation, He Cd, $L/D_p = 45$, $D = 50$ mm. | 168 |
| 100. Half Power Point Variation for the Chernov-Sutton Calculation, He Cd, $L/D_p = 45$, $D = 30.58$ mm | 169 |
| 101. Half Power Point Variation for the Chernov-Sutton Calculation, He Cd, $L/D_p = 45$, $D = 14.03$ mm | 170 |
| 102. Half Power Point Variation for the Chernov-Sutton Calculation, He Ne, $L/D_p = 34.5$, $D = 50$ mm. | 171 |
| 103. Half Power Point Variation for the Chernov-Sutton Calculation, He Ne, $L/D_p = 34.5$, $D = 26$ mm. | 172 |
| 104. Half Power Point Variation for the Chernov-Sutton Calculation, He Ne, $L/D_p = 34.5$, $D = 8$ mm | 173 |
| 105. Chernov-Sutton Calculation for the Centerline Value of Intensity for a He Cd Beam | 176 |
| 106. Centerline Value of Intensity for a He Cd Beam, $L/D_p = 28$, $D = 50$ mm. | 177 |
| 107. Centerline Value of Intensity for a He Cd Beam, $L/D_p = 28$, $D = 30.58$ mm | 178 |
| 108. Centerline Value of Intensity for a He Cd Beam, $L/D_p = 28$, $D = 14.03$ mm | 179 |

| <u>Figure</u> | <u>Page</u> |
|--|-------------|
| 109. Centerline Value of Intensity for a He Cd Beam, $L/D_p = 34.5$, $D = 50$ mm | 180 |
| 110. Centerline Value of Intensity for a He Cd Beam, $L/D_p = 34.5$, $D = 30.58$ mm. | 181 |
| 111. Centerline Value of Intensity for a He Cd Beam, $L/D_p = 34.5$, $D = 14.03$ mm. | 182 |
| 112. Centerline Value of Intensity for a He Cd Beam, $L/D_p = 45$, $D = 50$ mm | 183 |
| 113. Centerline Value of Intensity for a He Cd Beam, $L/D_p = 45$, $D = 30.58$ mm. | 184 |
| 114. Centerline Value of Intensity for a He Cd Beam, $L/D_p = 45$, $D = 14.03$ mm. | 185 |
| 115. Centerline Value of Intensity for a He Ne Beam, $L/D_p = 34.5$, $D = 50$ mm | 186 |
| 116. Centerline Value of Intensity for a He Ne Beam, $L/D_p = 34.5$, $D = 26$ mm | 187 |
| 117. Centerline Value of Intensity for a He Ne Beam, $L/D_p = 34.5$, $D = 8$ mm. | 188 |

LIST OF TABLES

| <u>Table</u> | | <u>Page</u> |
|--------------|--|-------------|
| 1 | Aperture Percentage of Beam Diameter | 84 |
| 2 | Range of Independent Experimental Parameters | 96 |
| 3 | λ Dependence on Beam Spread. | 140 |
| 4 | Diameter Dependence of Beam Spread | 158 |
| 5 | Calculated Gaussian Scale from Mean Tunnel Profiles. . . | 159 |
| 6 | Comparison of Λ_T and ℓ_0 Scales from Half Power Values of R/R ₀ Measurements with Their Measured Values. | 174 |
| 7 | Comparison of Λ_T and ℓ_0 Centerline Laser Intensity Measurements with Their Measured Values. | 190 |

LIST OF SYMBOLS

| | |
|-----------|--|
| A | Area |
| A_1 | Correlation station location |
| A_2 | Calibration constant for velocity sensor |
| A_{2T} | Calibration constant for temperature sensor |
| $A(t)$ | Arbitrary time varying function |
| B_1 | Correlation station location |
| B_2 | Calibration constant for velocity sensor |
| B_{2T} | Calibration constant for temperature sensor |
| $B(t)$ | Arbitrary time varying function |
| C | Constant |
| C_1 | Correlation station location |
| C_D | Drag coefficient |
| C_p | Specific heat of air |
| C_w | Specific heat of anemometer sensor wire |
| D | Diameter of laser beam |
| D_g | Structure function |
| D_p | Turbulence generator perforation diameter |
| E | Anemometer sensor voltage |
| E_m | Mean anemometer sensor voltage |
| \bar{E} | The electric field of propagating laser beam |
| F | Constant |

| | |
|-----------|---|
| F_T | A random function |
| G | Constant |
| Gr | Grashof number |
| H | Constant |
| I | Local intensity of laser beam |
| I_0 | Reference intensity of laser beam |
| I_1 | Anemometer sensor current |
| J | Constant |
| K | Constant |
| K_1 | Thermal conductivity of air |
| Ku | Knudsen number |
| L | Location of centerline of the laser beam from the velocity turbulence generator |
| L_0 | Path length of the laser beam through the turbulent medium |
| M | Mach number |
| \dot{M} | Mass flow rate of the tunnel fluid |
| M_0 | Constant |
| M_1 | Constant |
| M_2 | Constant |
| M_3 | Constant |
| Nu | Nusselt number |
| OH | Overheat ratio of the anemometer sensor |
| Pr | Prandtl number |

| | |
|-------------|--|
| ΔP | $P_B - p$, tunnel velocity pressure |
| P | Pressure |
| P_B | Barometric pressure |
| P_S | Standard pressure |
| P_0 | Stagnation pressure |
| Q | Temperature grid heater power |
| R | Local radius of the laser intensity distribution in the focal plane |
| R_0 | Reference value of the radius of the focal spot of the laser |
| R_1 | Resistance of anemometer sensor |
| R_3 | Resistance of anemometer bridge |
| Re | Reynolds number |
| R_g | Constant |
| R_Λ | Reynolds number with the integral scale of turbulence as the characteristic diameter |
| S | Constant |
| S_0 | Constant |
| S_t | Stanton number |
| T | The static temperature of the fluid |
| T_1 | The static temperature of the fluid, test cabin entrance |
| \bar{T} | The spatial average of the fluid temperature transverse to the fluid flow direction |
| T_0 | Stagnation temperature |
| T_f | The fluid temperature |

••

| | |
|------------|--|
| T_i | A locally measured fluid temperature |
| T_m | The arithmetic average temperature |
| T_s | Standard temperature |
| T_T | Temperature turbulence intensity |
| T_u | Velocity turbulence intensity |
| T_w | The anemometer sensor temperature |
| ΔT | RMS value of temperature |
| U_0 | Reference value of velocity |
| \bar{U} | The spatial average of fluid velocity transverse to the fluid flow direction |
| ΔU | RMS value of velocity |
| V | Anemometer voltage |
| V_0 | Anemometer reference voltage |
| V_1 | Indicated fluid velocity |
| V_2 | Indicated fluid velocity |
| V_m | Arithmetic mean indicated fluid velocity |
| a | Energy containing turbulence wave length |
| b | Constant |
| c | Constant |
| c_1 | Constant |
| c_2 | Constant |
| C_N^2 | Constant |
| d | Characteristic diameter |

| | |
|------------------|---|
| f | Focal length |
| f_1 | Frequency |
| $g(r)$ | Lateral correlation function |
| h | The heat transfer coefficient |
| h_0 | Dimension of square mask |
| h_f | Film heat transfer coefficient |
| k | $2\pi/\lambda$, wave number |
| \dot{m} | Mass flow rate of the tunnel fluid |
| n | Calibration constant of anemometer sensor |
| p | Static pressure |
| q | Heater power, $Q/\text{tunnel fluid mass flow rate}$ |
| r | A vector |
| r_{eff} | Local radius of the laser intensity distribution in the focal plane |
| t | Time |
| u | Fluctuating component of velocity |
| u_i | Local rms value of the fluctuating component of velocity |
| u'_i | RMS value of the fluctuating component of velocity |
| x | Coordinate |
| x_1 | Coordinate in the fluid flow direction |
| x_2 | Coordinate transverse to the fluid flow direction |
| Δx_i | Incremental local traverse location along the laser beam centerline |
| Δy | Reference value for the radius of the focal spot of the laser |

| | |
|----------------------------|--|
| α | Extinction coefficient |
| $\beta(t_f)$ | Terms proportional to the fluid temperature |
| ϵ | Turbulent kinetic energy |
| λ | Wave length |
| n | Index of refraction |
| $\langle \Delta n \rangle$ | RMS value of the fluctuating component of the index of refraction |
| μ | Viscosity |
| μ_0 | Reference value of viscosity |
| ν | Kinematic viscosity |
| ρ | Density |
| ρ_s | Standard density of air |
| ρ_w | Density of anemometer sensor material |
| γ | Ratio of specific heats |
| θ_0 | Reference value of the half angle subtended by the laser beam intensity distribution |
| θ_T | Reference value of the half angle subtended by the laser beam intensity distribution |
| σ_0 | Resistivity of anemometer sensor at reference temperature |
| τ | Small increment of time |
| τ_0 | Integral time scale of turbulence |
| τ_e | Decay time of anemometer sensor |
| τ_u | Integral velocity time scale of turbulence |
| τ_T | Integral temperature time scale of turbulence |

| | |
|-------------|--|
| δ | Temperature coefficient of resistance |
| ζ | Coordinate location of anemometer sensor |
| ζ_1 | Coordinate location of anemometer sensor |
| ζ_2 | Coordinate location of anemometer sensor |
| Λ | Integral scale of turbulence |
| Λ_u | Velocity integral scale of turbulence |
| Λ_T | Temperature integral scale of turbulence |
| ℓ | Length of anemometer sensor |
| ℓ_0 | Microscale of turbulence |
| ℓ_{0u} | Velocity microscale of turbulence |
| ℓ_{0T} | Temperature microscale of turbulence |

CHAPTER I

INTRODUCTION

Since the development of the first flow cooled CO_2 laser in 1960, there has been a steady progression in the development of flow cooled lasers. Pulsed and continuous lasers have evolved which are well understood from a physical standpoint. The useful applications of the laser as a precise diagnostic tool in flow field measurements, as a manufacturing tool for drilling, cutting, and welding various materials, and as a communications or power link, has necessitated higher power densities and improved beam quality. Increases in the average level of power has increased the emphasis on the use of a flowing medium to separate the high entropy lasing medium from the lasing cavity. The continual replacement and the transport of the lasing medium through the lasing cavity introduces fluctuations in the physical properties of the lasing medium. These fluctuations in time and spatial dimensions of the physical properties of the fluid can be of the same general magnitude as the optical parameters (time and spatial dimensions) of the laser beam. When optical and fluid characteristic times and dimensions are similar in magnitude, a coupling may occur between the random variations in the fluid properties and the electromagnetic propagation of a wave through the medium.

Analytical descriptions of the coupling of the electromagnetic field and the fluctuating fluid properties results in equations which have the randomly variable fluid properties as a coefficient of the sought wave function solution. An exact analytical solution to this problem is not known. Analytic approximations which make use of varying degrees of smallness of the fluid, transport, physical, and optical properties allow qualitative predictions of the effect of the randomly fluctuating medium on the electromagnetic wave propagation through the medium. Current analytical models developed to predict the degradation in beam quality, as a result of propagation through a turbulent flow field, yield results which only agree within an order of magnitude with the observable results.

The qualitative effect of random fluctuations or turbulence on beam spreading is well demonstrated. Turbulence causes scattering of photons as a result of spatial and temporal changes in the index of refraction of the medium with a resultant decrease in energy per unit area.

The increase in total average power of lasers is limited basically by economic considerations and physical space limitations. However, the improvement in laser beam quality and average power density (up to atmospheric breakdown) is dependent in part on a better understanding of the interaction between the fluctuations of the physical transport properties of the fluid through which the beam is propagating and the physical quantities which characterize the laser beam. The degradation in beam quality in flow cooled lasers is within the accuracy of the theoretical predictions of focal spot size in the presence of turbulence.

A better correlation of theoretical and experimental knowledge of the effects of turbulence on beam quality is required to assess the possibility of further improvements in beam quality for flow cooled lasers.

The fluctuations of physical properties of the lasing fluid or a fluid through which a beam may propagate are caused by the interaction of the flow with an assortment of physical boundaries, the mixing of dissimilar component gases of the lasing medium, and chemical reactions. Examples of disturbance generators include: nozzle arrays, mirrors, input windows, extraction windows, electrodes, chemical reaction sources, thermal sources, wall boundary layers, and even vortex generators which are used to stabilize some electrical discharge lasers. Specific examples will be illustrated in Chapter II.

The number of theoretical solutions available in the literature for the propagation of an electromagnetic wave through a randomly varying medium are quite numerous. The reason for many theoretical solutions is due to the lack of an exact solution to the wave equation. The wave equation will next be examined and the solutions grouped into generic types as they are found in the literature. This section will then be concluded with a historical listing of some of the publications which deal specifically with predicting beam spread and the measurement of beam spread in the presence of turbulence.

The intensity amplitude, intensity distribution, rms level of the fluctuations of intensity, and the spectrum of the fluctuations in the presence of turbulence are quantities of interest for several applications and for which appropriate theoretical predictions are possible. Each of these quantities is a direct measure of the effects of

turbulence. However, a clear and exact relationship between the causes and the observable effects does not exist.

The lack of an exact relationship is due to the way in which the random fluctuations of the medium enter the propagation equations. The general form of the differential equation for an electromagnetic wave propagating in a random medium is obtained by eliminating the magnetic field from Maxwell's equations which eventually results in:

$$\nabla \cdot \bar{E} + k^2 \bar{n}^2(r,t) \bar{E} + 2\nabla (\bar{E} \cdot \nabla \ln \bar{n}(r,t)) = 0 \quad (1)$$

The last term in equation (1) represents the effects of depolarization. Strohbehn and Clifford have calculated that this contribution to the field of the propagating wave is 160 db less than the incident wave. Saleh attempted to measure this component with a sensitivity of -45 db and was unsuccessful (Lawrence and Strohbehn, 1970). There have been no attempts to estimate the contribution to the depolarization term by scattering. All previous analyses reviewed seek a solution for the electric field which neglected the depolarization term. Dropping the last term results in the scalar wave equation, which represents the simplest theoretical description possible:

$$\nabla \cdot \bar{E} + k^2 \bar{n}^2(r,t) \bar{E} = 0 \quad (2)$$

The random fluctuations are seen to enter the above equation as a coefficient of the sought solution for the field \bar{E} . This is the source of the mathematical difficulties, since there is no known exact solution for this form of equation. Various approximations and degrees of smallness are required along with their implicit ranges of validity in order to obtain even approximate solutions. The solutions which are found in the literature are generally characterized by one of the following

methods, or range of geometric parameters: (1) geometric optics; (2) method of small perturbations; (3) method of smooth perturbations (Rytov); (4) modulation transfer function or mutual coherence function; and (5) multiple scattering. Experimentally usable results are obtained from the first four methods. All of the above methods are adequately documented in the literature.

The first three methods are detailed in the Russian works by Chernov and Tatarski, which were translated to English in 1960 and 1961 respectively. Many of the papers which appear in the literature for the following eight years deal with modifications, variations, and attempts to confirm observations resulting from these publications. Huffnagel and Stanley introduced the fourth method, the modulation transfer function and an average coherence function in an analytical solution published in 1964. In 1965, Collins and Wortendyke published experimental scattering measurements for a finite plane wave, propagating through a wind tunnel, which were based upon one of Tatarski's solutions. In 1966, Schmeltzer published an iterative solution based on Tatarski's Rytov approximation (Method 3) for a focused, initially gaussian beam, propagating through a turbulent atmosphere. Schmeltzer's results were given in integral form. In 1968, Gebhardt evaluated the integral solutions given by Schmeltzer for focused and collimated gaussian beams. After 1969, nearly all analytical solutions involve Method 4. Sutton, in 1969, published a calculation of a numerical solution using the modulation transfer function, which included the case in which the turbulence scale and the beam diameter are of the same order.

In 1970, Lutomirski also published a solution for a finite beam for some restricted path lengths based upon the mutual coherence function.

There are several excellent surveys currently available in the literature. Lawrence and Strohbehn published "A Survey of Clear-Air Propagation Effects Relevant to Optical Communications" in the Proceedings of the IEEE in 1970. An extensive survey of Russian efforts may be found in the 1971 Soviet Physics article, "Status of the Theory of Propagation of Waves in a Randomly Inhomogeneous Medium," by Barabanenkov, Kravtsov, Rytov, and Tamarskii.

Lutomirski and Yura published numerous reports separately and together. Most of their reports are summarized and referenced in Rand publication, "Degradation of Laser Systems by Atmospheric Turbulence," which was published in 1973. The majority of the solutions presented by the Rand Report also evolve from the mutual coherence function. Although this effort will not deal with scintillation effects, a very good scintillation review is given by Meyer-Arendt and Emmanuel in the 1965 NBS Technical Report 225, "Optical Scintillation: A Survey of the Literature."

CHAPTER II

DEFINITION OF THE PROBLEM

In this chapter some examples of laser cavity flows will be illustrated to show the types of turbulence conditions which may be encountered in laser cavity flows. The lack of adequate experimental measurements to confirm existing analytic solutions will be illustrated as the problem to be investigated in laser cavity-like flows. Next, the experimental conditions will be examined and selected so that beam spreads of the order of three times that of a diffraction limited beam may be produced for geometric conditions such as are encountered in laser cavities. Finally, the scope or range of experimental conditions to be investigated will be stated.

Examples of Laser Cavity Flows

Examples of simulated laser cavity flows are shown in Figures 1 and 2. The first figure represents the proposed injection of the lasing medium for a pulsed electrical discharge laser (EDL). The first figure, a schlieren photograph, shows the injection of the lasing medium from a series of parallel manifolds which contain a large number of small jets. The pressure ratio across the jet orifices is greater than critical. The shear layers surrounding the jets are seen to remain well defined for approximately 100 jet diameters downstream. This ordered level of

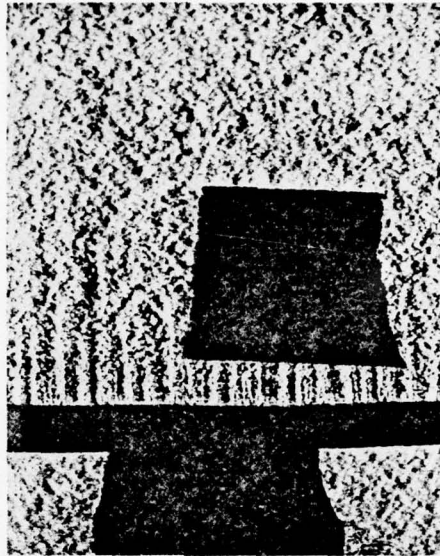


Figure 1. Simulated Cold Flow of a Proposed Injection Technique for an EDL

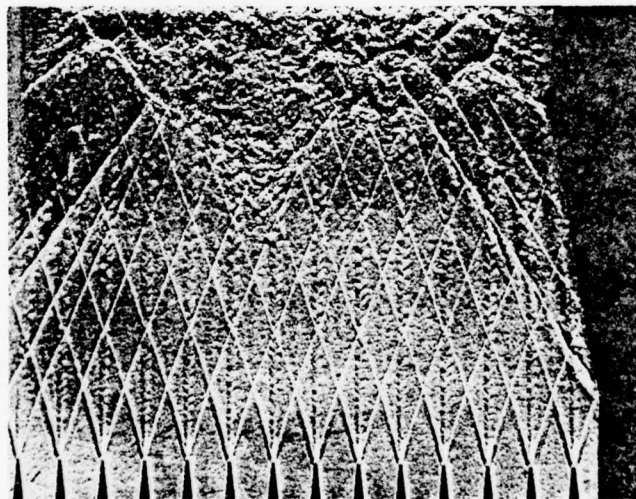


Figure 2. Simulated GDL Cold Flow Courtesy, Dr. Shine, AFIT Aero-Mechanical Engineering Department

turbulence then decays into a region of isotropic turbulence in the upper portion of the figure where the scale size of the turbulence is observed to be approximately the same in all directions. A further problem encountered with large numbers of jets, which is not specifically illustrated by Figure 1, is the interaction of individual jets to produce both unsteady motion and various degrees of coalescence by the interaction of individual jets, thereby increasing the integral scale of turbulence which is observed. The lasing path for this particular device would be in the plane of the photograph and normal to flow. The pressure of the lasing medium in an electrical discharge laser would typically be on the order of an atmosphere and the mean flow would be at a Mach number on the order of .1. The turbulence Reynolds number of this flow would be on the order of 7000. For injection techniques of this type, the lasing path would include regions of both isotropic and nonisotropic turbulence. The turbulence intensities in the nonisotropic regions of supercritical jets, such as shown in Figure 1, are on the order of 50%; as the region approaches isotropic turbulence, the turbulence intensity decreases to a few percent.

The second figure shows a multiple element supersonic nozzle array similar to that encountered in gas dynamic (GDL) and chemical lasers where the throat diameters are on the order of a few hundredths to a few thousandths of a centimeter. This schlieren photograph shows Mach waves and a shear layer leaving each nozzle. The combination of a low lasing medium pressure and the very small characteristic lengths of the throat and boundary layer results in a value of turbulence Reynolds number on the order of a few hundred. A comparison of Figures 1 and 2

shows that the wakes are propagated for much longer distances as viscous and inertial forces approach one another. The wakes are terminated only by the formation of regions of even greater turbulence intensity. Similar weaker wakes will also be observed at the intersection of shocks of unequal strength or turning angle. The velocity turbulence intensity in these wakes can again approach 50%.

In AIAA Paper 73-626 (Director, 1973), density variations ($\Delta\rho/\rho$) observed in simulated cavity flows from wakes and wall contours with interferograms range from a few tenths of a percent to approximately five percent for flows similar to that shown in Figure 2. The displacement boundary layer thickness, or one half wake thickness, was calculated to be on the order of .05 centimeter in cold flow. In AIAA Paper 73-641 (Hyde and Hosack, 1973), the thermal boundary layer was calculated for a chemical laser flow nozzle. The energy boundary layer was observed to be four times the thickness of the velocity boundary layer, on the order of .76 to 1 centimeter, a very significant portion of the exit area of the nozzle, even with nozzle area ratios which are quite large. The thermal wake is the region of interest in terms of its influence on the ability of turbulence to introduce disturbances and defocus a beam propagating through the medium.

In the electro aerodynamic laser (EAL), a series of half cylinders are arranged in a picket fence fashion as the anode support structure at the entrance of the lasing cavity. Each of these cylinders sheds vortices or streaks periodically. The turbulence Reynolds number of the flow in the electrical discharge laser cavity is on the order of a few thousand due to the low density and also low velocity. Since the

Reynolds number is low, the shedding structure embedded in the flow remains for long distances just as the wakes do in the GDL and EAL.

The low pressure lasing mediums in cavities such as the GDL, EAL, and chemical lasers may also require aerodynamic windows. These windows may involve shocks and the intersection of complex patterns of shock waves. At the intersection of complex or unequal strength shock waves, complex regions of turbulence also exist.

The turbulence Reynolds numbers are observed to be very small in laser cavities compared to the turbulence Reynolds numbers encountered in atmospheric propagation. The Reynolds number in atmospheric propagation problems are large due to the scale of the disturbances. In cavities the beam diameter to turbulence scale can range from much less than 1 to ~ 1 . Turbulence intensities may be quite high ($\sim 50\%$) and the turbulence conditions range from nonisotropic to isotropic. The path length through the lasing medium is short in comparison to atmospheric propagation problems, ranging only to a few tens of meters. The lasing beam is near gaussian or enters the cavity as a gaussian beam. The lasing beam would normally be a constant diameter, although on long path length devices, some refocusing is desirable. If the laser is to be utilized at its focal plane, the spread of the beam in the focal plane, due to turbulence in the lasing medium, is of interest.

Examples of Correlation of Experiment with Theory and Comparison of Similar Theories

In the literature, the majority of the publications on the propagation of an electromagnetic wave through a randomly varying medium are of

a theoretical nature. This experiment will be concerned with only the prediction and measurement of beam spread. The 1965 paper by Collins and Wortendyke reported one of the efforts to correlate the propagation of finite rectangular plane wave with one of Tatarski's solutions. This effort is one of the better attempts to make measurements in a controlled environment. The turbulence properties of the flow field were not measured, but calculated from the results of a similar experiment in another facility. The claim of Collins and Wortendyke's work was order of magnitude agreement with theory, with factors typically ranging from two to seven times the theoretical value of the power scattered. Experimental results are presented of power scattered or spread as a function of mean temperature rise, angle of scattering, and scattering volume. In general, the slopes of the curves in addition to differing in absolute value from the analytical predictions, they also differ in the relative amount of parametric change in the experimental curves from the analytical predictions. Further examination of the experimental results also shows that two of the three experimental curves for the volume dependence of beam spread have the opposite slope of the theoretical curves. There exists in the literature very weak experimental documentation of even the trends of the simplest analytical models. There are virtually no thorough experimental investigations of the limits of applicability of the theoretical models. As a result, when examining much of the experimental work, it is not clear whether the theoretical models are inadequate or whether the lack of accurate turbulence measurements precludes an accurate prediction.

A report which should be included in the literature surveys is the 1971 Riverside Research Institute's, "How Well Can Laser Radiation be Focused Through the Atmosphere," by Greenbaum. Greenbaum points out the significantly different theoretical predictions of spot size obtained by Gebhardt and Collins (Gebhardt and Collins, 1969, a paper based on Gebhardt's 1968 paper) and that of Freid (Freid, 1966). Greenbaum's figure comparing the two theories is shown in Figure 3. Greenbaum's Reference 3 curves refer to Gebhardt and Collins' work and his Reference 4 refers to Freid's work. The possibility of more than order of magnitude differences between similar theories is clearly indicated by Greenbaum's comparison.

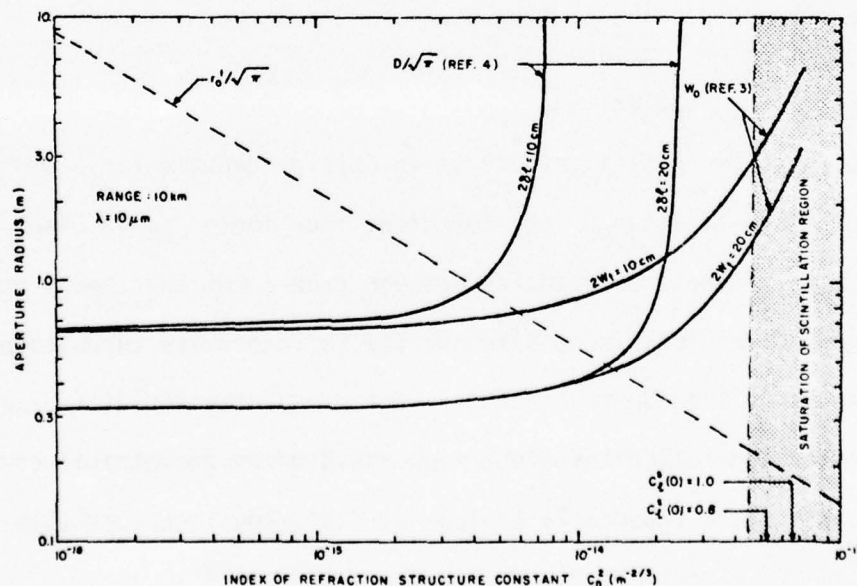


Figure 3. Greenbaum's Comparison of Required Initial Beam Radii Given Maximum Allowable Focal Spot Diameter

It is apparent that the experimental data currently available are inadequate so that neither the trends nor the quantitative predictions of the numerous analytical approaches which are available can be judged. The experimental information which is missing most often is an accurate description of the turbulent flow field. This is in part due to the fact that design and control of experimental parameters to cover all ranges and explore the boundaries of even one theory's variables is a sizable undertaking.

Since the initial interest in this problem arose from the desire to accurately predict what portion of the beam spread of fast flow lasers might be due to turbulence, within the lasing cavity, the selection of the experimental parameters will be based upon those typical of laser cavities rather than the values which are necessary to prove or disprove any one particular theory.

Statement of the Problem

The objective of this effort is to obtain adequate experimental data, both in definition of the turbulent flow field and in beam spread, to determine if the discrepancies between experiment and theory for the prediction of the focal spot size are due to inadequate turbulence measurements or inadequate theories. These measurements will be accomplished in a controlled turbulent flow field under geometrical constraints which are reasonably typical of fast flow laser cavities.

Selection of Experimental Parameters and Their Ranges

The parameters which appear in the theoretical expressions (Chernov, 1960; Tatarski, 1961; Freid, 1966; Gebhardt, 1968; Gebhardt and Collins,

1969; Sutton, 1969; Lutomirski, 1970; Lutomirski et al, 1973) for beam spread include the fluctuation in the index of refraction $\langle \Delta n \rangle$, the laser beam diameter to wave length ratio, the laser beam diameter to integral scale of turbulence ratio, the path length, and under some conditions, the ratio of laser beam diameter to the microscale of turbulence (Lutomirski et al, 1973). For integral formulation, the ratios to the beam diameter to wave length or turbulence scale are not always readily apparent (Lutomirski, 1970).

Initially, consideration was given to making turbulence measurements in a fast flow CO_2 laser cavity. The expected range of experimental conditions is then rather limited to a specific laser's limited range of operation. Beam quality can also be coupled with the particular operating point.

While cold flow turbulence measurements can be obtained in actual laser cavities with conventional techniques, hot flow turbulence measurements or measurements with excitation and lasing of the flowing medium would be exceedingly difficult to obtain. Since analytical predictions and experimental measurements currently differ by an order of magnitude, the confirmation of the predicted analytical trends are the first issues to be resolved. Selection of a very simple and controllable turbulent flow field is in order to eliminate the uncertainties associated with unconventional measurement techniques which would be required in a laser cavity.

The investigation of focal spot size for laser wave lengths, such as CO_2 , requires additional analytic considerations since the wave length and the scale of turbulence are of the same order of magnitude.

Once again, it must be considered that even when the wave length is much smaller than the turbulence scale size (in the visible spectrum of wave lengths), the analytic prediction and experimental measurements are at best only within an order of magnitude of each other, and even then trends are not necessarily consistent with theoretical predictions as was shown previously. The use of a CO_2 wave length and the associated complications with windows, stability, alignment, and safety requirements are not necessary to resolve the fundamental issues. Two wave lengths, He Ne, 532.8nm, and He Cd, 441.6nm, were selected for this investigation.

It was previously indicated in Examples of Laser Cavity Flows that the ratio of laser beam diameters to turbulence scale size ranges from $\ll 1$ to ~ 1 . Figure 4 shows the range of beam diameters which are possible with a conventional Spectra Physics collimator and beam expanding telescope for He Ne and He Cd. Also shown in Figure 4 are the comparable curves for HF, DF, CO, and CO_2 lasing mediums for the range of beam diameter to wave length which can be obtained from the He Ne and He Cd beams with the conventional Spectra Physics beam expanding telescope. Apertures and lenses were selected for the Spectra Physics beam expander to give nominally 50mm, 26mm, and 8mm He Ne beams.

The scale of turbulence is controlled by the physical dimensions of the turbulence generator, the diameter of a rod, the diameter of the perforation, or the mesh size. The turbulence Reynolds numbers typical of laser cavities were indicated (in Examples of Laser Cavity Flows) to be quite low. The integral scale of Reynolds number will later be shown to be related to the microscale by the relation:

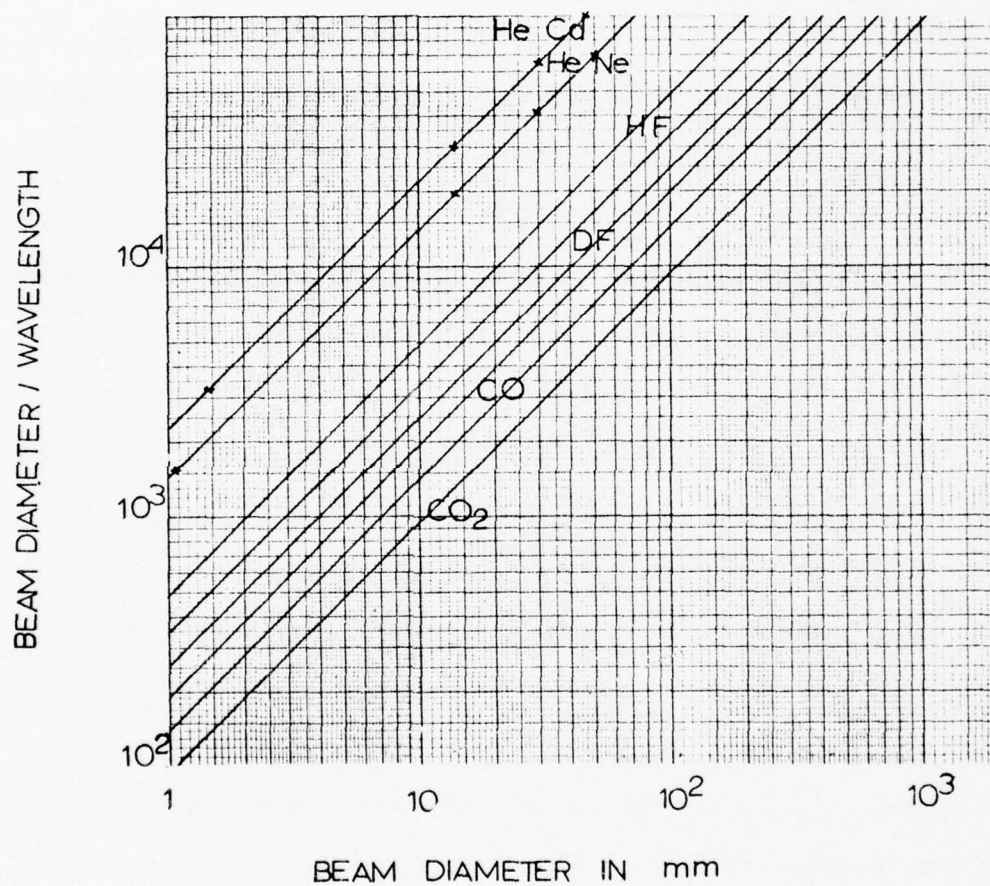


Figure 4. Beam Diameter Scaling

$$\lambda_0/\Lambda = \frac{\sqrt{A_g}}{\sqrt{R_\Lambda}} \quad (3)$$

where A_g is a constant which ranges between 4 and 30. Relation (3) is displayed in Figure 5. The range of microscales to integral scales, which would be expected to be found in the different types of laser cavities, has been indicated in Figure 5. The Reynolds numbers are seen to run from the critical range to 20,000. The EAL has integral Reynolds numbers in the range from 300 to 8,000 due to the low velocities and cavity densities. Typical pulsed laser cavities exhibit integral Reynolds numbers on the order of 10,000. Even the wakes from GDL nozzles are seen to be in the range of 200 to 20,000. The size of the wake shed by a nozzle is proportional to the boundary layer thickness. Scaling of the boundary layer thickness is $\propto Re^{.5}$ to $Re^{.2}$, depending on whether the flow is laminar or turbulent. Since the boundary layer in the nozzles is quite small, the Reynolds number is likewise, quite small. Simulation of turbulence Reynolds numbers in the range of 100 to 10^4 is of interest in terms of scaling the effects of the integral and the microscales on beam quality for the GDL. Pulsed lasers generally operate at higher pressures and turbulence Reynolds numbers are on the order of 9,000 to 17,000. The range of turbulence Reynolds numbers, which are of interest for cavity propagation problems, ranges from 100 to 20,000.

The range of turbulence Reynolds numbers which are feasible in the AFIT 23 centimeter wind tunnel are indicated in Figure 6. Figure 6 shows lines of constant velocity, on which the tunnel is capable of operating. The tunnel will control and repeat tunnel velocity settings from .61 meters per second to 16.8 meters per second with an empty test section.

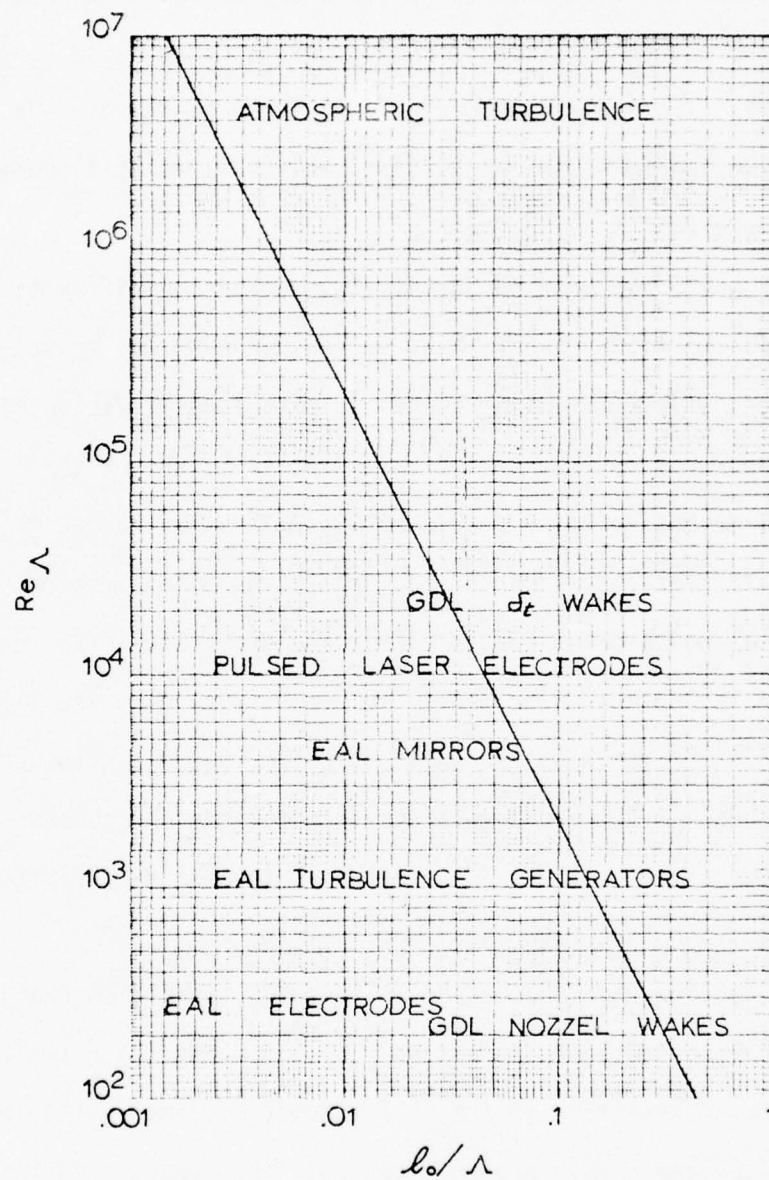


Figure 5. Laser Cavity Scales of Turbulence

Turbulence generators with characteristic diameters of .045, .64, and 1.27 centimeters were chosen as the dimensions of the turbulence generators for this work. The scales associated with these generators are indicated by the horizontal lines across the range of available tunnel velocities in Figure 6.

The criteria which are used to justify the neglect of diffraction effects state that the microscale λ_0 must be greater than the square root of the product of the wave length and the path length, $\sqrt{\lambda L_0}$. Figure 7 displays the range of $\sqrt{\lambda L_0}$ in typical laser cavities for the lasing mediums of He Cd, He Ne, HF, CO, and CO₂. The $\sqrt{\lambda L_0}$ ranges from .5 centimeter to 13 centimeters for HF and from 1 to 30 centimeters for CO₂. The figure also indicates that a microscale greater than .5 centimeter is required in the AFIT wind tunnel in order to neglect the diffraction effects for helium neon and helium cadmium lasers. Although the results from this effort are not intended to include any consideration of diffractive effects, the results may nevertheless have limited direct implications for fast flow laser applications.

The path length and the fluctuation in index of refraction remain as experimental parameters to be specified. A single pass path length of 23 centimeters was available in the AFIT tunnel; however, multiple passes could be achieved. Only a single pass will be reported in this work, although limited data were also collected for three and five passes. The fluctuations in index of refraction are introduced by heated wires such that beam spreads up to three times a diffraction limited beam could be achieved.

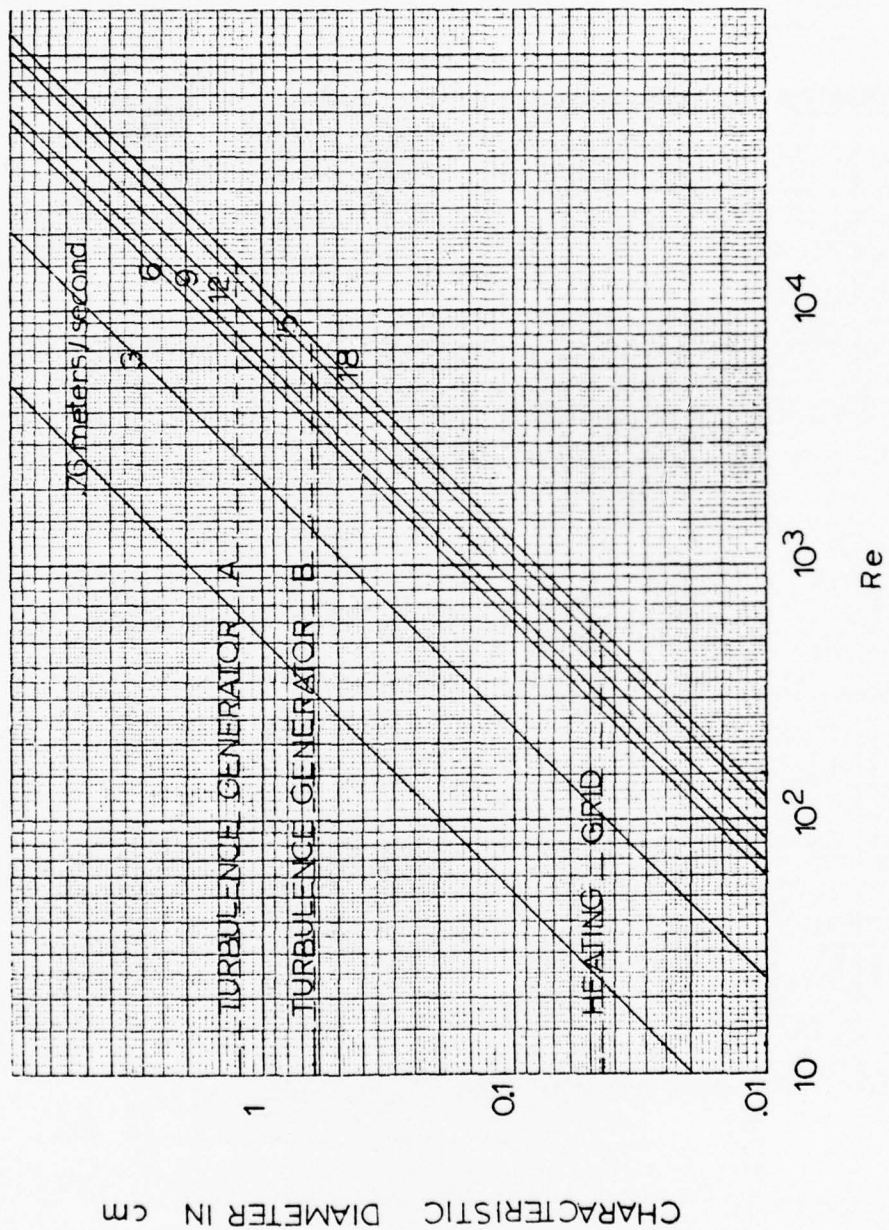


Figure 6. Reynolds Number and Turbulence Scale Capability of the 23 cm AFIT Tunnel

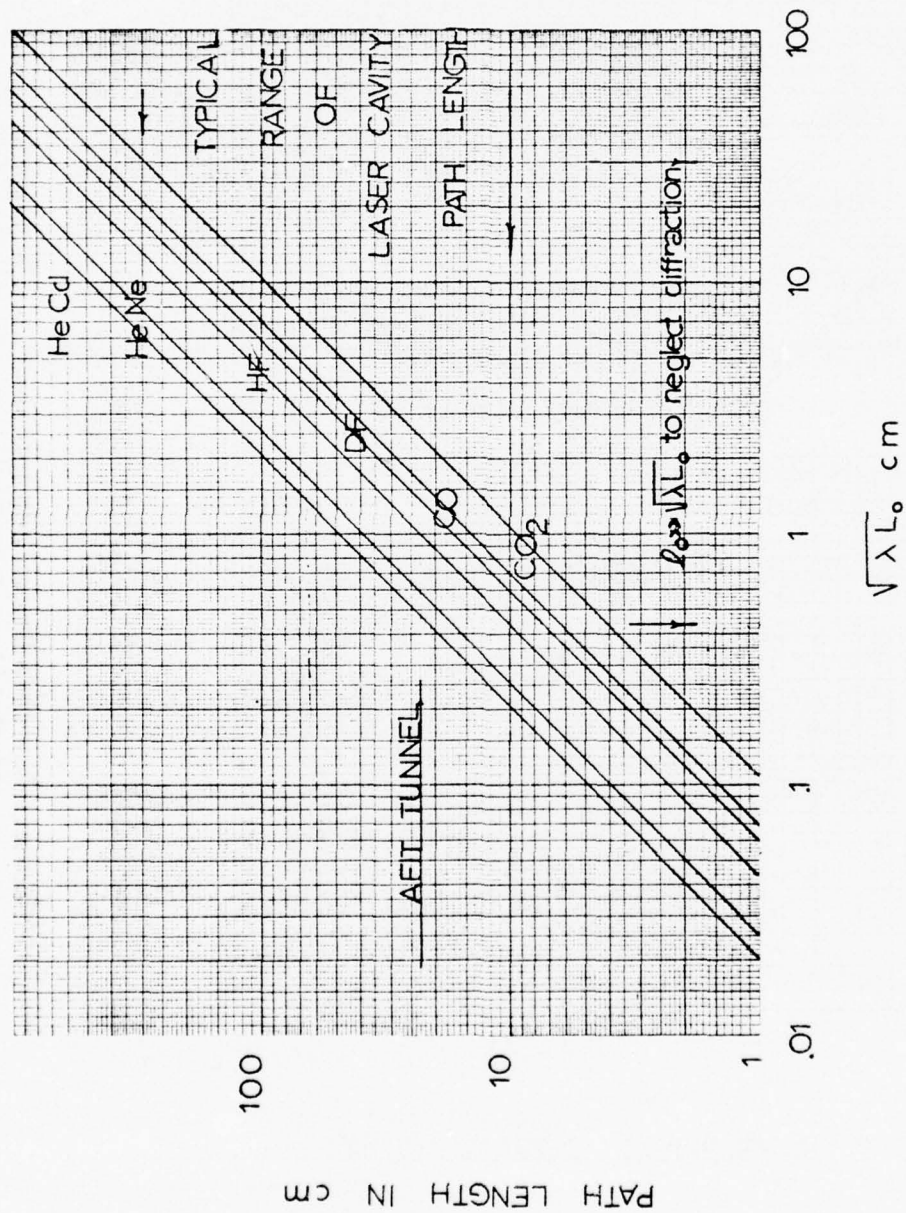


Figure 7. Path Length Limitations for Geometric Optics or the Neglect of Diffractive Effects

Scope of the Investigation

By varying optical and fluidic lengths, temperature, and temporal scales, the range of flow parameters applicable to fast flow laser cavities will be considered in order to determine whether the analytical predictions are functionally correct, accurate, and to improve the base of experimental information from which the predictions of beam spot size may be formulated for laser cavities. The experimental investigation will emphasize low values of turbulence Reynolds numbers where there is very limited experimental data. The fluctuations in index of refraction will range through strong turbulence conditions.

The range of parameters which will be investigated are as follows:

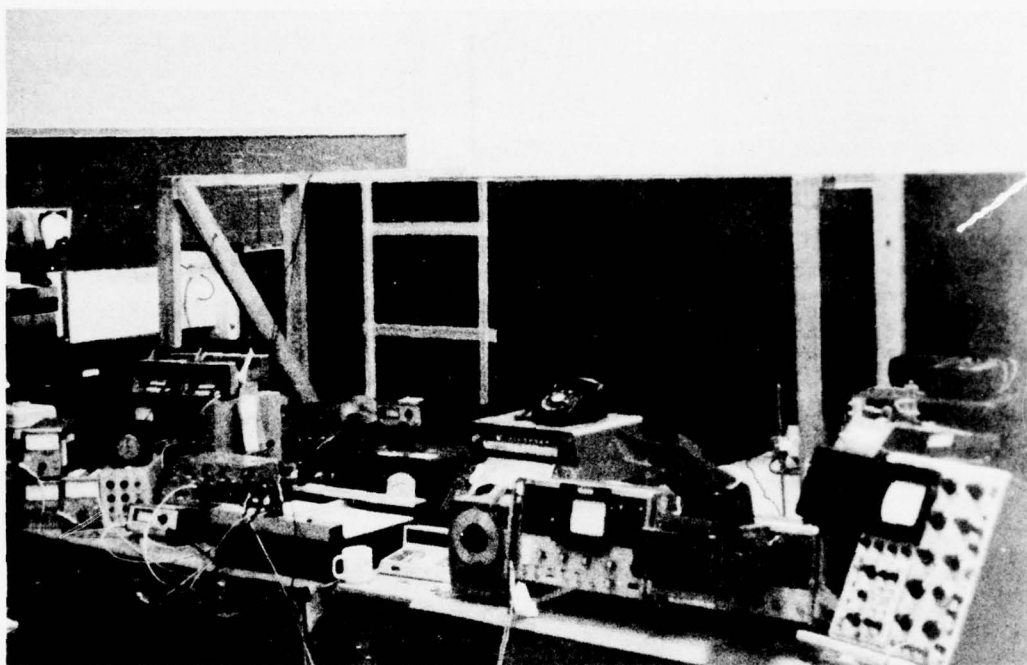
1. Mean fluid velocity ranged from zero to 20 meters per second
2. Turbulence Reynolds numbers to 16,000
3. Velocity turbulence intensities to 40%
4. Temperature turbulence intensities to .6%
5. Index of refraction fluctuations to 3.7×10^{-6}
6. Propagation path length - 23 cm
7. Nominal laser beam diameters - 50mm, 30mm, 14mm, and 1.5mm
8. Wave lengths of the laser beams of 632.8nm and 441.6nm
9. Beam diameter/turbulence scale - $D/\Lambda \ll 1$ to $D/\Lambda \sim 1$
10. Attenuation coefficient (to be defined in Chapter IV) -
 $\alpha L_0 \ll 1, \alpha L_0 \sim 1, \alpha L_0 > 1$

CHAPTER III

APPARATUS AND INSTRUMENTATION

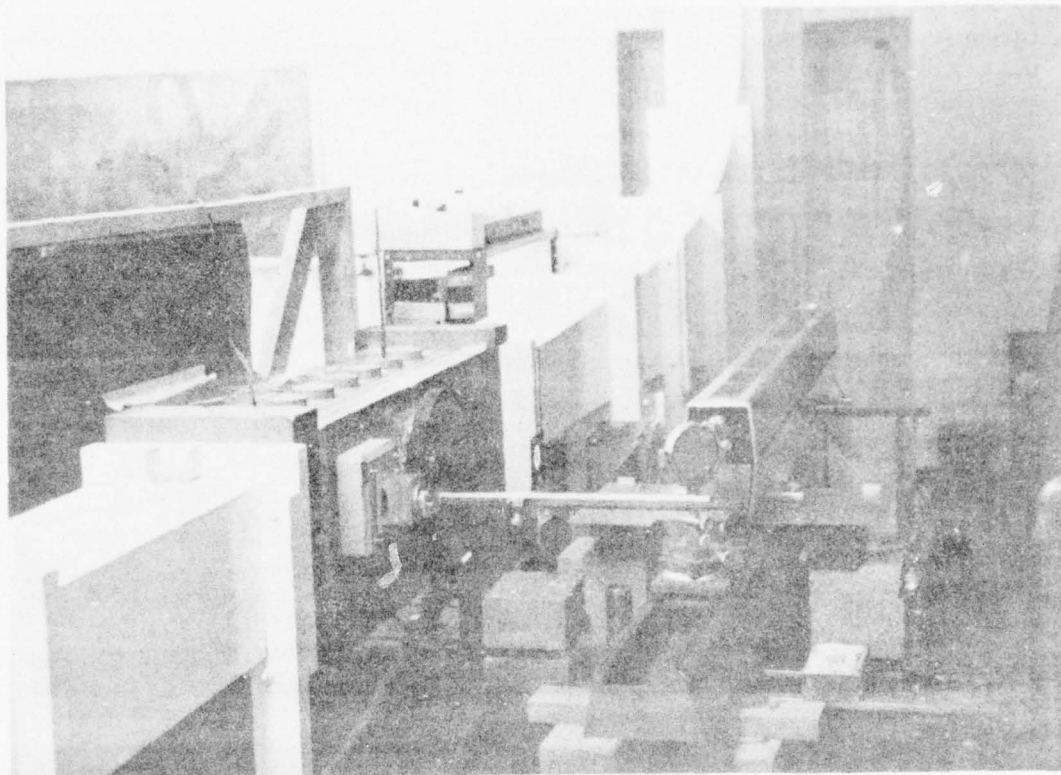
Schematic of the Experimental Apparatus

The experimental set-up will be traced from the open circuit wind tunnel through the instrumentation employed for data acquisition, including the on-line real time computer used for calculation of the correlation function. Photographs identifying the major components of the apparatus and instrumentation are shown in Figures 8 and 9. The laser is mounted either normal or parallel to the longitudinal tunnel centerline and then turned through 90° on the tunnel horizontal centerline. Figure 8 shows the 50 milliwatt He Cd laser in position. The laser beam is expanded and spatially filtered. The output beam is then passed through a final aperture of the desired diameter. The laser beam may be positioned ± 10 centimeters along the tunnel centerline by moving either the laser or the 90° turning mirror on an optical bench parallel to the tunnel axis. A schematic of the experiment and the optical path is shown in Figure 10. A template was used to relocate and position the beam to the same geometric location in the tunnel. The expanded laser beam enters and leaves the turbulent medium through interferometer quality windows which are parallel and flush with the tunnel walls. The turbulence is controlled and generated at a fixed location upstream of the tunnel windows. The beam, upon emerging from the tunnel, enters a



- | | | |
|----------------------|--------------------------|----------------------|
| 1. Mean Velocity | 9. x y Plotter for | 14. Light Pipe |
| 2. Mean Temperature | Display of Laser | 15. Power Supply for |
| 3. Anemometer | Focal Plane | Temperature |
| 4. RMS Velocity | Traverse | Turbulence Gen- |
| 5. RMS Temperature | 10. 3-D Traverse Control | erator |
| 6. RMS Laser Power | 11. Correlator | 16. Visicorder for |
| 7. Mean Laser Power | 12. Spectrum Display | Dynamic Display |
| 8. Laser Power Meter | 13. AFIT 23 cm Tunnel | of Laser Focal |
| | | Plane Traverse |
| | | 17. Optical Table |

Figure 8. Identification of Apparatus and Instrumentation



- | | |
|--|------------------------|
| 1. AFIT 23 cm Tunnel | 5. Optical Bench C |
| 2. Test Section of Tunnel | 6. Optical Bench D |
| 3. Horizontal Traverse Mechanism for Hot Wire | 7. 45° Turning Mirror |
| 4. Helium Cadmium Laser | 8. Beam Aperture |
| | 9. Tunnel Window Mount |

Figure 9. AFIT 23 cm Tunnel with 50 Milliwatt Helium Cadmium Laser

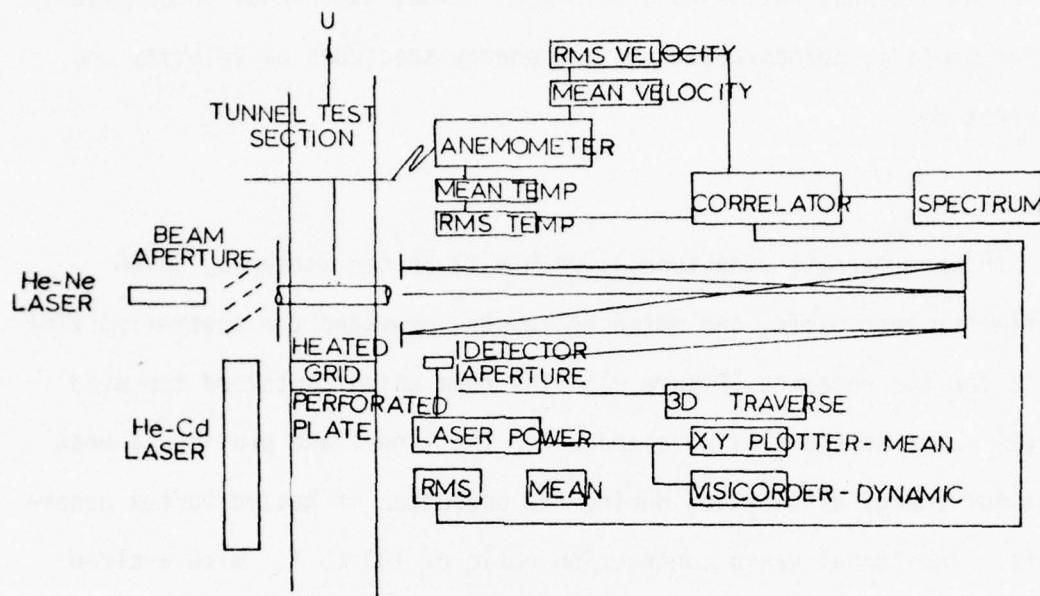


Figure 10. Schematic

light pipe in which it makes six traverses in order to reach the far field for the largest beam diameter used. Although near field measurements or data are also of interest in laser cavities, only far field measurements will be reported in this work. The rationale being to examine the effect at a target due to cavity disturbances. The beam for all measurements to be reported in this work was focused at 45.7 meters. At the focal plane, an aperture is traversed across the plane and the transmitted power measured with a thermopile. The spatial distribution of the energy spectrum and autocorrelation of the laser beam was measured for the laser beam at the focal plane. The turbulence parameters were obtained by double parallel hot wires. The wires were operated at

different overheat ratios to obtain mean value, turbulence intensities, tunnel profile, autocorrelation, and energy spectrums of velocity and temperature.

Wind Tunnel

An open circuit wind tunnel, with a 22.86 centimeter by 22.86 centimeter test cabin, one meter in length, provided the controlled flow field for the research (Figure 9). The room which contained the wind tunnel acted as the closing element for the tunnel and provided a heat sink for energy dissipation during the operation of heated vortex generators. The tunnel has a contraction ratio of 100 to 1. With a clean test cabin, the tunnel is capable of velocities of 18.34 meters per second, with a turbulence intensity level (u'/\bar{U}) of 10^{-3} and a wall boundary layer 0.025 meters thick at the mid-point of the test cabin. The test cabin was fitted with two interferometer quality windows 0.203 meters in diameter, isolated and independently suspended from the tunnel by a mounting on an optical bench. The windows were aligned parallel to the flow and held to a divergence angle less than one part in 7000.

Vortex Generators

Two vortex generator systems were utilized to introduce random fluctuations into the flow field. First, a perforated plate mounted normal to the flow upstream of the mid-point of the test cabin provided controlled velocity fluctuation. Second, an array of parallel nichrome wires normal to the flow and located between the mid-point of the test cabin and the perforated plate provided temperature fluctuation.

Two different perforated plates were used to provide fluctuations in the velocity field and variation in turbulence scale. Plate A was 0.317 centimeter thick with a sixty degree array of .197 centimeter diameter holes with a blockage of 52.5 percent. The plate was located 14 hole diameters upstream from the test cabin mid-point. The other plate, Plate B, was 0.317 centimeter thick with a sixty degree array of .098 centimeter diameter holes and a blockage of 65.2 percent. The plate was located 34.5 hole diameters upstream from the test cabin mid-point.

The empirical relationship between the microscale and the integral scale was given previously by equation (3) as:

$$\lambda_0/\Lambda = \frac{\sqrt{A}g}{\sqrt{R_\Lambda}}$$

The scale size of turbulence may be controlled experimentally by varying the mesh size or the characteristic length of the shedding element and the free stream velocity as is shown by the equation above for the microscale. The relationship between integral and microscale may be controlled experimentally as shown by the empirical equation (3) by varying the Reynolds number of the flow. The dependence of the integral scale upon the free stream velocity and the characteristic length of a shedding element is illustrated by the Strouhal relationship:

$$f = D_p/\bar{U} \quad (4)$$

where f is the frequency, S the strouhal number, and D_p the diameter of the shedding element.

Experimental control of temperature fluctuations is required, since the primary effect of random fluctuations on the laser beam being

propagated through the medium results from fluctuations in temperature which cause fluctuation in the index of refraction. Temperature fluctuations were introduced into the tunnel by a grid of electrically heated nichrome wires. The wires were .046 centimeter in diameter, on 2.54 centimeter centers, beginning 2.54 centimeters from the tunnel upper wall. The power input into the wire grid ranged from .57 to ~ 1.2 kilowatts, or a mean temperature rise of the flow field of up to 53°C . The wire grid was located 10.16 centimeters downstream from the perforated plate and in a plane normal to the windows. Temperature fluctuations, although they decay slower than velocity fluctuations, show similar relationships to those of velocity fluctuations. Similar decay curves for both velocity and temperature have been measured (Mills, Kistler, Obrien and Corrsin, 1958, p. 47, Figure 17, and p. 50, Figure 19). The decay rate of the ratio of velocity to the temperature field approaches .6 for large values of x/D_p . The ratio of integral temperature scale to the integral velocity scale is greater than .9 for temperature and velocity turbulence generators which have the same characteristic diameter (Mills, Kistler, Obrien and Corrsin, 1958, p. 66, Figure 30).

Anemometer System

Mean and rms velocity and temperature profiles of the tunnel were obtained with a Thermo'Systems (TSI) Model 1050 anemometer, Model 1057 signal conditioner, and Model 1052 polynomial linearizer. The signal conditioner was used primarily as an amplifier for cases of very small temperature fluctuations. The linearizer was used only for x probe

measurements since higher accuracies are achievable with direct readings, particularly at low velocities (~ 1 m/sec). The measurement of temperature and velocity will be discussed in detail in Chapter IV.

The local temperatures and velocities were obtained with parallel wires, Thermo Systems Probe Model 1244 T 1.5. During optical measurement, the wires were located at the downstream edge of the beam on the horizontal centerline of the beam and at the lateral center of the tunnel. Tunnel traverses will be reported with the wire at the beam centerline location.

Optical Components

Optical Bench

A three-ton cast iron bed plate, two by three meters, isolated from building vibrations by 2.54 centimeter thick pads of 40 durometer rubber, was used as a table to support optical benches. Two optical benches were utilized. Bench C supported the tunnel windows and the helium neon laser. Bench D supported the helium cadmium laser. Bench D was necessary due to the size of the helium cadmium laser and the lack of room normal to the propagation path. Bench E was a two-ton bed plate (1 by 2.5 meters). It was located seven meters from the wind tunnel on a line normal to the tunnel at the test cabin mid-section. The table supported the common mirror used to fold the laser beam back and forth across the room.

Laser Sources

A 15 milliwatt Spectra Physics Model 124A helium neon and a 50 milliwatt Spectra Physics Model 185 helium cadmium laser were used

as the sources. The long term drift for the sources was indicated by the manufacturer to be less than 5% and the beam amplitude noise and ripple to be less than .3% rms from 120 Hertz to 100 Kilohertz. The output beam diameter at $1/e^2$ for the helium neon laser is 1.1 millimeters and 1.5 millimeters for the helium cadmium laser. The output beams of these lasers were expanded with the Spectra Physics Model 336 and 332 collimating lens, expanding lens, and spatial filter assembly. Nominal beam diameters of 50 millimeters, 26 millimeters, and 8 millimeters in diameter were obtained for the helium neon and helium cadmium lasers. Results with the 1.5 millimeter helium cadmium beam will also be reported. The laser beam was focused by the Model 336 collimating lens at a distance of 45.70 meters. The beam remains approximately constant in cross section across the tunnel. $D_{\text{enter}}/D_{\text{exit}}$ for the 50 millimeter diameter beam is 1.0025. The 50 millimeter diameter beam overfilled the collimating lens such that the lens assembly acts as a 50 millimeter aperture. Additional exit apertures were used for the smaller diameter beams to reduce the fringing and provide a clean gaussian input beam to the tunnel test section.

The Light Pipe

Because the total optical path was 200 times the turbulent medium path, a light pipe was required to reduce the background noise to acceptable levels. The laser beam path length, measured from the exit of the wind tunnel test cabin to the focal plane, ranged from 6 to 45.7 meters. This path length was provided by folding the beam inside of a light pipe. Three light pipes were utilized during the course of the investigation. Light Pipe A was a 20 centimeter diameter aluminum

duct seven meters long. Due to the limited laser beam space in Pipe A, a second light pipe, Pipe B, was built. It was a .92 by .92 meter rectangular duct, seven meters long, fabricated from visqueen wrapped on a wood framing. In order to enhance the signal to noise ratio of the output of the laser beam and minimize the breathing observed with the visqueen, the visqueen light pipe was replaced by a solid structure fabricated from masonite as shown in Figure 7. After enclosure of the external optical path, the rms value of laser fluctuations at the focal spot, after traversing the external optical path, was nominally within the laser stability specifications of .3%. Both the visqueen and masonite enclosures met the laser stability criteria.

Beam Diagnostics

The distribution of laser beam intensity and fluctuations in intensity at the focal spot are the two simplest observable qualities which can be analytically predicted at this time. A large number of simultaneous intensity or local power measurements are required to accurately describe the statistics of a beam which has been propagated through a random medium. For a number of C. W. laser applications, the time averaged laser beam power at the focal spot is of interest as well as the dimension averaged spot size. A measurement of the time averaged distribution of spot size will be reported in this work.

To obtain the distribution of the time averaged laser beam power, a circular aperture was traversed across the focal plane of the laser beam. The local beam power was obtained from a Spectra Physics Model 401C power meter. The traverse of the focal plane was accomplished by an electrically driven three-dimensional traverse mechanism, shown in

Figure 11, located within the light pipe. Also shown in Figure 11 is a manual traverse which had a resolution of 3.93×10^{-5} centimeters, which was discarded in favor of the electrical unit to further reduce the background noise level. The manual traverse exhibited a higher noise level due to the required opening for the manual traverse in the light pipe. All traverses were made in the vertical plane beginning at the bottom of the focal spot. The focal plane was located at a distance of 45.7 meters from the test cabin. Traverses were made after initially determining the location of the focal plane along the beam path. Subsequent measurements were made after maximizing the power normal to the path of propagation, $I_{x_{\max}}$, $I_{y_{\max}}$.

Correlator

The scales of the random fluctuations were obtained from the correlation function as will be discussed in Chapter IV. The correlation function for temperature and velocity was obtained from a Hewlett Packard Model 3721A correlator. The energy spectrum of the fluctuations was obtained by taking the Fourier transform of the autocorrelation function with a Hewlett Packard Model 3720 spectrum analyzer. The correlation function is given by:

$$\lim_{t \rightarrow \infty} \frac{1}{t} \int_0^t [A(t) B(t-\tau)] dt \quad (5)$$

where τ is the delay time between each calculated point and $A(t)$ and $B(t)$ are the real time functions for which correlation is desired. The correlator calculates the correlation function for 100 points, each delayed from one another by τ where τ is variable from 1 usec to 333 millisec. The correlator accepts inputs from DC to 250 Kiloherztz. The

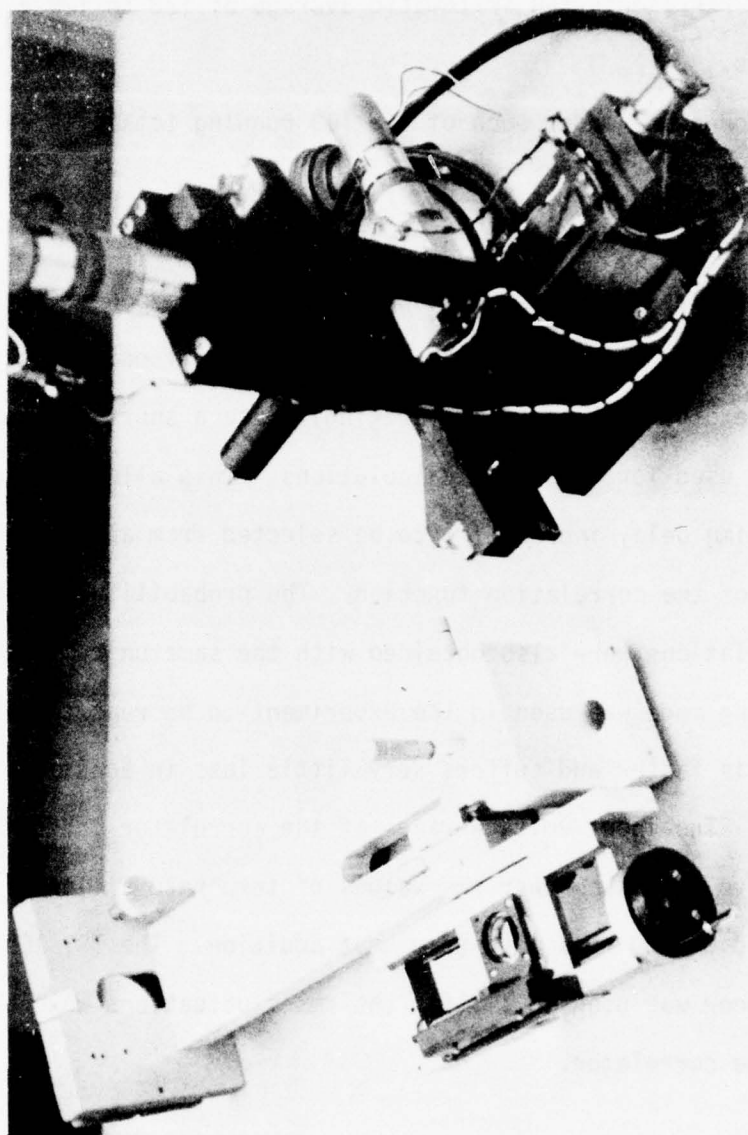


Figure 11. Traverse Mechanisms

correlator is digital and has two averaging processes, an arithmetic average or summation mode, and an exponential average. In the summation mode each point represents the arithmetic average of 128 to 128×1024 (N) calculations.

In the exponential mode, each of the 100 running totals is calculated as:

$$\text{Old Total} + (\text{New Sample} - \text{Old Running Total})/N$$

The number of samples or sweeps for each point in the exponential mode is 1 to 100 times N. A quick look at the correlation function is possible with the exponential mode of averaging, since a short time constant $N \times \tau$) is used for the early calculations. This allows the proper amplitude and time delay increment τ to be selected from a few seconds of observation of the correlation function. The probability density and cross correlations were also obtained with the same unit. The exponential averaging mode was used in the experiment to be reported in this work, since it is faster and suffers very little loss in accuracy to the summation mode. The input voltage range of the correlator is from .04 volts rms to 4 volts rms. Lower rms values of temperature fluctuations were encountered during runs with zero heat addition. The TSI 1057 signal conditioner was used to amplify the rms fluctuations when below the range of the correlator.

CHAPTER IV

EXPERIMENTAL TECHNIQUES AND PARAMETER CALCULATION PROCEDURES

In order to quantitatively evaluate the effect of turbulence on a laser beam propagating through the turbulent medium, experimental evaluations of analytical expressions such as Sutton's (Sutton, 1969, p. 1741) equation for beam spread

$$\frac{\theta_T}{\theta_0} = \left(\frac{\alpha L_0}{2\pi} \right)^{1/2} \frac{D}{\Lambda}, \quad \alpha L < 1 \quad (6)$$

α = the extinction coefficient

θ = the angle of the point where the laser intensity curve has fallen to $1/2 P_0$

$$\alpha = 2 k^2 \Lambda \langle \Delta \eta^2 \rangle \left(1 + \frac{k^2 a^2 \lambda^2}{D^2} \right)^{-5/6}$$

$k = 2\pi/\lambda$

$\Delta \eta$ = the fluctuations in the index of refraction

Λ = the integral scale of turbulence

L_0 = the light path through the turbulent medium

D = the laser beam diameter

a = energy containing turbulence wave length

is typically required. The fluctuating component of the index of refraction is in turn related to the fluctuating component of temperature. In order to control and measure the fluctuating component of temperature,

both velocity and temperature must be measured. The velocity determines the mean temperature rise of the turbulent medium through the tunnel mass flow rate. This mean temperature rise then bounds the level in fluctuations in temperature. In the first section of this chapter, Flow Field Measurement, the applications, calibration, and frequency response limitations of a hot wire anemometer to measure both the mean and fluctuating components of velocity and temperature will be discussed in detail. The calculation of the fluctuating component of index of refraction from the temperature fluctuations will be given in the Flow Field Measurement section. Because the analytical calculations of laser beam spread require the integration of the fluctuations in the index of refraction (in planes perpendicular to the propagation direction) along the laser propagation path, the temperature, velocity, and fluctuating components of temperature and velocity, as well as the calculated value of index of refraction and its fluctuating component values, were obtained along the laser beam centerlines. The procedure for calculation of these mean profile values will be given in the Flow Field Measurement section. The second section of Chapter IV, Correlation Measurements, will discuss techniques for calculating the scales of turbulence which appear in equation (6). The scales of turbulence will be obtained from the autocorrelation functions of temperature and velocity. Section two of this chapter will formulate the autocorrelation functions and develop three calculations of the microscale and one calculation of the integral scale. The third section of this chapter will discuss the techniques and calculations which were employed to obtain measurements of the laser beam spread in the focal plane, θ_T/θ_0 .

Flow Property Measurement

The measurement and interpretation of velocity and temperature in a highly turbulent flow field is non-trivial, even when the flow in the test section is very slow. The heat addition required to create significant fluctuations in the index of refraction results in even larger fluctuations in both temperature and velocity, further complicating an accurate measurement of fluctuating properties.

If Rayleigh flow is considered through the test section for tunnel velocities from .3 to 18 meters per second and for non-dimensional heat additions ($q/C_p T_1$) of 3.15×10^{-3} to .187, the observed static and stagnation temperatures are found to correspond to one another within the measurement accuracy of temperature. The mean temperature rise ranges from .9° to 53°C. Static and total pressure remain about ($\Delta P/P_0 = .0024$) constant and equal to barometric pressure. On the other hand, density and Mach number also change significantly for Rayleigh flow and may not be assumed equal to the preheat addition values.

Even though the use of a hot wire for determining the flow and turbulence properties of the test section gives only approximate results, this method of measurement is one of the best and conventionally employed techniques available. The problems which must be considered in the use of a hot wire for measurement of the test section properties include: separation of the effects of temperature, velocity, and density on the probe, the effect of high turbulence levels on heat transfer, the effect of large values of turbulence on the mean value of velocity and temperature, the frequency response of the probe and definition of the flow regime (continuum to free molecular) in which the probe must operate.

The flow regime is defined by the Knudsen number:

$$Ku \equiv 1.26 \sqrt{\gamma} M/Re \quad (7)$$

Due to the small probe diameter and the wire operating temperatures, slip and even free molecular flow can occur for very slow flows (Sandborn, 1972, p. 55-88). Knudsen number for the range of conditions expected ranges from .27 to .013. For a flow to be considered to be continuous, Ku should be $\leq .01$. This definition is somewhat arbitrary and the range of values given above will be considered to represent continuum flow. A change in flow from continuum to slip flow should exhibit itself as a discontinuity in the heat transfer relation.

The Stanton number

$$S_t \equiv Nu/(Re \times Pr) \quad (8)$$

is normally used to describe fluid dynamic heat transfer; however, (Bradshaw, 1971, p. 113-114) there is a lack of systematic work in assessing the importance of the Prandtl number on wire calibration, the empirical relation given by Kramer and Van der Hegge Zijnen gives a Pr dependence as follows:

$$Nu = .42 Pr^{.20} + .57 Pr^{.33} Re^{.50} \quad (9)$$

for a Prandtl number of .714

$$Nu = .393 + .51 Re^{.50} \quad (10)$$

Bradshaw indicates that Bourke used

$$Nu = .75 Pr^{.20} + .67 Pr^{.9} Re^{.50} \quad (11)$$

giving:

$$Nu = .70 + .495 Re^{.50} \quad (12)$$

Equation (10) and (12) indicate that there is a wide range of weak dependencies upon Prandtl number. Neither of these efforts considered the specific application to hot wires. The systematic investigation of heat transfer from wires by Collis and Williams and the empirical relationship they developed represents the most accurate correlation of hot wire heat transfer data currently available. The heat transfer relation proposed (Collis and Williams, 1968, p. 369) is:

$$Nu \left\{ \frac{T_m}{T} \right\}^{-.17} = A_2 + B_2 Re^n \quad (13)$$

Where Nu is the Nusselt number given by:

$$Nu \equiv \frac{hd}{K} \quad (14)$$

Where h, the heat transfer coefficient, is defined by:

$$Q = \frac{E^2 R_1}{(R_1 + R_3)} = h \pi D \ell (T_w - T_f) \quad (15)$$

The wire heat transfer relationship then becomes:

$$\frac{E^2 R}{(R_1 + R_3)^2 \pi \ell K (T_w - T_f)} \left\{ \frac{T_m}{T} \right\}^{-.17} = A_2 + B_2 Re^n \quad (16)$$

A value of .45 is recommended for the exponent n (Collis and Williams, 1968, p. 370) for Reynolds numbers in the range of .02 to 44. In this expression, T_m is a mean film temperature coefficient defined as $(T_w + T_f)/2$. The thermal conductivity, density, and viscosity are all evaluated at this mean film temperature, T_m . The wire temperature is set by the overheat ratio selected for probe operation:

$$O H \equiv \frac{\text{Resistance Hot}}{\text{Resistance Cold}} = 1 + \delta (T_w - T_f) + \dots \quad (17)$$

It is clear that the sensitivity of the probe to temperature fluctuation can be increased by reducing the overheat ratio and likewise the

sensitivity to velocity can be increased by increasing the overheat ratio. One also has the option of operating a wire in a constant current mode or a constant temperature mode. The constant temperature mode has the advantage of a significantly higher frequency response since the wires thermal inertia is partially compensated for by an electronic feedback loop. Mean temperature and velocity can be measured by operation of two wires at different overheats such that both wires are sensitive to both temperature and velocity. This method requires the storage of large amounts of data for future processing or the instantaneous normalizing, squaring at the minimum, and addition and subtraction. Some time period must be allowed as an averaging period. However, the commercially available circuits to perform the arithmetic functions were found to be unacceptable for this experiment. The transfer functions and frequency responses appear inadequate for even well behaved inputs such as sine waves. The loss of experimental information due to the processing would have to be defined with a known source and this loss then extrapolated to this experiment. The taping and later reduction of data offers the possibility of the best accuracy; however, it represents a significant undertaking when time samples less than a millisecond are required. The experiment was expected to exhibit Strouhal frequencies up to 700 Hertz. Taped reduction of data was, therefore, considered feasible but not attractive until an initial assessment of the beam spread had been made.

The approach which initially appeared to offer an acceptable measurement capability and accuracy was to operate a double parallel wire, one wire at a high overheat for velocity and the other at a low overheat

for temperature. By operating the velocity wire in the constant temperature mode, and the temperature wire in the constant mode, a satisfactory selectivity between temperature and velocity was possible.

A Thermo Systems Model 1244 Probe was selected for measuring the velocity and temperature properties of the tunnel. The Model 1244 is a double parallel 3.81 μm diameter wire configuration. The probe was orientated with the wires in the vertical plane in the tunnel to minimize convective and mutual interference effects. The wire was selected over the more rugged thin films due to its increased frequency response. The frequency response of the velocity wire of Probe 1244, Serial Number 8712, is shown in Figure 12.

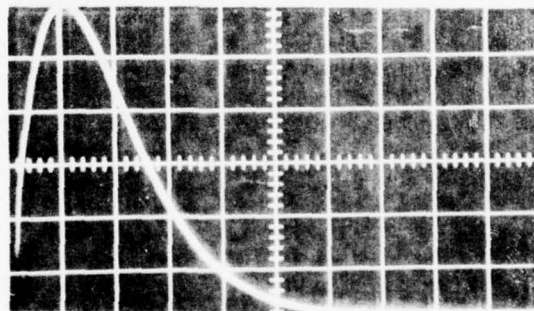


Figure 12. Frequency Response of Probe 8712, Wire No. 1,
Horizontal Time Scale 5×10^{-6} Seconds/Division
Constant Temperature - $0^\circ\text{H} = 1.5$

The frequency response indicated by superposition of a 1 KHz square wave upon the bridge probe combination, as is recommended by TSI and Freymuth (Freymuth, 1967, p. 680), is given by:

$$f_1 = \frac{1}{1.5\tau} \quad (18)$$

where τ is the time to return to 3% of the peak voltage. The frequency response given by Figure 12 is 22 KHz for the velocity wire. Although both the film and wire have adequate frequency response for the velocity and velocity turbulence intensity measurement, in the constant current mode, which is used to measure temperature, the electronic feedback circuit is removed and the frequency response of the probe is limited to that naturally exhibited by the probe itself. The 3.81 μm diameter wire, according to the manufacturer, has a 750 Hertz response at the -3db point in the constant current mode. A check of the wire frequency response may be made by illuminating the constant current wire with a laser which is mechanically chopped or by using a pulsed laser source. A helium cadmium laser, operating at 5 milliwatts, was used with two mechanical choppers to obtain the experimental frequency response of the wire in the constant current mode. A schematic of the arrangement which was used to measure the frequency response of the temperature sensor is illustrated in Figure 13.

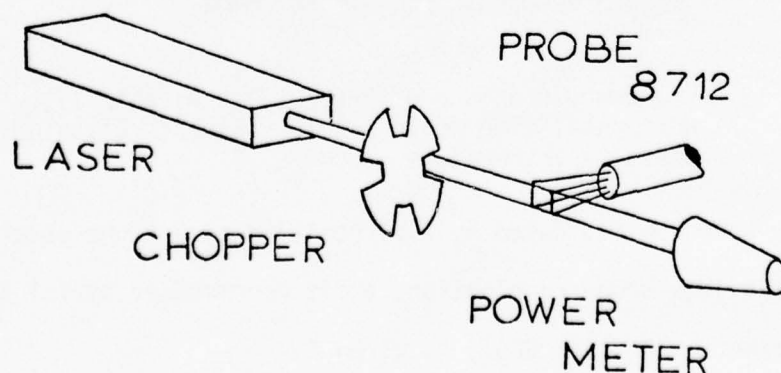


Figure 13. Schematic of Frequency Response Measurement

Figure 14 shows the chopped signal from the Spectra Physics 401C power meter located behind the wire, as the upper trace with the lower trace the temperature signal as the probe, in still air, is illuminated by the chopped laser beam. The power meter response shows that the wire is heated by a square pulse. The time to decay to $1/2 V_0$ corresponds to 812 Hertz, if the rise time of the pulse is neglected. If the time to decay definition given by equation (18) is used with Figure 14, the frequency response of the temperature wire would be 83 Hertz.

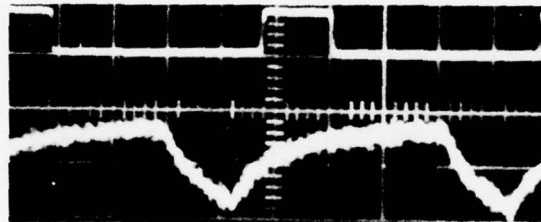


Figure 14. Frequency Response of Probe 8712, Wire No. 2,
Horizontal Time Scale 2×10^{-3} Seconds/Division
Constant Current Mode - 0 H = 1.15
Chopper Blade with Four Slots

Figures 15 and 16 show a sequence of photos of the frequency response of a wire in the constant current mode obtained with an Infrared Industries Model 830 Chopper, with a 40 slot blade, as the frequency was varied from 200 to 1200 Hertz. The normalized response curve obtained from Figures 15 and 16 is shown in Figure 17. The frequency response of the single pulse of Figure 14 is shown in Figure 18. The frequency scale of Figure 18 was expanded in Figure 19 to examine the single pulse curve below 800 Hertz.

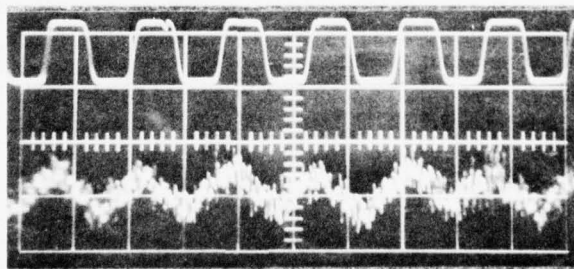
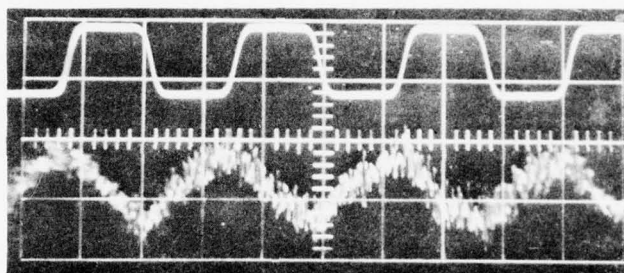
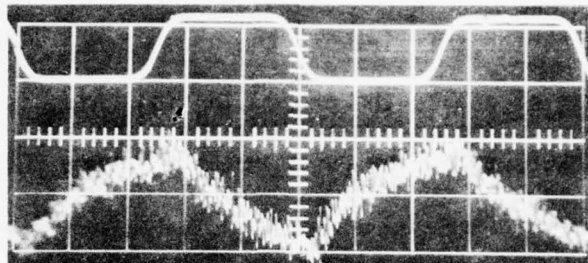


Figure 15. Frequency Amplitude for Probe 8712, Wire No. 2,
200, 400 and 600 Hertz Temperature Pulse

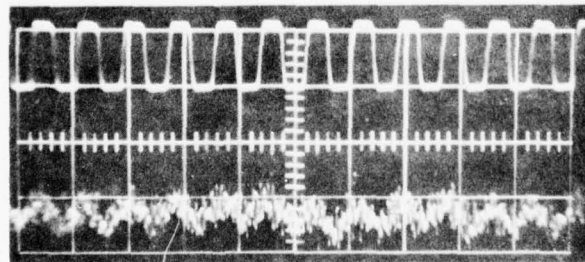
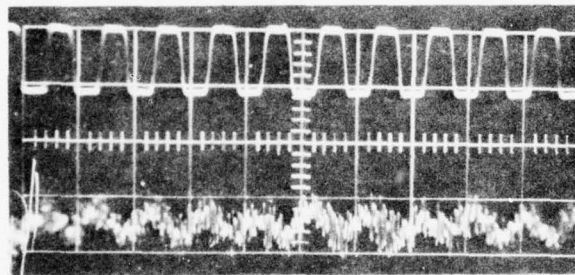
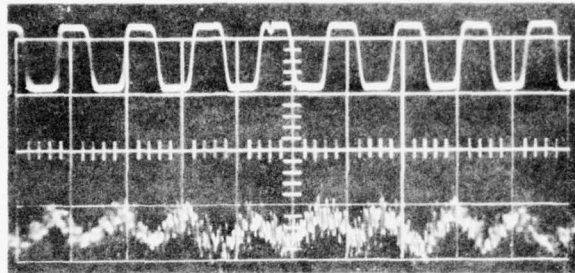


Figure 16. Frequency Amplitude for Probe 8712, Wire No. 2,
800, 1000 and 1200 Hertz Incident Temperature Pulse

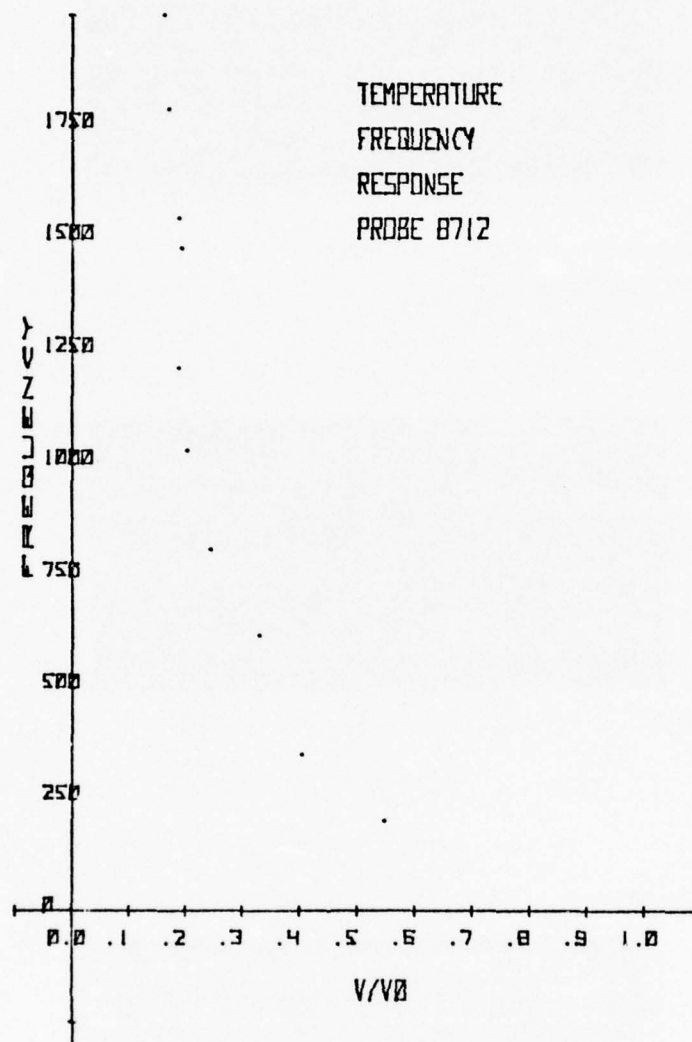


Figure 17. Temperature Frequency Response of Probe 8712 with
IR Industries Model 830 Chopper - Multiple Pulse

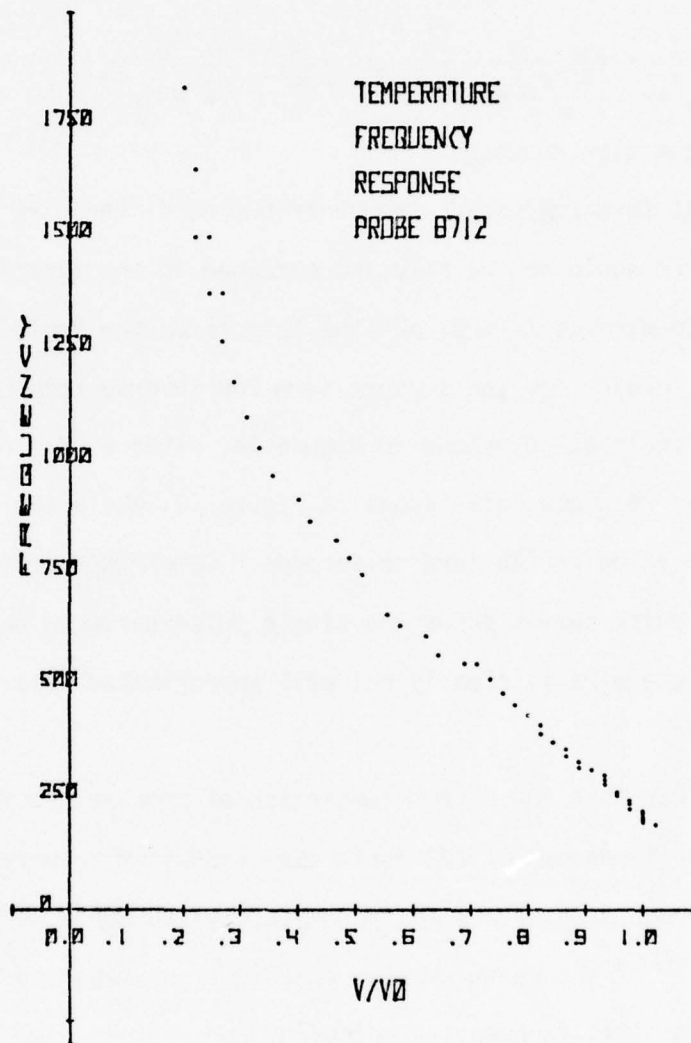


Figure 18. Temperature Frequency Response of Probe 8712 with Four-Slotted Blade Chopper - Single Pulse

The analytical solution for the transient response of a wire to a step change in fluid temperature is given, for first order terms, by (Sandborn, 1972, p. 105):

$$\frac{1}{\tau_e} = \left(\frac{\pi}{\ell}\right) \frac{K_w}{\rho_w C_w} + \frac{4h_f d}{\rho_w C_w d} - \left(\frac{4}{\pi d^2}\right)^2 \frac{\sigma_0^{-1} \delta}{\rho_w C_w} I_1 \quad (19)$$

where τ_e is the time constant.

The first term represents the contribution of the wire supports, the second term would be the solution obtained in the limiting condition of an infinite wire as $I_1 \rightarrow 0$, and the last term, the Joule heating of 8057 inverse seconds and the support term 258 inverse seconds. The approximate single pulse, shown in Figure 14, gives a $1/\tau_0$ of 600 inverse seconds, as the response curve shows in Figure 19, while the repetitive pulse shows a value of 125 inverse seconds. Comparison of the single and multiple pulse curves shows the single pulse curve to be rather optimistic and the wire is clearly not well approximated by an infinite wire.

It is clear that any direct comparison of temperature fluctuations at frequencies in excess of 200 Hertz can be subject to very large errors. Although frequencies to approximately 700 Hertz were anticipated, the bulk of the measurements, which will be reported for large beam spread, exhibit frequencies below 100 Hertz.

In the constant current mode the heat transfer relationship of equation (16) becomes:

$$Nu \left\{ \frac{T_m}{T} \right\}^{-.17} = \left\{ \frac{T_m}{T} \right\}^{-.17} \frac{EI_1 G}{\pi \ell K (T_w - T_f)} = A_{2T} + B_{2T} Re^n \quad (20)$$

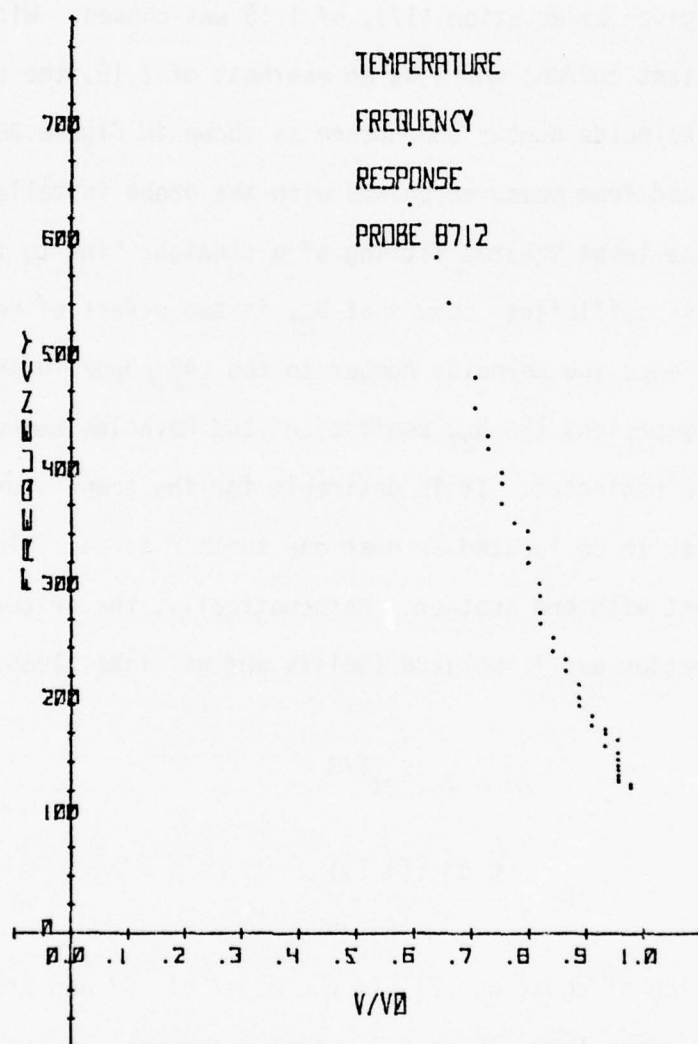


Figure 19. Temperature Frequency Response of Probe 8712
for Single Pulse

It is desirable to select the wire temperature through the overheat just above the maximum temperature to be measured. For this experiment, an overheat, as given by equation (17), of 1.15 was chosen. With the wire in the constant current mode, at an overheat of 1.15, the experimental observed Reynolds number dependence is shown in Figure 20. Figure 20 was obtained from measured points with the probe installed in the tunnel and the least squares fitting of a straight line to the data. The least squares coefficients show that B_{2T} is two orders of magnitude less than A_{2T} . Since the Reynolds number to the .45 power in this case is of order unity or less the B_{2T} coefficient and Reynolds number dependence may be neglected. It is desirable for the temperature and the velocity wires to be located as near one another as possible and still not interact with one another. Mathematically, the criteria for neglect of convection was formulated (Collis and Williams, 1968, p. 382-383) as:

$$Re > 2 (Gr)^{1/3} \quad (21)$$

where

$$Gr \equiv \frac{g d^3 (T_w - T_f)}{\nu^2 T_f} \quad (22)$$

The right hand side of equation (21) is the order of .02 and probe wire Reynolds numbers range from .15 to 4.7, which justifies the neglect of any free convection interaction between the double parallel probes. The radiated power is on the order of 50 microwatts, which is several orders of magnitude below the probe power and therefore negligible. Figure 20, which varied the Reynolds number for the temperature wire, remains the same regardless of whether the velocity wire is operating

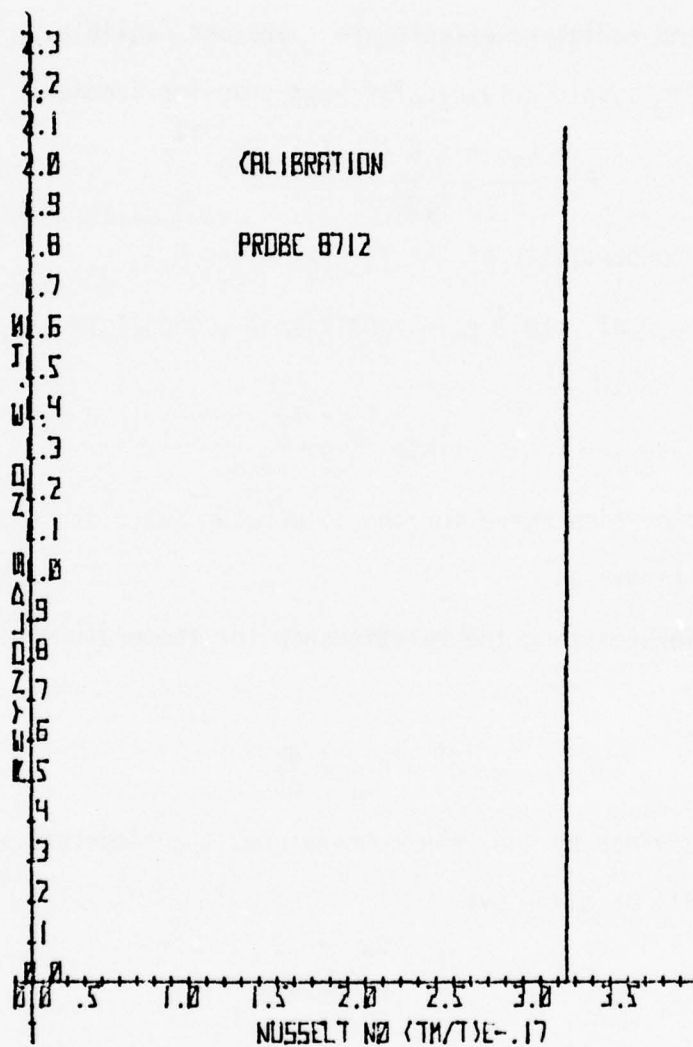


Figure 20. Reynolds Number Dependence of the Temperature Wire, Probe 8712

at its normal hot temperature or left at room temperature, providing there is a measurable flow (>1 foot/second) over the probe. The free convective and radiative effects are therefore negligible.

The relationship obtained for heat transfer becomes:

$$E = \frac{B_{2T} \pi \ell K (T_w - T_f) \left\{ \frac{T_m}{T} \right\}^{.17}}{I_1 G} \quad (23)$$

The thermal conductivity of the film is given by:

$$K = 2.41 \times 10^{-4} (1 + .00317 T_m - .0000021 T_m) \quad (24)$$

where

$$T_m \equiv \frac{T_w + T_f}{2} \quad (25)$$

A sample calibration curve for the temperature wire and equation (23) is shown in Figure 21.

By differentiating the relationship for temperature with respect to time:

$$\frac{dT}{dt} = B_{2T} \pi \frac{dE}{dt} \quad (26)$$

which when divided by the mean temperature, the temperature turbulence intensity will be given by:

$$T_T \equiv \frac{dT}{T} = \frac{B_{2T} \pi dE}{A_{2T} \pi + B_{2T} \pi E} \quad (27)$$

The calculation of the index of refraction and the fluctuation in the index of refraction, which have been employed in the majority of the propagation efforts, is developed by Tatarski as follows (Tatarski, 1961, p. 55-56):

$$n = 1 + 79 \times 10^{-6} \frac{P_B}{T_f} \quad (28)$$

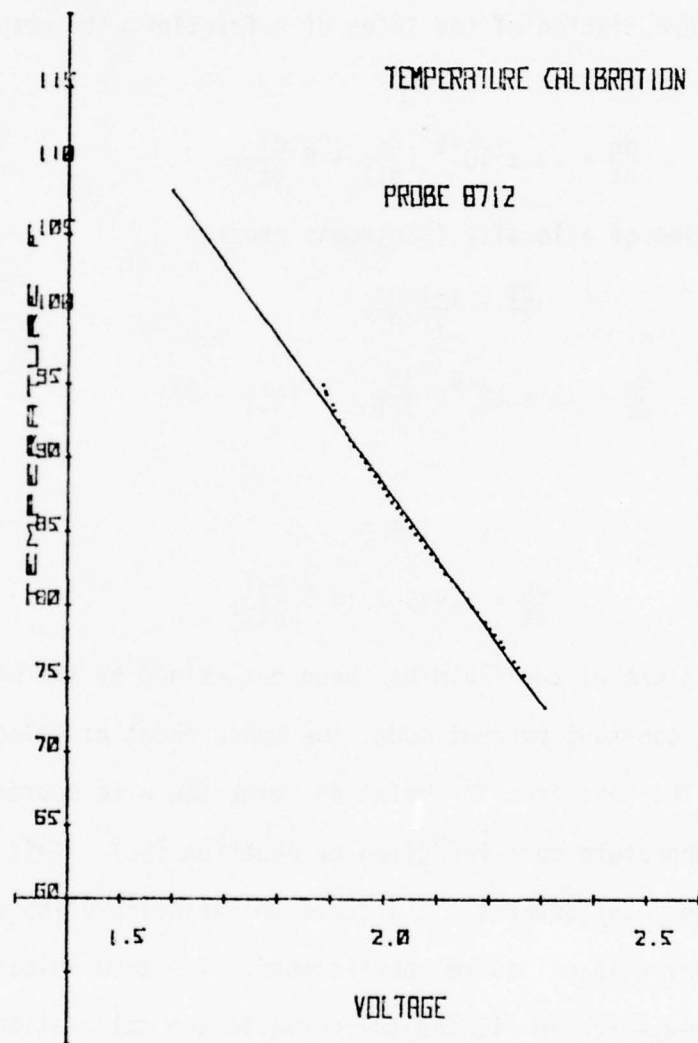


Figure 21. Calibration of Temperature Wire, Probe 8712

where P_B is pressure in millibars and T is the temperature in $^{\circ}\text{K}$, providing the effect of humidity on the value of index of refraction is neglected. Differentiation of the index of refraction with respect to time yields:

$$\frac{d\eta}{dt} = 79 \times 10^{-6} \left\{ \frac{dp}{dt} - P \frac{dT}{dt} \frac{1}{T^2} \right\} \quad (29)$$

with the assumption of a locally isentropic process

$$\frac{dT}{T} = \frac{\gamma-1}{\gamma} \frac{dp}{P} \quad (30)$$

$$\frac{d\eta}{dt} = 79 \times 10^{-6} \left\{ \frac{dT}{dt} \times P \left(\frac{\gamma}{\gamma-1} - 1 \right) \right\} \quad (31)$$

with

$$\gamma = 1.4$$

$$\frac{d\eta}{dt} = 1.975 \times 10^{-4} \frac{PdT}{dtT^2} \quad (32)$$

After the temperature of the fluid has been determined by the wire operating in the constant current mode, the measurement of velocity may be undertaken. The heat transfer relation with the wire operating in the constant temperature mode was given by equation (20). This relation was programmed to least squares fit a curve to the calibration data and calculate the curves least square coefficients. The zero velocity point has been neglected in fitting the curve to the calibration data. The zero velocity point has been neglected since there is only free convection heat transfer with negligible radiation at zero velocity (Bradshaw, 1971, p. 116). Calibration curves were also plotted using the zero flow point; however, this results in larger errors for all calibration points. Sample calibration points are shown in Figure 22. Figure 23 shows a least squares fit of calibration data. The calibration

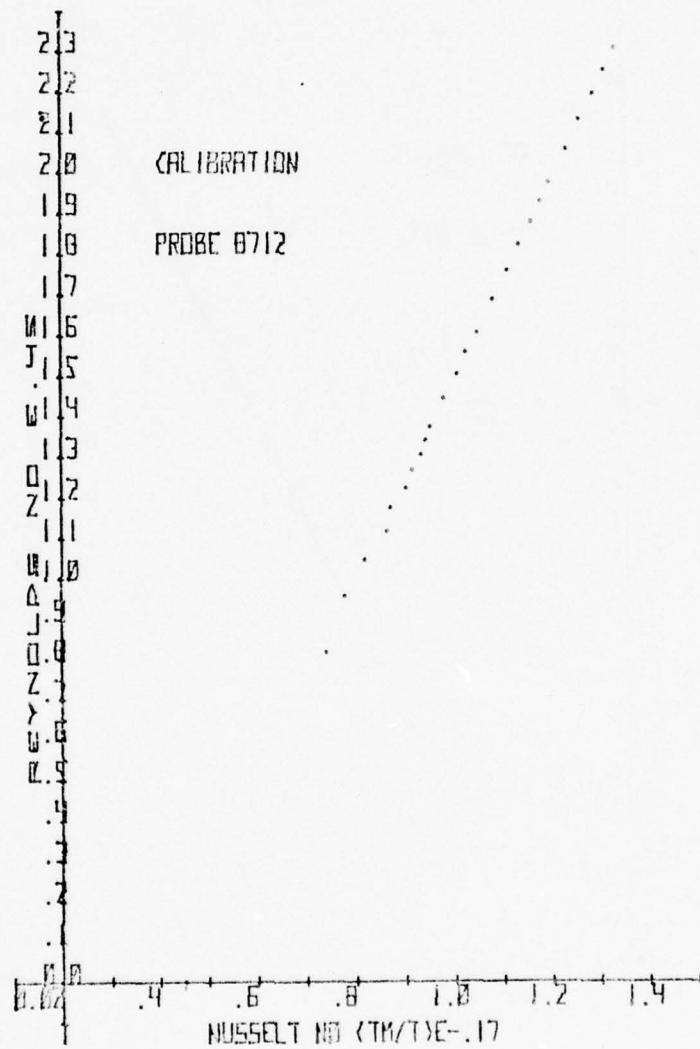


Figure 22. Velocity Calibration of Probe 8712

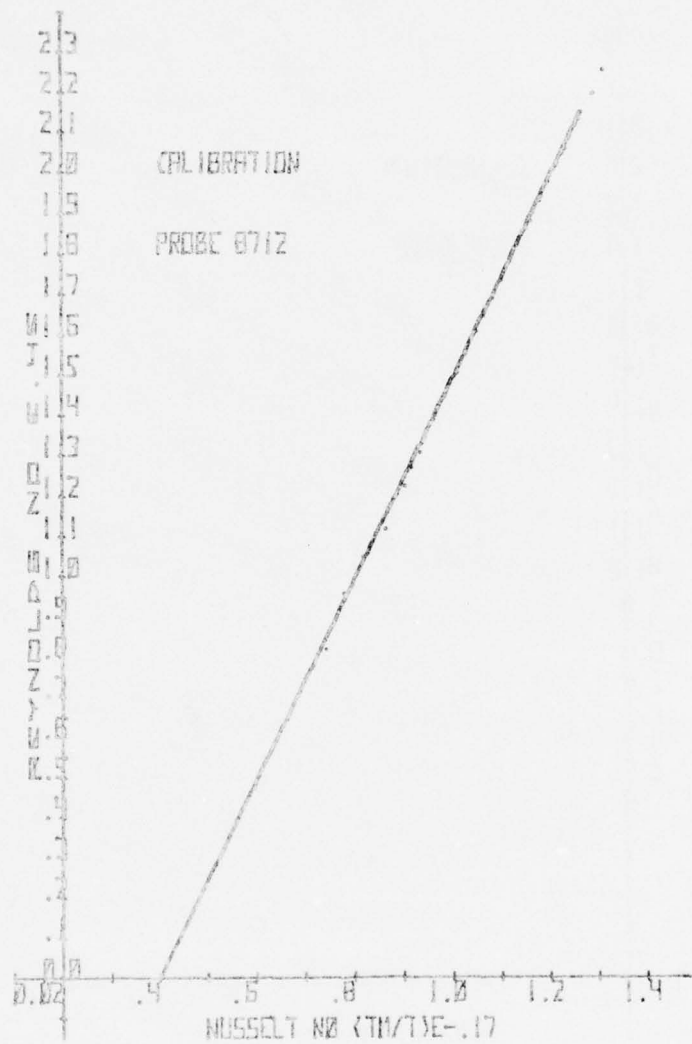


Figure 23. Velocity Calibration of Probe 8712 with Least Squares Fit of the Data

curve shows no free convection effects at low values of Reynolds number and shows no transition from slip flow to continuum flow over the calibration range. The fluctuations in velocity may now be calculated and the turbulence intensity, Tu , obtained:

$$Tu \equiv \frac{du}{U} \quad (33)$$

$$\frac{d}{dt} \{ Nu \left\{ \frac{T_m}{T} \right\}^{-.17} \} = \frac{d}{dt} (A_2 + B_2 Re^{.45}) \quad (34)$$

Rewriting to collect the temperature effects in one term:

$$\frac{d}{dt} (E^2) = \frac{d}{dt} \left\{ \left(\frac{R_1 + R_3}{R_1} \right)^2 \pi \times K (T_w - T_f) \left\{ \frac{T_m}{T} \right\}^{.17} \right\} (A + B Re^{.45}) \quad (35)$$

Let the first bracket be defined as $\beta (T_f)$.

Giving the density used in Reynolds number calculations as:

$$\rho = \frac{\rho_s P_B T_s}{\frac{(T_w - T_f)}{2} P_s} \quad (36)$$

Viscosity in the Reynolds number is likewise evaluated at the mean film temperature:

$$\mu = \mu_o \left(\frac{T_w + T_f}{273} \right)^{3/2} \left(\frac{385}{\frac{(T_w + T_f)}{2} + 113} \right) \quad (37)$$

with the temperature in $^{\circ}K$.

Differentiating the expression for the square of the wire voltage with respect to time yields:

$$2E \frac{dE}{dt} \equiv .45 B_{2T} \frac{Re^{.45}}{U^{.45}} U^{-.55} \beta(T_f) + \frac{d}{dt} (B_{2T} Re^{.45} \beta(T_f)) + \frac{d}{dt} (A_{2T} \beta(T_f)) \quad (38)$$

While evaluation of the temperature contributions could be carried out, there is a very complex relationship for an accurate description. Assuming viscosity, thermal conductivity, and $\left\{\frac{T_m}{T}\right\}^{.17}$ constant would result in the following expression for velocity turbulence intensity:

$$T_u = \frac{du}{U} = \frac{2E dE}{.45 Re^{.45} B(T_f)} + \frac{\left\{ \frac{T_w}{(T_w+T_f)^{.55}} + \frac{T_f}{(T_w+T_f)} - \frac{1}{.45} + \frac{A_{2T}}{B_{2T} Re^{.45} .45} \right\} dT_f}{T_w - T_f} \quad (39)$$

The temperature term corrections, as given by equation (39) were included for calculation of T_u values on the tunnel centerline. For the case of zero heat addition, the term:

$$T_u \approx \frac{2 e dE}{.45 Re^{.45} B_{2T} K \pi \ell \frac{(R_1+R_3)^2}{R_1} (T_w-T_f)} \quad (40)$$

was calculated for the traverses. This relationship is shown in Figure 24 for the wire calibration curve of Figure 23.

Because the levels of turbulence are exceeding high and beyond the range of values in the conventional application of wires, the effect of high levels should be examined on both the heat transfer and also the possible non-linear effects on determination of mean values. Sandborn (Sandborn, 1971, p. 235, Fig. 6.6) shows significant increases in heat transfer, 1.65 times, for a T_u of 12% at Λ/d ratios of 1.5. This effect is reduced to the order 1.1 times the heat transfer at a Λ/d of 8, where Λ is the scale of turbulence and d the hot wire diameter. Since the ratio of Λ/d for this experiment is of the order 120, this effect should be negligible. High levels of turbulence can also cause the mean value

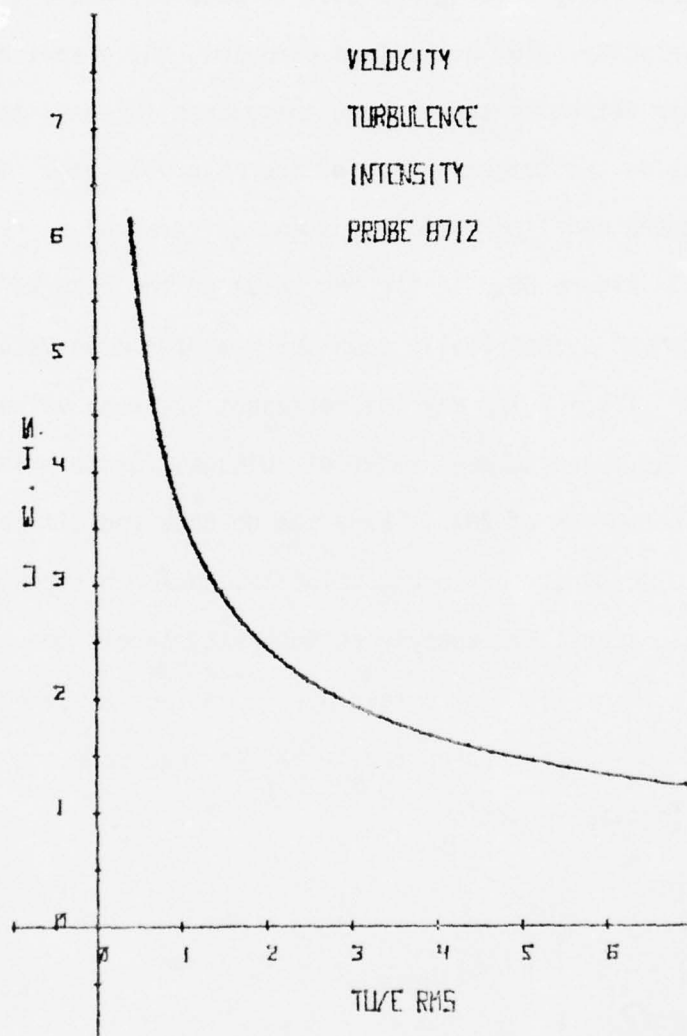


Figure 24. Tu for Probe 8712 at a Fluid Temperature of 23°C

of voltage observed on the probe not to correspond to the mean value of velocity. When this happens, it is necessary to use more elaborate techniques, either analytic or graphical, to make corrections to the mean value of velocity. For evaluation purposes, the graphical technique was used to determine the highest turbulence intensities observed and their effect on the determination of the mean velocity. This problem arises when the non-linear region of the calibration curve is used as illustrated in Figure 25. If the rms value of the observed fluctuation is superimposed symmetrically upon the measured mean value of D.C. voltage as shown: $(V_1 + V_2)/2$ may not represent the mean value of velocity implied by the measured mean value of voltage, for turbulence intensities of the order of 20%. There was no observed difference in mean value of velocity at the lowest velocity, where this consideration is most critical. For a 60% turbulence intensity level, the correction amounted to a 7% error in V_m at 5 feet per second and a subsequent 3% error in Tu . A non-linear correction to V_m was therefore not considered to be required in data reduction.

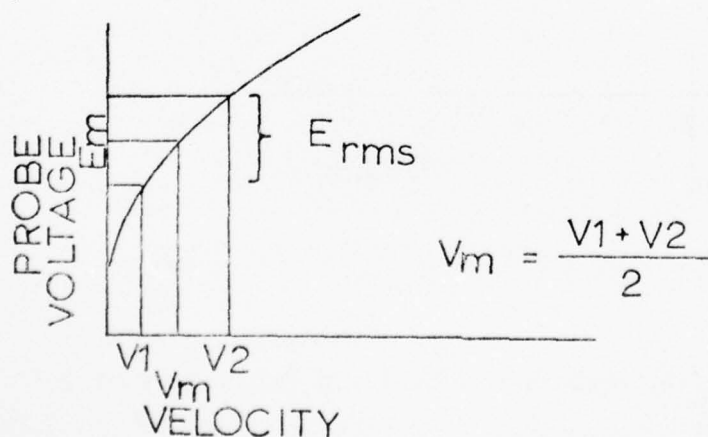


Figure 25. Schematic of Graphical Computation of V_m for Large Values of Tu

Tunnel profiles of mean velocity, mean temperature, rms velocity, and rms temperature traverses on the horizontal centerline of the tunnel were made at the three L/D_p stations for which the beam spread was obtained. A traverse was also performed in the vertical plane to ensure that any natural convective effects were small. The heater wires used were .046 centimeter diameter Nichrome wires, for which the Grashof number is of the order of 2.37. A Reynolds number of less than 1.33 would be required to neglect free convective effects. Free convective effects may be neglected since the Reynolds number for the tunnel heater wire is on the order of 19 to 560, which satisfies the criteria of equation (18).

For each incremental Nusselt number and Reynolds number, a traverse was obtained which consisted of the mean velocity, temperature, rms velocity, and rms temperature. The nominal sequence run during tunnel and beam traverses was no heat addition, low heat (527 watts), medium heat (783 watts), high heat (1166 watts), and then a rerun of no heat addition to check that the tunnel mean velocity had remained constant. The traverse extends to within 2.9 centimeters of the tunnel side walls. The two wire probe holders prevented closer approach of the side walls.

Traverses were performed at four L/D_p ratios, three of which are illustrated in Figure 26. For each traverse, three correlations of velocity and temperature were obtained at the stations designated A_1 , B_1 , and C_1 . These stations are symmetric about the tunnel centerline and are shown schematically in Figure 27. Two Hewlett Packard 3400A rms meters were used for measurement of the fluctuation components of velocity and temperature. The rms meter plotter combination was calibrated with a 100 Hertz sine wave.

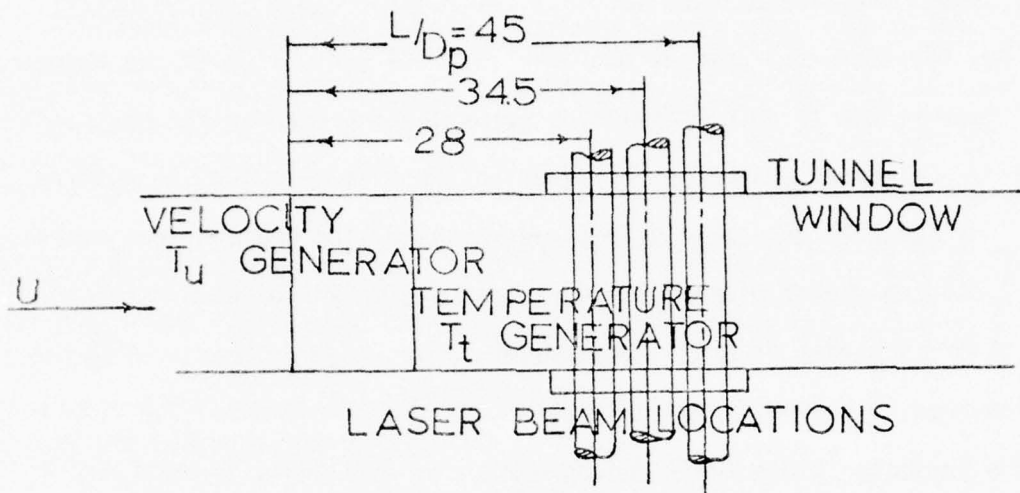


Figure 26. Top View of Tunnel Illustrating Horizontal Traverse Locations for .64 cm Perforation Diameter T_u Generator

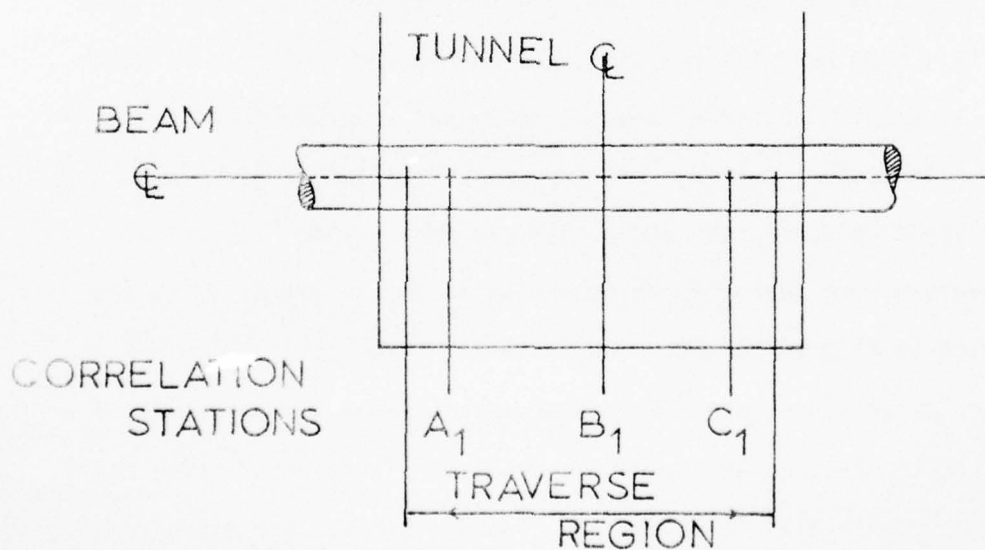


Figure 27. End View of Tunnel Illustrating Correlation Stations and Traverse Region

Tunnel Profile Calculations for Mean Temperature, Mean Velocity,
Mean Index of Refraction, RMS Temperature, RMS Velocity, RMS Index of
Refraction, T_u , T_T , and T_n

For each profile the centerline value of temperature is first calculated, then a mean value of temperature is determined by continuously digitizing the temperature with $[(T_i + T_{i+1})/2] \Delta x_i$ accumulated. In excess of a 100 data points is accumulated in the calculation of a mean value. In most cases the centerline value is representative of the value determined by:

$$\bar{T} = \frac{(\sum (\frac{T_i + T_{i+1}}{2})) \Delta x_i}{\sum \Delta x_i} \quad (41)$$

Knowing a mean value of temperature next allows a mean value of velocity to be calculated on the tunnel centerline. A centerline velocity is calculated followed by the determination of a mean value of velocity by a continuous digitization of the velocity traverse similar to the temperature calculation, doing a simple trapezoid integration, and then dividing the result by the accumulated machine traverse:

$$\bar{U} = \frac{(\sum (\frac{U_i + U_{i+1}}{2})) \Delta x_i}{\sum \Delta x_i} \quad (42)$$

A minimum of 75 points would typically be accumulated in calculation of \bar{U} . The centerline and mean value again generally agree. A mean Reynolds number is also calculated.

The fluctuation in temperature is next calculated:

$$dT = \frac{(\sum (\frac{dT_i + dT_{i+1}}{2})) \Delta x_i}{\sum \Delta x_i} \quad (43)$$

and combined with the mean temperature to give the temperature turbulence intensity. The index of refraction and the fluctuation in the index of refraction is next calculated, assuming that the pressure is barometric pressure as was indicated by Rayleigh flow considerations. The integral of the index of refraction and the square of the fluctuating components are to be later used in calculation of beam spread, so these values were also printed out. The rms level of both temperature and velocity show considerable variation and so a maximum and minimum value of temperature turbulence intensity and velocity T_u is also calculated. Approximately 300 points are typically accumulated in the measurement of a mean fluctuating value.

Finally, the mean value of velocity turbulence intensity is obtained in a similar fashion after calculating a mean value of the rms level of velocity:

$$\overline{dU} = \frac{\sum \left(\frac{dU_i + dU_{i+1}}{2} \right) \Delta x_i}{\sum \Delta x_i} \quad (44)$$

Examination of the profiles shows that both temperature and velocity exhibit a turbulent distribution. Both the mean temperature and velocity are reasonably uniform across the traverse, with the centerline values being representative of the spatial mean values. When beam spread measurements were made, the centerline tunnel velocity was set to the same centerline profile conditions.

The rms profiles showed much larger spatial variations than were anticipated and, therefore, a space average value is very important for the selection of a realistic rms average value and turbulence intensities.

Determination of Integral Scale and Microscale of Turbulence from Correlation Functions

The prediction of beam spread by optical calculation requires information about the integral scale and microscale of turbulence for the flow field through which the beam is propagating. These scales of turbulence may be deduced from the correlation function of velocity, temperature, and optical fluctuations. A Hewlett Packard 3721A correlator was employed to obtain the autocorrelation function of interest in the time domain. The algorithm of the correlator's computer was periodically verified by inputting a sine wave of known amplitude and frequency.

In this section the correlation function will be defined and Taylor's Hypothesis will be invoked in order to transform the results from the time domain to the spatial domain. The integral scale of turbulence will then be obtained in a straight forward manner from the correlation function. The microscale of turbulence may be deduced from the correlation function by several procedures. These procedures will be discussed and the microscale will then be determined.

The integral scale of turbulence represents the larger set of eddies contained in the flow field. These eddies are controlled by the boundary conditions and are proportional to the greatest distance between two points in the flow field for which there exists a correlation.

The correlation function may be obtained for fluctuation in both scalar and vector fields. The correlation function for temperature (scalar field) and velocity (vector field) are shown schematically in Figure 28 with the mean flow in the X direction.

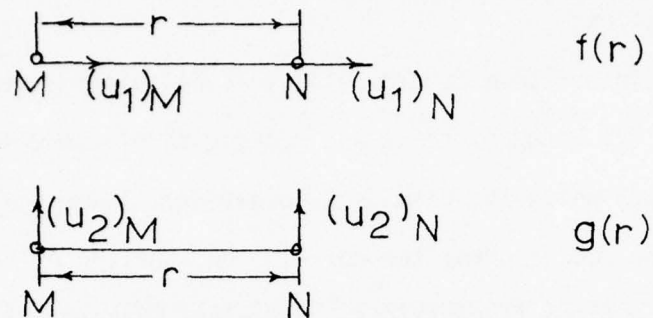


Figure 28. Schematic of Longitudinal and Lateral Correlation Functions (Hinze, 1959, p. 30, Fig. 1-14)

Here $f(r)$ and $g(r)$ are respectively the longitudinal and the lateral velocity correlation functions and $T(r)$ is the temperature correlation function. The lateral correlation function will be the experimental quantity to be measured to determine the scales of turbulence. The correlation function is a fundamental property which is used to characterize random processes. If M is denoted by the distance ζ and N by $\zeta + x_2$, then the lateral correlation function is given by:

$$g(r) = U_2(\zeta) U_2(\zeta + x_2) \quad (45)$$

$$g(r) = [U_2(\zeta) - \overline{U_2\zeta}] [U_2(\zeta + x_2) - \overline{U_2(\zeta + x_2)}] \quad (46)$$

The integral scale of turbulence can now be defined in terms of the correlation function by:

$$\Lambda = \int_0^\infty g(r) dx \quad (47)$$

Following Tatarski (Tatarski, 1961, p. 29), the qualitative connection between the microscale and the integral scale, which was stated in

equation (2), will be outlined. The turbulent kinetic energy ($u' \cdot u'$), which is converted to thermal energy by dissipation, can be expressed by:

$$\varepsilon \sim (u' \cdot u') / \tau \quad (48)$$

where τ is a characteristic period defined as $\tau \equiv \frac{\Lambda}{u}$, for a fluctuation or

$$\varepsilon \sim (u' \cdot u') / \tau = u'^3 / \Lambda \quad (49)$$

This is assumed to hold for all eddies except the smallest for which

$$\varepsilon \sim \nu U_0^2 / \ell_0^2 \quad (50)$$

and

$$U_0 = (\varepsilon \ell_0)^{1/3} \quad (51)$$

or

$$\ell_0 \sim \sqrt[4]{\nu^3 / \varepsilon} \quad (52)$$

where ℓ_0 is the microscale of turbulence. The microscale can then be expressed in terms of the integral scale by

$$\frac{\ell_0}{\Lambda} = \frac{1}{(\text{Re}_\Lambda)^{3/4}} \quad (53)$$

At this point it should be noted that the prediction of the scales of turbulence and relationship between the scales is in reality very empirical. Previously equation (2) was introduced which gave a somewhat different empirical relationship between ℓ_0 and Λ than equation (53). Corrsin gives equation (2) as:

$$\frac{\ell_0}{\Lambda} \approx \frac{\sqrt{A} g}{\text{Re}_{\ell_0}} = \frac{\sqrt{A} g}{\sqrt{\text{Re}_\Lambda}} \quad (54)$$

where

$$Re_{\Lambda} \sim Re \quad (55)$$

$$Re_{\lambda_0} \sim \sqrt{Re} \quad (56)$$

assuming Λ/D_p and u'/U are independent of Reynolds number at a fixed distance downstream of a turbulence generator such as a grid. Then A_g is assumed to be constant. The value of A_g ranges from 2 to 30 for Biplanar cylindrical grids (Corrsin, 1963, p. 528) (Goldstein, 1965, p. 228). Although the deduction of a microscale and an integral scale of turbulence from the autocorrelation function is recognized as an inadequate specification of actual scale sizes for many turbulent flow fields, these representative scales are employed in many optical calculations such as those of equation (6) for beam spread.

There exist a variety of ways to deduce the microscale of turbulence from the correlation function, three of which will follow. Because the flow is considered to be homogeneous, $g(x_2) = g(-x_2)$, Hinze (Hinze, 1959, p. 35-36) shows that

$$\left[\frac{\partial^{(n+m)} g}{\partial x_2^{(n+m)}} \right]_{x_2=0} = \frac{1}{u_1'} \left[\frac{\partial^n u \partial^m u}{\partial x_2^n \partial x_2^m} \right]_{x_2=0} = 0 \quad (57)$$

for $n + m$ odd and $n + m$ even by:

$$\left[\frac{\partial^{2n} g}{\partial x_2^{2n}} \right]_{x_2=0} = \frac{1}{(u_1')^2} \left[\frac{\partial^{2n} u}{\partial x_2^{2n}} \right]_{x_2=0} = (-1)^n \frac{1}{(u_1')^2} \left[\frac{\partial^n u}{\partial x_2^n} \right]_{x_2=0}^2 \quad (58)$$

The general and complete shape of the correlation function of course depends upon the nature of the turbulent flow field. However, at $x_2=0$, the correlation function can be described in terms of its derivatives

at the origin. Expanding $g(x)$ in a Taylor series, the noting that $g(x)$ is symmetrical with respect to x_2 :

$$g(x_2) = 1 + \frac{1}{2!} (x_2)^2 \left[\frac{\partial^2 g}{\partial x_2^2} \right]_{x_2=0} + \dots \quad (59)$$

Substitution of the partial derivative of g into the expansion gives:

$$g(x_2) = 1 - \frac{(x_2)^2}{2!} \frac{1}{(u_1')^2} \left[\frac{\partial u_1'}{\partial x_2} \right]^2_{x_2=0} + \dots \quad (60)$$

which for small values of x_2 may be approximated by a parabolic function of x_2 :

$$g(x_2) \approx 1 - \frac{x_2^2}{\ell_0^2} \quad (61)$$

or

$$\frac{1}{\ell_0^2} \approx -\frac{1}{2} \left[\frac{\partial^2 g}{\partial x_2^2} \right]_{x_2=0} = \frac{1}{2(u_1')^2} \left[\frac{\partial u_1'}{\partial x_2} \right]^2_{x_2=0} \quad (62)$$

in which ℓ_0 is the microscale of turbulence.

The above expressions for the microscale suggest two techniques for the measurement of the microscale. $g(x_2)$ near the origin can be used to fit a parabola through the origin and another point near the origin.

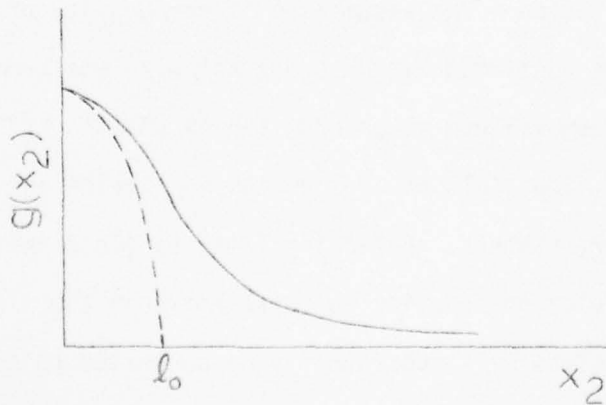


Figure 29. Parabolic Definition of the Microscale of Turbulence

The second expression of equation (62) can be evaluated either with electronic differentiation of the rms value squared of the parameter from which the correlation function is calculated or by mathematically taking the second partial of the autocorrelation curve at $x_2 = 0$. The frequency response and average time for the measurements, as well as the response to a random wave function are questionable using electronic differentiation. The electronic differentiation was discarded in favor of fitting a cubic equation

$$g(x_2) = M_0 + M_1 x + M_2 x^2 + M_3 x^3 \quad (63)$$

to the first four points of the autocorrelation function and then solving for $\partial^2 g(x_2)/\partial x_2^2$.

A third method of calculation of the microscale may be developed by examination of the predicted behavior of the autocorrelation curve as x_2 becomes large. To accomplish this calculation procedure, it is necessary to relate the correlation function to the structure function. For the measurements to be reported, the turbulent flow field may be considered to be locally homogeneous (Batchelor, 1953, p. 133) at any given transverse station. The assumption of homogeneity of the turbulent flow field was confirmed with x probe hot wire measurements for both velocity and temperature at an L/D_p tunnel station of 28.

A homogeneous flow field at a given tunnel station may be represented by stationary process. Following Tatarski (Tatarski, 1961, p. 8-33), the correlation function is represented in the time domain (all scale calculations will subsequently be converted to the time domain) approximately by a random function with stationary increments

by examining the function about some small increment in time, τ . The stationary function is obtained by subtracting the random function $F(\tau)$.

$$F_{\tau}(x) = f(\zeta + x) - f(\zeta) \quad (64)$$

Then employing the identity

$$(a-b)(c-d) = \frac{1}{2} [(a-d)^2 + (b-c)^2 - (a-c)^2 - (b-d)^2] \quad (65)$$

The stationary correlation function becomes

$$g(\zeta_1, \zeta_2) = g(\zeta_1) g(\zeta_2) \quad (66)$$

$$g(\zeta_1, \zeta_2) = \frac{1}{2} [g(\zeta_1+x) - g(\zeta_2)]^2 + \frac{1}{2} [g(\zeta_1) - g(\zeta_2+x)]^2 \quad (67)$$

$$g(\zeta_1, \zeta_2) = -\frac{1}{2} [g(\zeta_1+x) - g(\zeta_2+x)]^2 - \frac{1}{2} [g(\zeta_1) - g(\zeta_2)]^2 \quad (68)$$

This linear combination of stationary functions is defined as the structure function

$$D_g(x) = [g(\zeta+x) - g(\zeta)]^2 \quad (69)$$

or for a random process with a zero mean value

$$D_g(x) = [g(\zeta+x)]^2 + g(\zeta)^2 - 2g(\zeta+x)g(\zeta) \quad (70)$$

Since $g(t)$ is stationary

$$[g(\zeta)]^2 = [g(\zeta+x)]^2 = g(0) \quad (71)$$

which gives

$$D_g(x) = 2[g(0) - g(x)] \quad (72)$$

There is a transverse and longitudinal structure function which are functionally related.

For x such that $\lambda_0 \ll x \ll \Lambda$ dimensional arguments give the "two-thirds law" for the form of the structure function:

AD-A038 667

AIR FORCE AERO PROPULSION LAB WRIGHT-PATTERSON AFB OHIO
THE EFFECT OF TURBULENCE ON LASER BEAM QUALITY.(U)
NOV 76 R B RIVIR

F/G 20/5

UNCLASSIFIED

AFAPL-TR-76-94

NL

2 OF 3

AD
A038667



$$D_g(x) = c_1(x)^{2/3} \quad (73)$$

for values of x_2 less than ℓ_0

$$D_g(x) = c_2(x)^2 \quad (74)$$

Although the constants vary, the form and functional dependence for both the longitudinal and lateral structure function is the same as given in equations (73) and (74). Recalling that the structure function was given in terms of the correlation function by equation (72), the structure function may be obtained by displacing the origin to the first point of the autocorrelation function, reflecting the curve about the new axis, and multiplying the ordinate by 2. The microscale may be found by equating $S_{0x}^2 - S_x^3 = 0$ or $x = S_0/S$. c_1 of equation (73) may be calculated at a time greater than the time of the point of inflection for the autocorrelation curve. The microscale may then be taken as the point where the cubic is less than the value of the autocorrelation curve as is shown in Figure 30.

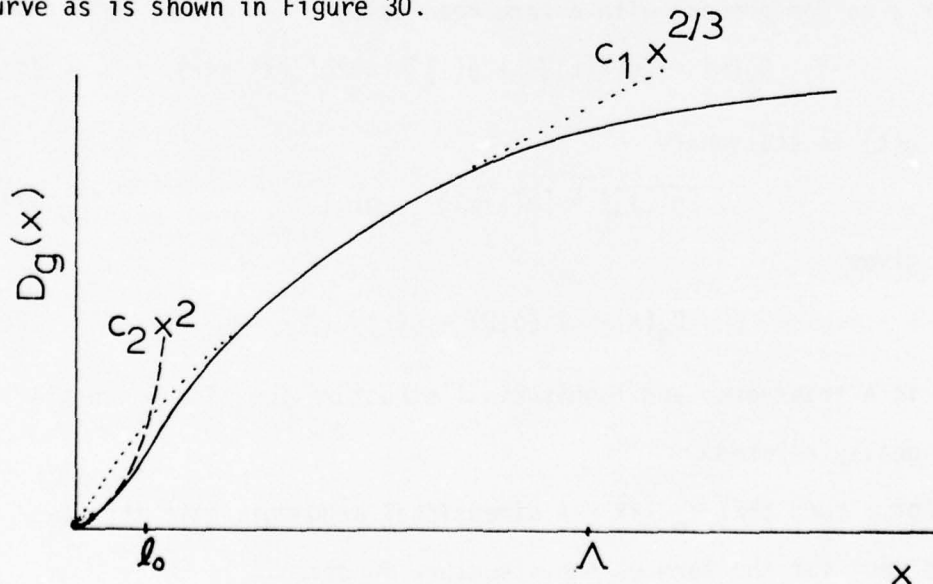


Figure 30. The Scales of Turbulence from the "Two/Thirds Law"

The integral scale, Λ , is the value at which the curve for the structure function begins to saturate as is shown in Figure 30.

All turbulence scale measurement techniques are more convenient to employ if the averaging process is accomplished in the time domain rather than the space domain for which the correlation functions were originally defined. If the time varying correlation function is examined at a single point in the flow field, similar relations are obtained for the expansions of the correlation function (Hinze, 1959, p. 40-41).

$$g(t) = 1 - \frac{t^2}{\tau_o^2} \quad (75)$$

$$\frac{1}{\tau_o^2} = \frac{1}{2u_1'^2} \left[\frac{\partial u_1'}{\partial t} \right]_{t=0}^2 \quad (76)$$

$$\frac{1}{\tau_o^2} = - \frac{1}{2} \left[\frac{\partial^2 g(t)}{\partial t^2} \right]_{t=0} \quad (77)$$

with an integral time scale given by:

$$\tau_o = \int_0^\infty dt g(t) \quad (78)$$

The exact relationship between $g(t)$, $f(x)$, and $g(x)$ is unknown (Hinze, 1959, p. 40-41). If the turbulent field is homogeneous with a constant mean velocity in the x_1 direction = \bar{U} , then the temporal and spacial observations may be interchanged through Taylor's hypothesis:

$$\frac{\partial}{\partial t} = - \bar{U} \frac{\partial}{\partial x} \quad (79)$$

providing u_1 is small compared to \bar{U} . The requirement for u_1/\bar{U} results from consideration of the equation of motion:

$$\frac{dU_1}{dt} = \frac{du_1}{dt} + (\bar{U} + u_1) \frac{\partial u_1}{\partial x_1} = - \frac{1}{\rho} \frac{\partial p}{\partial x_1} + \frac{u \partial^2 u_1}{\partial x_k \partial x_k} \quad (80)$$

Since $p_1 \propto \rho u_1^2$ the approximation, "Taylor's Hypothesis," will be valid if $u_1/\bar{U} \ll 1$. Taylor's Hypothesis will be applied in this case also when the u_1/\bar{U} criteria is not met. The connection between the integral time scale, τ , and the integral spatial scale is given by:

$$\Lambda_U = \bar{U} \tau_U = \bar{U} \int_0^\infty g(t_U) dt \quad (81)$$

$$\Lambda_T = \bar{U} \tau_T = \bar{U} \int_0^\infty g(t_T) dt \quad (82)$$

Likewise

$$\frac{1}{\lambda_{oU}} = \frac{1}{\bar{U}} \left[-\frac{1}{2} \frac{\partial^2 g(t_U)}{\partial (t_U)^2} \right]_{t=0} \quad (83)$$

$$\frac{1}{\lambda_{oT}} = \frac{1}{\bar{U}} \left[-\frac{1}{2} \frac{\partial^2 g(t_T)}{\partial (t_T)^2} \right]_{t=0} \quad (84)$$

Sample autocorrelation functions will next be shown to illustrate the range of conditions encountered in this experiment. Approximately 1700 autocorrelations of temperature and velocity were taken to document the turbulent flow field. Three sample curves are shown in Figures 31, 32, and 33. The upper most curve is the autocorrelation function and the lower curve the Fourier transform of the autocorrelation function which is the energy/frequency spectrum of the turbulence. Figures 31 and 33 are velocity autocorrelations and Figure 32 is a temperature autocorrelation at the centerline of the tunnel at the L/D_p station of 45. Comparison of Figures 31, 32, and 33 with Townsend's (Townsend, 1956, p. 4-20) examples would indicate that Figure 31 is representative of isotropic turbulence with a single eddy size. Figure 32 appears to be the sum of two distributions which indicates a field of isotropic turbulence with two characteristic eddy sizes, and Figure 33 has a

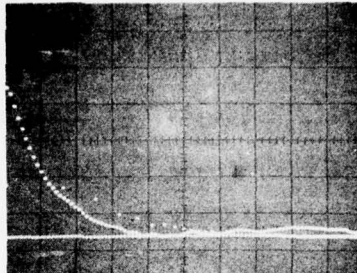


Figure 31. Autocorrelation of Velocity - Single Scale of Turbulence

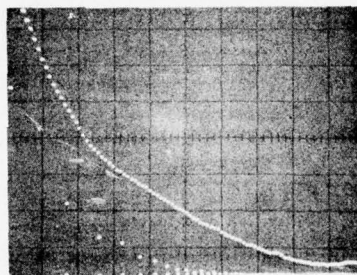


Figure 32. Autocorrelation of Temperature - Two Scales of Turbulence

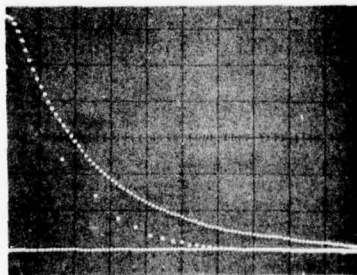


Figure 33. Autocorrelation of Velocity - Multiple Scales of Turbulence

steep decay near origin indicating isotropic turbulence with eddies of many differing sizes. The frequency spectrum in each use indicates a similar conclusion. The multiple scales can cause difficulties in curve fitting for the C_N^2 method of microscale measurement and near the origin there are clearly numerous points which have a quadratic function dependence with the abscissa, time.

Laser Beam Power Measurement and Calculation

The spread of the beam was measured as an intensity profile in the focal plane. This section will discuss the linearity and frequency response of the optical detector, the selection of an aperture for the focal plane traverse, and finally the calculation of the laser power profile and wander of the beam centroid from the measured traverse.

Detector Calibration and Frequency Response

The detector used behind the aperture was a Spectra Physics Model 401C power meter. The power meter was found to have a linear response, $\pm 2\%$. The frequency response of the power meter was measured with rotating mechanical choppers and the helium neon laser. The frequency response of the power meter is shown in Figure 34 where the power meter frequency was taken as the average of four to nine cycles. Figure 35 shows that frequency is faithfully tracked to 25 Kilohertz. The meter output was found to be constant to 3000 Hertz with a drop to 52% of the zero frequency output at 20 Kilohertz as shown in Figure 35. The corresponding frequencies associated with the integral and microscales of turbulence in this experiment were generally below 100 Hertz. The Fourier transform of the autocorrelation functions of velocity and

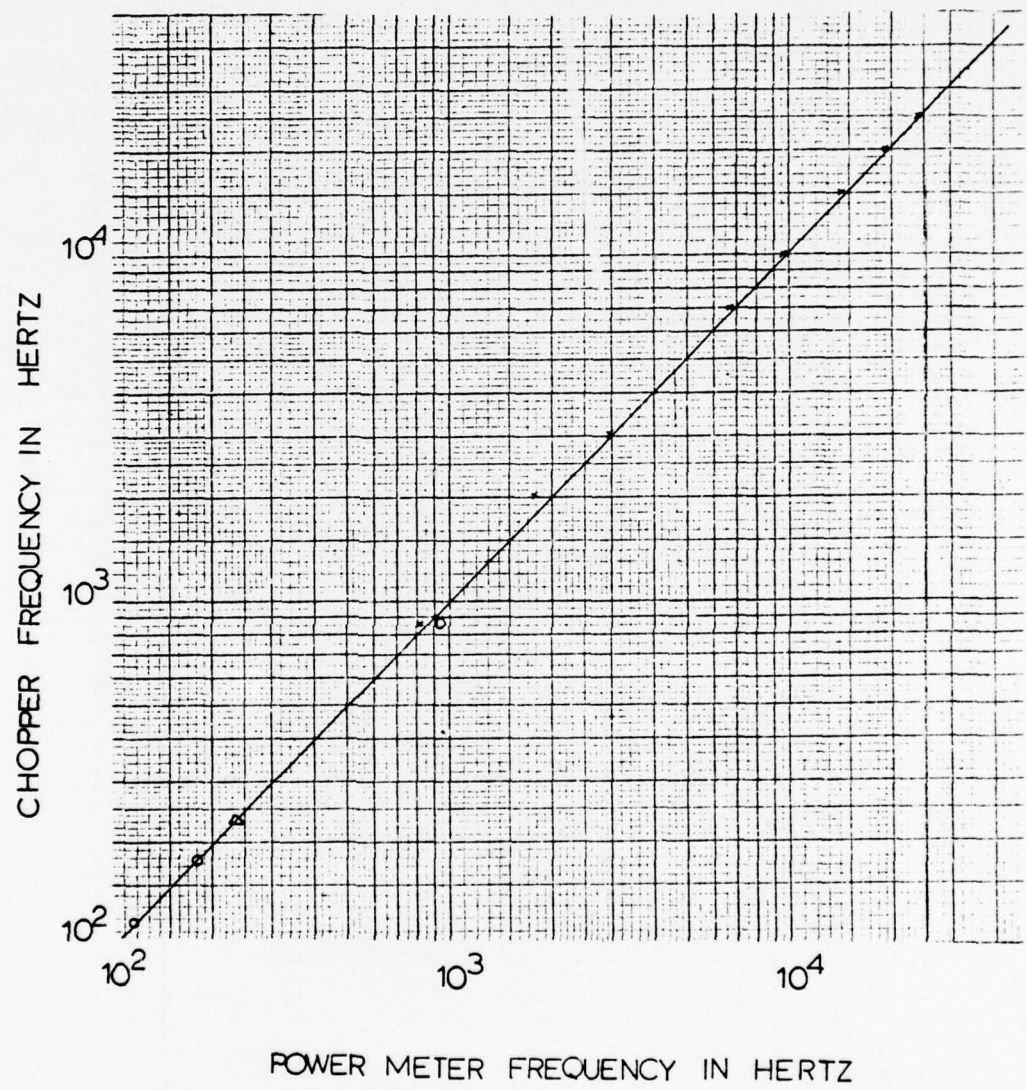


Figure 34. Power Meter Frequency Response

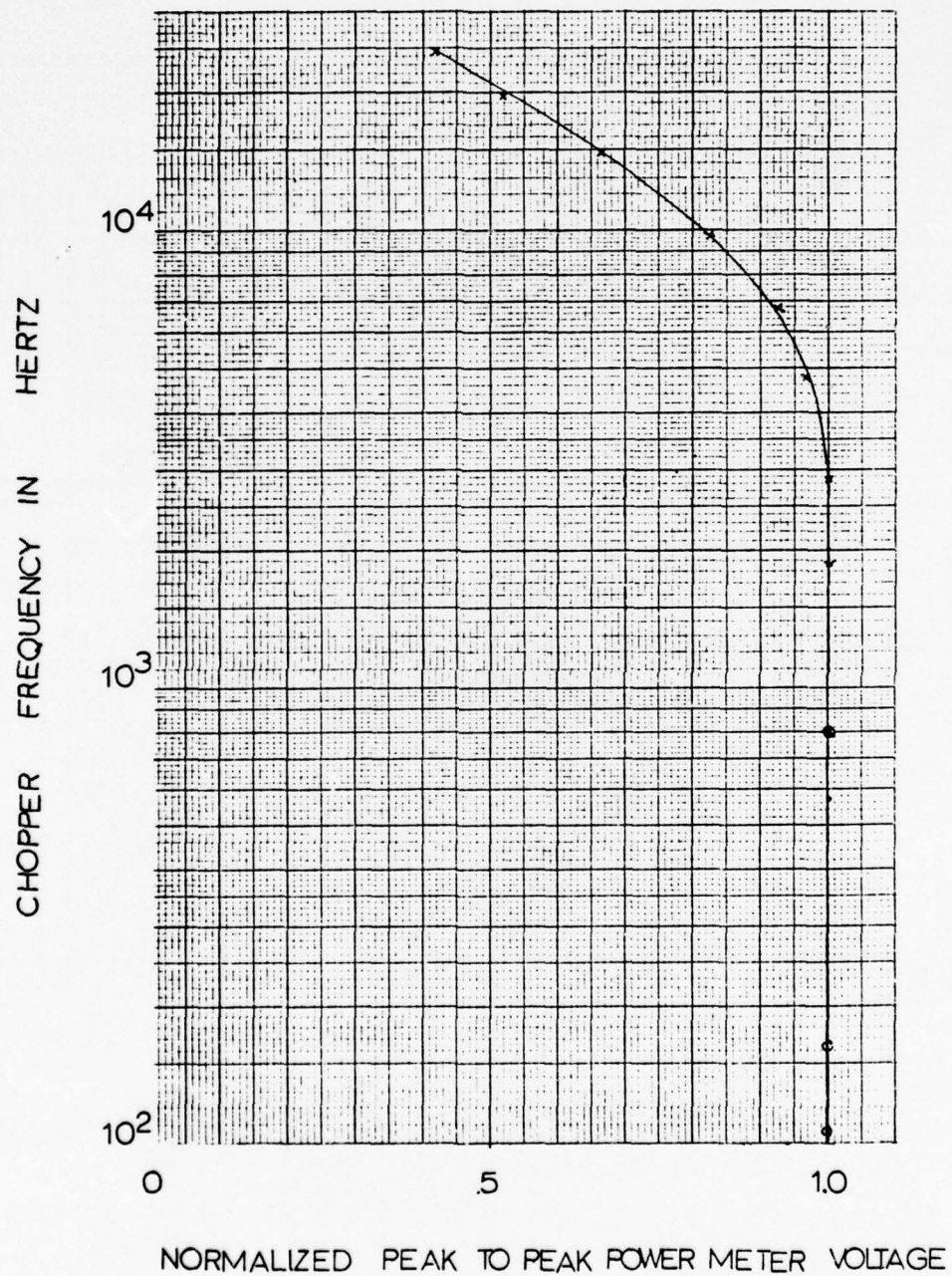


Figure 35. Power Meter Amplitude Frequency Response

temperature also confirmed the fact that there is very little turbulent energy at the higher frequencies. The frequency response of the detector was, therefore, considered adequate for this experiment.

The Selection of the Scanning Aperture Size at the Focal Spot

A number of methods may be employed to examine the intensity distribution of a laser beam in the focal plane. Microdensitometers, videcons, and apertures have been successfully used. Apertures are simple and inexpensive if the integration of the non-uniform distribution can be performed and the traversed distribution be shown to be an accurate representation. It would appear that the smallest aperture would give the most accurate measurement of the intensity distribution. However, the smaller the aperture, the more sensitive it is to scintillation effects. The signal is also reduced as the aperture diameter is decreased, while the background noise level, which includes building and room vibrations and circulation in the external optical path remains at a constant level, independent of aperture size. As a result, as smaller apertures are used, the signal to noise level is proportionally reduced. One hundred (100) to 800 micron diameter apertures were evaluated to choose an aperture diameter for the traverses. The aperture percent of beam diameter in the focal plane has been tabulated in Table 1 for the lasers and beam diameters to be reported in this work. Table 1 shows that the aperture diameter percent of beam diameter ranged from 5.5% to 47%. Figure 36 shows a comparison of the results of profiles obtained with 200 micron, 400 micron, and 600 micron apertures compared to a gaussian distribution. The 400 micron aperture with the 50 millimeter diameter helium cadmium beam is observed from Figure 34 to track the

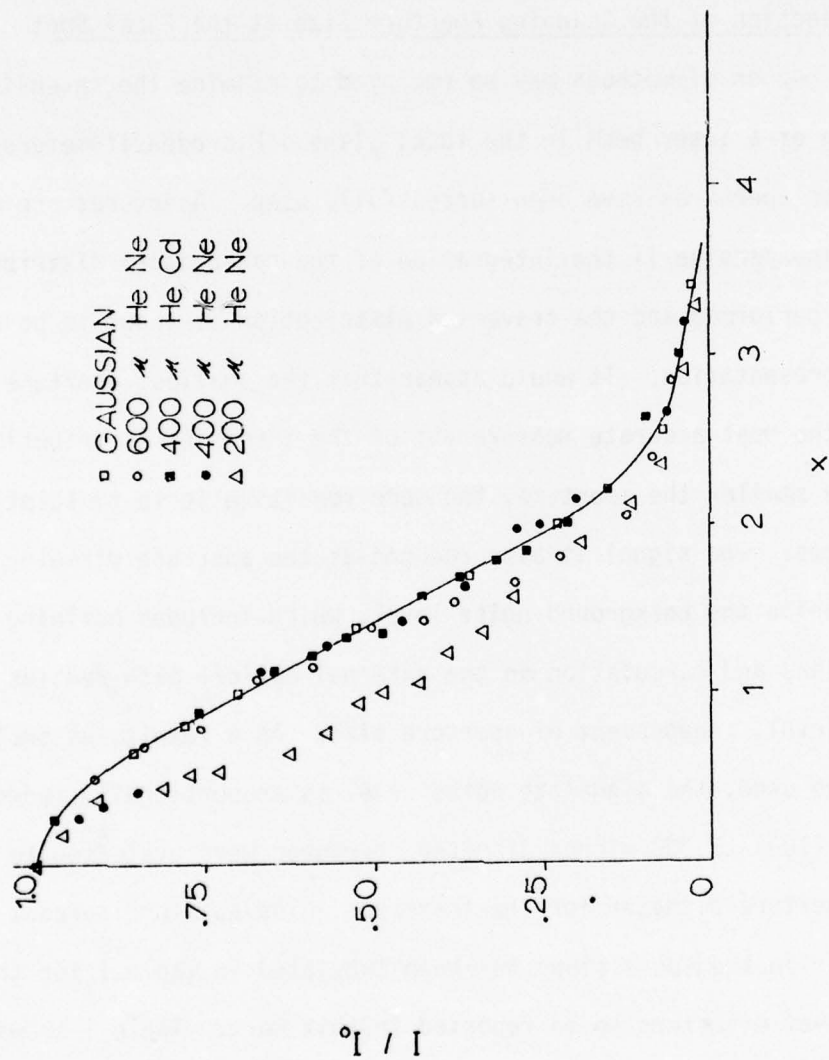


Figure 36. Comparison of Focal Plane Aperture Intensity Tracking

gaussian distribution to within 2%. Table 1 shows that the 400 micron aperture with the 50 millimeter diameter helium cadmium beam has an aperture to focal spot ratio of 23%.

The other aperture diameters evaluated exhibit comparatively poorer tracking ability as shown in Figure 36. The ratio of aperture diameter to focal spot diameter should be maintained constant in comparing helium neon and helium cadmium laser beam spread results. For example, a 600 micron diameter aperture would be selected for a helium neon beam of 50 millimeters diameter and a 400 micron aperture would be selected for a 50 millimeter diameter helium cadmium beam.

The Calculation of Integral Laser Power

The power profile obtained behind the circular aperture was digitized and the profile integrated on a Hewlett Packard 9800 series digitizer and calculator. The focal spot is located prior to taking a set of data. Prior to running a profile, the intensity or power is maximized in the plane of the focal spot. A single traverse requires 30-60 seconds and, therefore, includes a time average of the focal spot motion.

The integration calculation assumes that the profile is symmetric. The original experimental traverses were obtained on 27.9 x 43.2 centimeter paper. Due to the large size of the trace, no corrections were made for rotation of the trace relative to the digitizer table during the integral calculation. A base line was recorded on each trace and a line parallel to the base line was aligned with the digitizer base line. Vertical and horizontal scales are entered by digitizing the peak intensity and the two end points of the laser profile. Because the

Table 1. Aperture Percentage of Beam Diameter

| Beam Diameter In Millimeters | Focal Spot Size In Millimeters | Aperture Diameter In Microns | Aperture Diameter Focal Spot Size in % |
|---------------------------------|-----------------------------------|---------------------------------|---|
| 50 mm | 1.64 | 800 | 32.6% |
| | | 600 | 26.0% |
| | | 400 | 10.3% |
| | | 200 | 8.77% |
| | | 100 | 4.39% |
| 26 | 3.15 | 800 | 16.97% |
| | | 600 | 13.5% |
| | | 400 | 8.48% |
| 8 | 10.23 | 800 | 5.20% |
| | | 600 | 4.17% |
| 50 mm | 1.14 | 800 | 46.85% |
| | | 600 | 37.34% |
| | | 400 | 23.38% |
| | | 200 | 12.58% |
| 30.58 | 1.87 | 800 | 28.60% |
| | | 600 | 22.83% |
| | | 400 | 14.30% |
| 14.03 | 4.07 | 800 | 13.13% |
| | | 600 | 10.48% |
| 1.5 | | 800 | 5.52% |

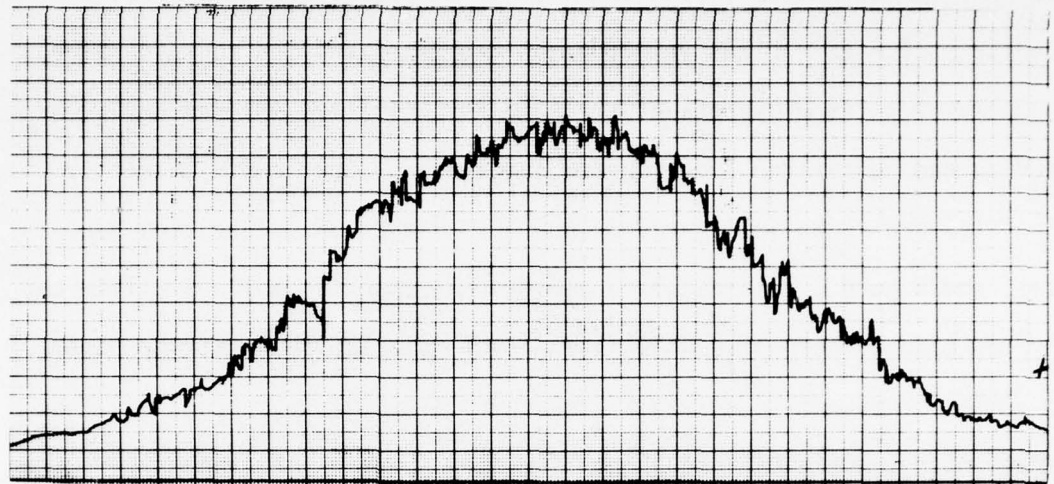


Figure 37. 14.03 mm Diameter He Cd Laser Beam Traverse at an L/D_p Station of 28, Medium Heat

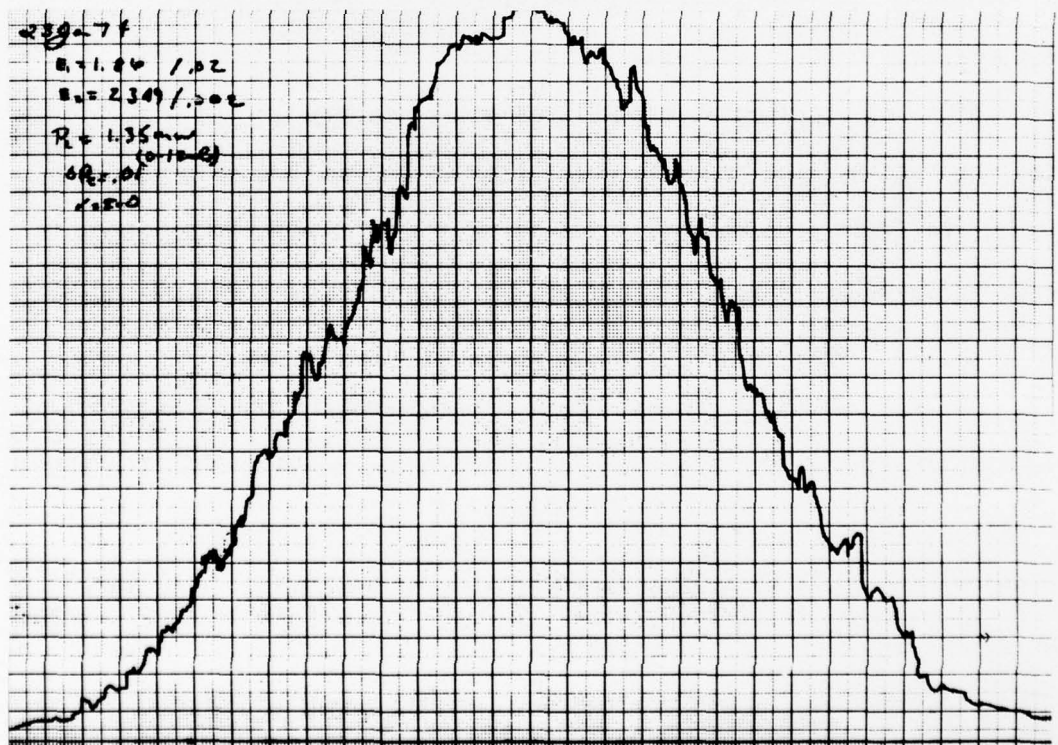


Figure 38. 14.03 mm Diameter He Cd Laser Beam Traverse at an L/D_p Station of 28, Zero Heat

centerline of the focal spot is moving, the average centerline is initially estimated and the zero for the digitizer shifted to this value. Successive pairs of points at the same intensity are entered and a mean radius and centerline location are calculated. Two sample intensity profiles are shown in Figures 37 and 38. Figure 38 is the zero heat case and Figure 37 represents a medium heat case for a 14.03 millimeter helium cadmium beam at an L/D_p station of 28. The intensity or power profile is reduced to a single average half-width power profile. The area under the fit of a straight line through pairs of successive points is integrated and then revolved through 2π . The integral under the straight line approximation is accumulated as total power as a function of the radial position, assuming the average half-width distributions to be symmetric in the focal plane. The actual values of centerline, average radius and incremental accumulated power are pointed out. For plotting the results, the power is normalized to the no flow value and the average half-width to the value of radius at the no flow integrated power value point. The digitized integral curves of Figures 37 and 38 are shown in Figures 39 and 40.

The volume of a right circular cylinder was calculated by hand and with the program to check the calculation procedure and assure that rotation of the records was not significant. The hand calculation agreed within .017% of the machine calculation for eight increments. The zero flow, zero heat calculations typically involve approximately 60 pairs of points. The digitizer has a machine resolution of .0254 machine centimeters. The centerline is shifted to the peak value of the laser intensity distribution at the beginning of the integral laser

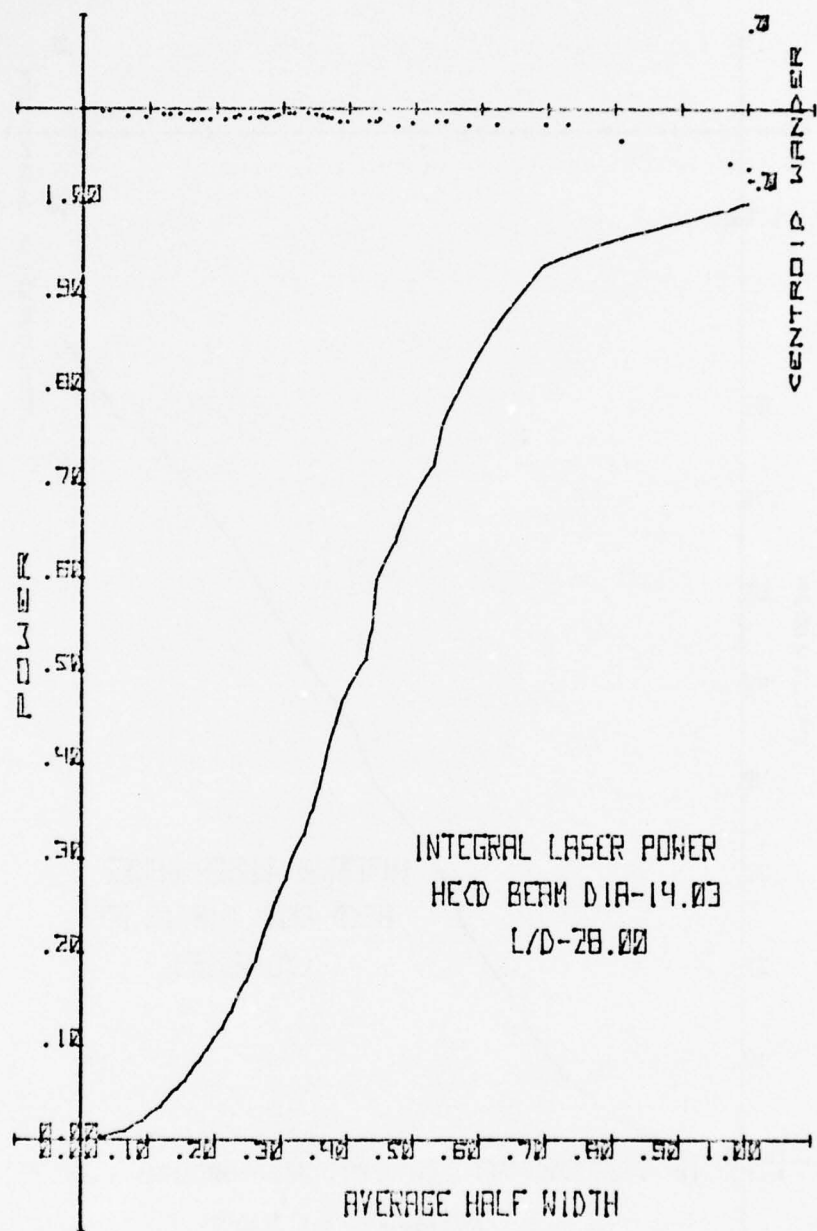


Figure 39. Integral Laser Power, Zero Heat

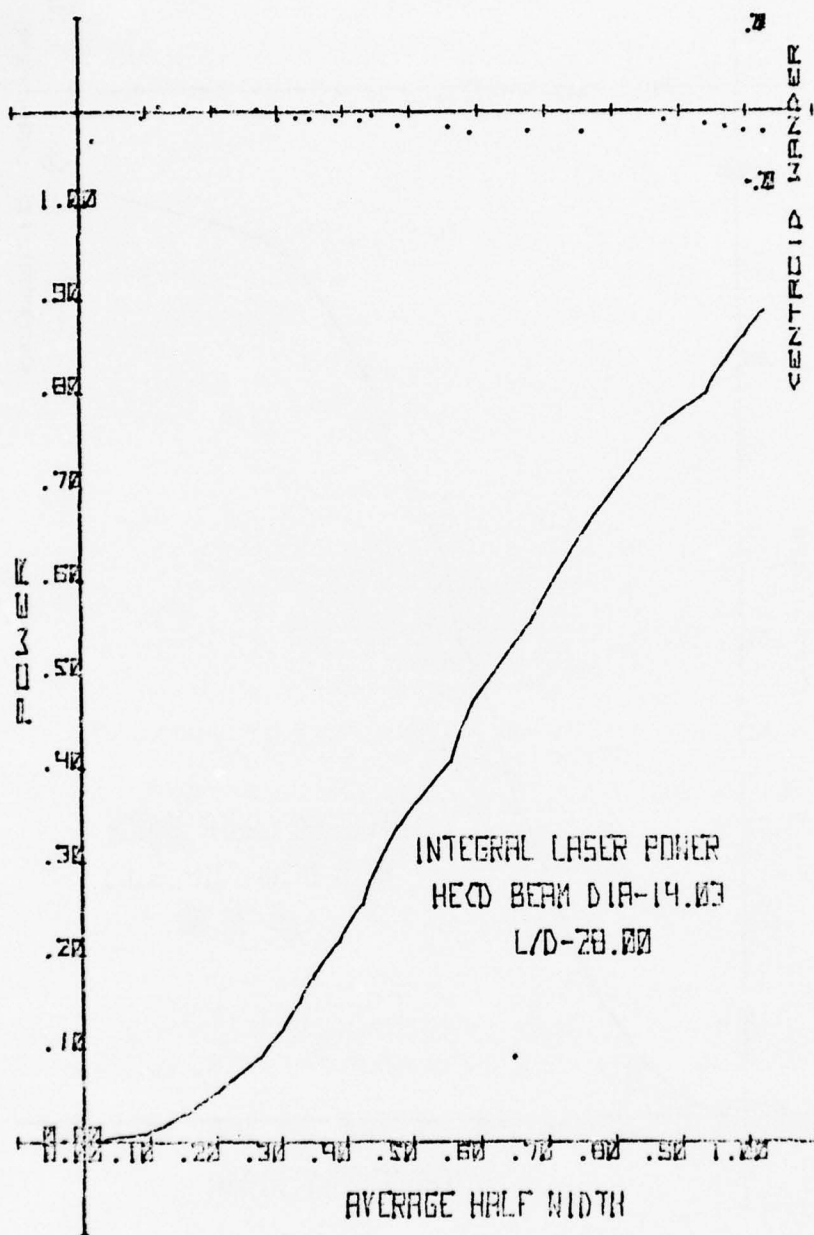


Figure 40. Integral Laser Power, Medium Heat

power calculation. The shift of the centerline location is convenient for the display of centerline wanders. The centerline was shifted from the original estimated location by 2.54 machine centimeters and the total integrated power recalculated to show the sensitivity of the centerline location. The original and the shifted powers differed by $\pm 0.01\%$. The largest error results from non-linear and oscillating junctions between digitized data points. These errors are estimated to be less than 2.5% in incremental area.

Power is conserved in the scattering process. If the digitizing process is carried out sufficiently far for both the turbulent case as well as the non-turbulent case, the total power is the same. The runs shown in Figures 42, 43, and 44 have power discrepancies of -2.23% and +10.14%, and -2.86% in total power, respectively, for Figures 42, 43, and 44 relative to the power shown in Figure 41. Since over 470 traverses were reduced, it is impractical to show all curves. Figures 41, 42, 43, and 44 are representative of the least well behaved traverse measurements. In general, the profile measurements become better behaved as L/D_p increases and smaller diameter beams are employed, as may be observed by comparing Figures 39 and 40 with Figures 41 and 43. The power discrepancies would also decrease with beam diameter and increase in L/D_p .

The total laser power was normally measured without the aperture in front of the power meter prior to collecting a set of data. The aperture measured and calculated powers agree with the total laser power measured without the aperture when the traverses are sufficiently large.

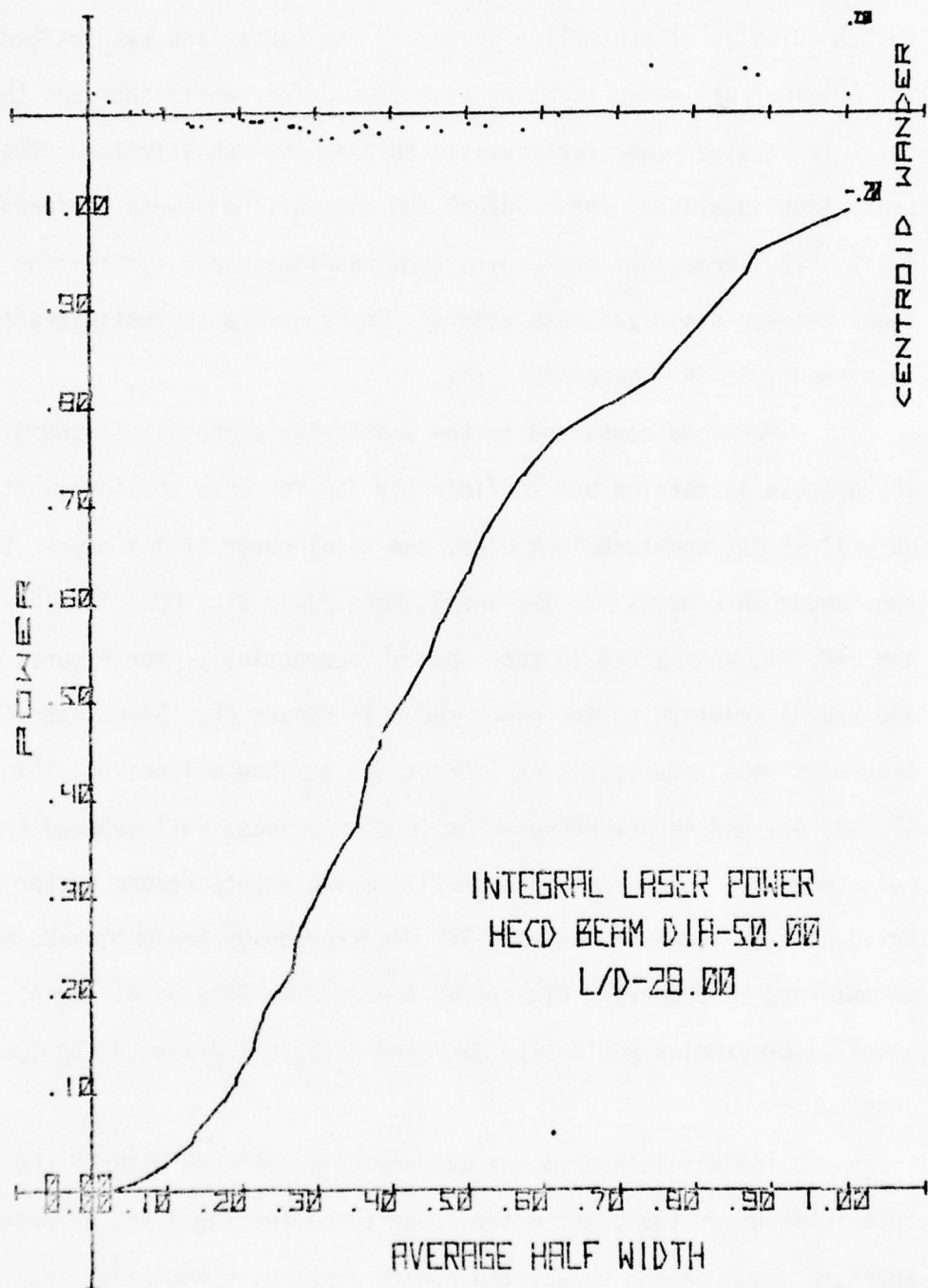
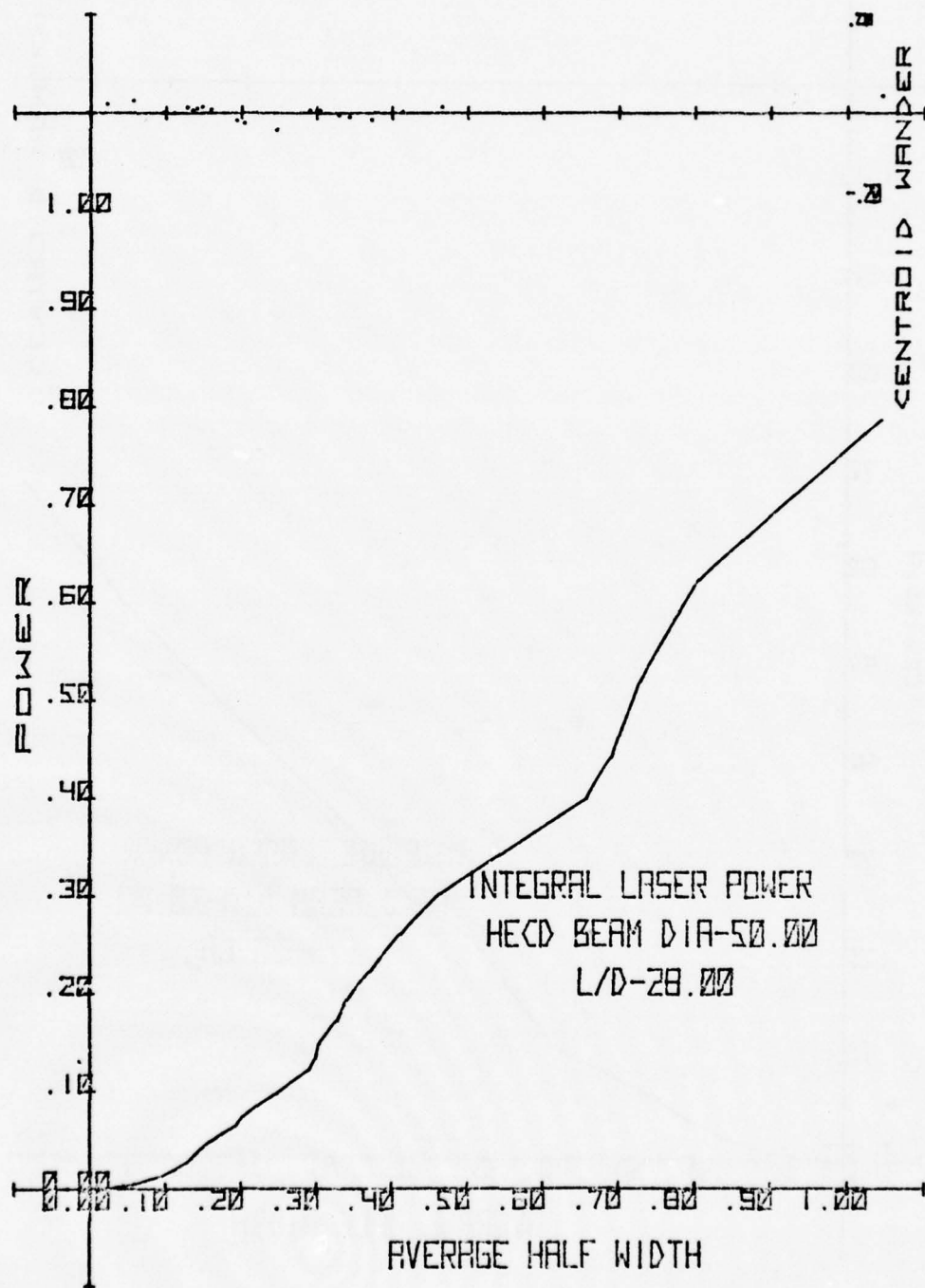


Figure 41. Integral Laser Power, Zero Heat



● Figure 42. Integral Laser Power, Low Heat

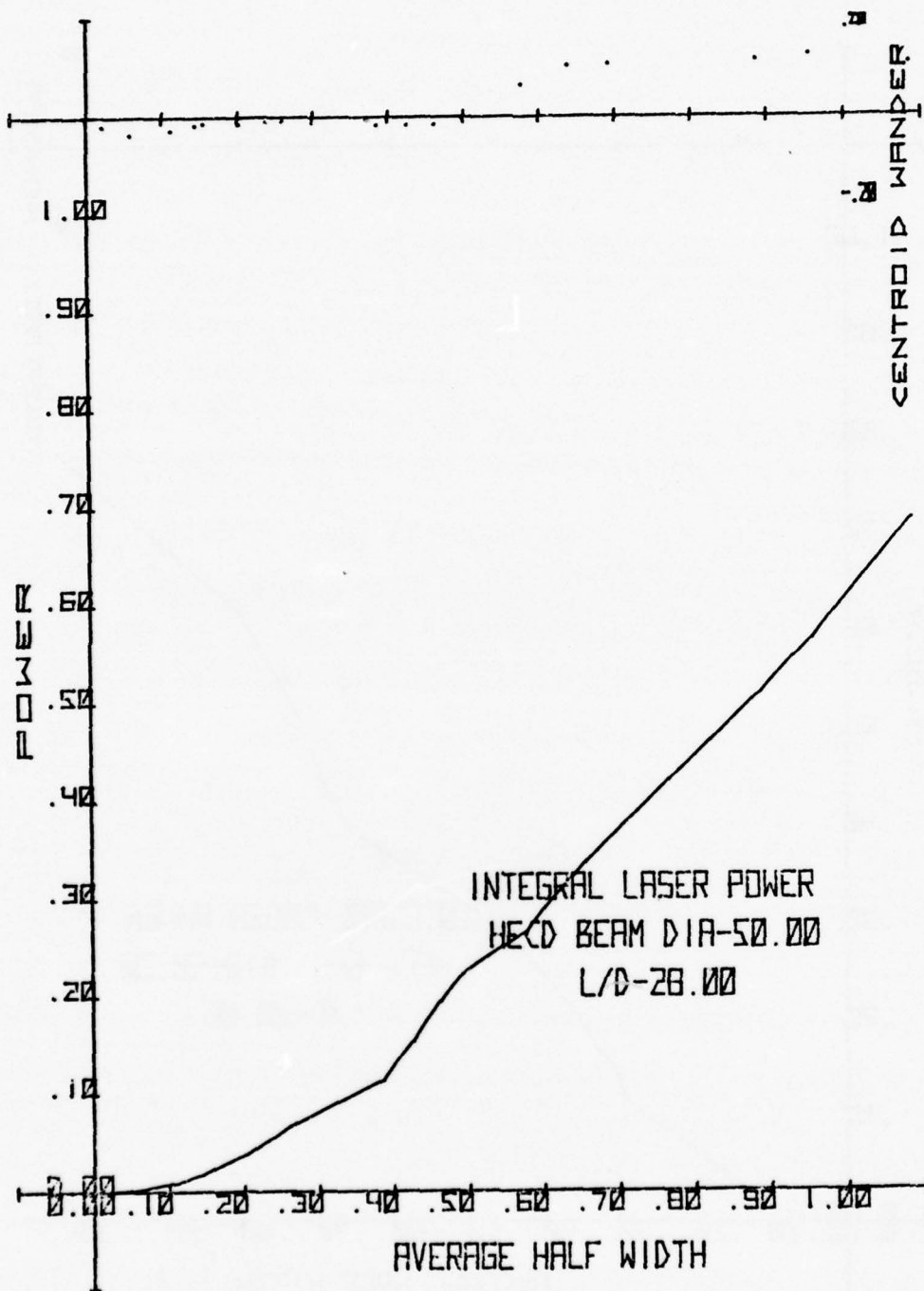


Figure 43. Integral Laser Power, Medium Heat

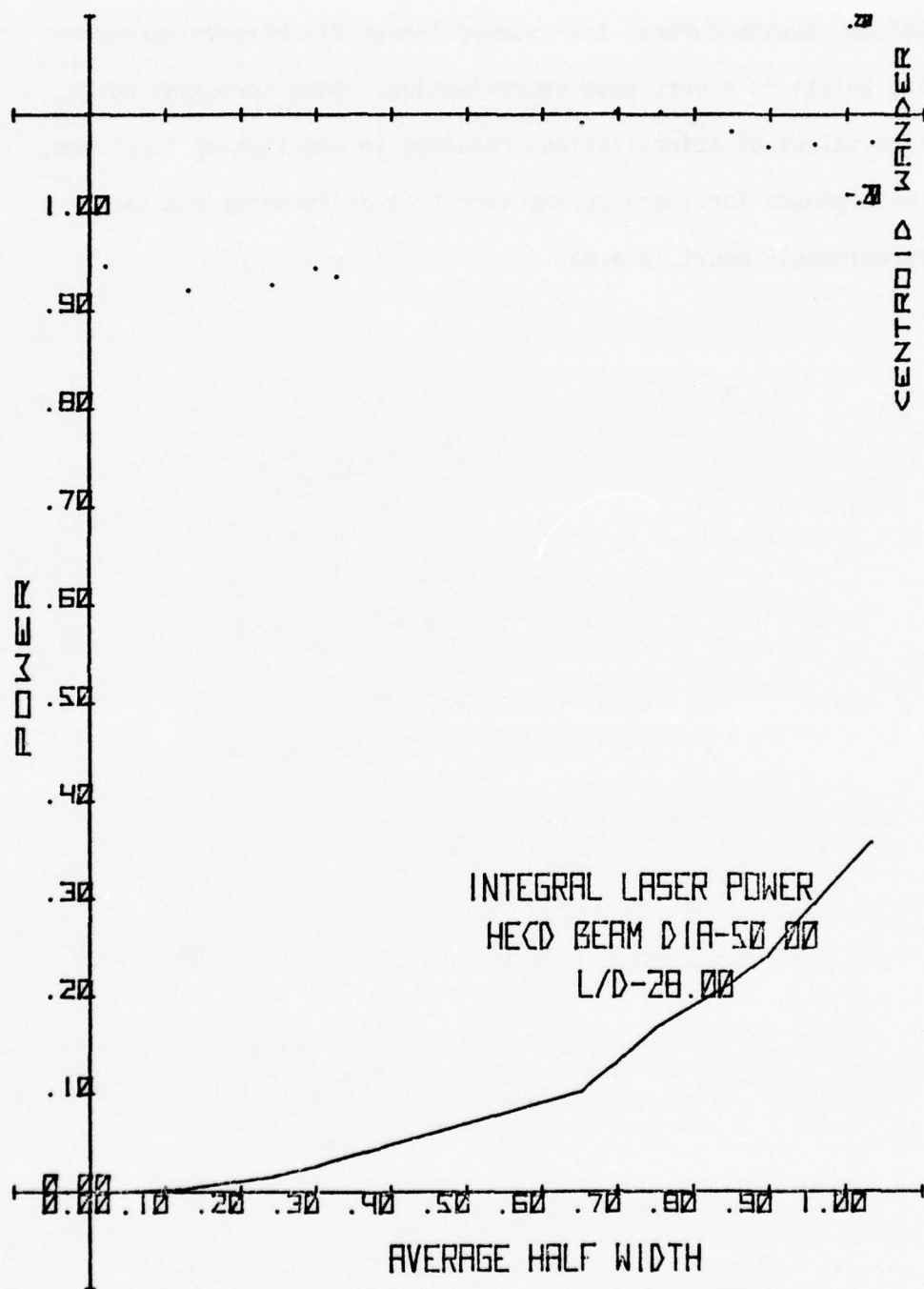


Figure 44. Integral Laser Power, High Heat

In digitizing smooth curves, the assumed linear fit between successive intensity points is a very good approximation. Some turbulent cases, with large values of scintillation, resulted in oscillating functions. Points were chosen for these curves such that differences and excesses were approximately equal in area.

CHAPTER V.

EXPERIMENTAL RESULTS

Summary

In this chapter the mean and fluctuating tunnel profiles will be presented for velocity, temperature, index of refraction, and scales of turbulence. Next, the experimental effects on a laser beam propagating through this defined turbulent medium will be examined by observing:

- a. The distribution of beam spread
- b. The increase of R/R_0 at the half power point of the turbulent laser profile
- c. The effect of $\langle \Delta \eta \rangle^2$ on laser beam spread
- d. The effect of λ on laser beam spread
- e. The effect of laser beam diameter on laser beam spread
- f. The effect of Λ on laser beam spread
- g. The effect of diameter of the laser beam/ Λ ratio on laser beam spread
- h. The reduction of centerline intensity of the laser beam

Table 2 illustrates the values of the independently variable parameters for which laser beam spread measurements were obtained. For example, the 50 millimeter diameter helium cadmium beam spread was measured at L/D_p stations of 28, 34.5 and 45 for at least three values of heat addition, at each L/D_p station, for each tunnel velocity pressure at which significant beam spread existed.

Table 2. Range of Independent Experimental Parameters

| | Tunnel Velocity ΔP in Cm Water | Laser Beam Diameter In Millimeters | Laser Wave Length In Nanometers | Nominal Heat Addition (In Watts) | L/Dp Station |
|---------------------------|---|--|---------------------------------------|--|-----------------|
| Turbulence Generator A | | | | | |
| 1.27 Cm Diameter | .025 | 50, 26, 8 | He Ne - 632.8 | Zero | 14 |
| Perforations | .501 | | | Low (527) | |
| % Blockage=.525 | .076 | | | Medium (783) | |
| | .127 | | | High (1166) | |
| | .254 | | | Zero | |
| | .508 | | | | |
| | .762 | | | | |
| | 1.016 | | | | |
| | 1.270 | | | | |
| | 1.524 | | | | |
| Turbulence Generator B | | | | | |
| .635 Cm Diameter | .025 | 50, 26, 8 | He Ne - 632.8 | Zero | 28, 34.5, 45 |
| Perforations | .051 | 50, 30.58, 14.03, 1.5 | He Cd - 441.6 | Low (527) | |
| % Blockage=.651 | .076 | | | Medium (783) | |
| | .127 | | | High (1166) | |
| | .254 | | | Zero | |
| | .508 | | | | |
| | .762 | | | | |
| | 1.016 | | | | |
| | 1.270 | | | | |
| | 1.524 | | | | |

Mean and Turbulent Tunnel Profiles

Due to the decreases, primarily in $\langle \Delta \eta \rangle^2$, which results in reduced beam spread, the number of spread measurements of interest decreases with the L/D_p ratio. The combinations of interest results in 150 tunnel profiles for turbulence generator B which were reduced in accordance with the procedures of Chapter IV. A similar set of spread measurements were performed for turbulence generator A at an L/D_p station of 14.

Sample profiles for the mean and fluctuating components of U and T , obtained with velocity turbulence generator B, are shown in Figures 45, 46, 47 and 48 for a nominal (tunnel velocity) pressure of .025 centimeter of water and heat additions of zero, 516, 814 and 1196 watts, respectively. The rms temperature scales of Figures 46, 47 and 48 are 10 times, 30 times and 30 times, respectively, the zero heat temperature scale of Figure 45. The mean temperature and velocity are well behaved with little structuring of the mean flow. The rms profiles, on the other hand, show rather wide variations of unpredictable structuring which indicates the desirability of calculation of a spatial mean value for the rms quantities. Vertical profiles were also evaluated for turbulence generator B at three L/D_p stations, three heats and a tunnel velocity pressure of .076 centimeter of water to ensure that the free convective effects were negligible. Figure 49 shows a vertical profile obtained for a nominal high heat (1166 watts) at a velocity pressure of .076 centimeter of water, at the L/D_p station of 34.5, indicating negligible free convective effects and reasonably uniform rms profiles over the central portion of the tunnel through which the beam traverses.

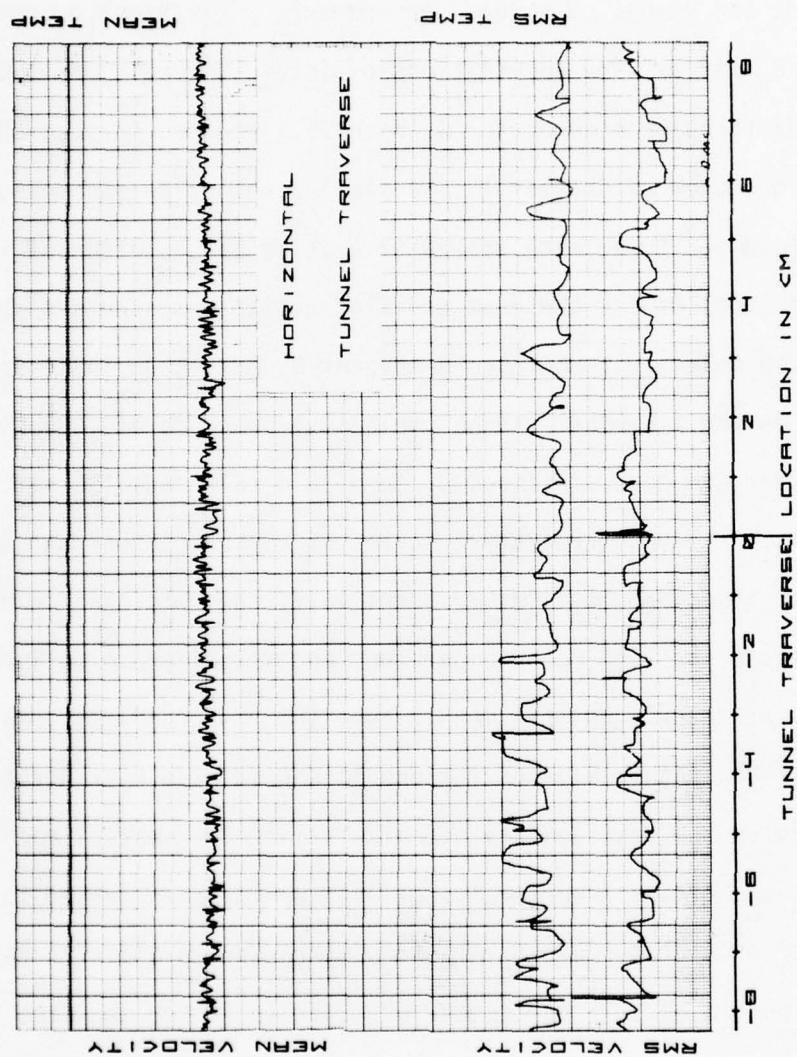


Figure 45. Horizontal Tunnel Traverse, $L/D_p = 45$, Zero Heat

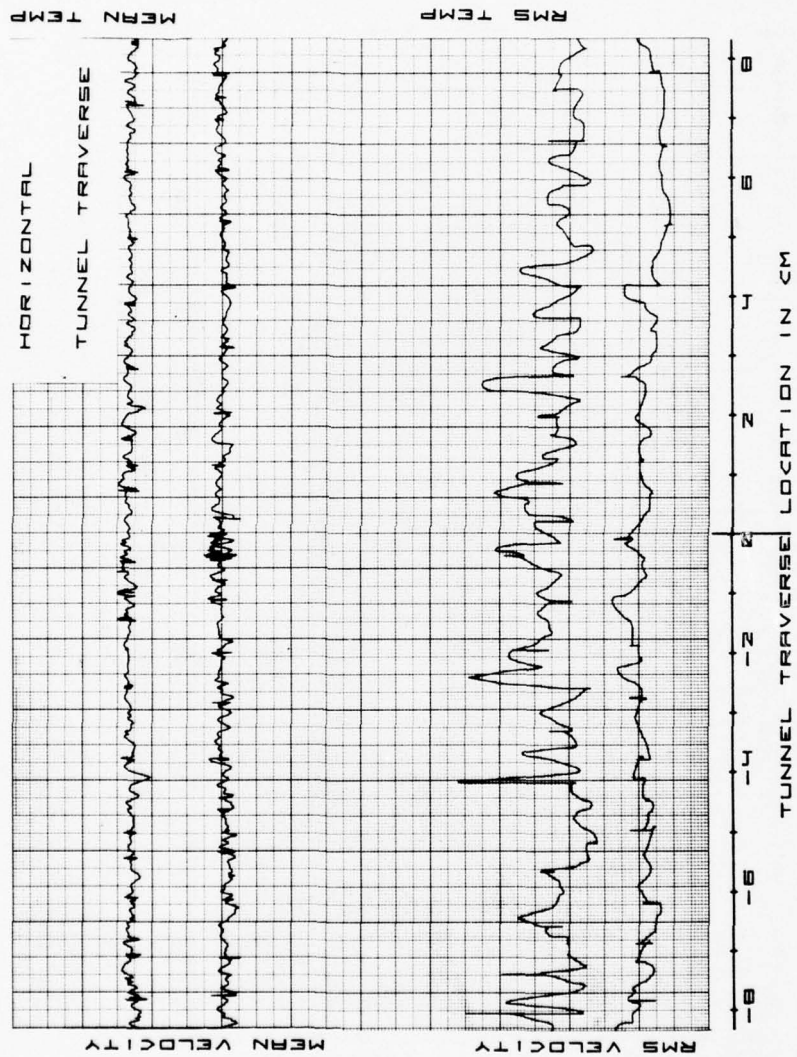


Figure 46. Horizontal Tunnel Traverse, $L/D_p = 45$, Low Heat

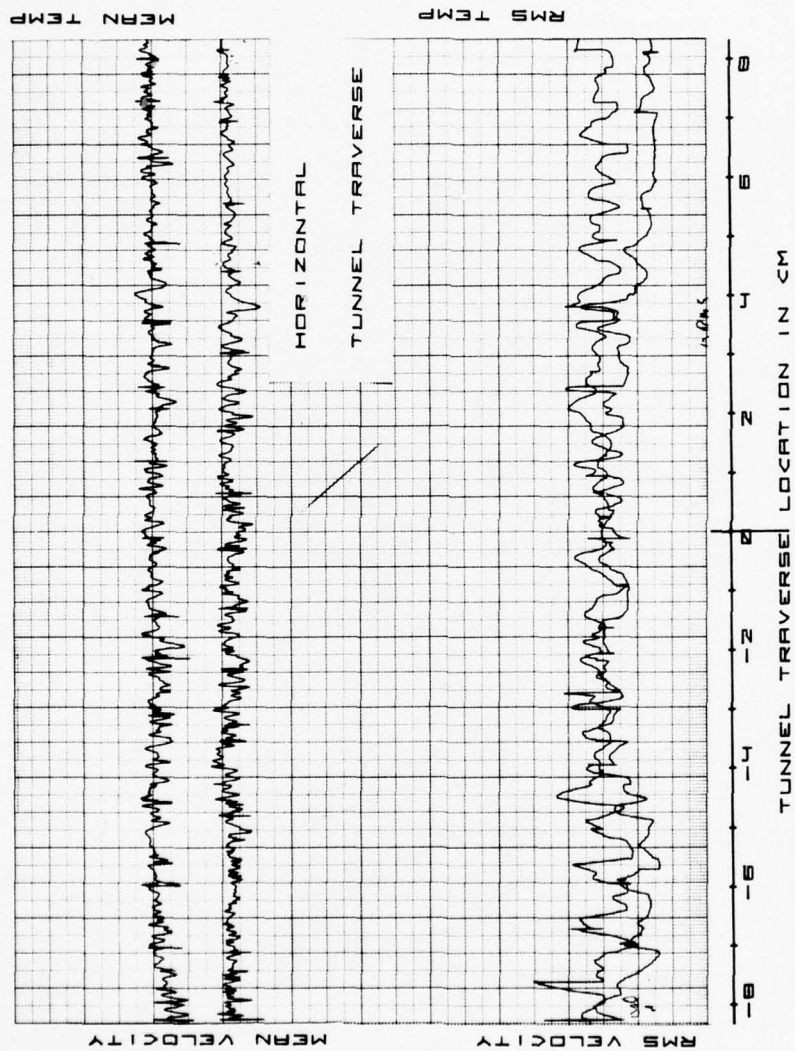


Figure 47. Horizontal Tunnel Traverse, $L/D_p = 34.5$, Medium Heat

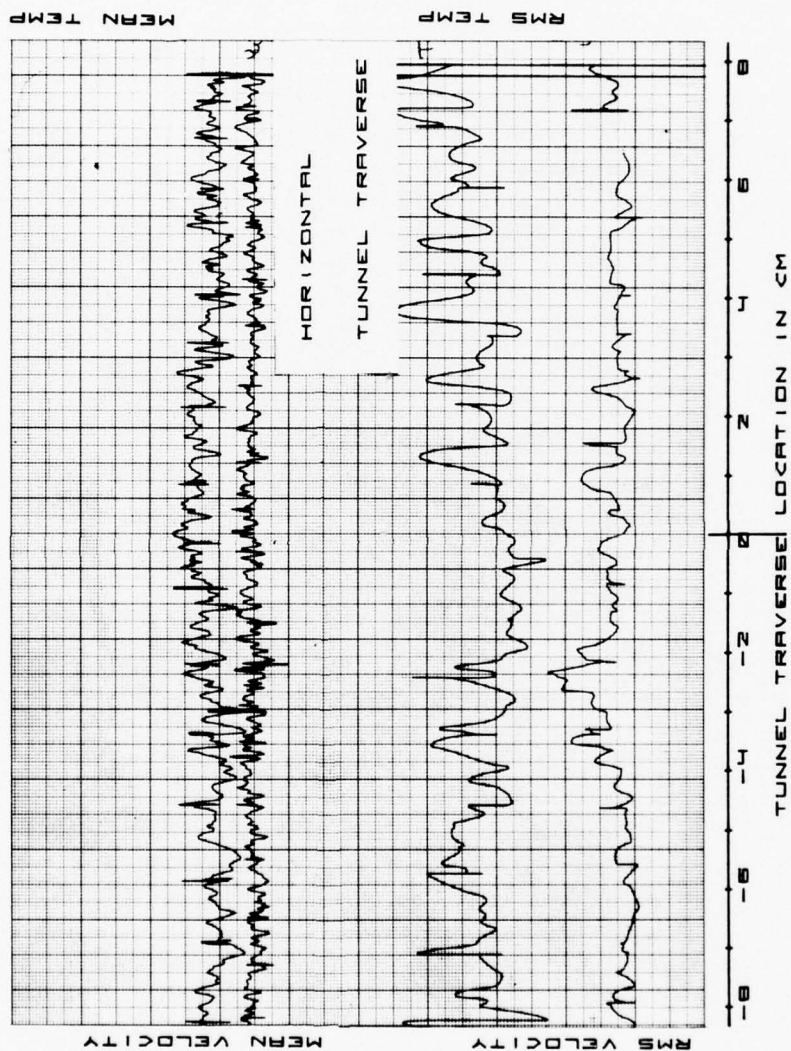


Figure 48. Horizontal Tunnel Traverse, $L/D_p = 28$, High Heat

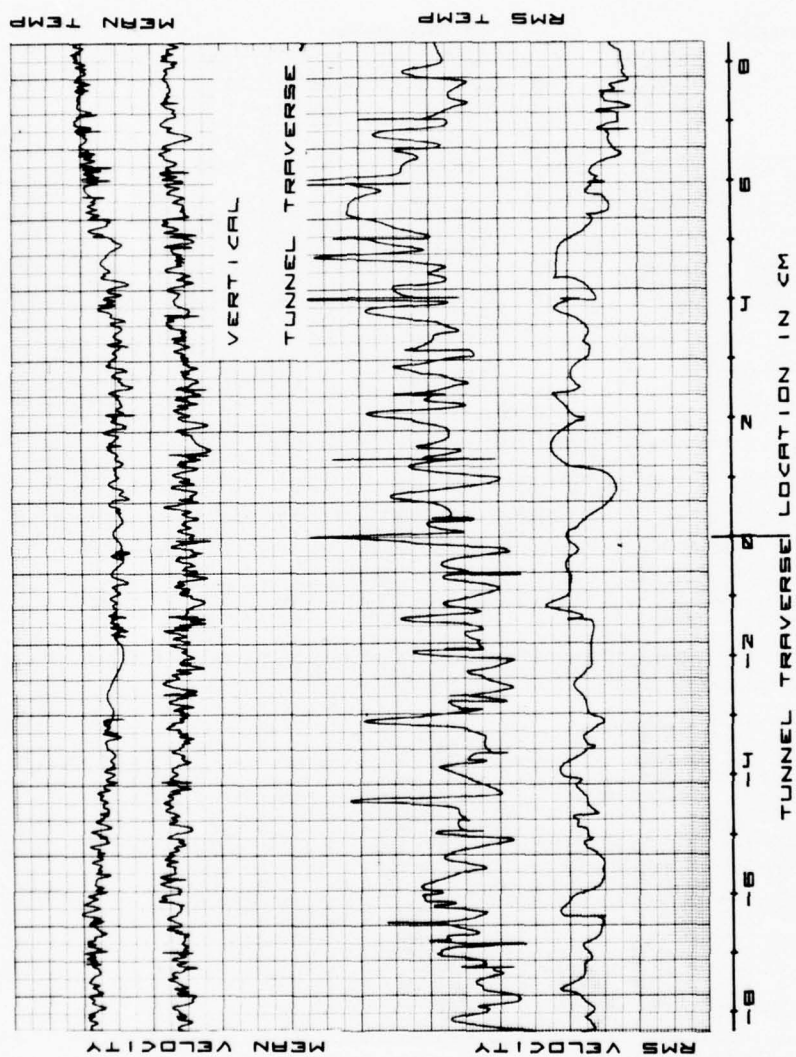


Figure 49. Vertical Tunnel Traverse, $L/D_p = 34.5$, High Heat

Variations of Fluid Properties Along the Tunnel Axis

Reduction of the profiles for low and medium heat additions at the same tunnel velocity pressure of .025 centimeter of water results in a well behaved variation with L/D_p ; in temperature fluctuation, temperature intensity, and index of refraction turbulence intensity as shown respectively in Figures 50, 51, and 52. The upper curve in Figure 50 represents the nominal high heat addition; intermediate, medium heat; lower, low heat. The points located just above the abscissa for these curves represent the zero heat addition case. Since η is very nearly 1, Figure 52 is also representative of $\langle \Delta\eta \rangle$. Figure 52 indicates a range of 4 to 1 in $\Delta\eta$ is available at the three tunnel stations between low and high heat additions. As tunnel velocity is increased, ΔT is reduced allowing the range in $\langle \Delta\eta \rangle$ between zero heat addition and the curves of Figure 52 to be investigated, giving a total available range of 1.4×10^{-11} in $\langle \Delta\eta \rangle^2$.

The velocity turbulence intensity and the scales of turbulence were found to be less well behaved. Temperature scales of turbulence will next be briefly reviewed and the experimentally obtained curves of velocity turbulence intensity and the temperature integral scale of turbulence given.

Equation (42) gives the semi-empirical relation between integral scale of turbulence and the microscale as:

$$\frac{\ell_0}{\Lambda} = \frac{\sqrt{A_g}}{\sqrt{R_\Lambda}} \quad (85)$$

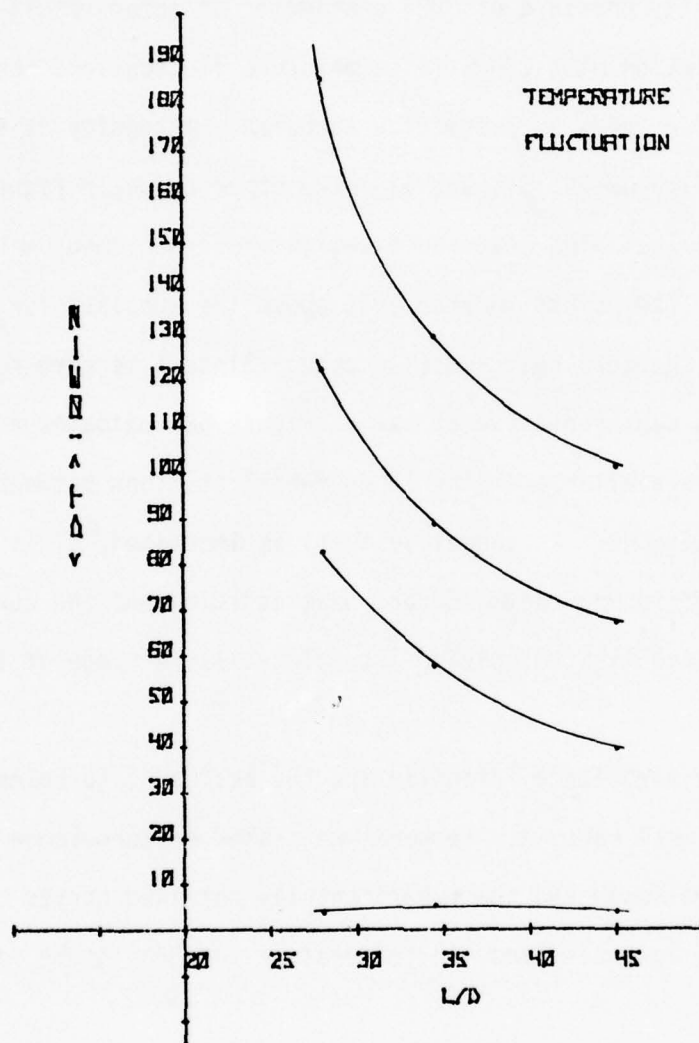


Figure 50. Temperature Fluctuations

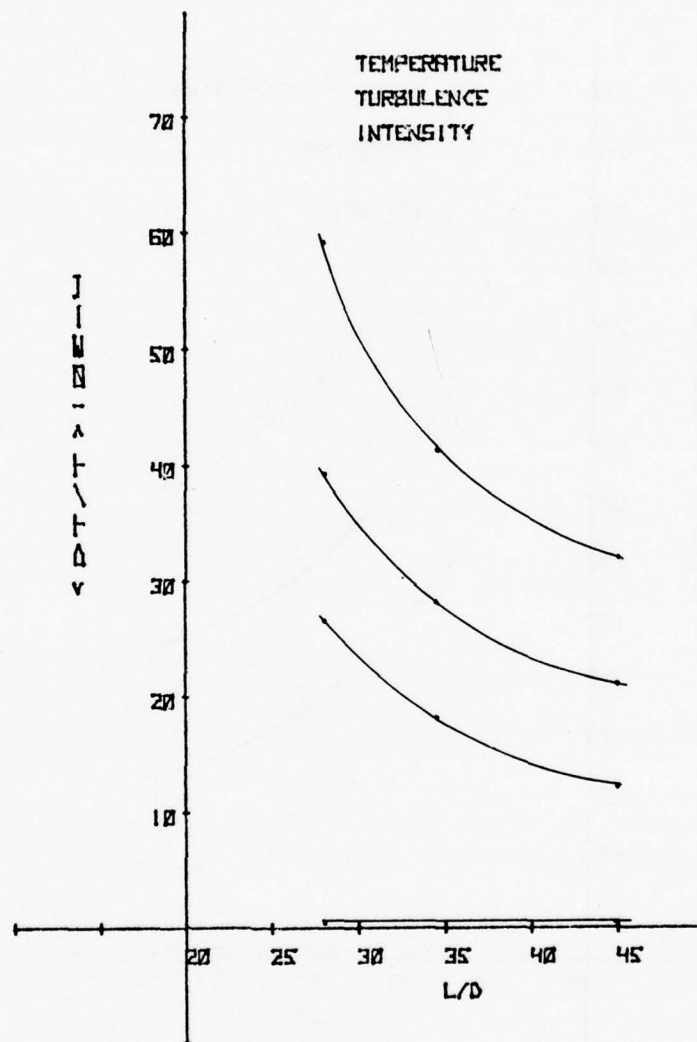


Figure 51. Temperature Turbulence Intensity

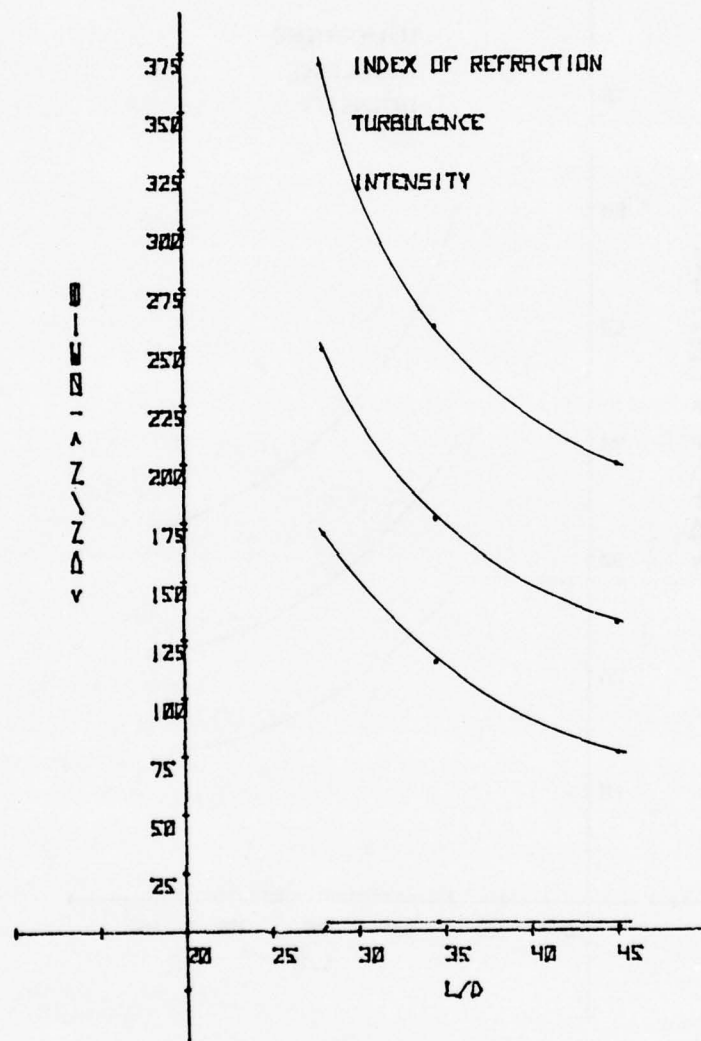


Figure 52. Index of Refraction Turbulence Intensity

Batchelor (Batchelor, 1953, p. 136) gives the decay curve for λ_0^2 for the initial period as:

$$\lambda_0^2 = \left(\frac{10 \nu D_p}{U} \right) \left(\frac{x_0}{D_p} \right) \quad (86)$$

Squaring equation (42) and substituting the λ_0^2 for the initial period of decay gives the integral scales decay as:

$$\Lambda = \frac{10 D_p}{A_g} \left(\frac{x_0}{D_p} \right) \quad (87)$$

The fluctuating velocity component parallel to the mean velocity is observed to decay according to (Townsend, 1956, p. 56):

$$\frac{1}{(u')^2} \propto (x - x_0)^\eta \quad (88)$$

where η takes on the values from 1.2 to 1.0 for non-isotropic to isotropic flows, respectively, or for isotropic turbulences in terms of Tu as:

$$\frac{1}{(T_u)^2} = \frac{U^2}{u'^2} = \frac{b}{C_D} \left(\frac{x - x_0}{D_p} \right) \quad (89)$$

where b is a constant dependent upon the turbulence generator geometry and C_D is the drag coefficient of the generator. b/C_D may, therefore, be expected to be weakly Reynolds number dependent.

The prediction of the integral scale and the turbulence intensity's behavior is not at all straightforward as is illustrated by Batchelor's Figure 6.1 in which he presents the graph of the relation (Batchelor, 1953, p. 106, Fig. 6.1)

$$\frac{du^2}{dt} = \frac{Cu^3}{\Lambda} \quad (90)$$

or

$$\frac{du^2}{dt} \frac{\Lambda}{Cu^3} = 1 \quad (91)$$

This relation is postulated from the experimental observation that the kinetic energy of turbulence decreases as u^3/Λ , with C being a constant of order unity. Batchelor's plot of this relation against experimental observations, as a function of L/D_p with Reynolds number and D_p as parameters, shows a spread from .8 to 1.45 in $du^2\Lambda/(dt Cu^3)$ at an L/D_p of 20. Likewise, there is not a consistent trend with Reynolds number change, nor in the amount of change in $du^2\Lambda/(dt Cu^3)$ with Reynolds number.

The behavior of the scales of turbulence may be expected to be extremely difficult to predict accurately and they must be measured for each configuration and location if a value is to be obtained. The wide range of variation of the integral scale's decay is additional reason for examination of the microscale's behavior and decay.

The zero heat addition velocity turbulence intensity is shown in Figure 53. A spread of 3 to 10% in the values of Tu with Reynolds number is observed from Figure 50. The .025 and .076 centimeters of water velocity pressure Tu points are well behaved. The curves through these have been used to construct the mean curve for the decay of Tu shown in Figure 54 for the zero heat addition case.

The velocity Tu generator was originally envisioned as an independent control on the integral scale of the temperature fluctuations. Comparison of the temperature integral scales with the velocity integral scales indicates they are approximately equal. The range of value for the velocity scale at an L/D_p of 34.5 was from .953 to 1.499 centimeters. The temperature scales at the 34.5 station ranged from .89 to 1.60 centimeters. Comparison of the velocity and temperature integral scales at the L/D_p stations of 28 and 45 were also similar in their variations.

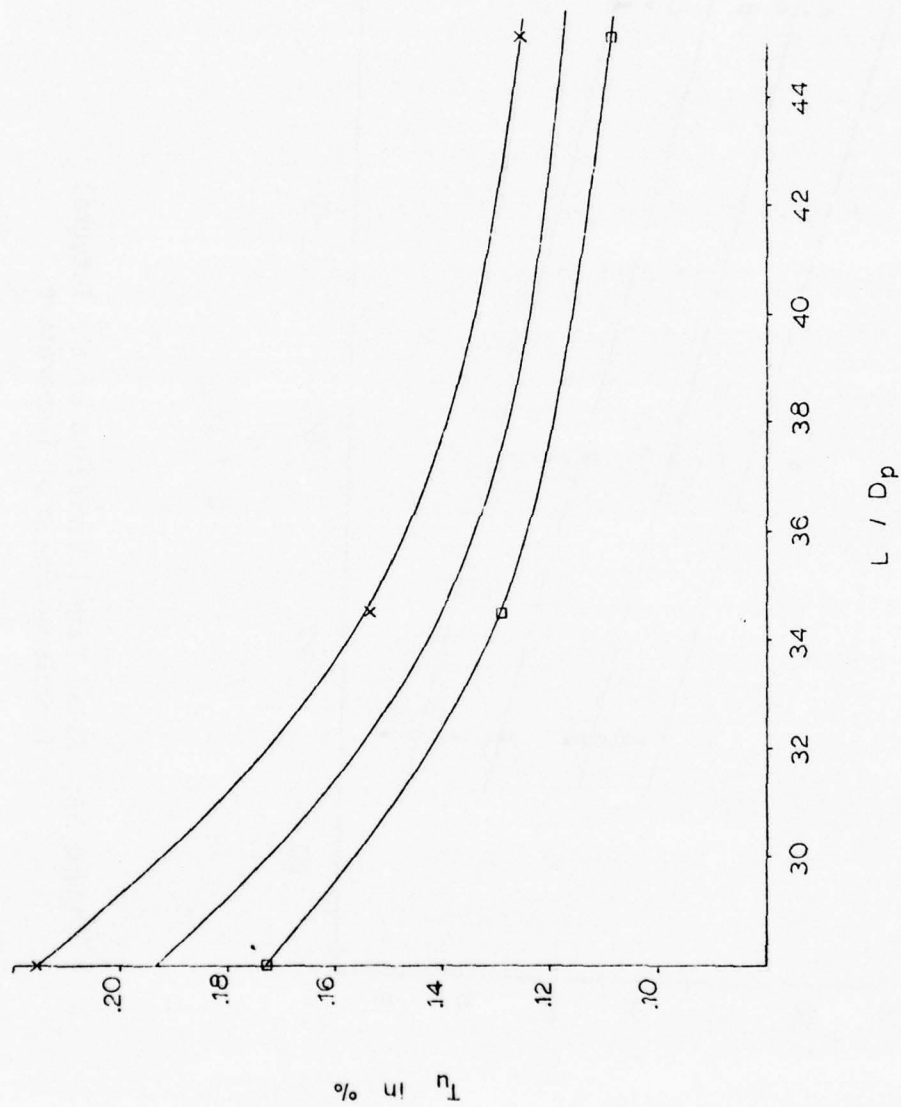


Figure 53. Axial Tunnel Variation of T_u

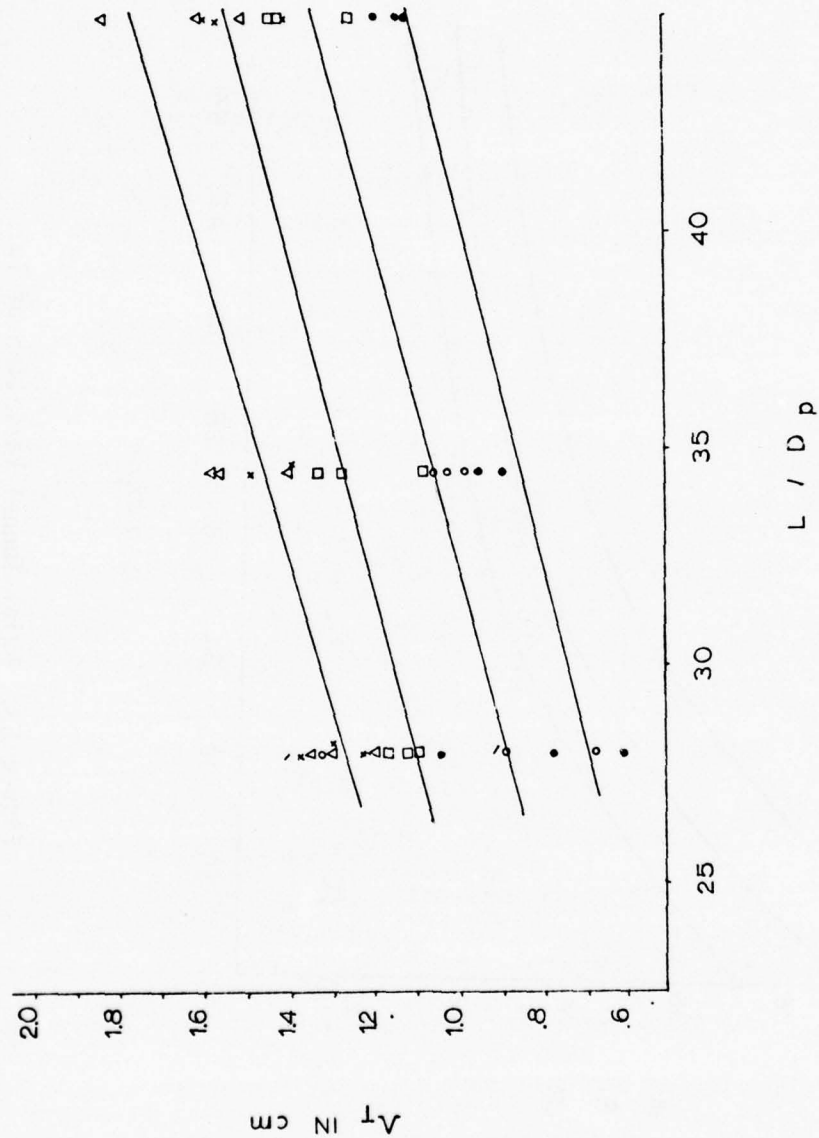


Figure 54. Axial Tunnel Variation of the Integral Turbulence Scale of Temperature

The temperature and velocity integral scales may be considered equivalent in magnitude. The temperature integral scale is shown in Figure 54. Examination of Figure 54 indicates that heat addition alters the apparent integral scale at a given L/D_p location in an irregular fashion. The trends with Reynolds number do, however, show some approximate ordering, as has been indicated by the appropriate curves, for velocity pressures of .025, .051 and .127 centimeters of water.

Variations of Fluid Properties Along the Tunnel Axis with the Non-Dimensional Heat Addition Parameter

A method for normalizing the fluctuations in index of refraction in the tunnel to account for changes in tunnel velocity and amounts of heat addition which varied from run to run and day to day is desirable, particularly at low tunnel velocities which were difficult to reproducibly set. Equation (27) gave:

$$\langle \Delta \eta \rangle \propto \frac{dT_{rms}}{T^2} \quad (92)$$

while T^2 is of course $\propto Q^2$, T is in absolute units, and for this experiment does not change by more than 7%. The variation in $\langle \Delta \eta \rangle$ will be nearly equivalent to the change in dT_{rms} . dT_{rms} is bounded by, but not equal to ΔT , the change in temperature of the tunnel flow. The assumption of $\langle \Delta \eta \rangle$ proportional to Q would be a reasonable choice. If Q is non-dimensionalized, the parameter becomes:

$$\frac{\dot{Q}}{\dot{M} C_p T} \quad (93)$$

or since p remains nearly equal to barometric pressure in this experiment, as was pointed out in Chapter IV, the non-dimensional parameter

becomes:

$$\frac{\frac{Q}{P_B C_p A U}}{R_g} = \frac{K Q}{U} \quad (94)$$

The measured values of ΔT_{rms} , T , and P_B were used to calculate $\langle \Delta \eta \rangle$ for the integrated tunnel profiles and also the tunnel centerline values in accordance with the procedures of Chapter IV. The mean tunnel traverse variation of $\langle \Delta \eta \rangle$ with the non-dimensional heat addition parameter $K Q/U$ is shown in Figures 55, 56 and 57 for turbulence generator B at the L/D_p stations of 28, 34.5 and 45 respectively. A least squares linear fit of the data shows the non-dimensional heat addition parameter to be a reasonable choice for comparing and predicting the $\langle \Delta \eta \rangle$ variation. At an L/D_p station of 45, Figure 58 shows an excellent fit with $K Q/U$ for low, medium, and high values of heat addition at approximately the same value of tunnel velocity.

Figure 59 shows the $\langle \Delta \eta \rangle$ variation with $K Q/U$ for turbulence generator A, the 1.27 centimeter perforation diameter turbulence generator, at an L/D_p station of 14. The slope of the $\langle \Delta \eta \rangle$ curve for the turbulence generator A is nearly equal to turbulence generator B at the L/D_p station of 28. The major difference between generator A and B is doubling of the turbulence scale.

The velocity turbulence intensity is shown in Figures 60, 61 and 62 against the parameter $K Q/U$ at the L/D_p stations of 28, 34.5 and 45 for turbulence generator B. The velocity turbulence intensity has been calculated to include the temperature correction terms as given by equation (38) of Chapter IV. A linear relation is again shown with the

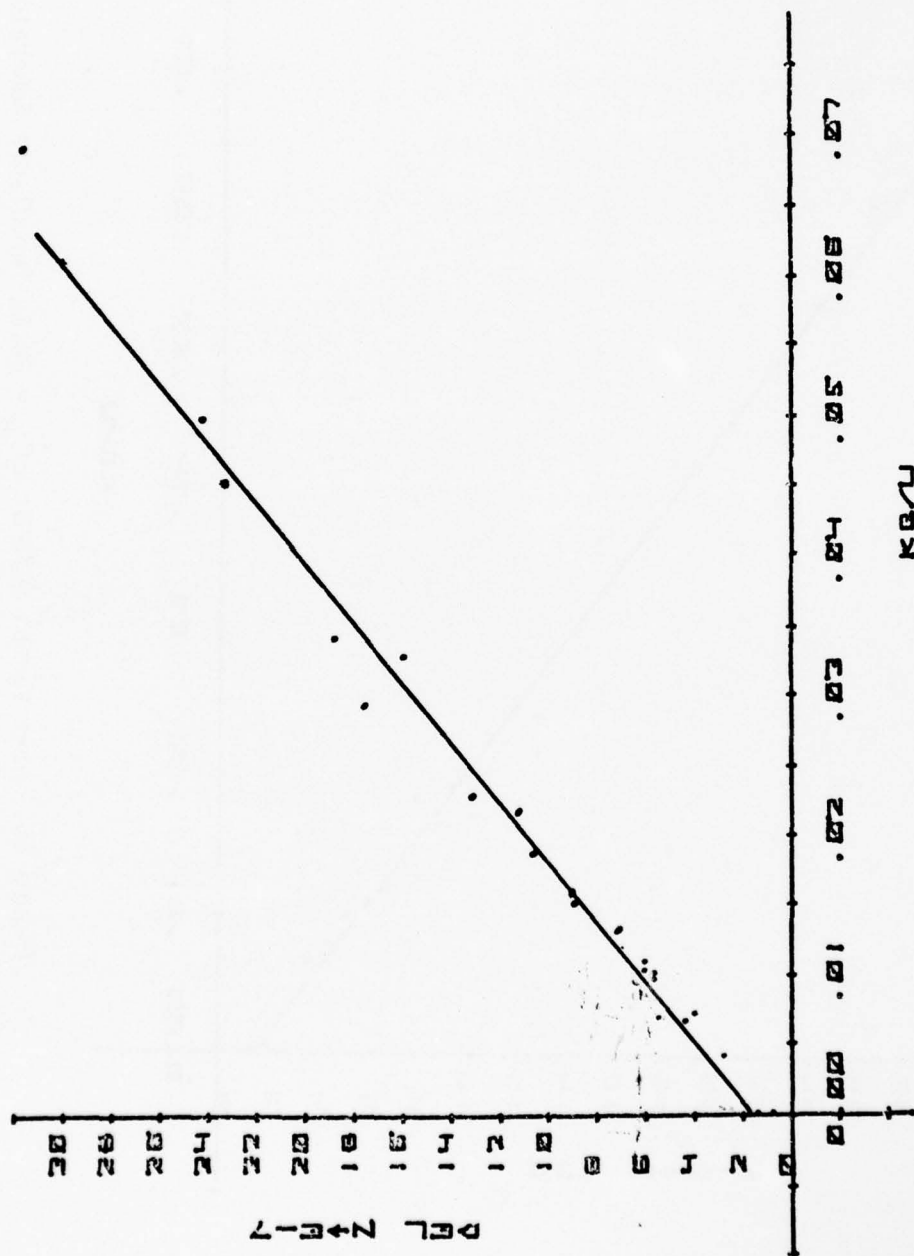


Figure 55. $\langle \Delta \eta \rangle$ versus KQ/U at $L/D_p = 28$, Turbulence Generator B

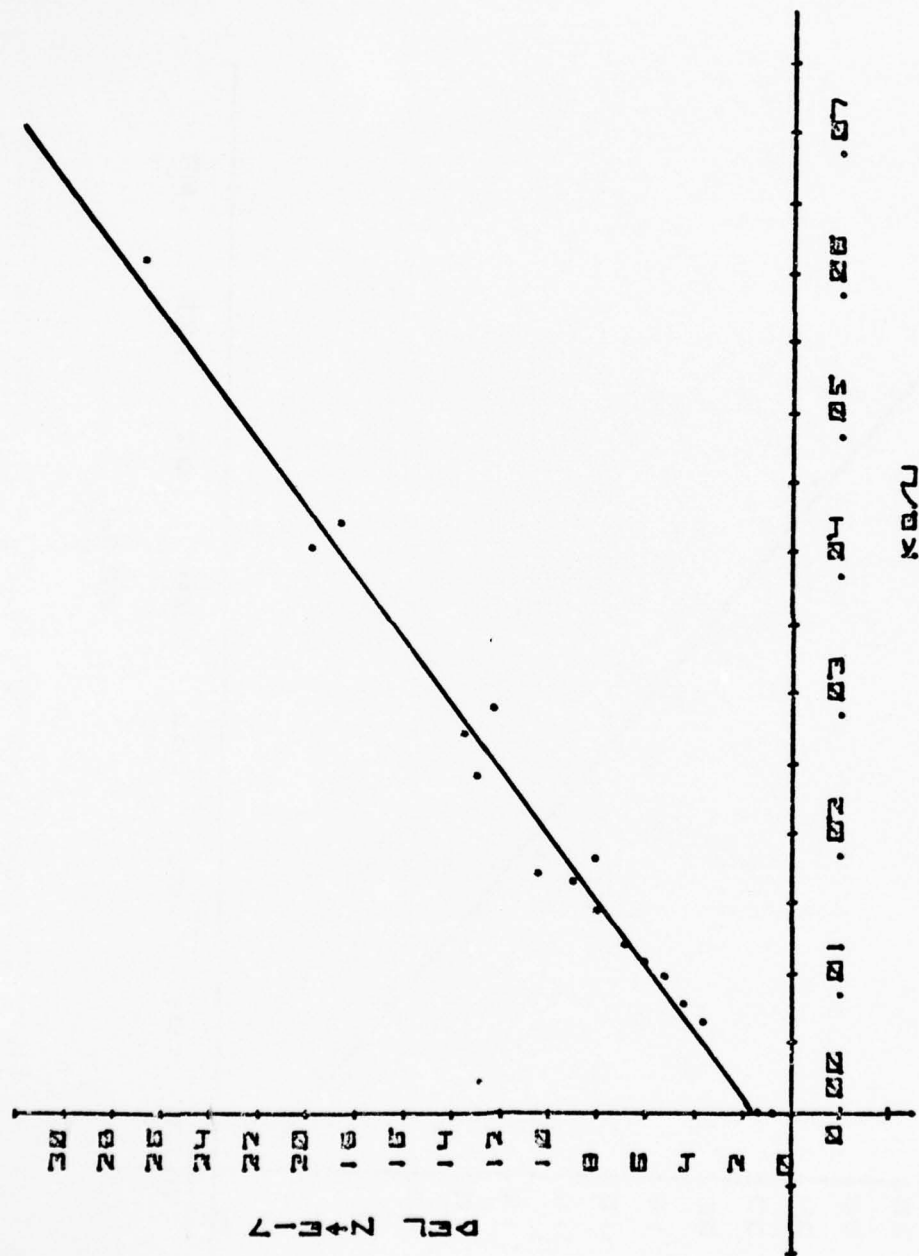


Figure 56. $\langle \Delta \eta \rangle$ versus KQ/U at $L/D_p = 34.5$, Turbulence Generator B

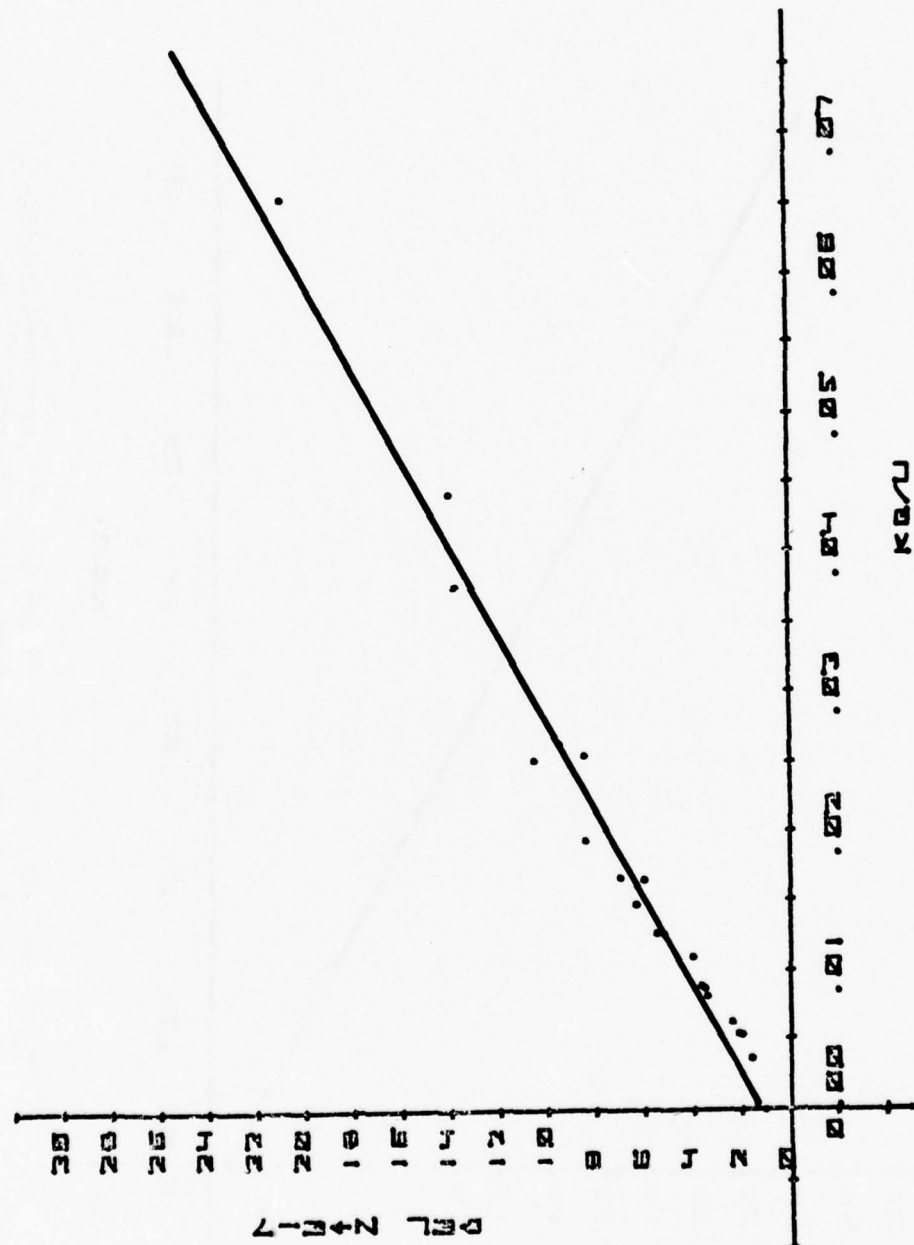


Figure 57. $\langle \Delta n \rangle$ versus KQ/U at $L/D_p = 45$, Turbulence Generator B

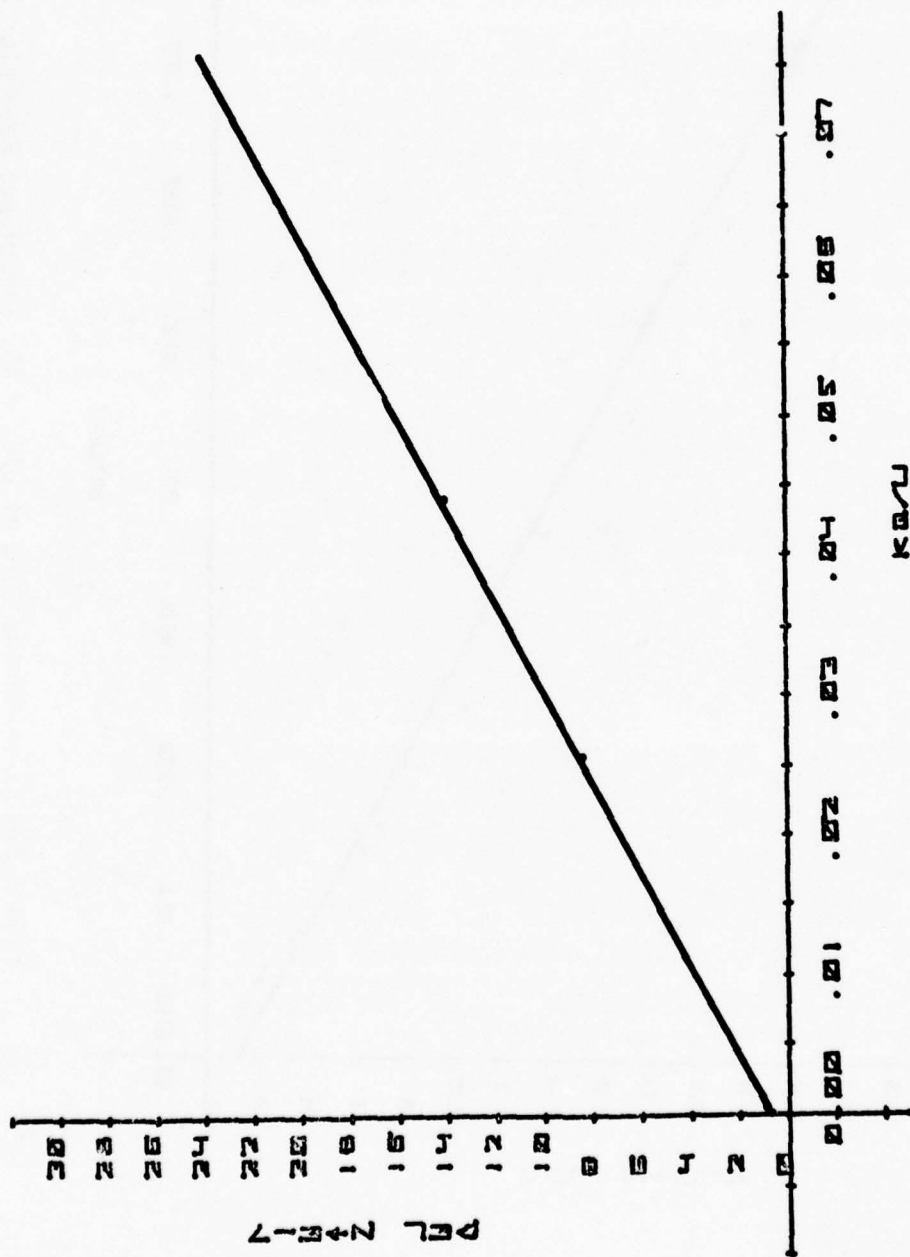


Figure 58. $\langle \Delta n \rangle$ at $L/D_p = 45$ for Low, Medium and High Heat Addition, $U = .99 \text{ m/sec}$ to 1.16 m/sec

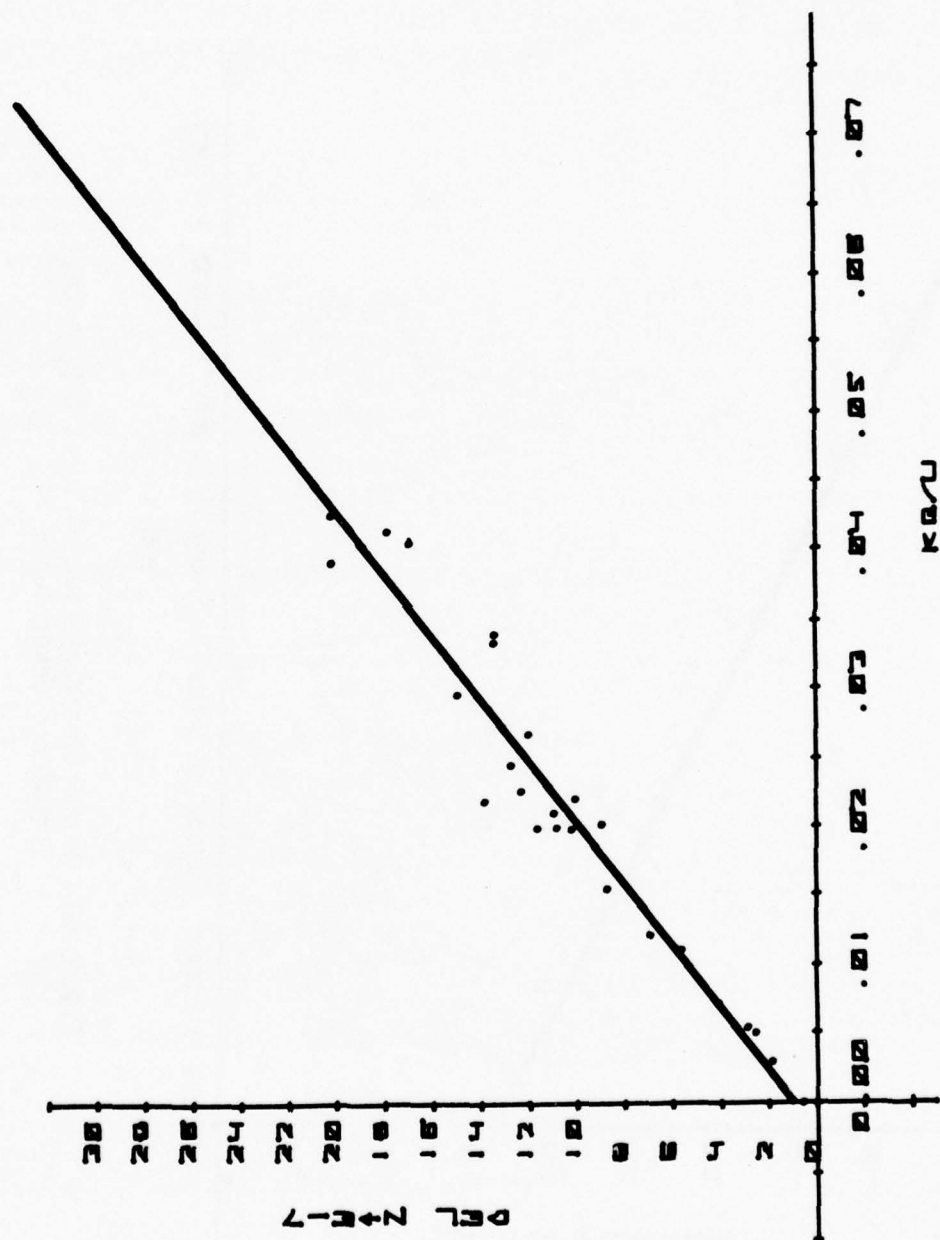


Figure 59. $\langle \Delta \eta \rangle$ versus KQ/U at $L/U_p = 14$, Turbulence Generator A

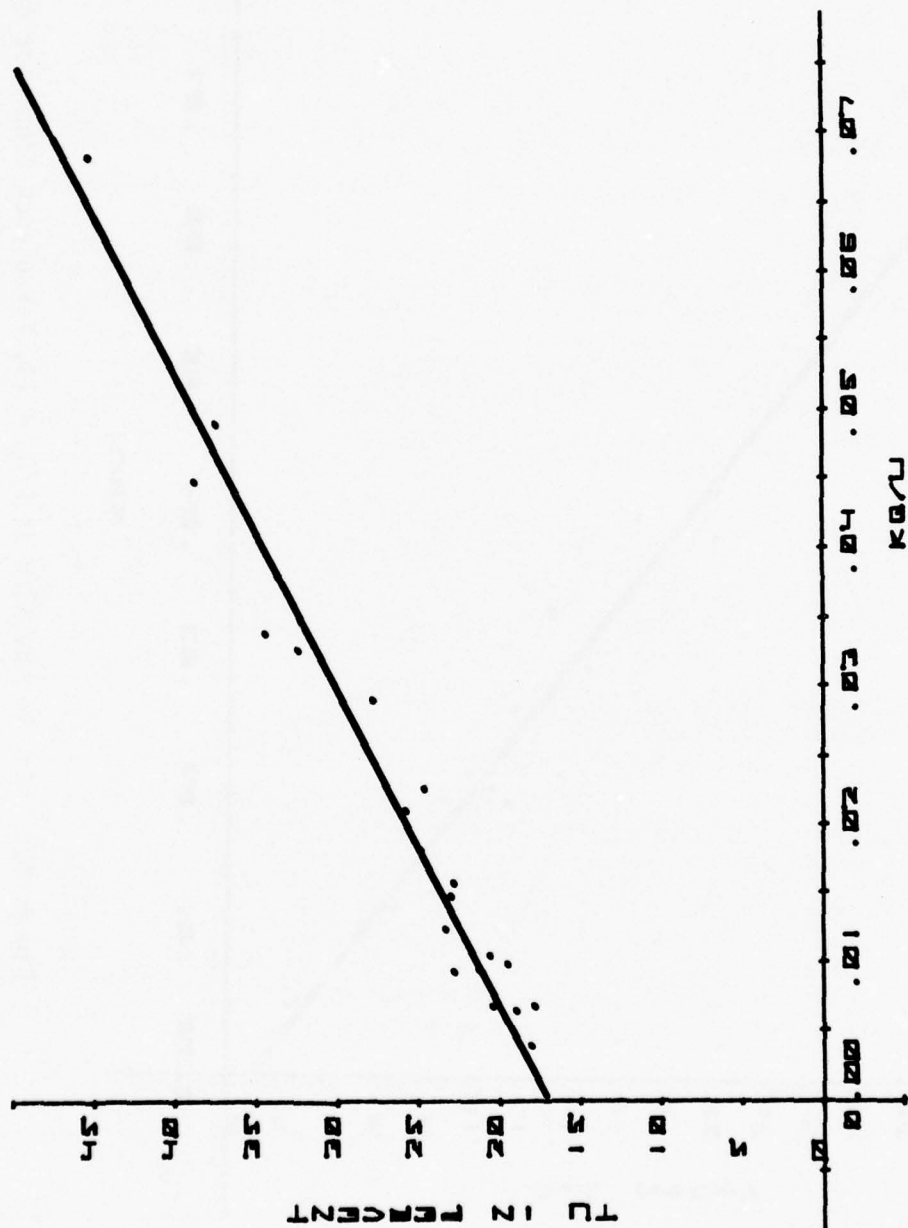


Figure 60. Centerline Variation of Tu at $L/D_p = 28$,
Turbulence Generator B

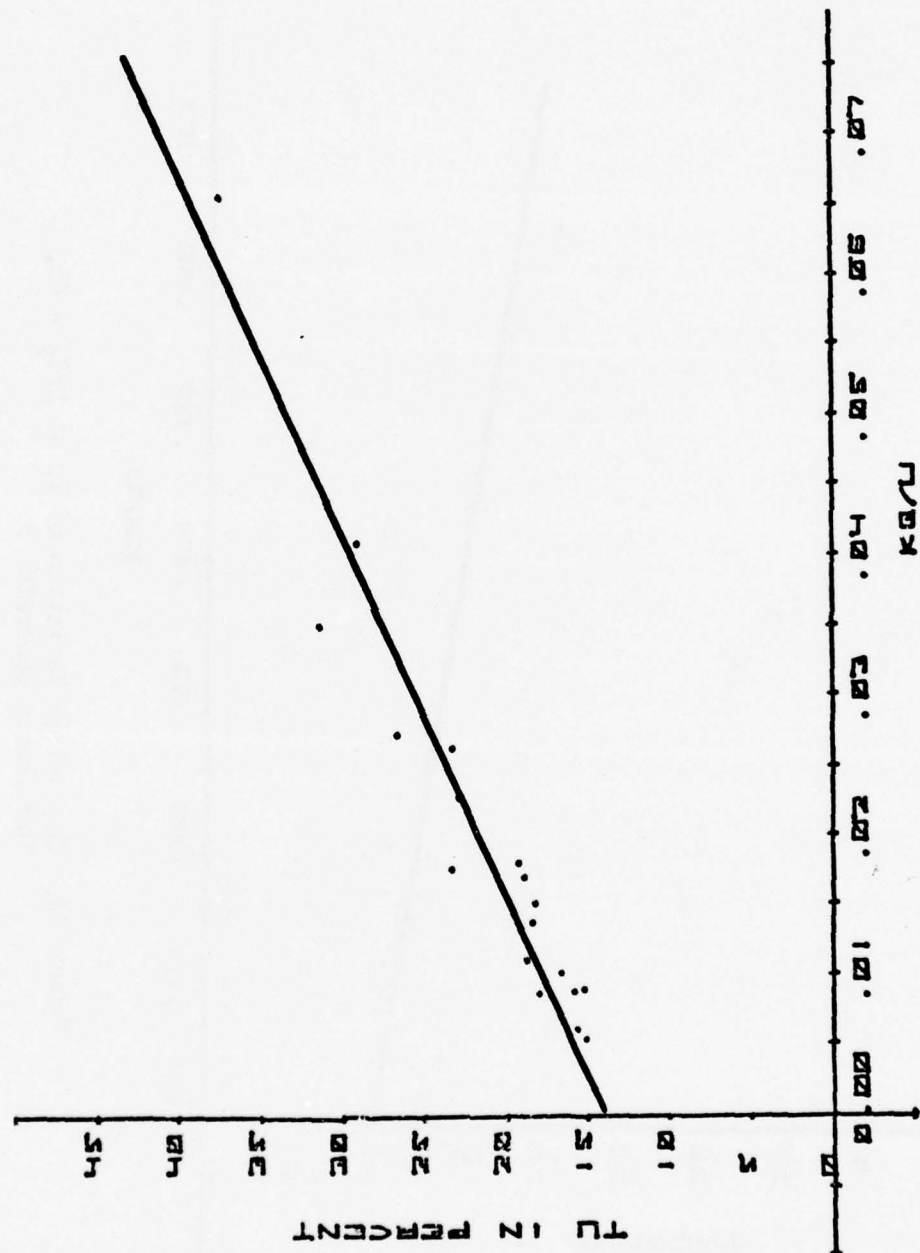


Figure 61. Centerline Variation of Tu at $L/D_p = 34.5$,
Turbulence Generator B

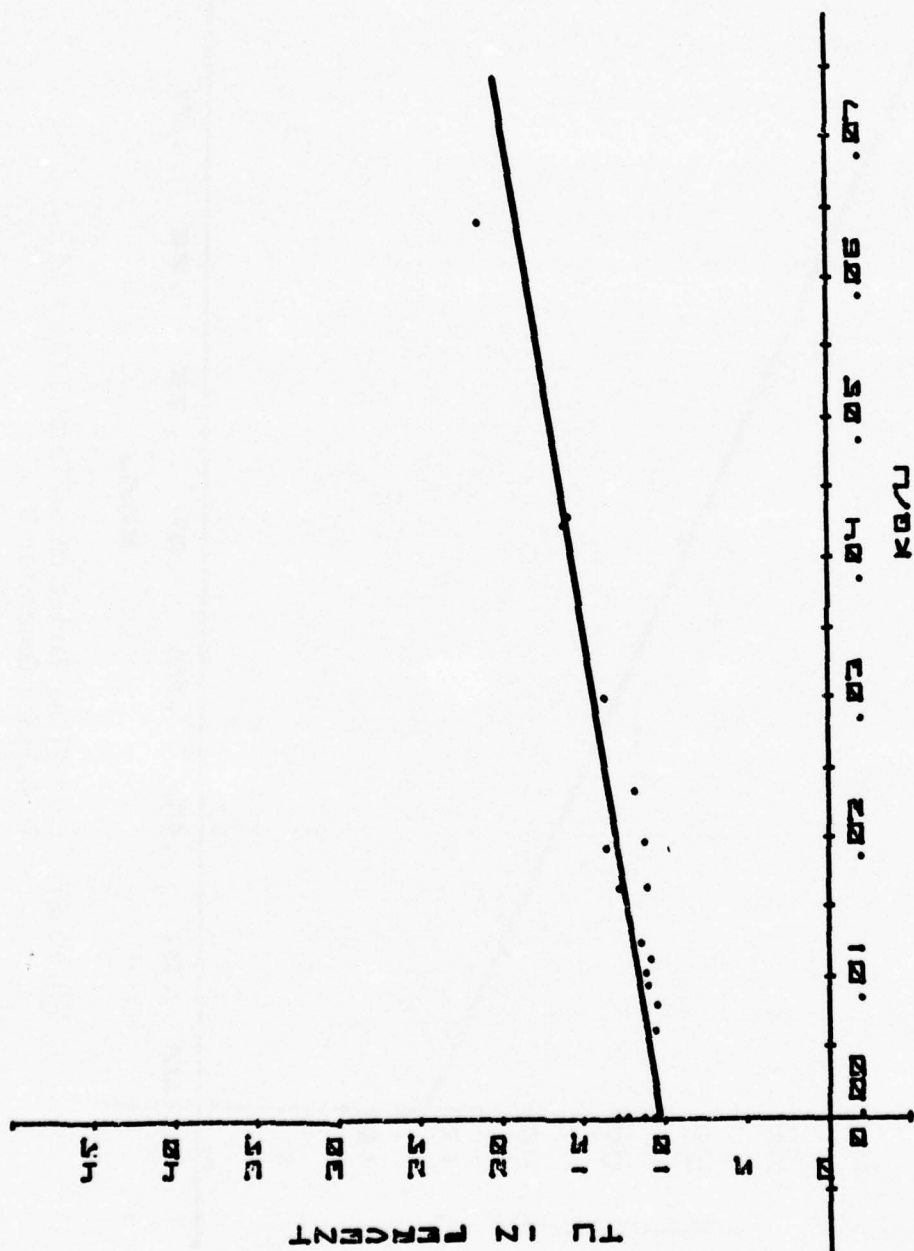


Figure 62. Centerline Variation of Tu at $L/D_p = 45$,
Turbulence Generator B.

non-dimensional heat addition parameter $K Q/U$. The temperature correction terms are very important in determining the value of T_u . The T_u curve for the turbulence generator A is shown in Figure 63 at an L/D_p station of 14. At the L/D_p station of 14, considerable structuring of the flow is observable and as a result comparably more data spread is present in Figure 63.

The scales of turbulence were previously indicated to be extremely difficult to predict. The measured values for the integral scale of temperature are shown in Figures 64, 65 and 66 against $K Q/U$. A general trend may be seen in Figures 64, 65 and 66, although an accurate prediction is not possible. Collapse of the data with any other parameter would not be expected from the observations of this data and also from the previously indicated variations of the scales (Batchelor, 1953, p. 106).

The rather large and unpredictable variation of the integral scale prompted consideration of the microscales' behavior, since the self-preserving character of the correlation function should allow the near zero time behavior to be constant (Townsend, 1956, p. 41). The microscales were obtained by the three methods indicated in Chapter IV. All of the methods discussed are very dependent upon the specific points chosen and the character of the correlation function. In general, the average parabola fit gives the smallest value of microscale, the fourth order polynomial fit, the next smallest value, and the C_N^2 method, the largest value of microscale. The average of several parabola fits was chosen to show the measured microscales' behavior with the non-dimensional heat addition parameter, since in absolute value it shows values nearer

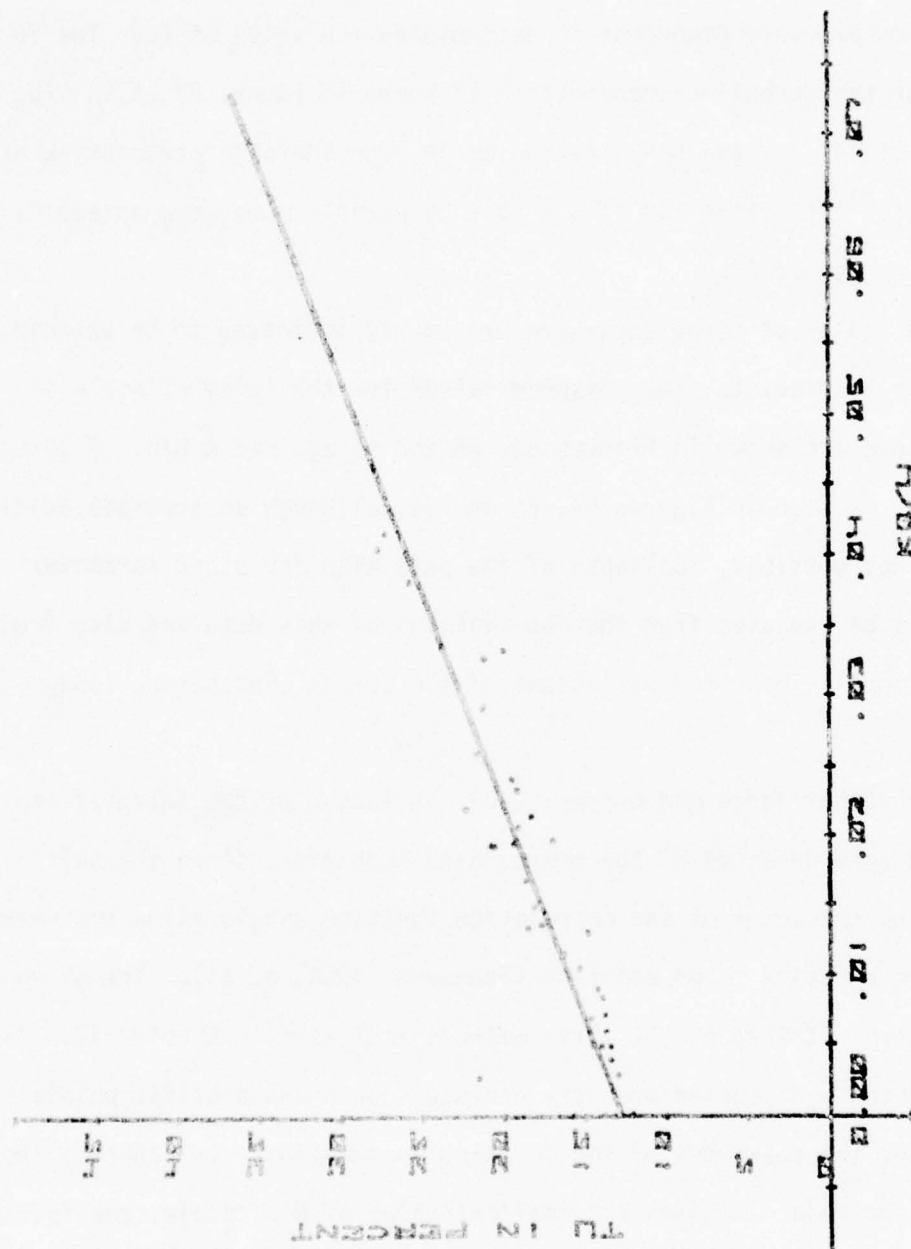


Figure 63. Centerline Variation of Tu at $L/D_p = 14$,
Turbulence Generator A

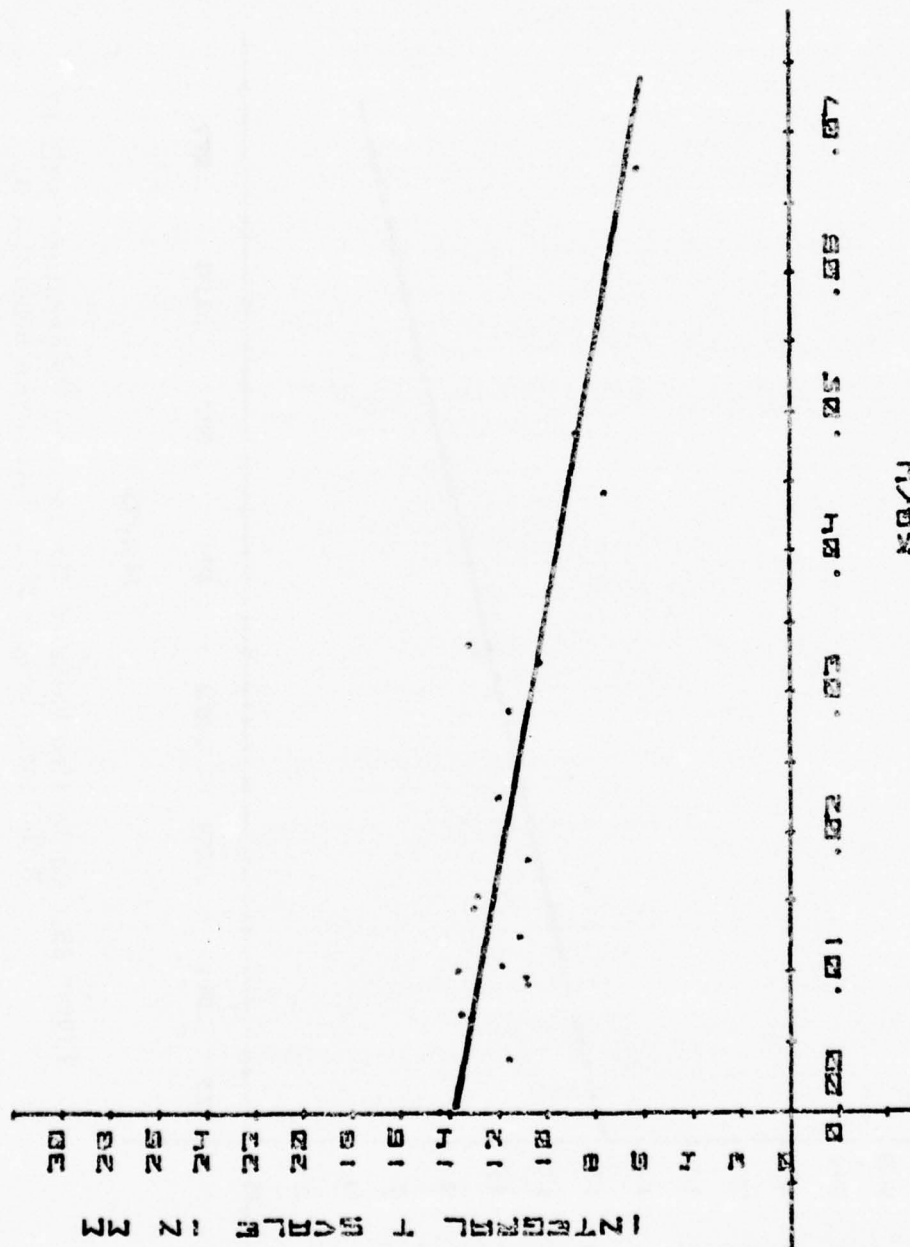


Figure 64. Centerline Value of the Integral Temperature Scale of Turbulence, $L/D_p = 28$, Turbulence Generator B

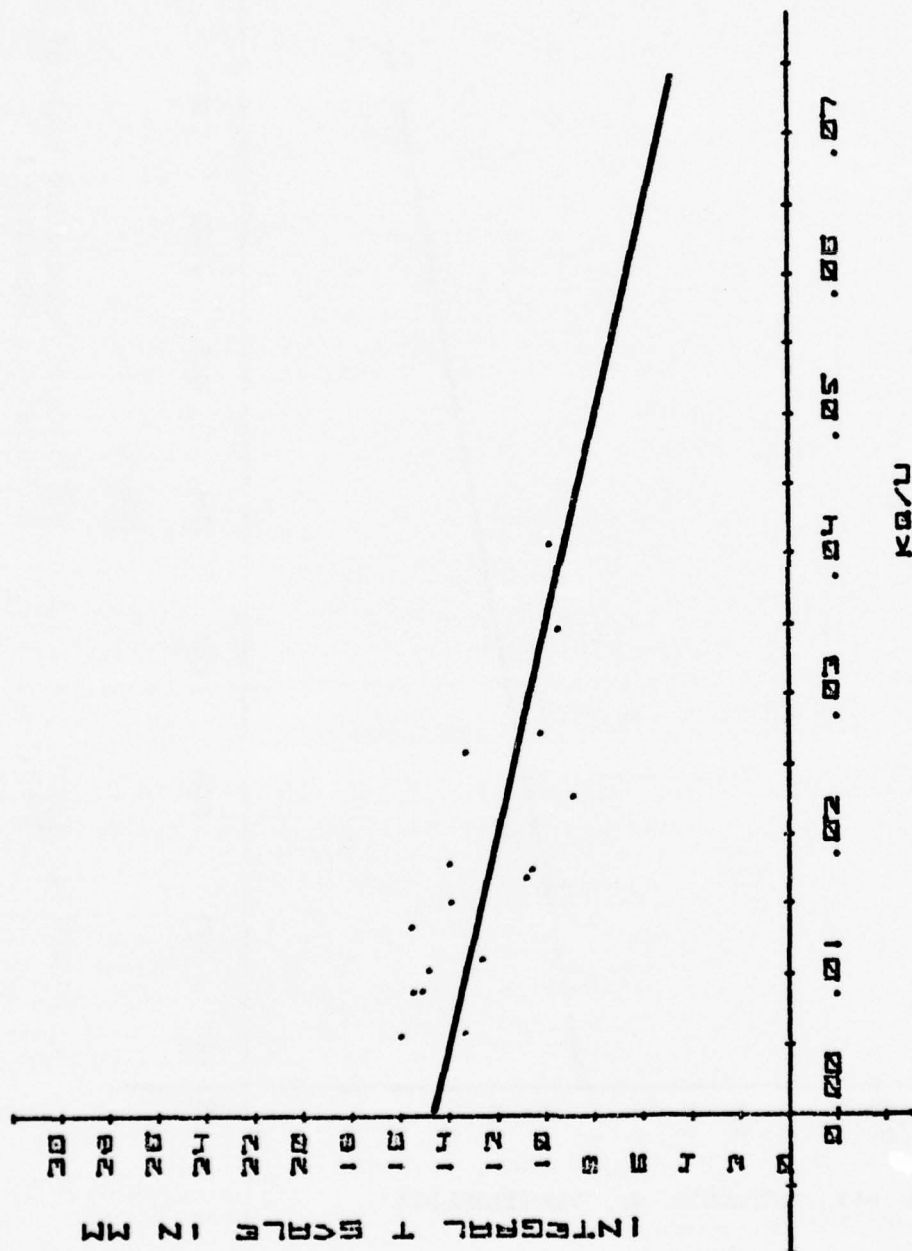


Figure 65. Centerline Value of the Integral Temperature Scale of Turbulence, $L/\delta_p = 34.5$, Turbulence Generator B

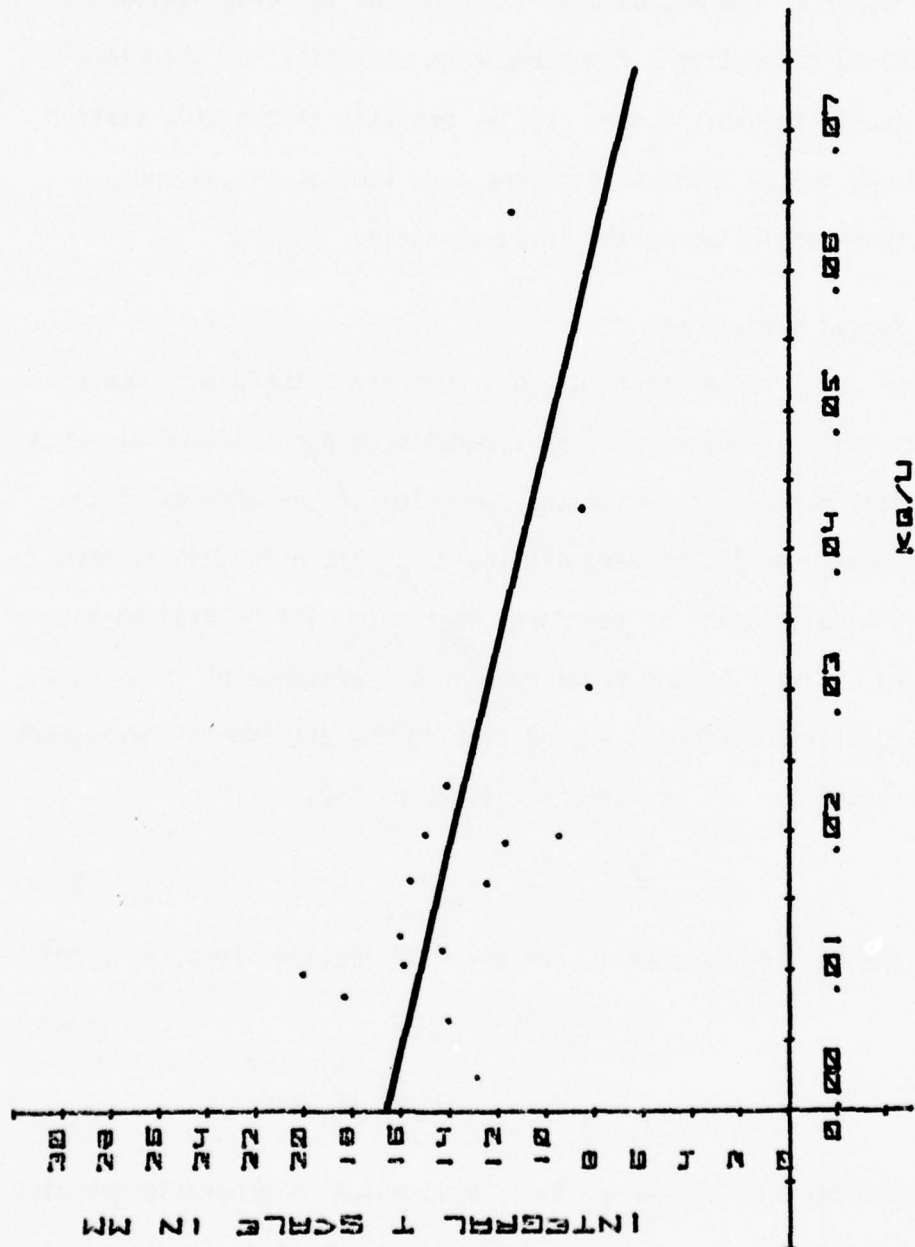


Figure 66. Centerline Value of the Integral Temperature Scale of Turbulence, $L/D_p \approx 45$, Turbulence Generator B

the empirical predictions of equation (85). Figures 67, 68, and 69 show the behavior of the microscale with $K Q/U$ at the L/D_p stations of 28, 34.5, and 45 respectively for turbulence generator B. The microscale does appear to exhibit more regular behavior at the L/D_p station of 28; however, the 34.5 and 45 stations show similar ranges and spreads to those exhibited by the integral scale.

Laser Beam Spread Measurements

From the axial tunnel profiles just presented, the prediction of beam spread with $\langle \Delta \eta \rangle$ may readily be accomplished for the general range of experimental parameters, while the deduction of the effects of the scales of turbulence will be very difficult to obtain in general terms.

Chernov's calculation of the focal spot size will be used to assess the predicted behavior at the focal spot in the presence of turbulence. Chernov calculates the effective spot size in the presence of turbulence to the non-turbulent case as (Chernov, 1960, p. 142):

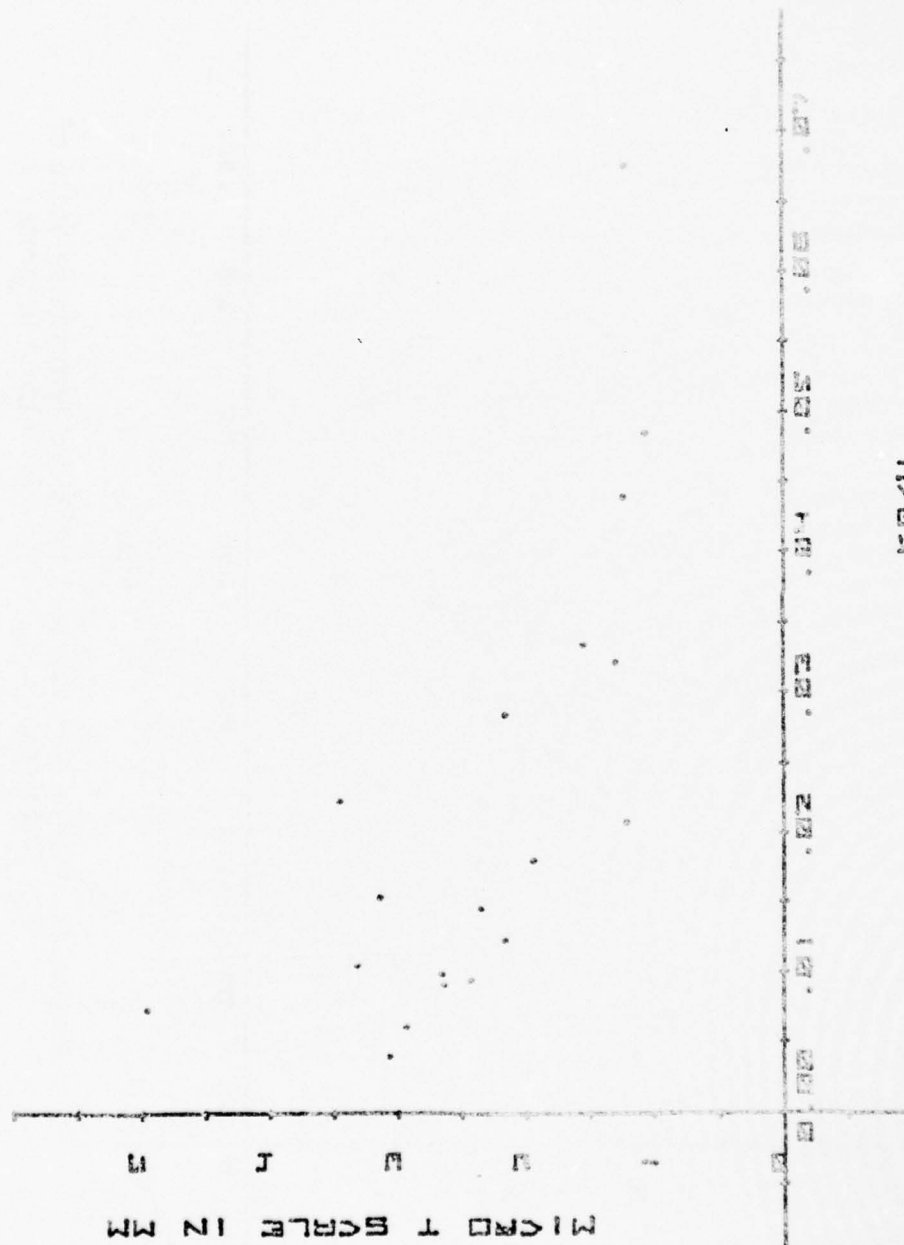
$$\frac{r_{\text{eff}}}{\Delta y} = \frac{\sqrt{\alpha} h_0}{\pi a} \quad (95)$$

where α is the scattering coefficient given by (Sutton, 1969, p. 1740):

$$\alpha \equiv \overline{\text{amplitude}^2} + \overline{\text{phase}^2} \quad (96)$$

$$\alpha = \sqrt{\pi} \langle \Delta \eta \rangle^2 k^2 a L_0 \left(1 + \frac{k^2 a^2 \lambda^2}{D^2} \right)^{-5/6} \quad (97)$$

for a gaussian distribution where $k\alpha$ is $\ll 1$, which is generally the case for this experiment. a is the correlation distance or scale associated with the disturbance - approximately the integral scale. The value of a for a three-dimensional turbulence spectrum is given by (Sutton, 1969,



K/M

Figure 67. Centerline Value of the Micro Temperature Scale of Turbulence, $L/D_p = 28$, Turbulence Generator B

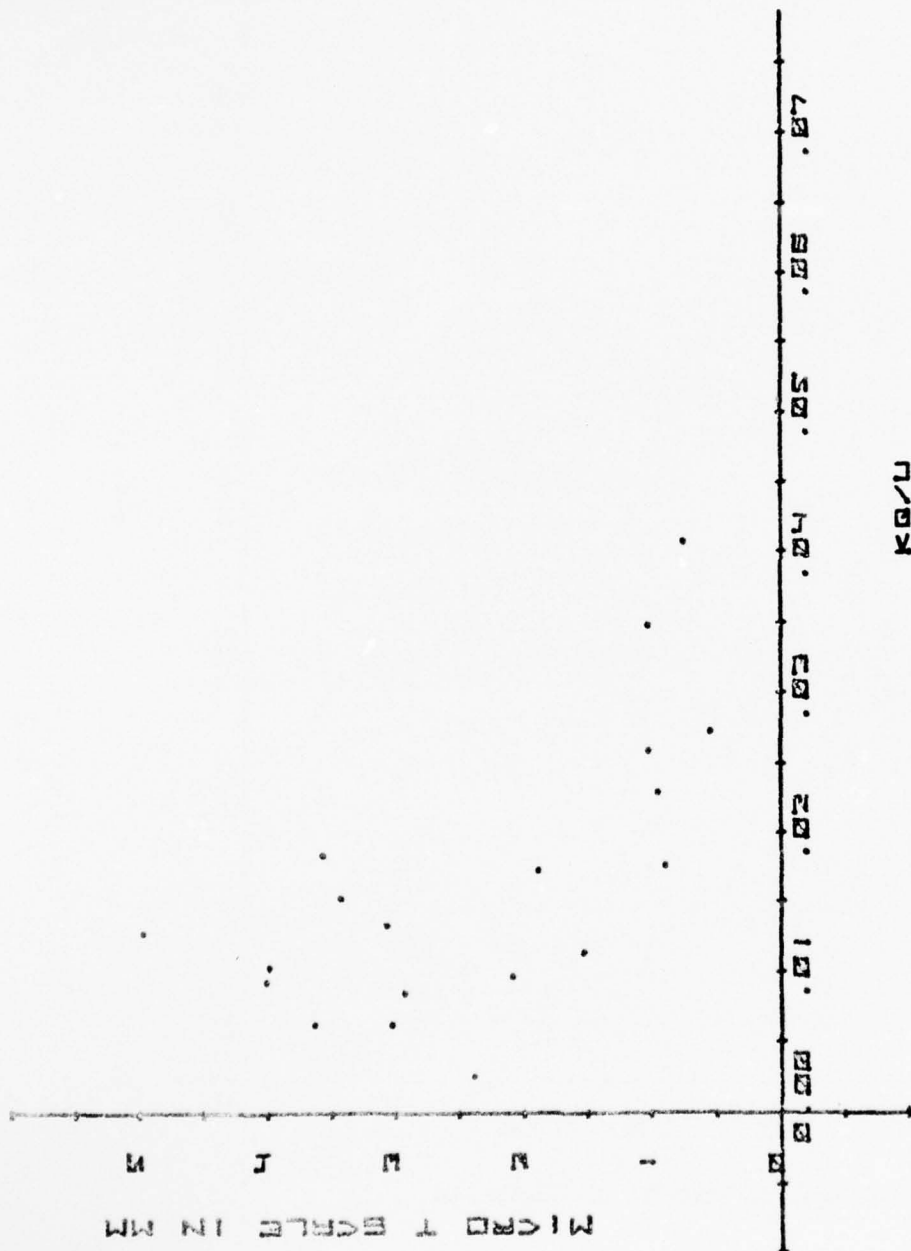


Figure 68. Centerline Value of the Micro Temperature Scale of Turbulence, $L/D_p = 34.5$, Turbulence Generator B

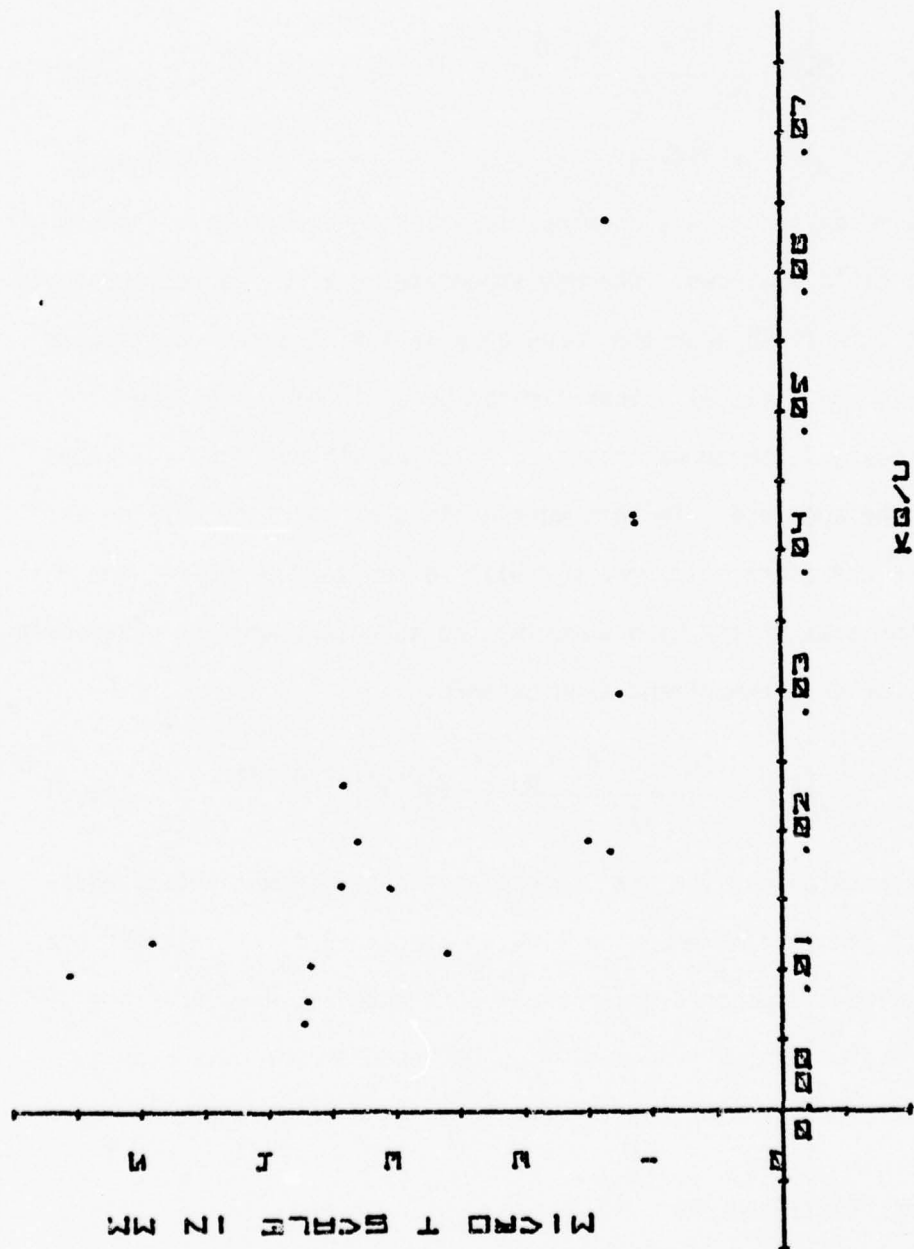


Figure 69. Centerline Value of the Micro Temperature Scale of Turbulence, $L/D_p = 45$, Turbulence Generator B

p. 1740):
$$a \approx \frac{\lambda}{.75} \quad (98)$$

Substitution of α into equation (94) gives:

$$\frac{r_{eff}}{\Delta y} = \frac{2 \sqrt[4]{\pi} \langle \Delta n \rangle h_0 \sqrt{L_0}}{\lambda \sqrt{a}} \left\{ \left(1 + \left(\frac{2\pi a}{D} \right)^2 \right)^{-5/6} \right\}^{1/2} \quad (99)$$

h_0 in Chernov's work was the dimension of the square aperture used to mask the beam leaving a lens on whose surface the amplitude and phase of the leaving field is known. Chernov speculates that it is reasonable to assume that "the field near the focus of a lens will agree in its main features with the field of a lens limited by a circular diaphragm." Chernov's square diaphragm was required to calculate the required integrals over the aperture. In this work a circular aperture will be used and the mask characteristic area h_0^2 will be replaced by $\pi D^2/4$, the mask area, and the area of the beam entering the turbulent medium. Chernov's expression for this experiment then becomes:

$$\frac{r_{eff}}{\Delta y} = \frac{3.54 \langle \Delta n \rangle D \sqrt{L_0}}{\lambda \sqrt{\lambda}} \left\{ \left(1 + \left(\frac{2\pi \lambda}{.75 D} \right)^2 \right)^{-5/6} \right\}^{1/2} \quad (100)$$

Sutton's expression for the beam spread at the half power point, equation (6), is the same as equation (100). Since nearly all mirrors used in laser cavities are circular, and all corresponding apertures are circular, the evaluation of principal $r_{eff}/\Delta y$ dependencies of a beam apertured with a circular stop, at the focus, is also very important.

Distribution of Beam Spread

The emergence of a gaussian beam, as a gaussian beam after propagating through a turbulent medium, is not a well documented assumption

in the literature. Therefore, the distribution of beam spread will be examined experimentally to determine if this assumption is valid and at what point of the distribution the $r_{\text{eff}}/\Delta y$ may be validly applied, if any. Associated with the distribution of intensity, there are two problems which need to be addressed.

The first arises simply in comparing runs from day to day, for geometric changes in beam size, and for comparison of only a portion of the total distribution to a total non-turbulent distribution. To examine and display the errors which are introduced by truncation of the distribution, where the traverse is not carried out to the same intensity, a gaussian distribution was digitized in accordance with the procedures of Chapter IV. The resulting curves are shown in Figure 70. The upper curve is referenced to r (distance from I_0) at values of e^{-x^2} of 3.94×10^{-4} , the second to 3×10^{-3} , the third to 1.83×10^{-2} , the fourth to 7.7×10^{-2} , and the fifth to .61. The experimental range of turbulent to non-turbulent profiles typically ranged from .0183 to .003 in e^{-x^2} . The error introduced by not obtaining the total turbulent distribution should not affect the runs in one set of data since the reference beam remains the same. However, in comparing sets of data, an error of up to approximately 10% in r at the half power point may be introduced when e^{-x^2} at the tail of the distribution is .003 instead of .000394.

Because each set of runs is normalized to the non-turbulent case, valid comparisons are possible between runs and any errors of this kind should only be significant if there has been a zero shift during a run. Normally, the data was discarded if a significant shift in zero or peak power occurred.

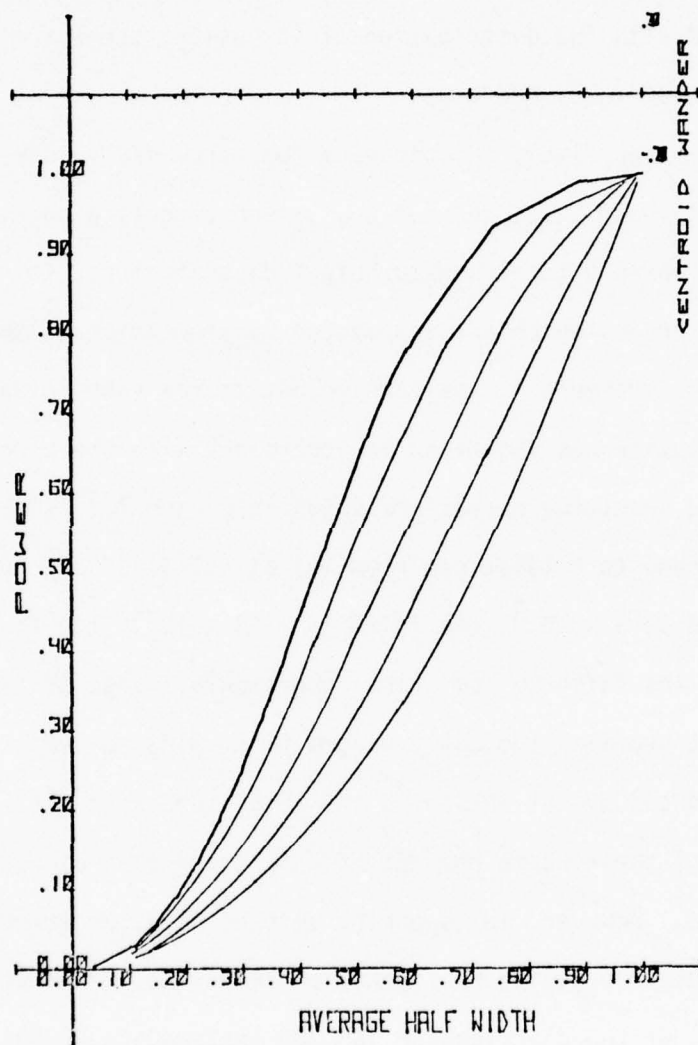


Figure 70. Comparison of Gaussian Profiles Normalized to Differing Radial Values of Integral Power

The second question of the beam intensity distribution is whether the beam maintains a gaussian profile after traversing the turbulent medium, as is assumed in many analyses. A limited comparison of the turbulent profiles to a gaussian profile shows differences on the order of 10%, as shown in Figure 71, in I/I_0 . The upper curve in Figure 71 represents the turbulent profile, the lower the gaussian. Both profiles were integrated to the same I/I_0 value to eliminate the effect shown in Figure 70. Several profiles show the half I/I_0 points and $1/e$ I/I_0 points remain very close to gaussian values. The half I/I_0 points were chosen for beam spread measurements. The measured profile was shown in Chapter IV to be dependent on the aperture which is selected for the traverse of the beam profile. Any conclusion as to the precise variation of the turbulent profile would require an additional investigation.

Several other formulations of the spot size have been published in the literature. Sutton's (Sutton, 1969, p. 1741) expression for the half power point was used in equation (6), to illustrate the quantities required in evaluation of beam spread. The functional dependence of Sutton's equation is identical to Chernov's for the case when $D/\lambda \gg 1$. If Sutton's equation is parametrically plotted, a helium cadmium beam with D/λ ranging from 5.5 to .5 in increments of .05 in D/λ , Figure 72 is obtained. Figure 72 shows that at the half power point of the distribution there is no discernible curvature introduced by the $-5/6$ power term. All subsequent plots at the half power point will, therefore, be shown against $\langle \Delta \eta \rangle$ or $K Q/U$.

The experimental measurements indicated the microscale and the integral scales varied with heat addition; however, there were cases such as

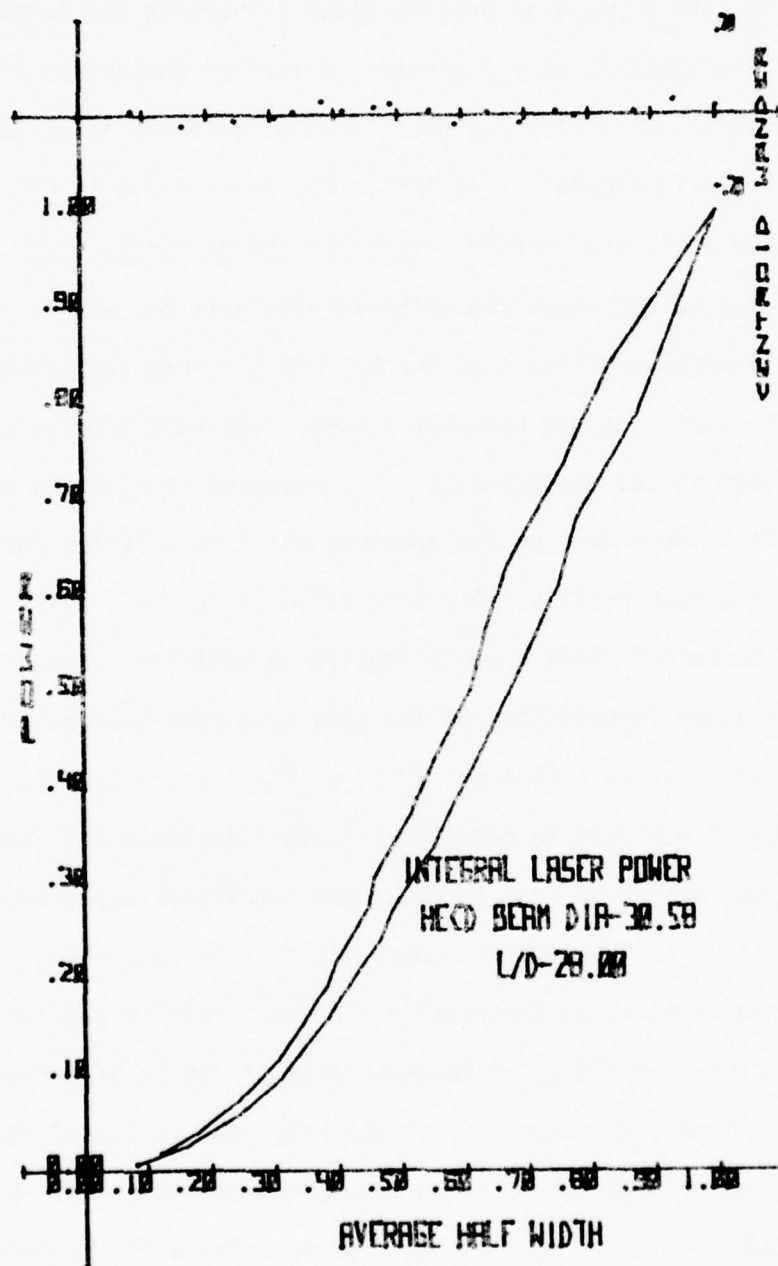


Figure 71. Comparison of a Turbulent Half-Width Power Profile to a Gaussian Half-Width Power Profile.

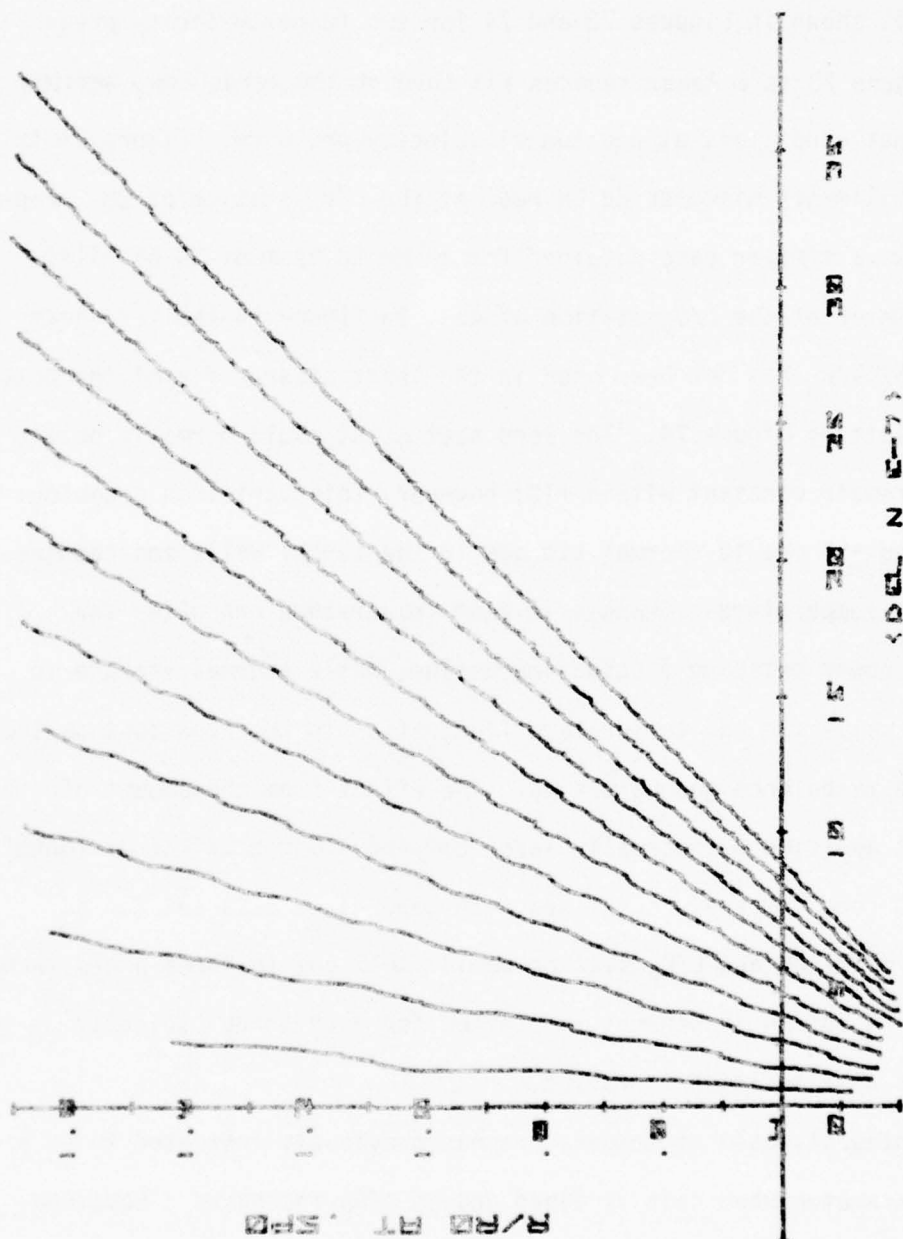


Figure 72. Sutton's 3-D Turbulence Approximation for Beam Spread at the $.5 P_0$ Point of the Distribution

.076 centimeter tunnel velocity pressure under which the integral scale of temperature stayed approximately constant. The half power point variation is shown in Figures 73 and 74 for two tunnel velocity pressures. Figure 73 is a least squares fit through the zero, low, medium, and high heat conditions at one tunnel velocity pressure. Figure 73 is for a 50 millimeter diameter He Cd beam at the L/D_p station of 28. Figure 74 shows a similar case obtained for an He Cd beam of 30.58 millimeters diameter at the L/D_p station of 45. In Figure 74 the zero heat point at $.52 R/R_0$ has not been used in the least squares fit of the data shown in plotting Figure 74. The zero heat point could normally be expected to remain constant within $\pm 1\%$; however, this variation occasionally reached $\pm 5\%$ due to thermal storage in the tunnel walls and changes in the room temperature. Changes in room temperature can alter the laser beam power entering fluctuating medium, while thermal storage in the tunnel walls can add temperature fluctuation to the flow just as the temperature turbulence generators do. The effect from the amount of tunnel heat addition was normally large compared to the effect of tunnel storage and room temperature changes. In general, a data set for a given beam diameter and L/D_p station would yield one to three plots such as Figures 73 and 74 if separately plotted for each tunnel velocity pressure as heat addition is varied.

The integral scale of temperature was previously indicated to be a variable parameter when heat is added and as L/D_p increases. Equation (100) shows the functional dependence of beam spread is a $(\sqrt{\Lambda})$ dependence. The plots of all tunnel velocity pressure operating points may be expected to exhibit some data spread due to changes in Λ .

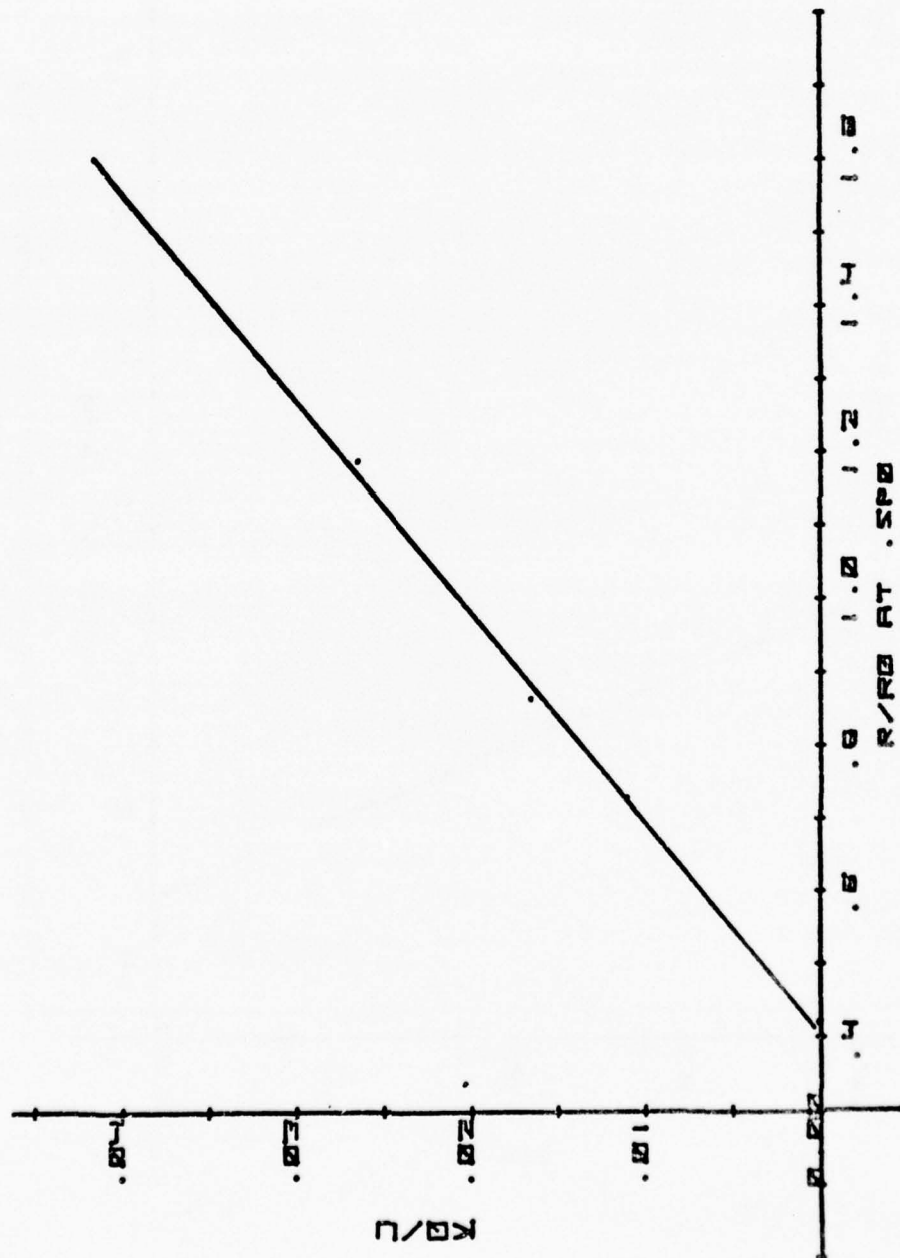


Figure 73. Half Power Point Variation of Focal Spot Size,
He Cd, $L/D_p = 28$, $D = 50$ mm

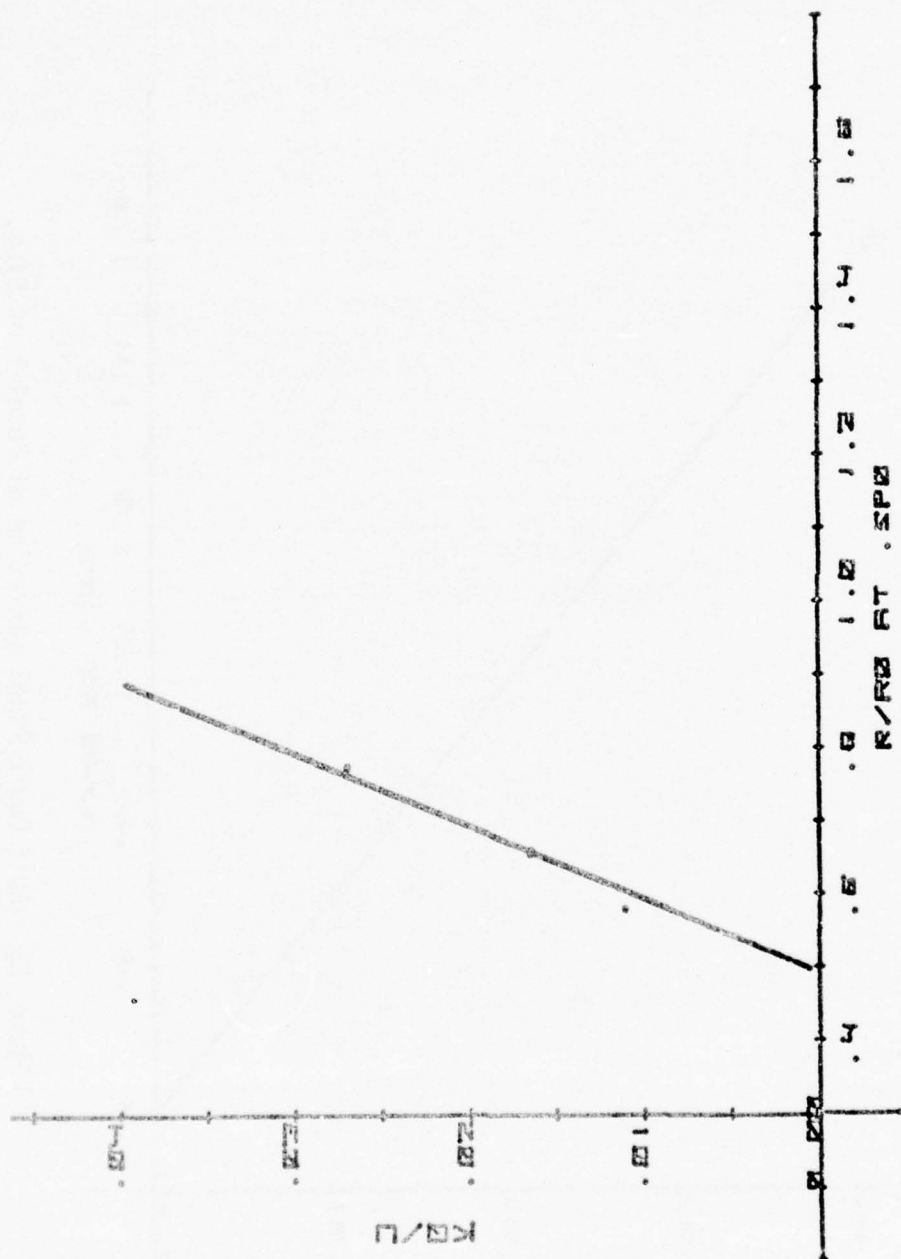


Figure 74. Half Power Point Variation of Focal Spot Size,
He Cd, $L/D_p = 45$, $D = 30.58$ mm

The least squares fitted curves obtained for beam spread or the R/R_0 ratio at the .5 power points of the turbulent and non-turbulent laser profiles obtained from the calculation of Chapter IV are presented in Figures 75 through 89. At the .5 P_0 point from equation (6)

$$\frac{d(\frac{r_{eff}}{\Delta y})}{d \langle \Delta \eta \rangle} = \frac{3.54 D \sqrt{L_0}}{\lambda \sqrt{\Lambda}} \left\{ \left(1 + \left(\frac{2\pi\Lambda}{.75D} \right)^2 \right)^{-5/6} \right\}^{1/2} \quad (101)$$

Differentiation of the two linear relations

$$d\left(\frac{KQ}{U}\right) = d(H + J R/R_0) \quad (102)$$

and

$$d(\Delta \eta \times 10^{-7}) = d(F + G \left(\frac{KQ}{U}\right)) \quad (103)$$

gives upon substitution of equation (102) into equation (103)

$$\frac{d(R/R_0)}{d \langle \Delta \eta \rangle} = \frac{1}{GJ} \quad (104)$$

which also may be equated to equation (101) giving:

$$\left[\left\{ 1 + \left(\frac{2\pi\Lambda}{.75D} \right)^2 \right\}^{-5/6} \right]^{1/2} \frac{D \sqrt{L_0}}{\lambda \sqrt{\Lambda}} = \frac{1}{3.54GJ} \quad (105)$$

Equation (105) may be used with the mean profile data at the L/D_p station of 28 for the He Cd and He Ne data to compare the wave length dependence of equation (105).

Taking the ratio of equation (105) for He Cd to He Ne:

$$\frac{\left[\left\{ 1 + \left(\frac{2\pi\Lambda}{.75D} \right)^2 \right\}^{-5/6} \right]^{1/2} \left(\frac{D \sqrt{L_0}}{\lambda \sqrt{\Lambda}} \right)_{\text{He Cd}}}{\left[\left\{ 1 + \left(\frac{2\pi\Lambda}{.75D} \right)^2 \right\}^{-5/6} \right]^{1/2} \left(\frac{D \sqrt{L_0}}{\lambda \sqrt{\Lambda}} \right)_{\text{He Ne}}} = \frac{(GJ)_{\text{He Ne}}}{(GJ)_{\text{He Cd}}} \quad (106)$$

or since Λ/D is approximately the same for the He Ne and He Cd beams:

$$\frac{(\lambda) \text{ He Ne}}{(\lambda) \text{ He Cd}} = \frac{(J) \text{ He Ne}}{(J) \text{ He Cd}} \quad (107)$$

The values experimentally obtained are given in Table 3.

Table 3. λ Dependence on Beam Spread

| Diameter of Beam-Laser | Experimental Value of $\lambda_{\text{He Ne}}/\lambda_{\text{He Cd}}$ | Calculated Value of $\lambda_{\text{He Ne}}/\lambda_{\text{He Cd}}$ |
|-----------------------------|---|---|
| 50mm-He Ne 50mm-He Cd | 1.375 | 1.433 |
| 26mm-He Ne 30.58mm-He Cd | 1.660 | 1.685 |
| 8mm-He Ne 14.03-He Cd | 2.660 | 2.513 |

Next, if the ratio of equation (105) is taken for the beam diameter at each station, the apparent Λ scale and λ are constant, as is the value of the slope of the $\langle \Delta \eta \rangle$ versus $K Q/U$ curve, G . The ratio of J 's or the slopes of the R/R_0 curves at $.5 P_0$ at the same wave length then gives the beam diameter ratio dependence. Taking the ratio of equation (104) to the same equation for the 50 millimeter diameter beam gives:

$$\frac{\{1 + (\frac{2\pi\Lambda}{750})^2\}^{-5/6} \}^{1/2}}{\{1 + (\frac{2\pi\Lambda}{750 \cdot 50})^2\}^{-5/6} \}^{1/2}} \frac{D}{D_{50}} = \frac{J_{50}}{J_D} \quad (108)$$

Neglect of Λ/D terms results in the experimental and actual values which are presented in Table 4. The *value was computed for a set of $\langle \Delta \eta \rangle$ vs. $K Q/U$ data which had a very linear experimental range and the corresponding R/R_0 data also had a corresponding linear range as is shown in Figures 90 and 91.

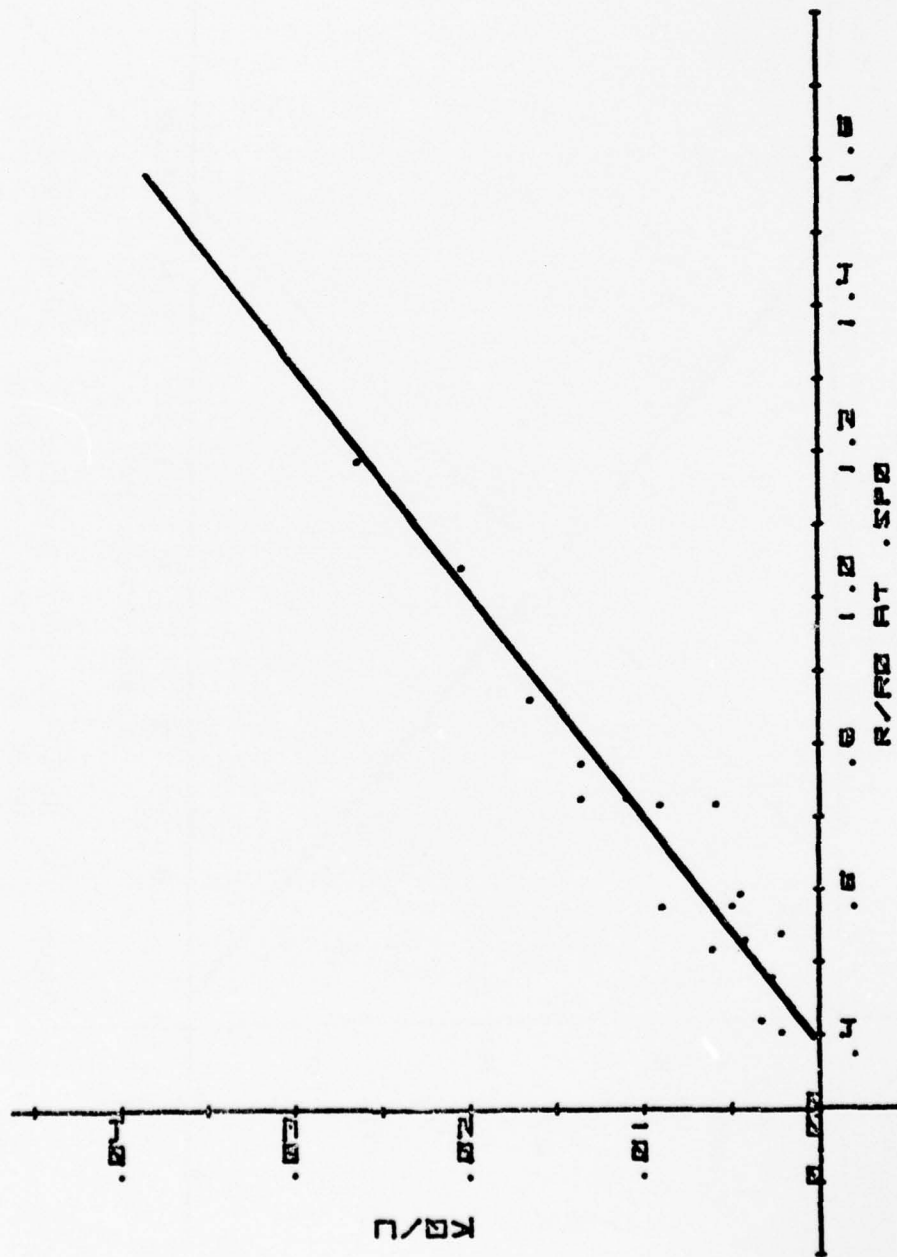


Figure 75. Half Power Point Variation of Focal Spot Size,
He Cd, $L/D_p = 28$, $D = 50$ mm

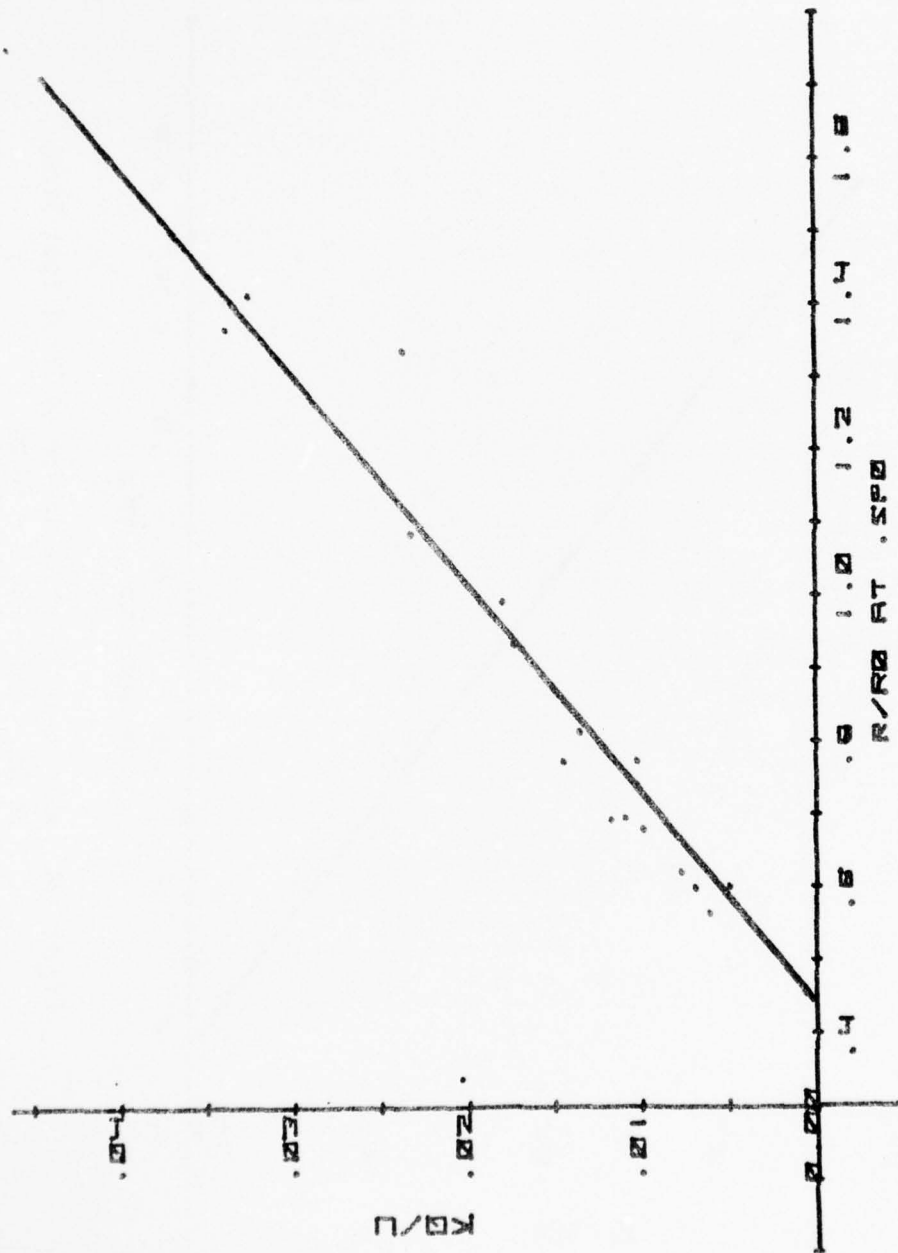


Figure 76. Half Power Point Variation of Focal Spot Size,
He Cd, $L/D_p = 28$, $D = 30.58$ mm

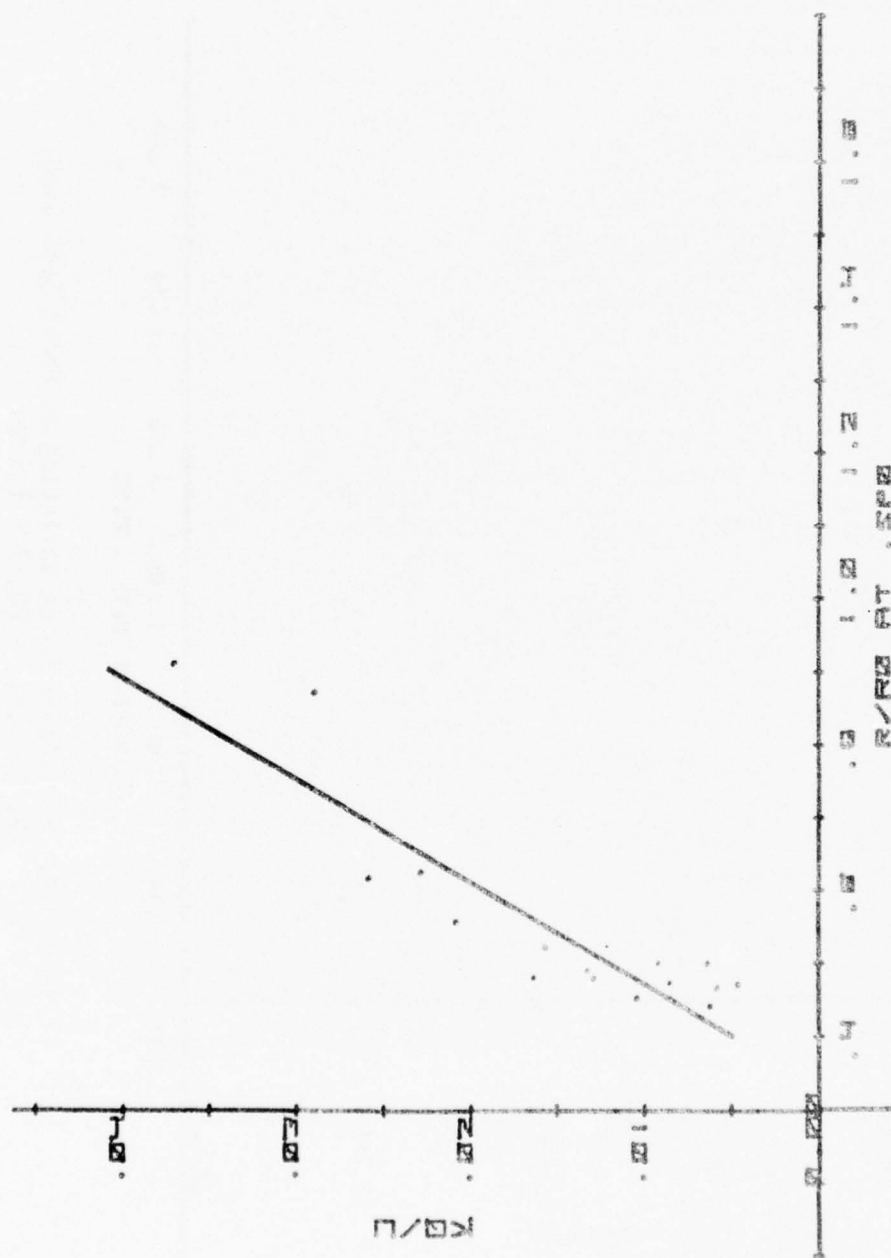


Figure 77. Half Power Point Variation of Focal Spot Size,
He Cd, $L/D_p = 28$, $D = 14.03$ mm

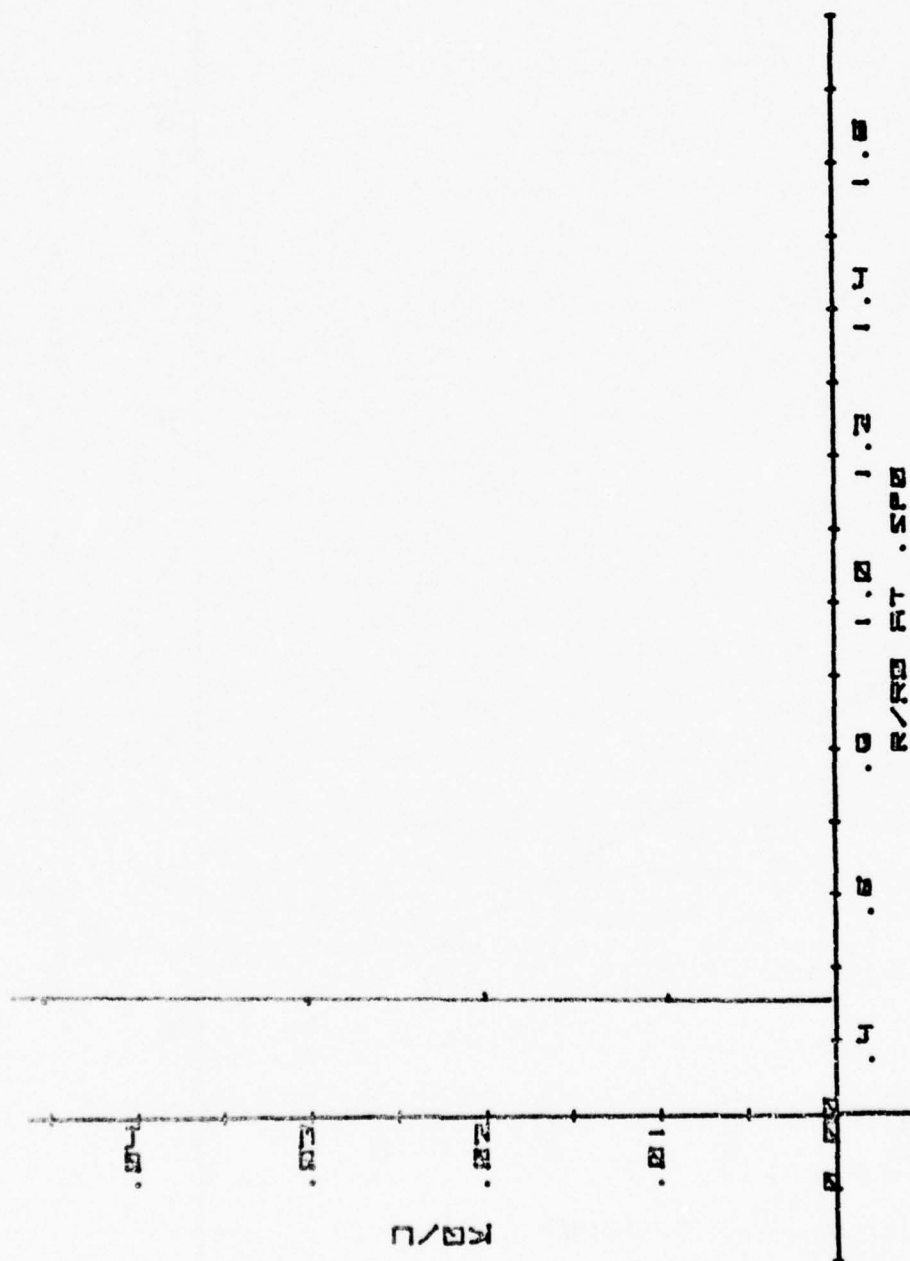


Figure 78. Half Power Point Variation of Focal Spot Size,
He Cd, $L/D_p = 28$, $D = 1.5$ mm

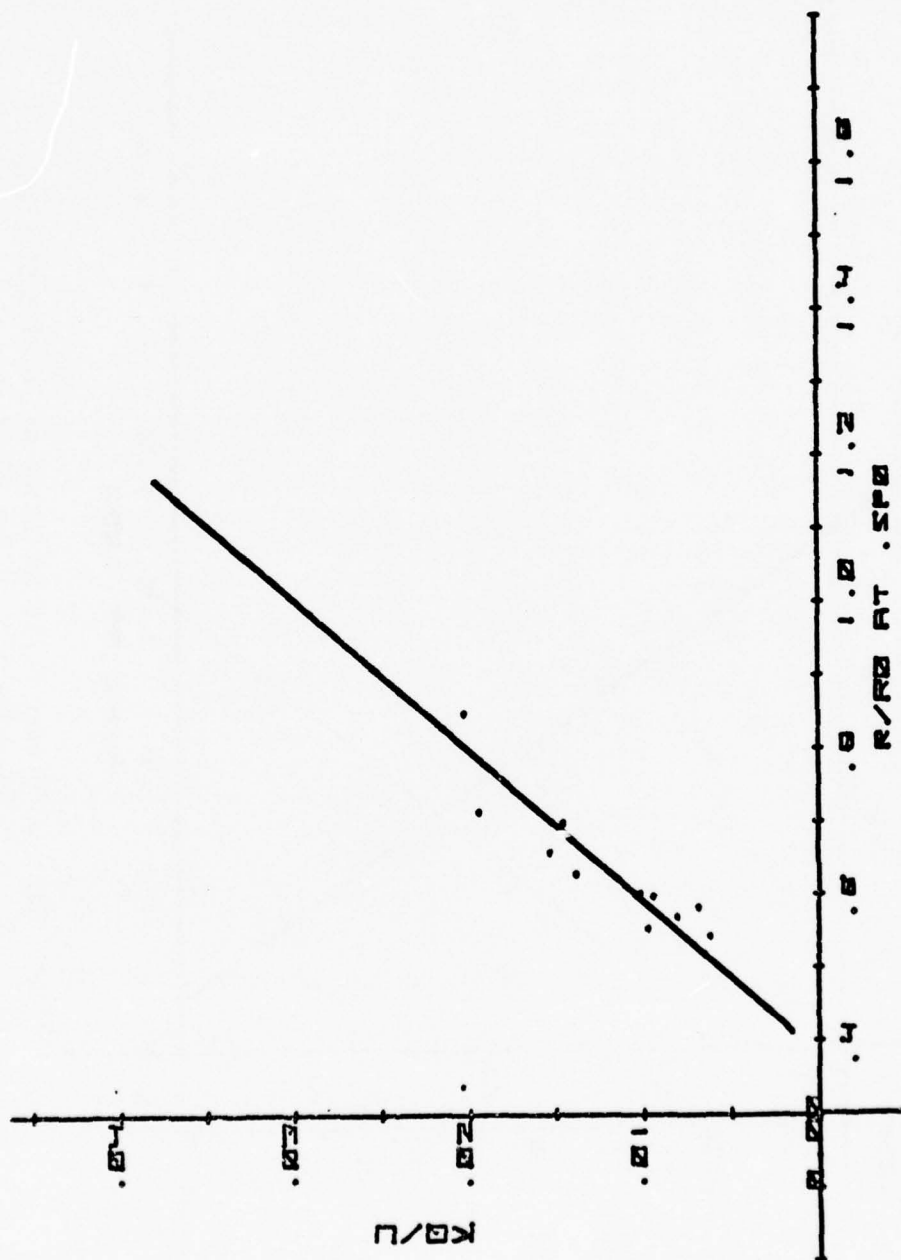


Figure 79. Half Power Point Variation of Focal Spot Size,
He Cd, $L/D_p = 34.5$, $D = 50$ mm

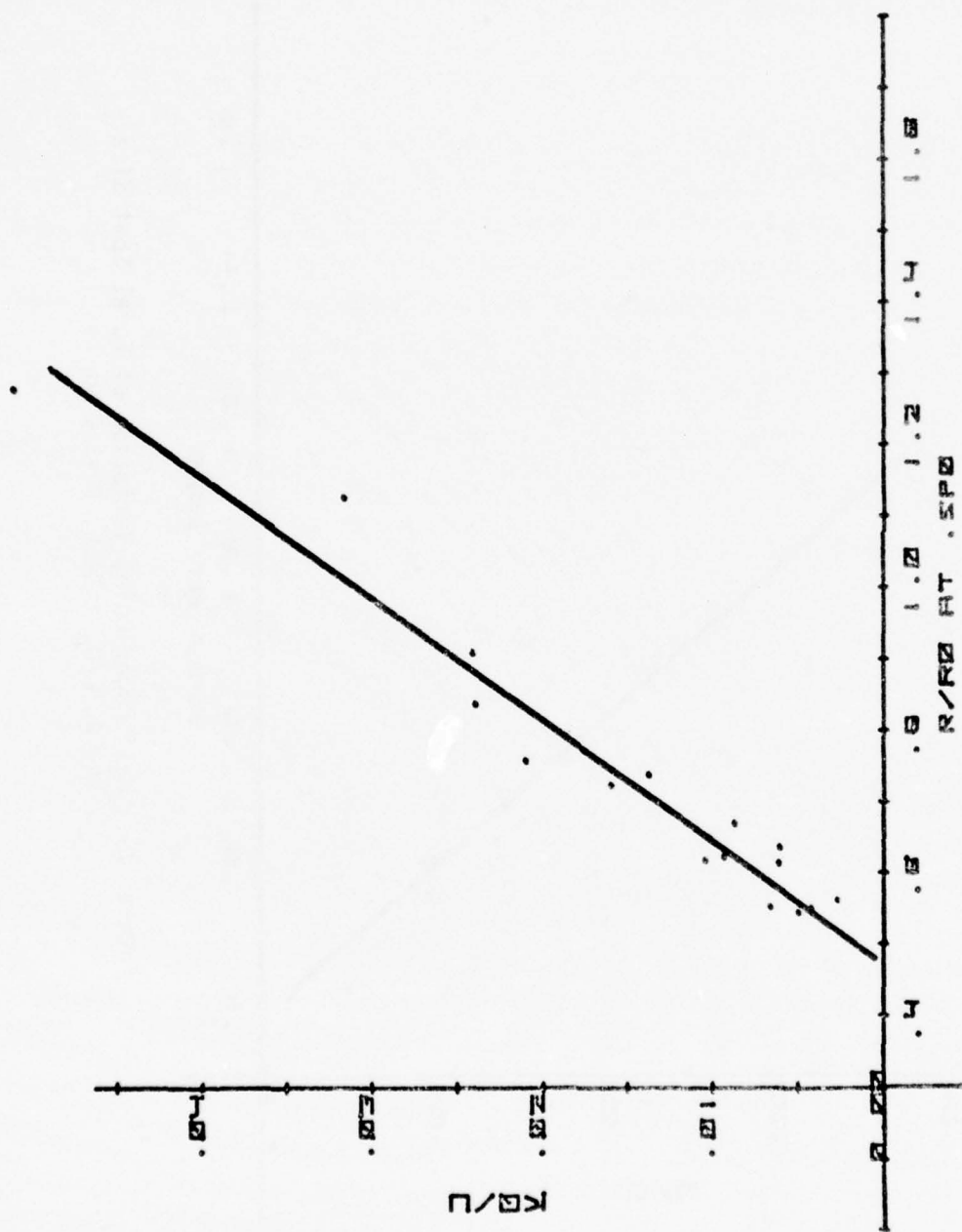


Figure 80. Half Power Point Variation of Focal Spot Size,
He Cd, $L/D_p = 34.5$, $D = 30.58$ mm

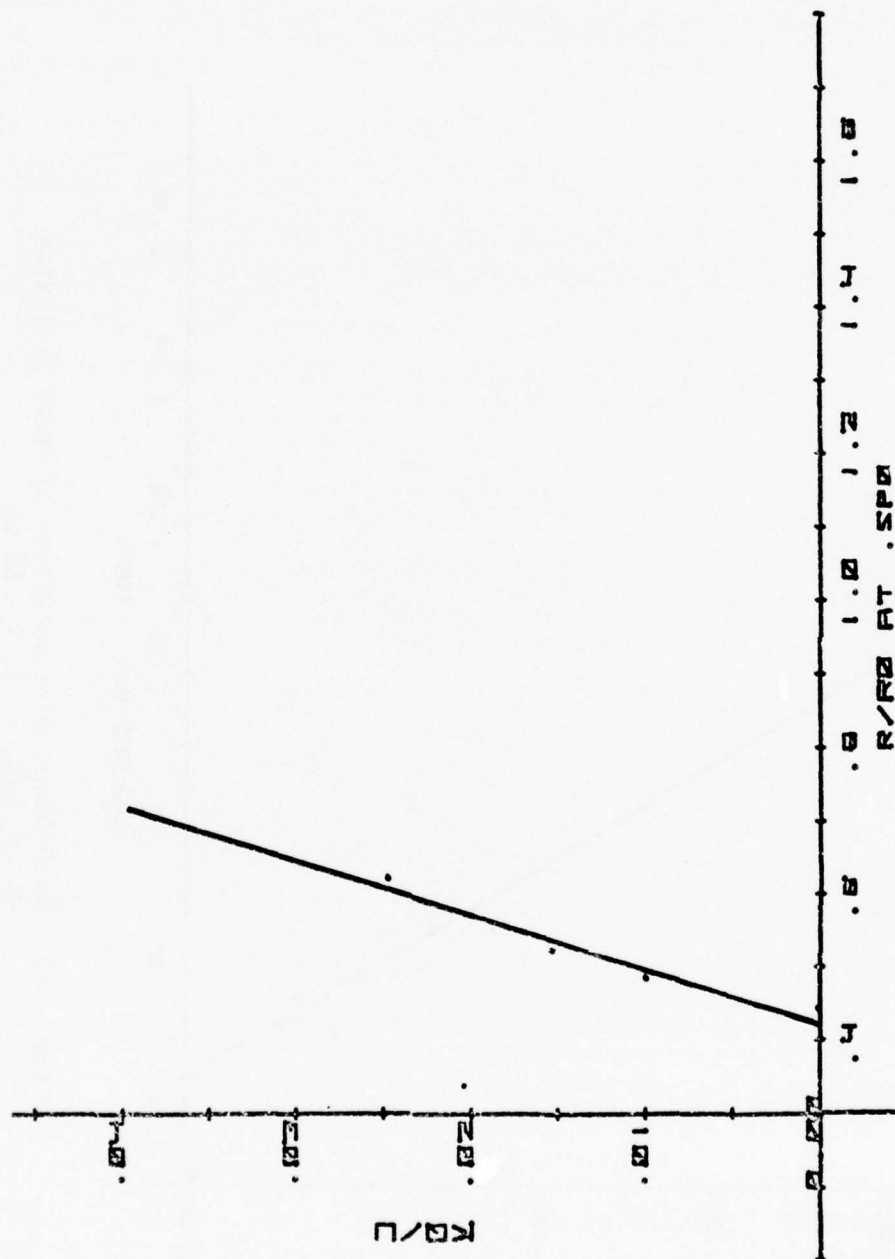


Figure 81. Half Power Point Variation of Focal Spot Size,
He Cd, $L/D_0 = 34.5$, $D = 14.03$ mm

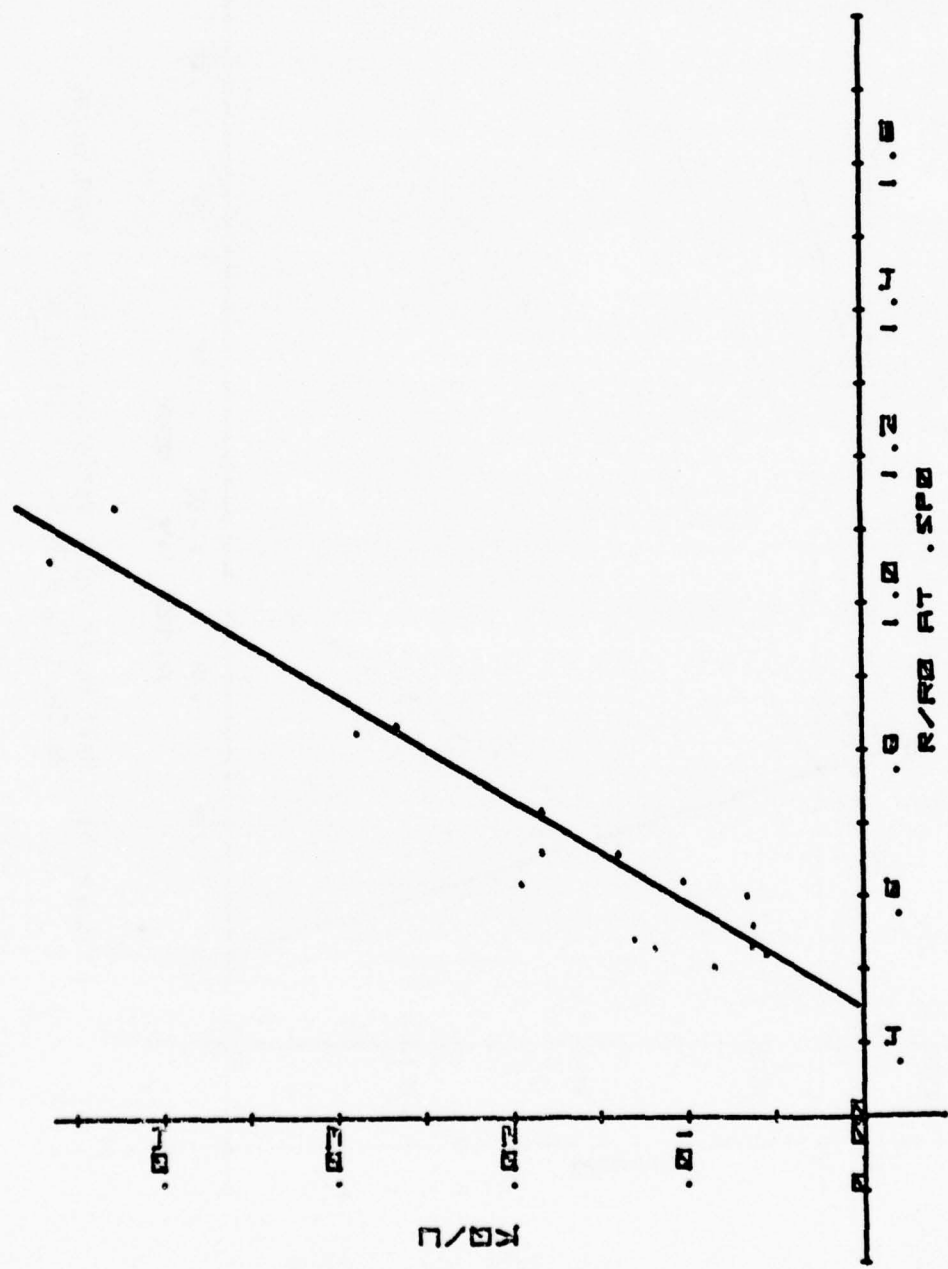


Figure 82. Half Power Point Variation of Focal Spot Size,
He Cd, $L/D_p = 45$, $D = 50$ mm

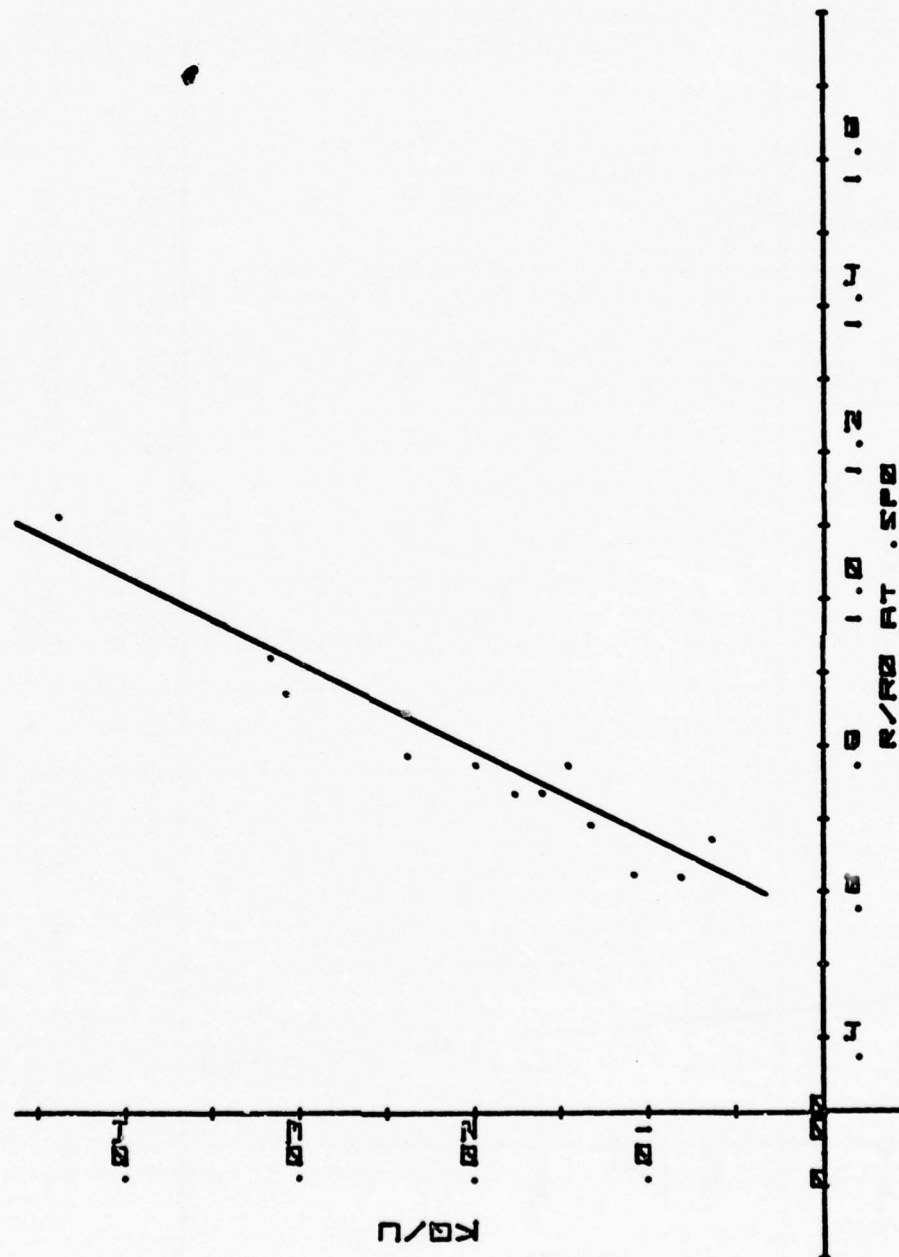


Figure 83. Half Power Point Variation of Focal Spot Size,
He Cd, $L/D_p = 45$, $D = 30.58 \text{ mm}$

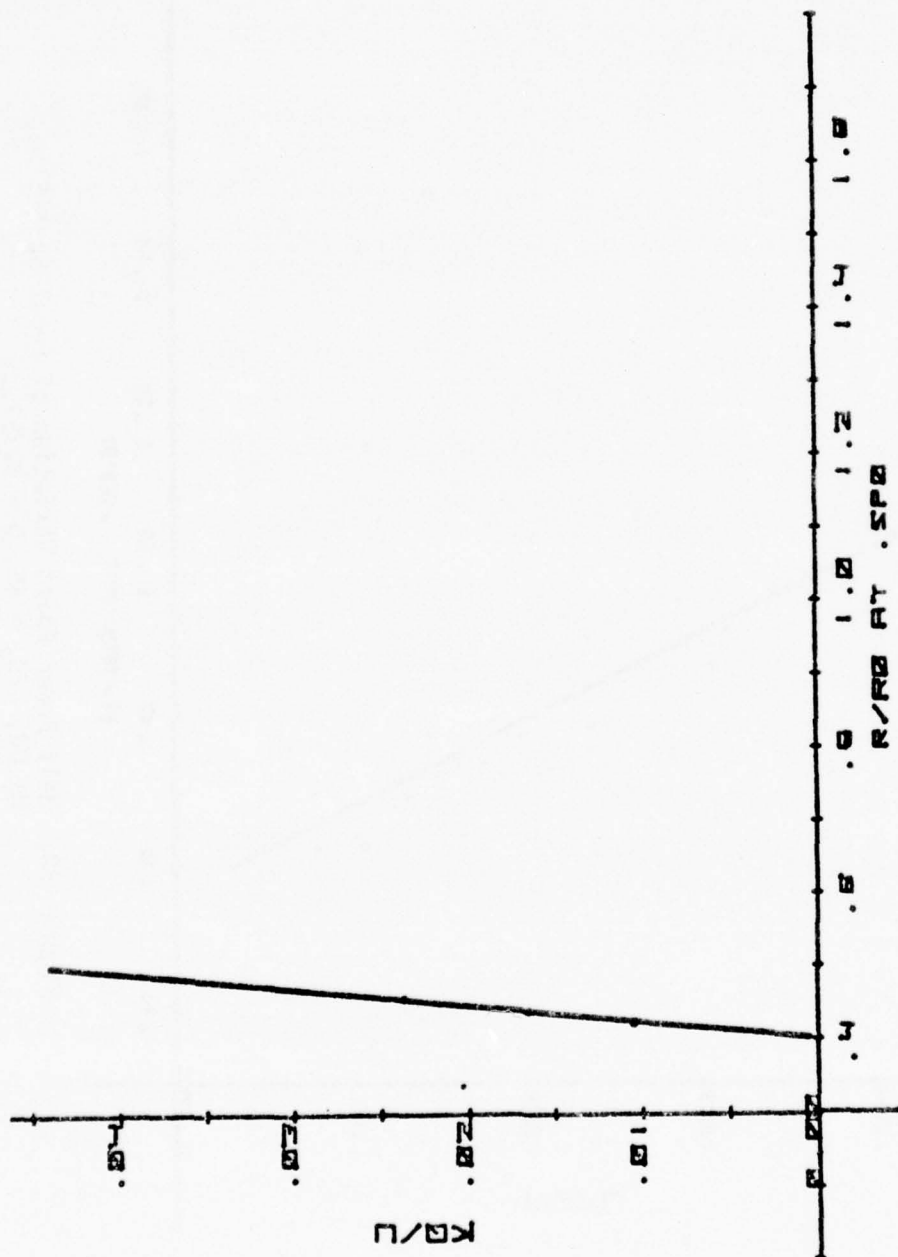


Figure 84. Half Power Point Variation of Focal Spot Size,
He Cd, $L/D_p = 45$, $D = 14.03$ mm

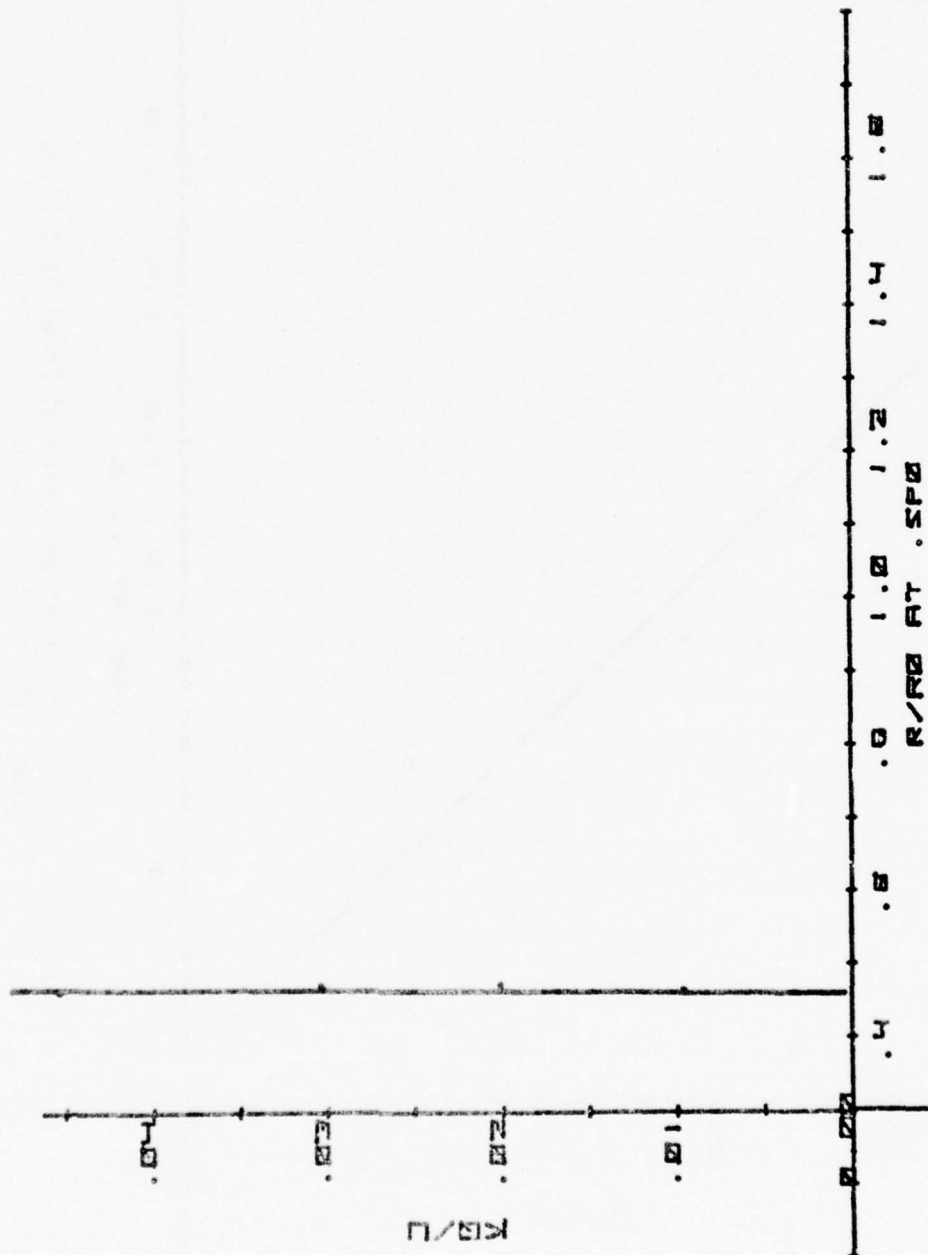


Figure 85. Half Power Point Variation of Focal Spot Size,
He Cd, $L/D_p = 45$, $D = 1.5$ mm

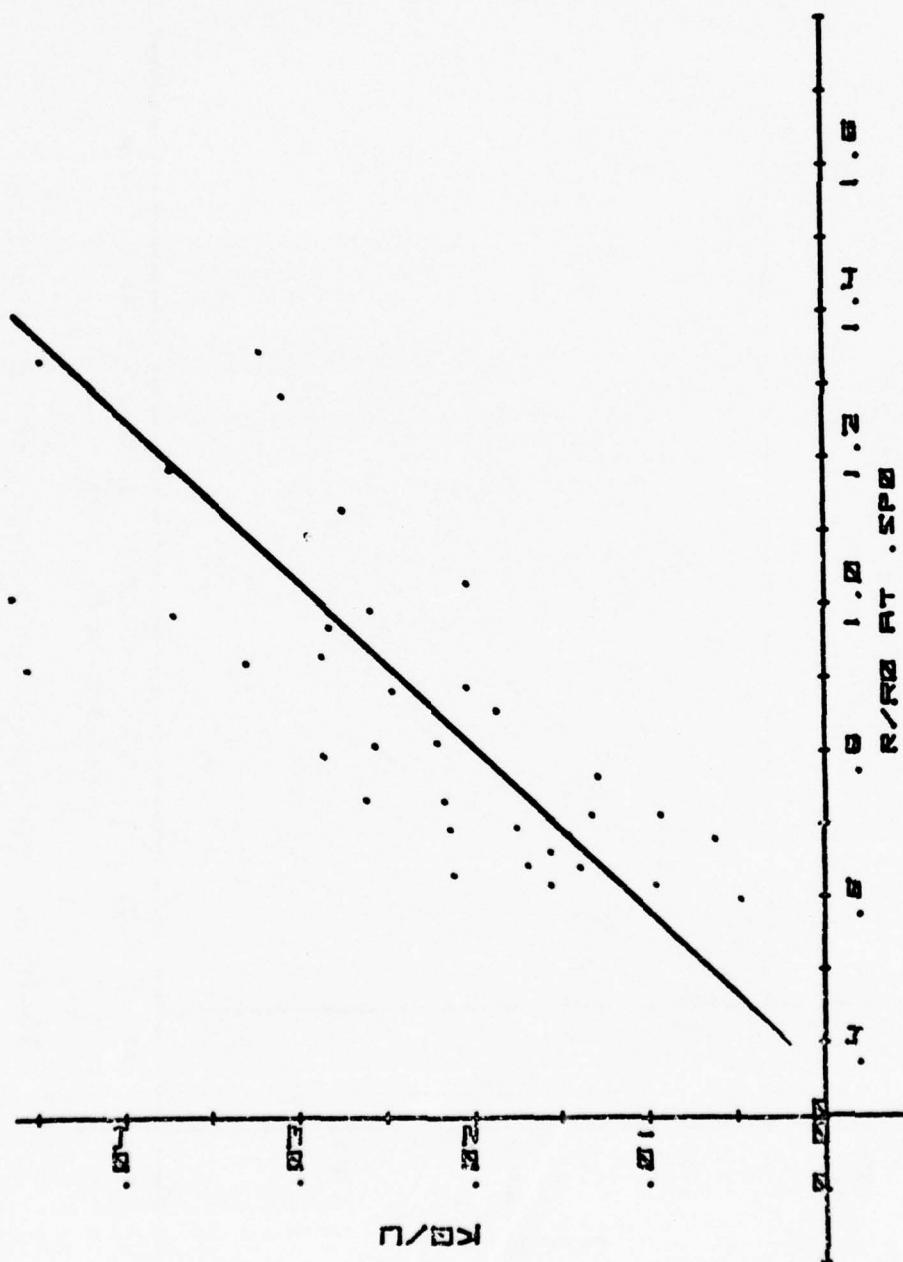


Figure 86. Half Power Point Variation of Focal Spot Size,
He Ne, $L/D_p = 28$, $D = 50$ mm

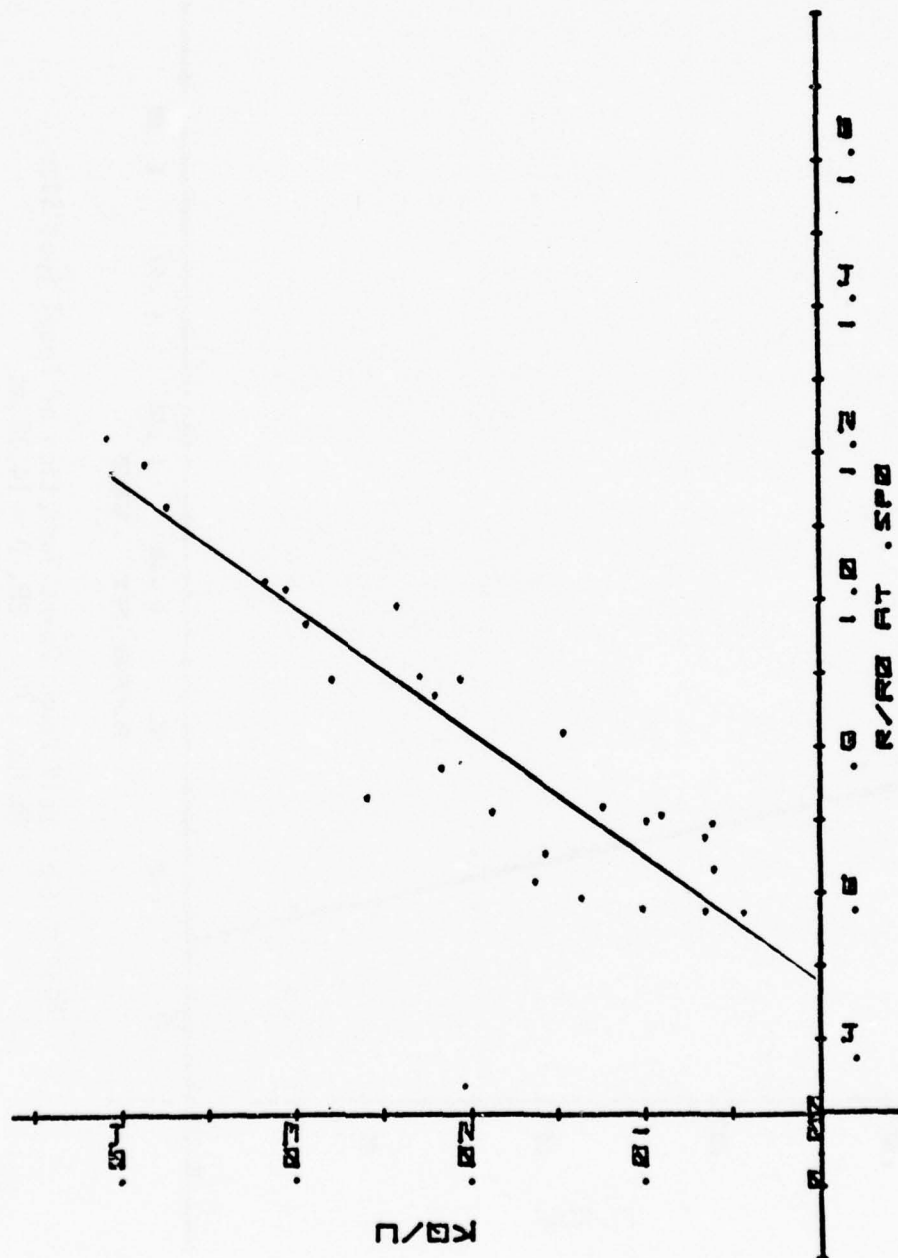


Figure 87. Half Power Point Variation of Focal Spot Size,
He Ne, $L/D_p = 28$, $D = 26 \text{ mm}$

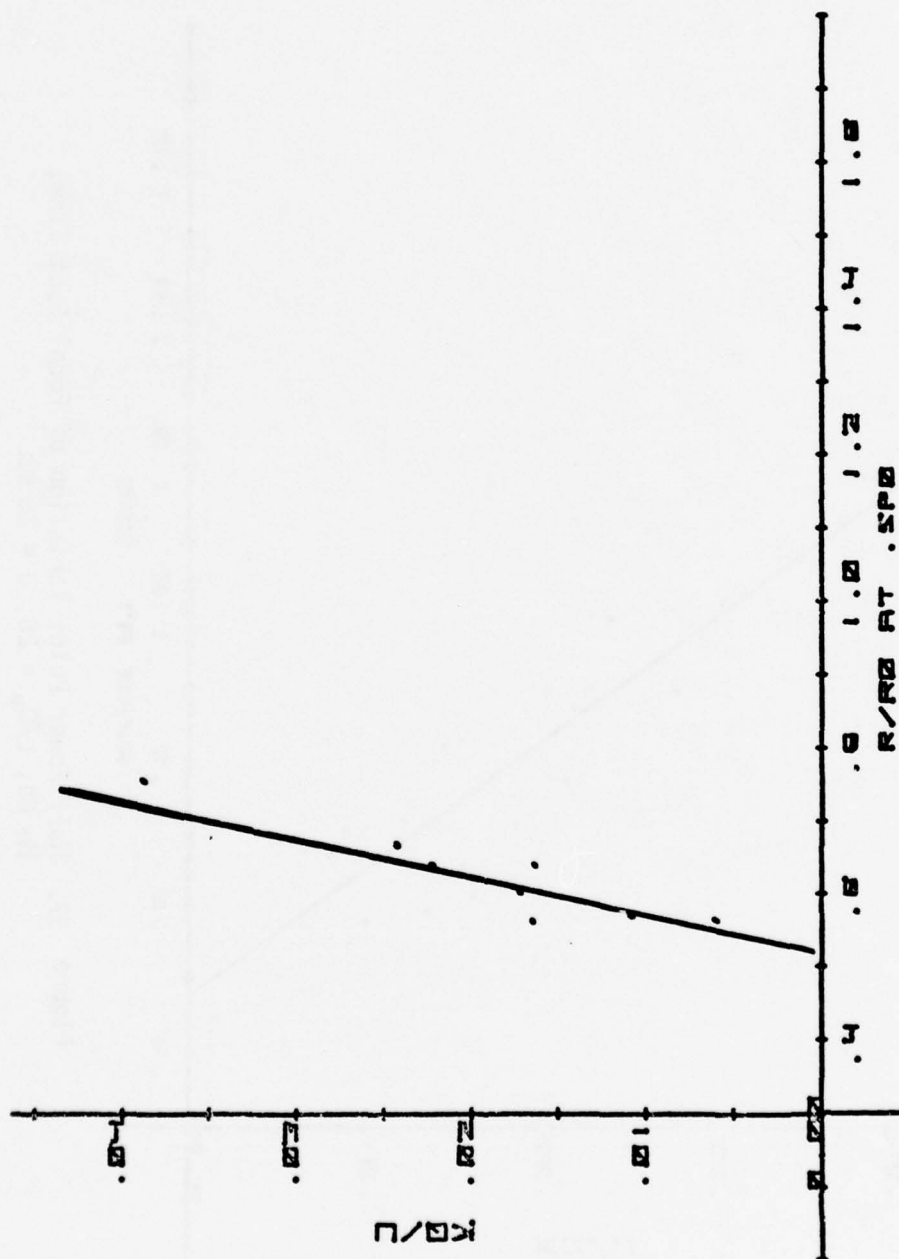


Figure 88. Half Power Point Variation of Focal Spot Size,
He Ne, $L/D_p = 28$, $D = 14.03$ mm

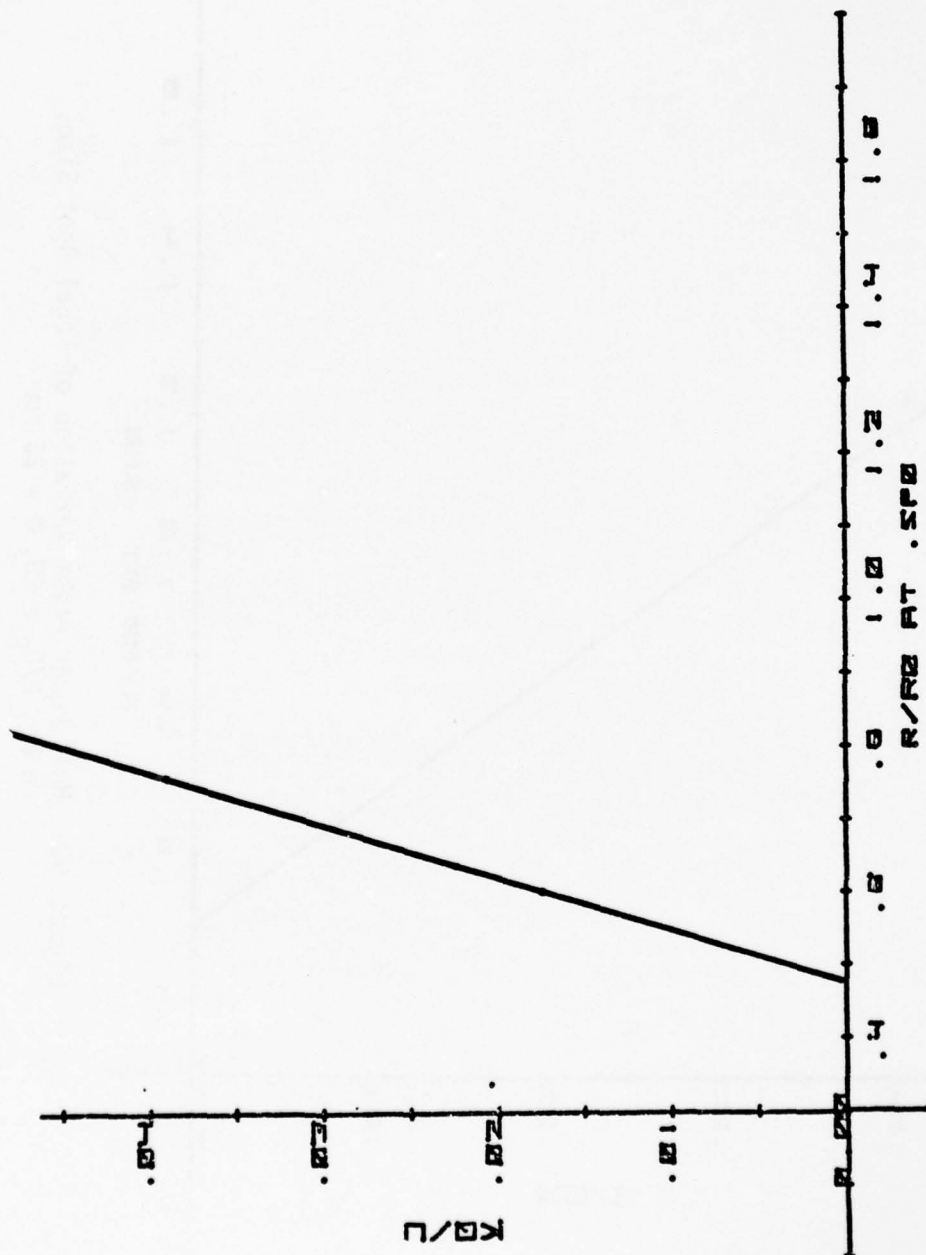


Figure 89. Half Power Point Variation of Focal Spot Size,
He Ne, $L/D_p = 28$, $D = 26$ mm

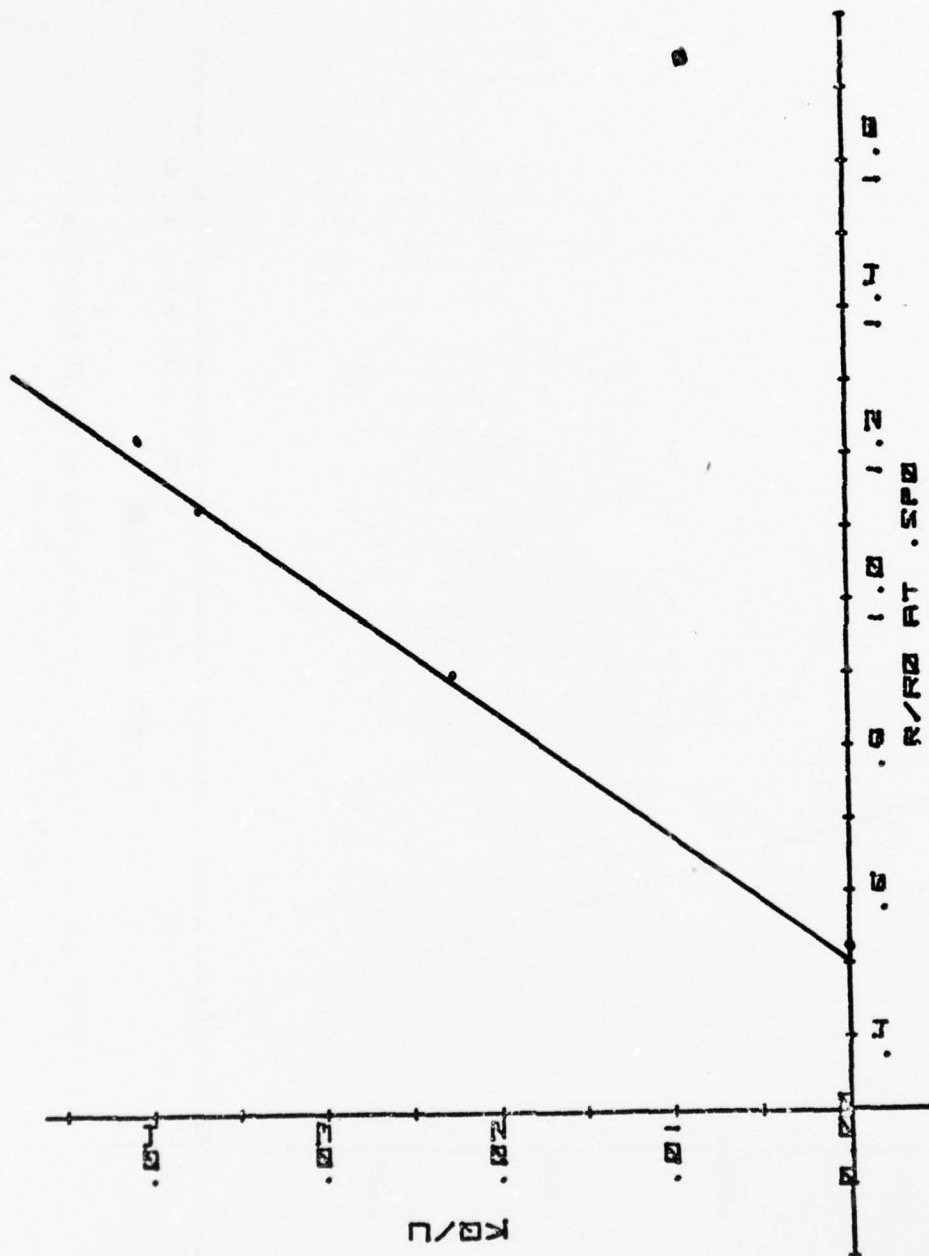


Figure 90. Half Power Point Variation of Focal Spot Size,
He Ne, $L/D_p = 28$, $D = 26$ mm

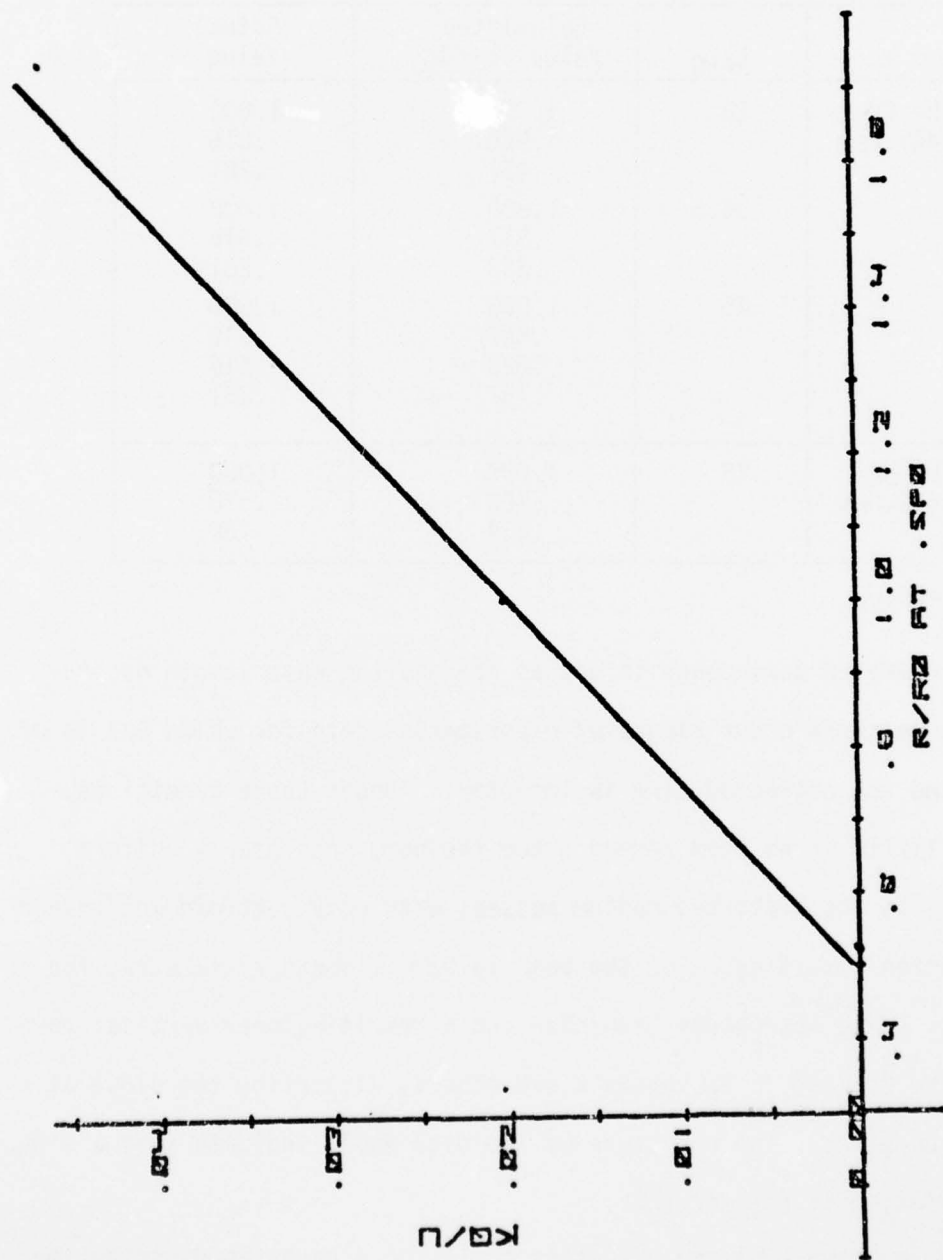


Figure 91. Half Power Point Variation of Focal Spot Size,
He Cd, $L/D_p = 28$, $D = 30.58 \text{ mm}$

Table 4. Diameter Dependence of Beam Spread

| λ | L/D _p | Calculated Value J ₅₀ /J ₅₀ | Actual Value |
|------------------|------------------|--|-----------------|
| He Cd 441.6mm | 28 | 1.000 | 1.000 |
| | | .920 | .616 |
| | | .451 | .281 |
| | 34.5 | 1.000 | 1.000 |
| | | .817 | .616 |
| | | .363 | .281 |
| | 45 | 1.000 | 1.000 |
| | | .697* | .616 |
| | | .823 | .616 |
| | | .157 | .281 |
| He Ne 632.8mm | 28 | 1.000 | 1.000 |
| | | .766 | .520 |
| | | .234 | .160 |

*Value

The diameter dependence is not as good as the wave length dependence because there occur ranges of experimental data for which D/λ is of order 1 and the neglected term is important. Under these conditions, there is little or no beam spread since the beam sees nearly uniform conditions as the distorted medium passes, with only centroid motion and scintillation resulting. For the beam 14.03 millimeters diameter, the turbulence scale approaches beam size and a resulting near vertical portion of the R/R_0 at $.5 P_0$ versus $K Q/U$ occurs, distorting the slope at a given value of $\Delta\eta$. The curvature of the data would indicate that a simple D variation is not correct.

From equation (95) the effective scale for a gaussian distribution may be calculated which would produce the measured beam spread. Correlation functions were obtained in this experiment which were typical of a single scale, three different scales, and even functions typical of an

infinite range of scales. A single scale is, therefore, not a realistic representation of the flow field actually encountered in this experiment. The implied effective gaussian scales are tabulated in Table 5 for the mean values of the tunnel profiles previously presented.

Table 5. Calculated Gaussian Scale from Mean Tunnel Profiles

| λ | L/Dp | Beam Diameter | \bar{a} |
|---|------|---------------|-----------|
| He Cd 441.6mm Turbulence Generator B | 28 | 50.00mm | 29.7mm |
| | | 30.58 | 13.0 |
| | | 14.03 | 11.6 |
| | | 1.50 | No Spread |
| | 34.5 | 50.00 | 3.0 |
| | | 30.58 | 2.5 |
| | | 14.03 | 1.1 |
| | 45 | 50.00 | 2.8 |
| | | 30.58 | 1.9 |
| | | 14.03 | 2.3 |
| | | 1.50 | No Spread |
| He Ne 632.8mm Turbulence Generator B | 28 | 50.00 | 3.1 |
| | | 26.00 | 1.1 |
| | | 8.00 | .7 |
| He Ne 632.8mm Turbulence Generator A | 14 | 50.00 | 3.0 |

The single gaussian scale is observed to be in the range of the measured integral and microscale shown previously. The very small value of (a) indicates very little beam spread. Integral scales from 6.4 to 2.3 millimeters were measured for turbulence generator B.

Turbulence generator A had twice the perforation diameter of turbulence generator B which resulted in the integral scale being comparable to the beam diameter for the 50 millimeter diameter beam. Very little

spread would be predicted for the 50 millimeter beam. The R/R_0 spread at $.5 P_0$ point for the He Ne beam and turbulence generator A is shown in Figure 92, further illustrating the difficulty in using a single effective scale when the integral scale approaches the beam diameter.

As a result of the inadequacies shown in Tables 4 and 5, which occur with neglect of the Λ/D terms of equation (100), the experimental laser beam spread at the half power point has been shown in Figures 93 through 105, along with the predicted values of spread for equation (100) as Λ_T is varied. The solid curves in Figures 94 through 104 are from equation (100), with the integral scale, Λ_T , varied from .254 cm in .254 cm increments. The curve nearest the ordinate represents equation (100) for an integral scale of .254 cm. In Figure 105, equation (100) is shown for Λ_T of .127 and .254 cm. Quantitatively, the diameter dependence shown in Figures 94 through 105 is much better than indicated in Table 4. The integral scale dependence is also shown to be in the range of the experimentally measured values. Equation (100) does appear to overestimate the integral scale and not be capable of accurately predicting the spread for very small values of $\langle \Delta \eta \rangle$. The larger values of $\langle \Delta \eta \rangle$ tend to have smaller measured values of the integral scale of turbulence. Figures 94 through 105 also show an increase in slope with $\langle \Delta \eta \rangle$ or indicate a reduction in the integral scale with increasing $\langle \Delta \eta \rangle$. Figure 105 indicates a turbulence scale of $\sim .178$ cm. The microscale of turbulence was indicated to range from .12 to .5 cm in Figures 67 to 69. The values of Λ_T , which are implied when the experimental data for beam spread at the half power point of the power distribution are compared against equation (100), are summarized in Table 6.

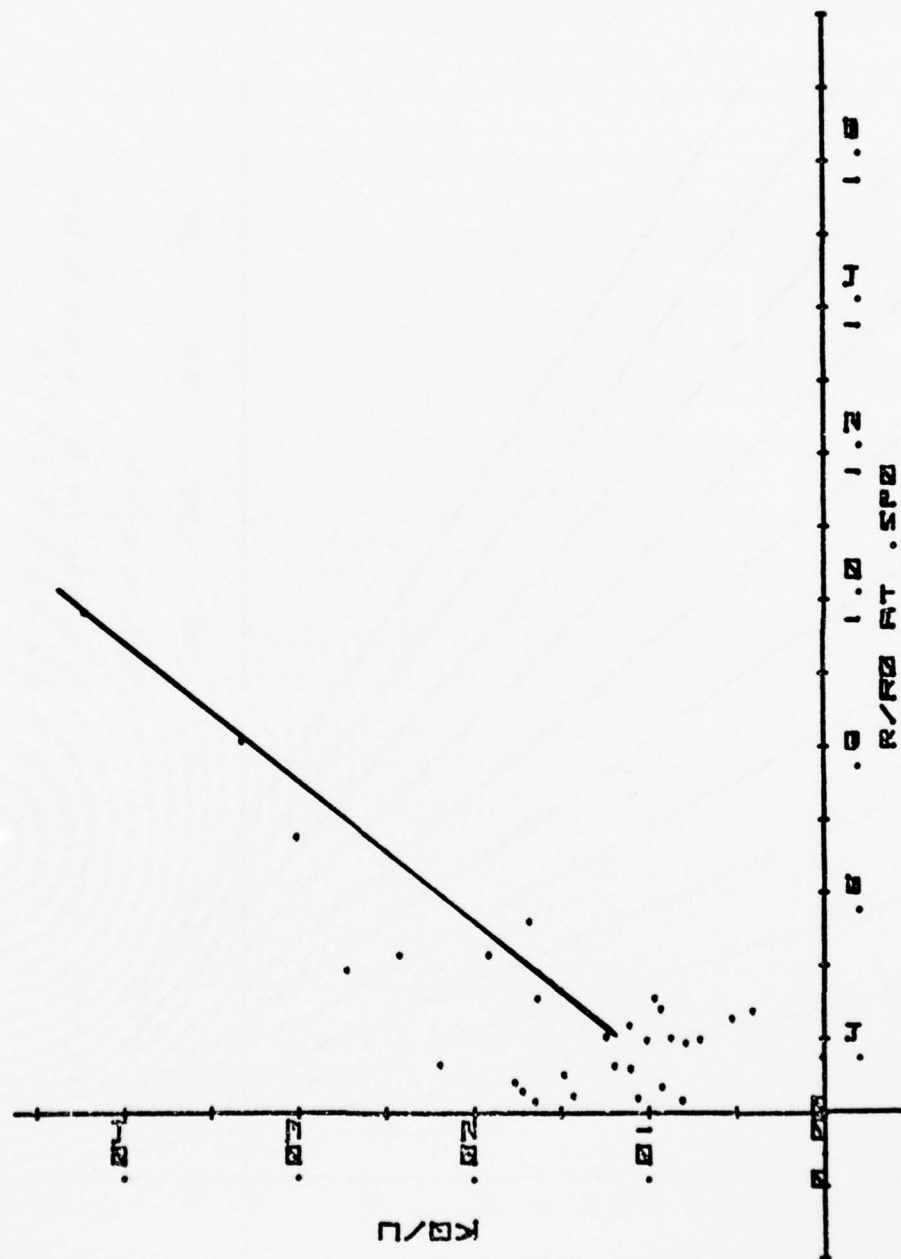


Figure 92. Half Power Point Variation of Focal Spot Size,
He Ne, $L/D_p = 14$, $D = 50$ mm

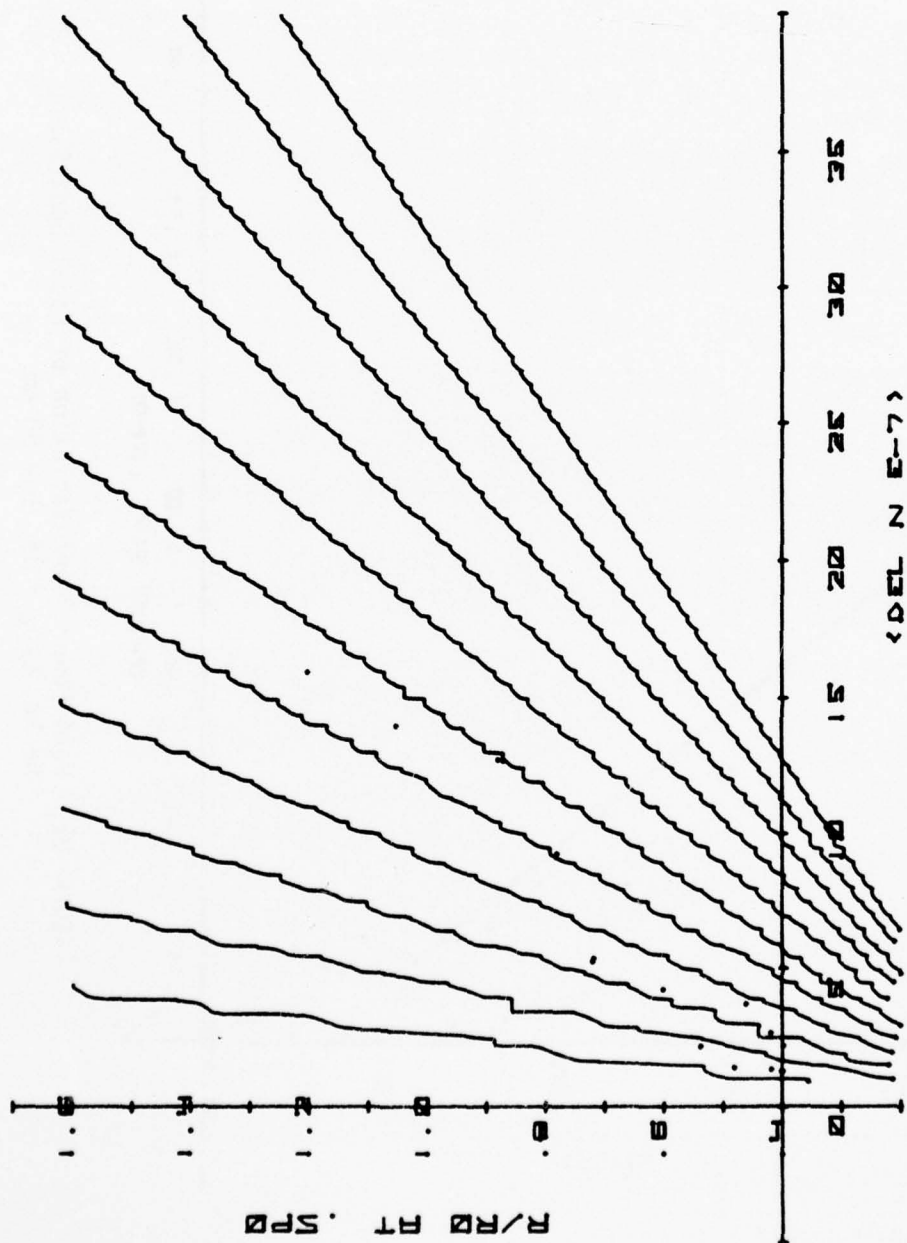


Figure 93. Half Power Point Variation for the Chernov-Sutton Calculation, He Cd, $L/D_p = 28$, $D = 50$ mm

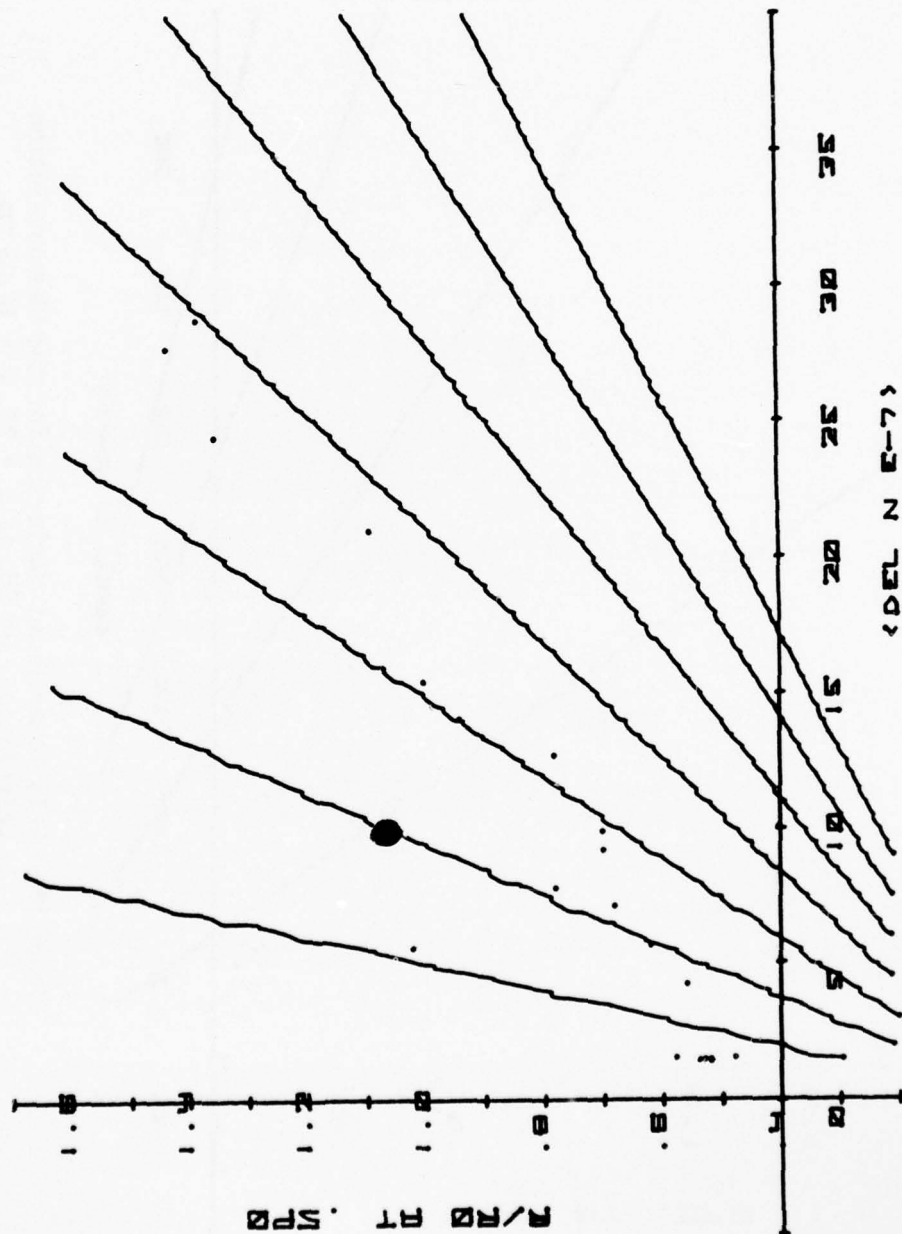


Figure 94. Half Power Point Variation for the Chernov-Sutton Calculation, He Cd, $L/D_p = 28$, $D = 30.58$ mm

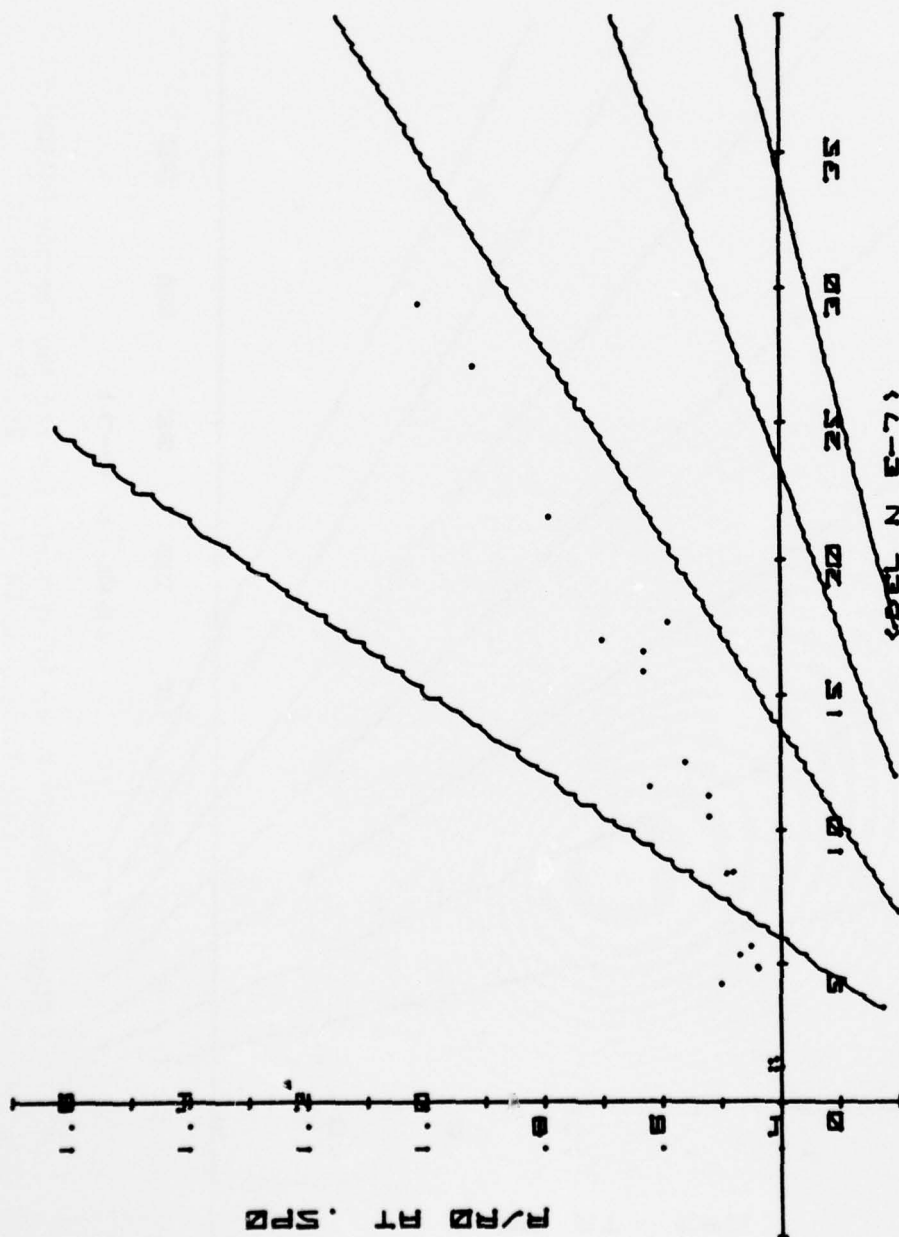


Figure 95. Half Power Point Variation for the Chernov-Sutton Calculation, He Cd, $L/D_p = 28$, $D = 14.03$ mm

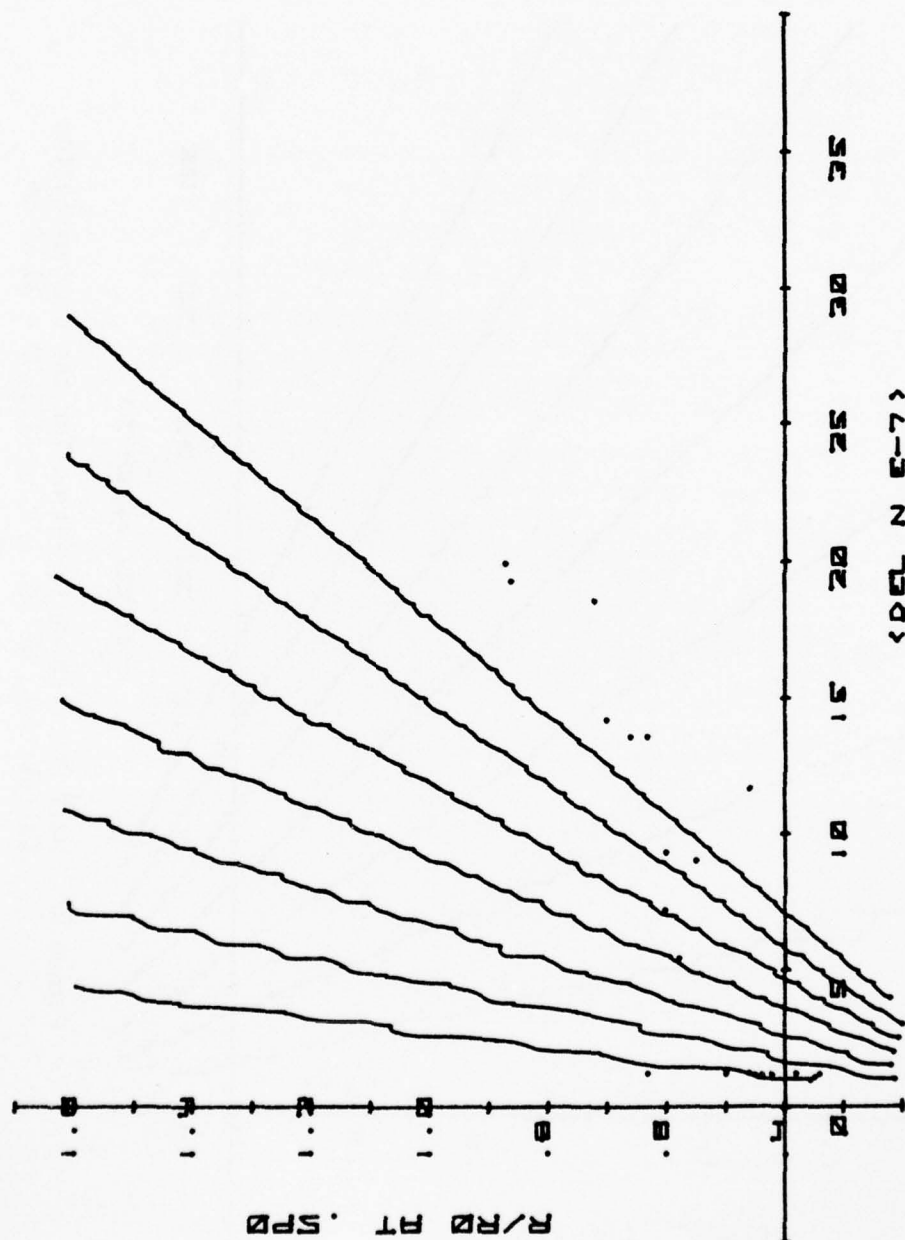


Figure 96. Half Power Point Variation for the Chernov-Sutton Calculation, He Cd, $L/D_p = 34.5$, $\bar{g} = 50$ mm

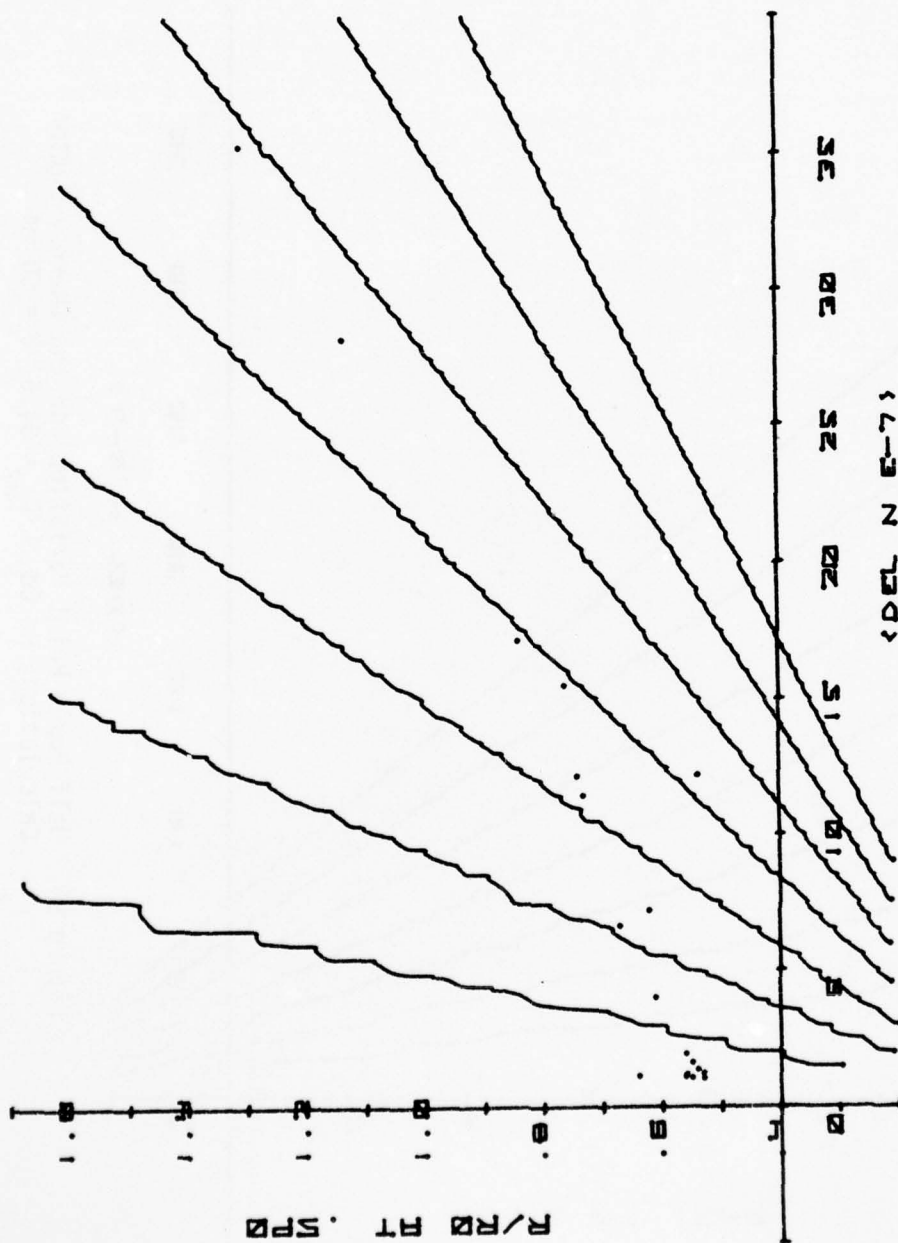


Figure 97. Half Power Point Variation for the Chernov-Sutton Calculation, He Cd, $L/D_p = 34.5$, $D = 30.58$ mm

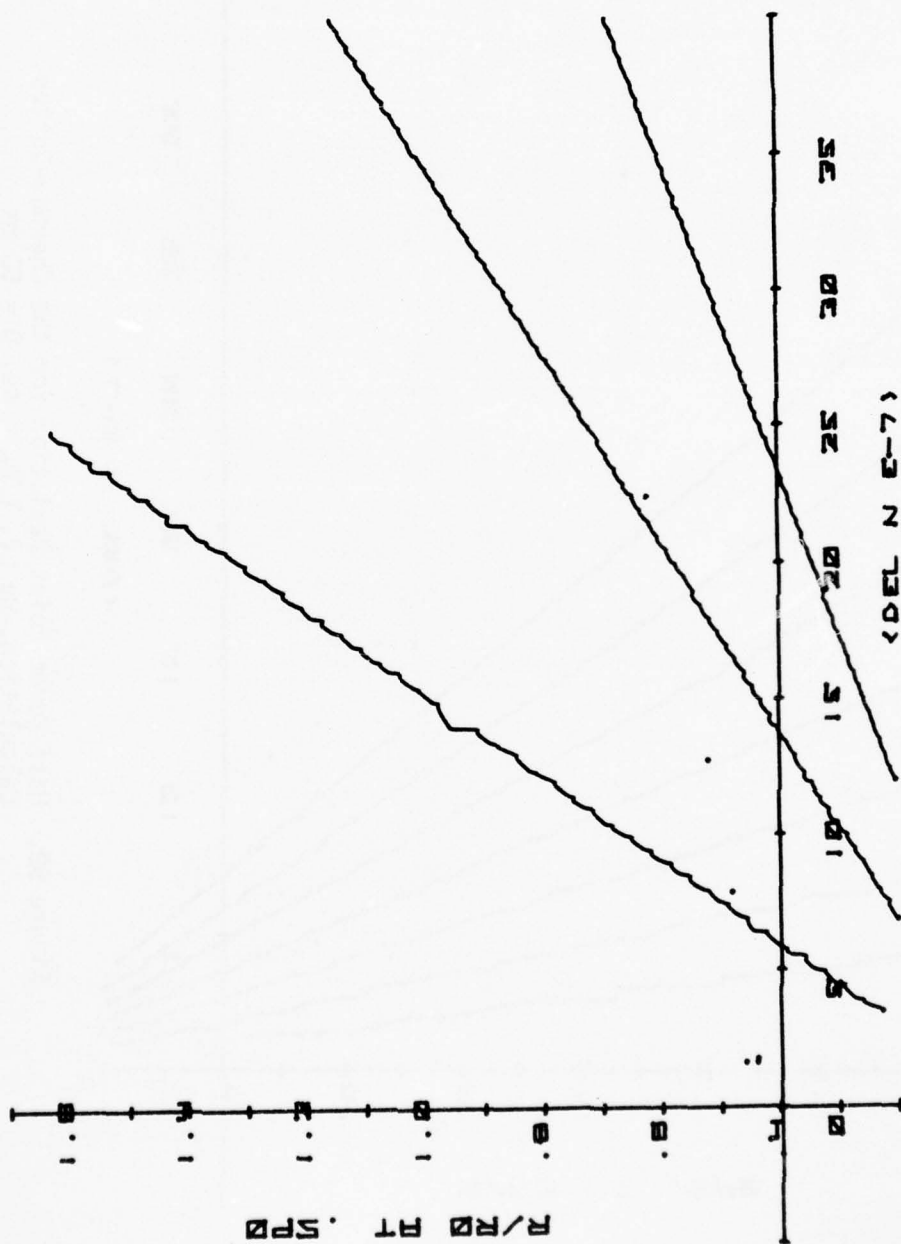


Figure 98. Half Power Point Variation for the Chernov-Sutton Calculation, He Cd, $L/D_p = 34.5$, $D = 14.03 \text{ mm}$

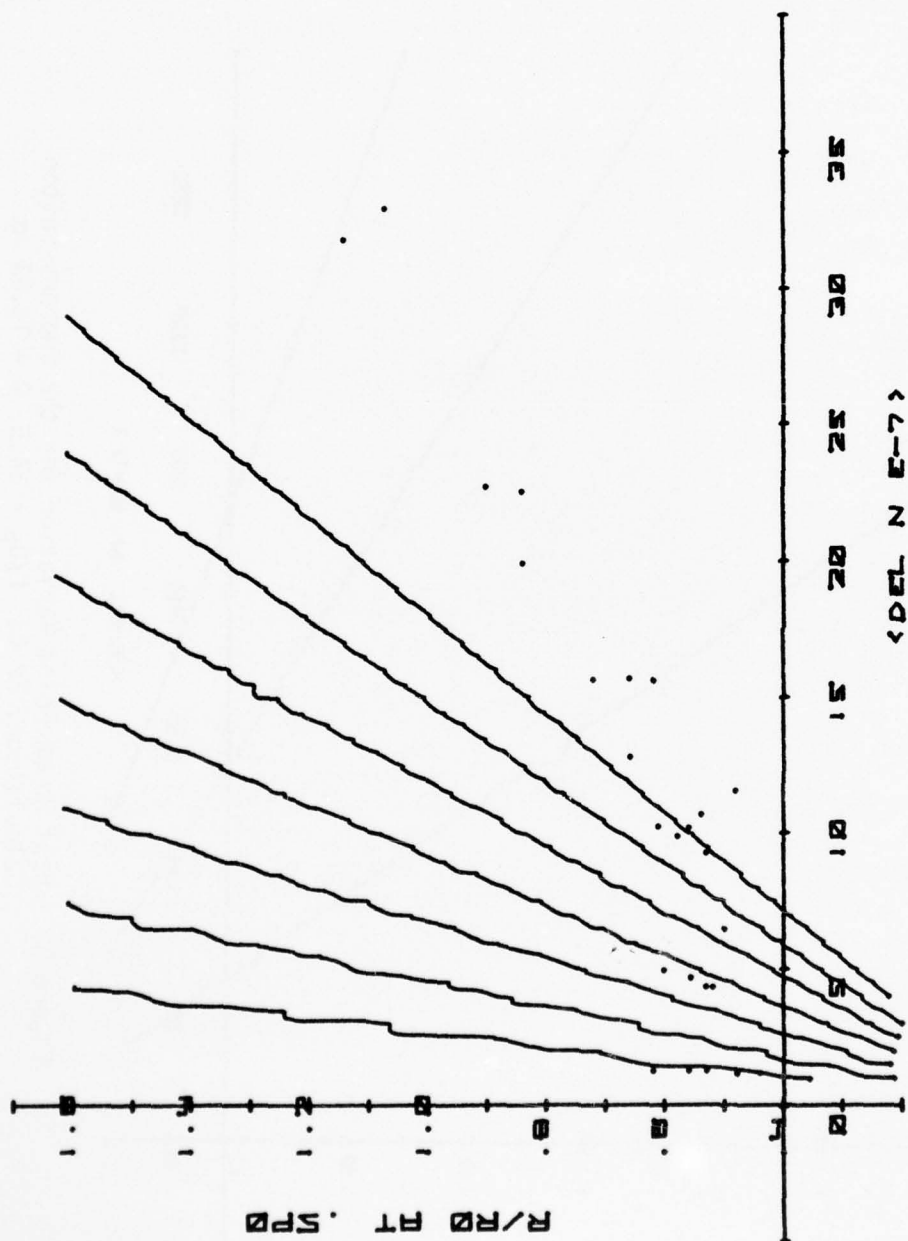


Figure 99. Half Power Point Variation for the Chernov-Sutton Calculation, He Cd, $L/D_p = 45$, $D = 50$ mm

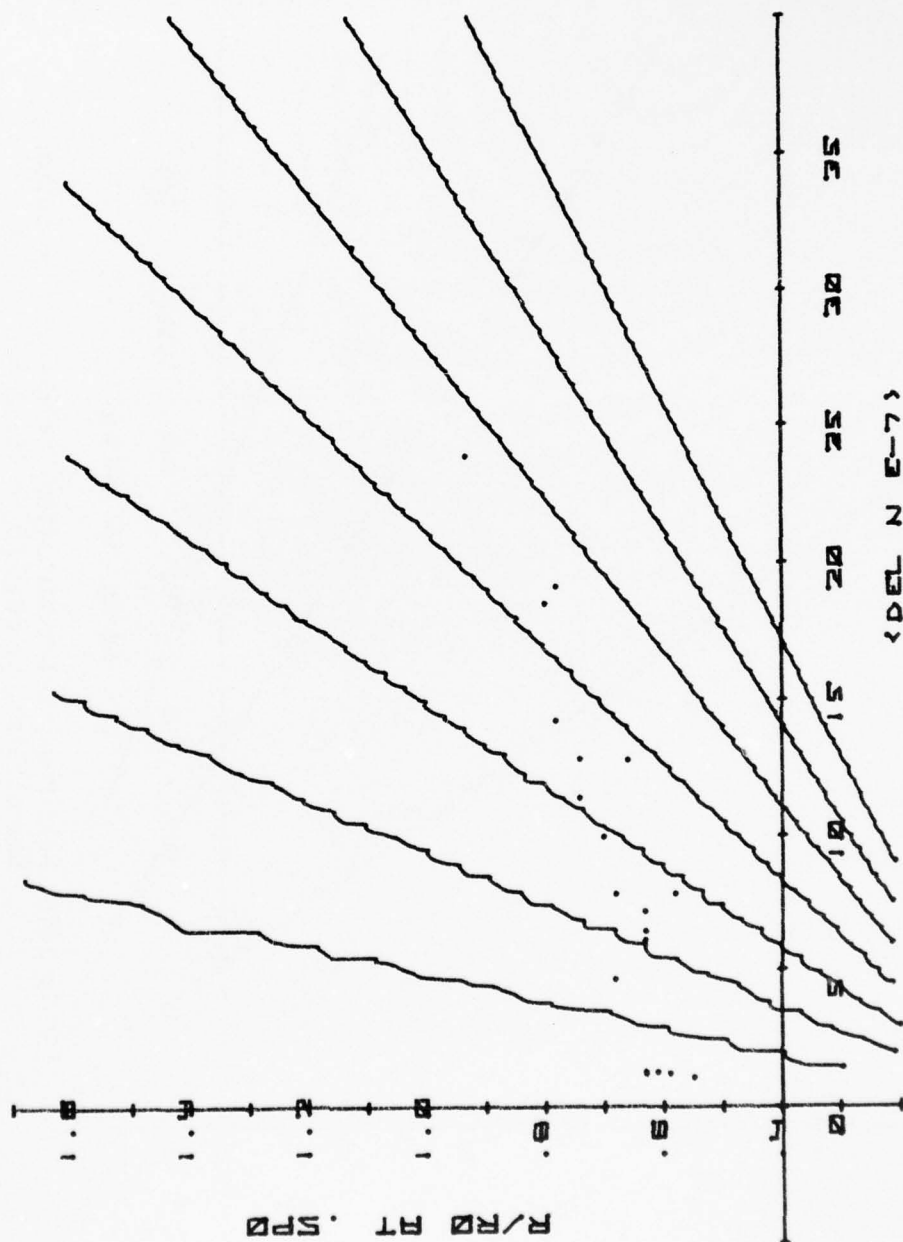


Figure 100. Half Power Point Variation for the Chernov-Sutton Calculation, He Cd, $L/D_p = 45$, $D = 30.58$ mm

AD-A038 667

AIR FORCE AERO PROPULSION LAB WRIGHT-PATTERSON AFB OHIO
THE EFFECT OF TURBULENCE ON LASER BEAM QUALITY.(U)
NOV 76 R B RIVIR

F/6 20/5

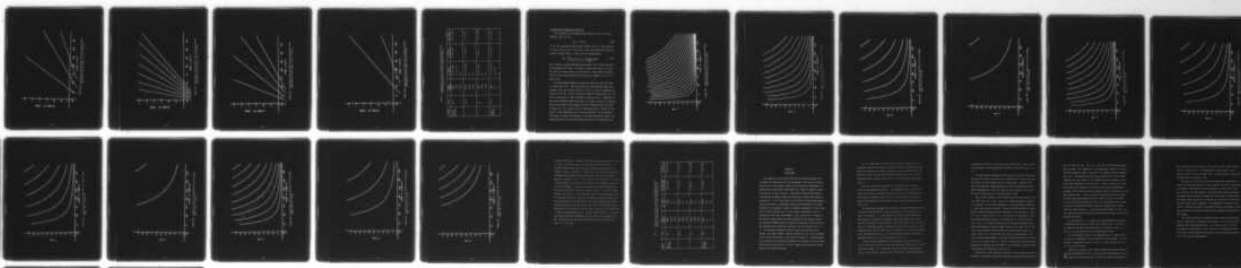
UNCLASSIFIED

AFAPL-TR-76-94

NL

3 OF 3

AD
A038667



END

DATE
FILMED

5-77

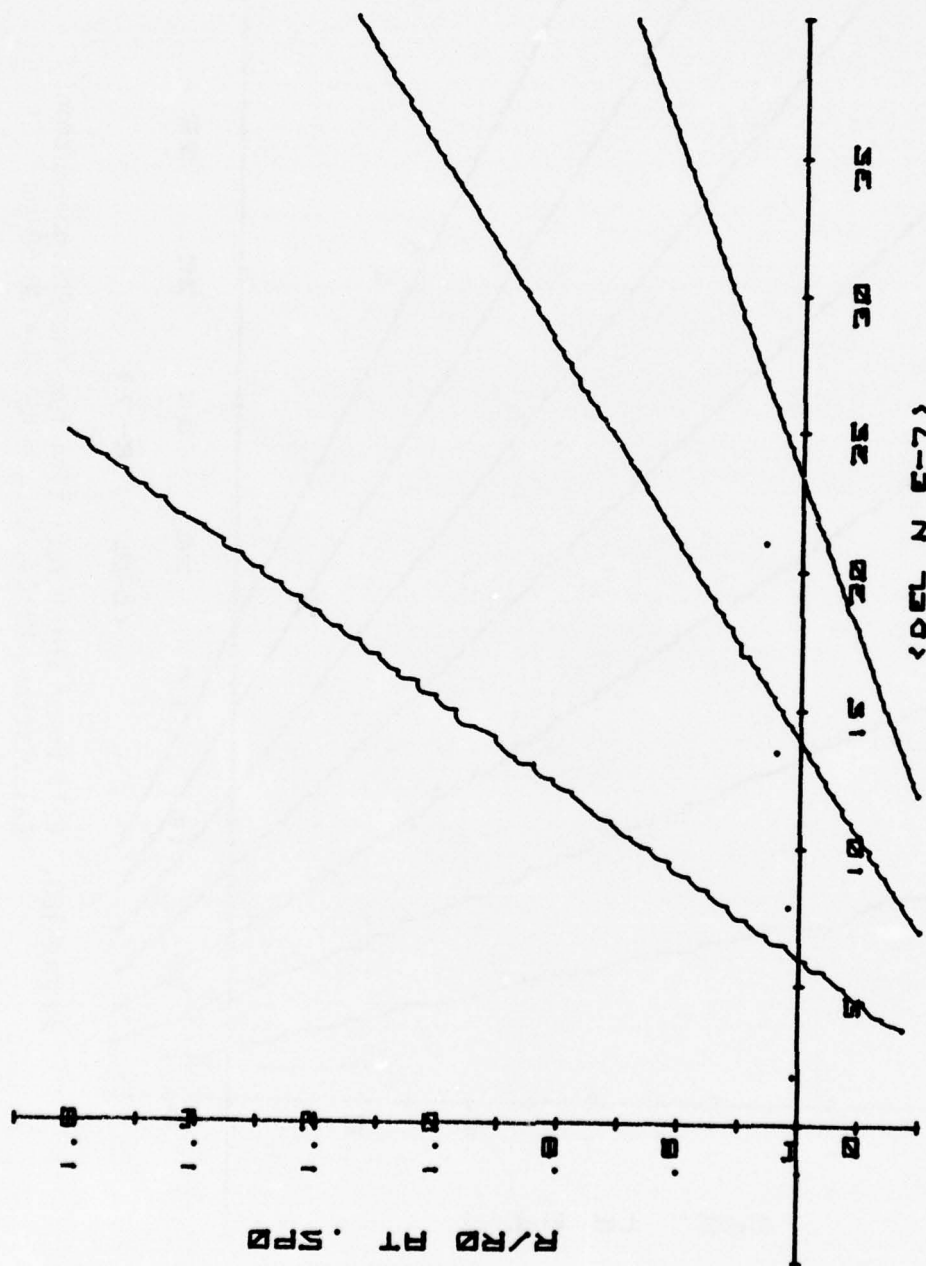


Figure 101. Half Power Point Variation for the Chernov-Sutton Calculation, He Cd, $L/D_p = 45$, $D = 14.03$ mm

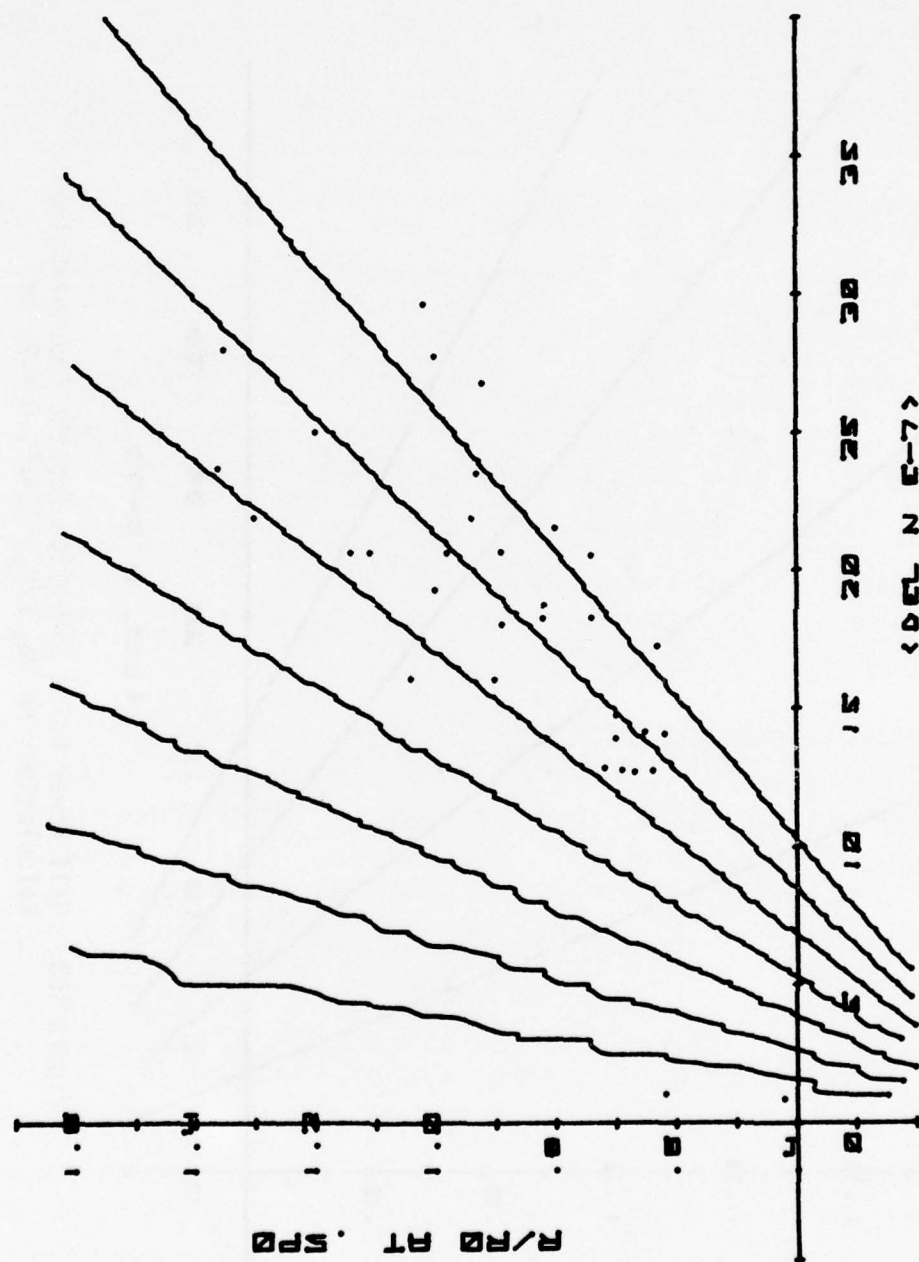


Figure 102. Half Power Point Variation for the Chernov-Sutton Calculation, He Ne, $L/D_p = 34.5$, $D = 50 \text{ mm}$

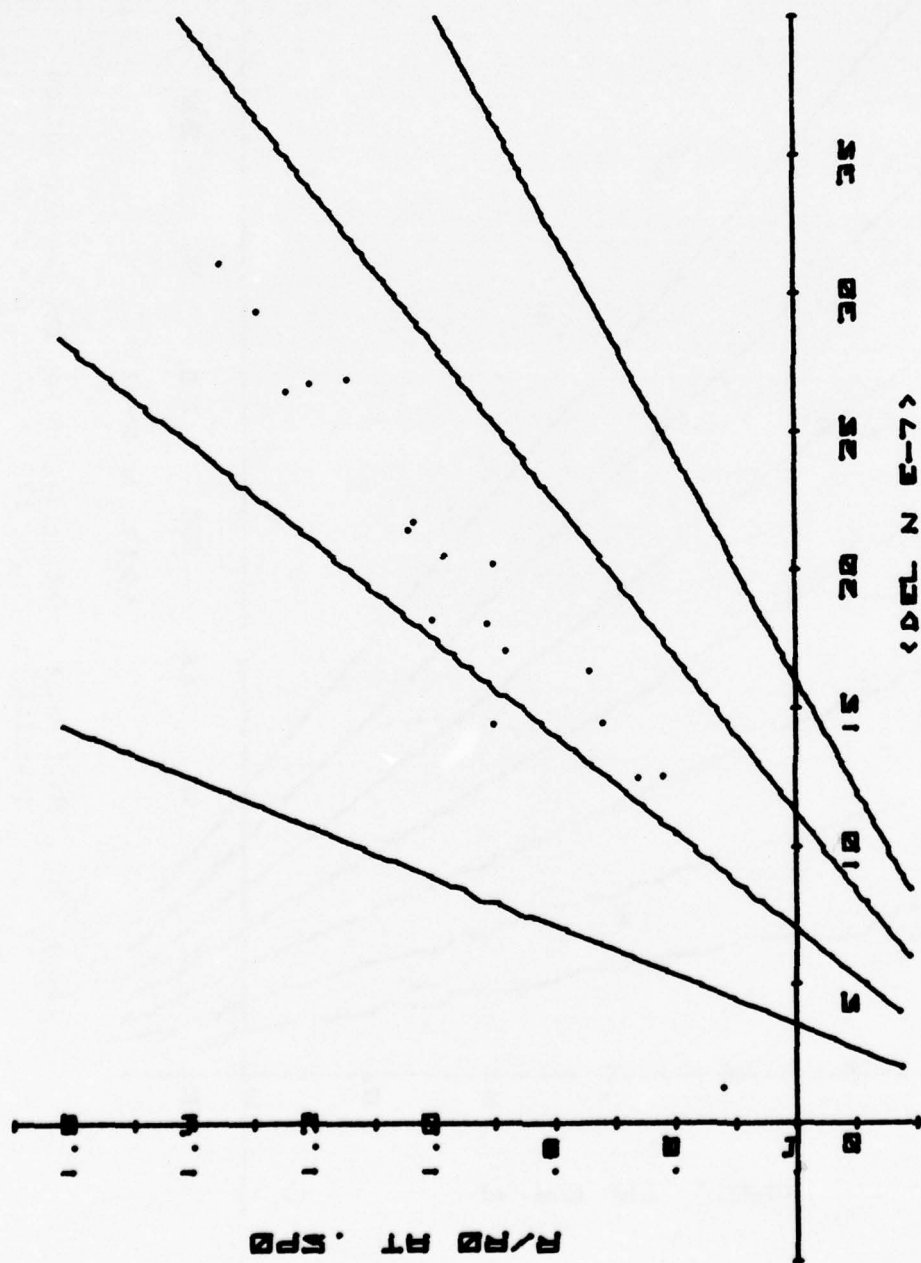


Figure 103. Half Power Point Variation for the Chernov-Sutton Calculation, He Ne, $L/D_p = 34.5$, $D = 26 \text{ mm}$

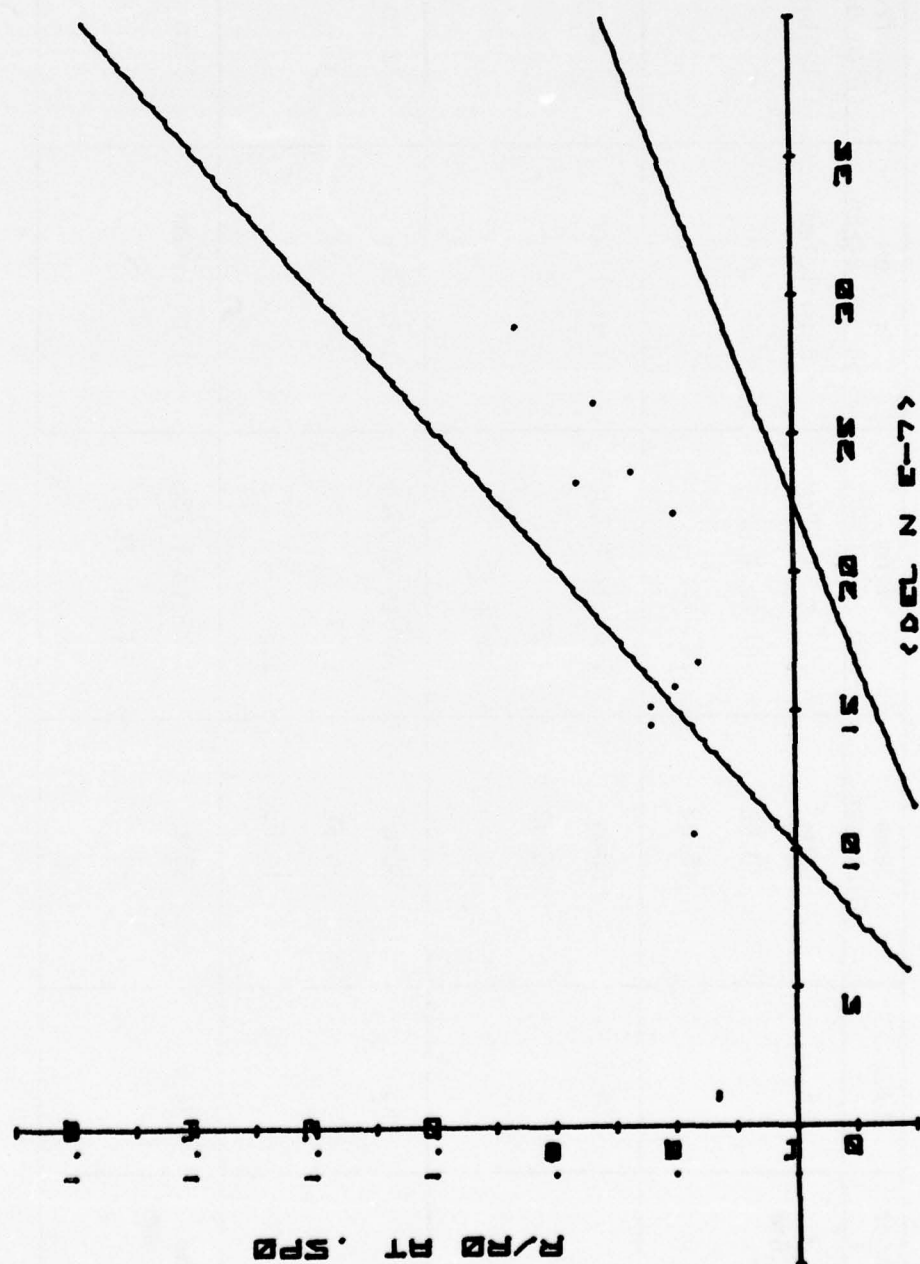


Figure 104. Half Power Point Variation for the Chernov-Sutton Calculation, He Ne, $L/D_p = 34.5$, $D = 8 \text{ mm}$

Table 6. Comparison of ΔT and λ_0 Scales from Half Power Values of R/Ro Measurements with Their Measured Values

| Laser λ | L/Dp | Beam Diameter | ΔT from Fig. 93-104 | ΔT from 54 and 64-66 | λ_0 from Fig. 67-69 |
|--------------------|------|------------------|--------------------------------|---------------------------------|--------------------------------|
| He Cd 441.6nm | 28 | 50mm | .76 to 1.52cm | .6 to 1.4cm | .12 to .5cm |
| | | 30.58 | .51 to 1.02 | | |
| | | 14.03 | .43 + | | |
| | 34.5 | 50mm | 1.02 to 2.03cm | 1 to 1.6cm | .1 to .4cm |
| | | 30.58 | 1.27 | | |
| | | 14.03 | .64 + | | |
| | 45 | 50mm | .97 to 2.29cm | 1 to 2cm | .12 to .57cm |
| | | 30.58 | 1.27 | | |
| | | 14.03 | .89 | | |
| He Ne 632.8nm | 34.5 | 50mm | 1.27 to 1.78cm | 1 to 1.6cm | .1 to .4cm |
| | | 26 | .51 to .76 | | |
| | | 8 | .18 | | |

The Reduction of Centerline Intensity

The turbulent to non-turbulent beam intensity ratio is given by (Chernov, 1967, p. 142):

$$\frac{I}{I_0} = \pi a^2 / \alpha h_0^2 \quad (109)$$

or for this experiment using Sutton's equation (6) for α and replacing a^2 and h_0^2 with $(\Lambda/.75)^2$, the value for the three-dimensional turbulence spectrum (Sutton, 1969, p. 1740), and $\pi D^2/4$ respectively:

$$\frac{I}{I_0} = \frac{\Lambda \lambda^2}{2(.75 D \pi \langle \Delta \eta \rangle)^2 L_0 (1 + (\frac{2\pi\Lambda}{.75D})^2)^{-5/6}} \quad (110)$$

This relation is plotted parametrically against Λ/D in Figure 105 for a 50 mm diameter He Cd beam. Λ/D takes on values from .025 to .5, with the .025 curve being closest to the abscissa. Figure 105 and equation (110) show that the expression I/I_0 does not go smoothly to 1.0 as $\langle \Delta \eta \rangle$ goes to zero.

The experimentally measured centerline intensity ratios are shown in Figures 106 to 117. The solid curves are the predicted values from equation (110), for integral scales of .254 cm in .254 cm increments for Figures 106 to 116. The solid curves of Figure 117 begin with λ_0 of .08 cm with increments of .0254 cm between successive curves. Comparison of the similar diameter beams at the same $\langle \Delta \eta \rangle$ values, as L/D_p is increased, shows the increase in the integral scale of turbulence which was shown in Figure 54. The integral scale of turbulence which is implied in comparison of the experimental data with the parametric plot of equation (110) shown in Figures 106 through 117 has been tabulated in Table 6 for comparison against the measured temperature scales of turbulence from

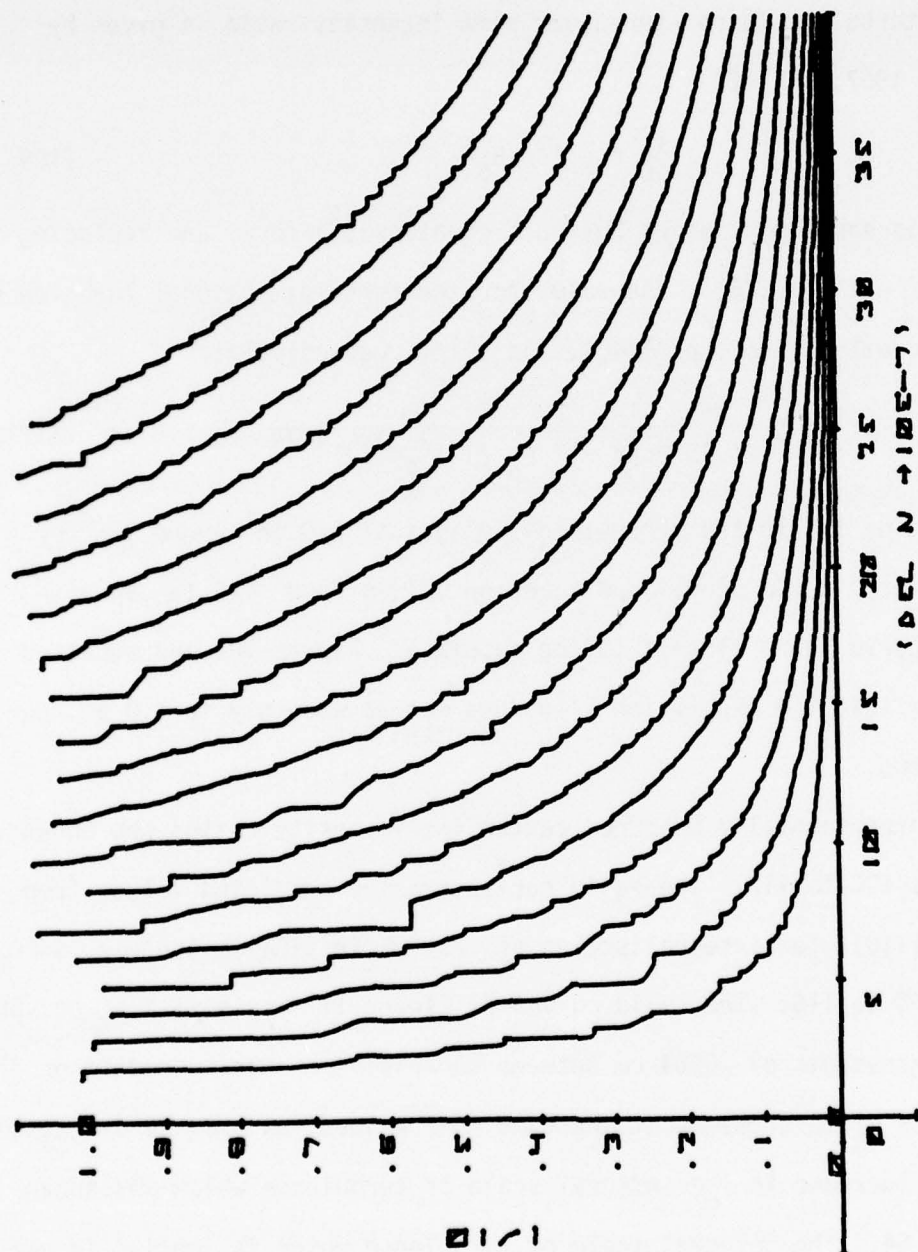


Figure 105. Chernov-Sutton Calculation for the Centerline Value of Intensity for a He Cd Beam

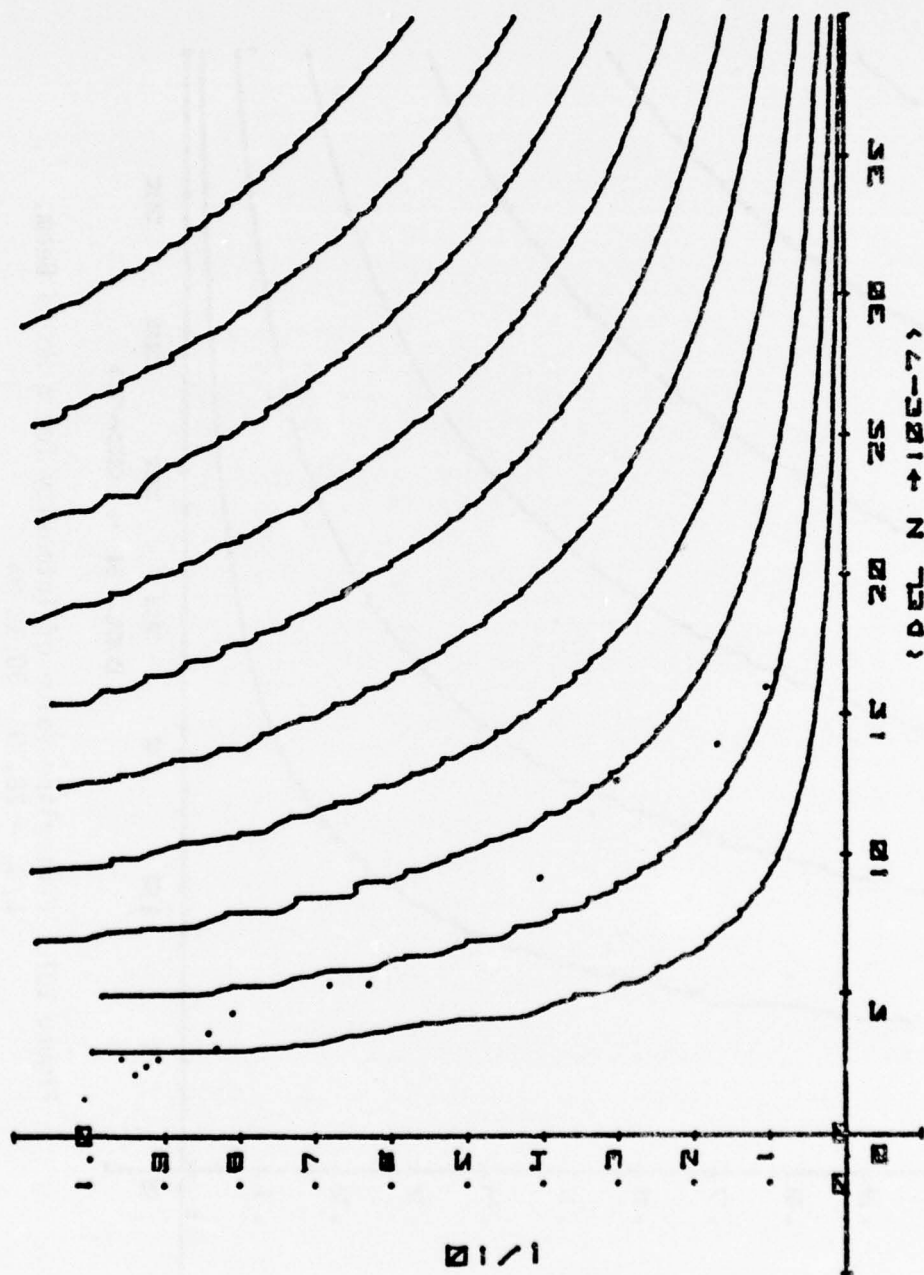


Figure 106. Centerline Value of Intensity for a He Cd Beam,
 $L/D_0 = 28$, $D = 50$ mm

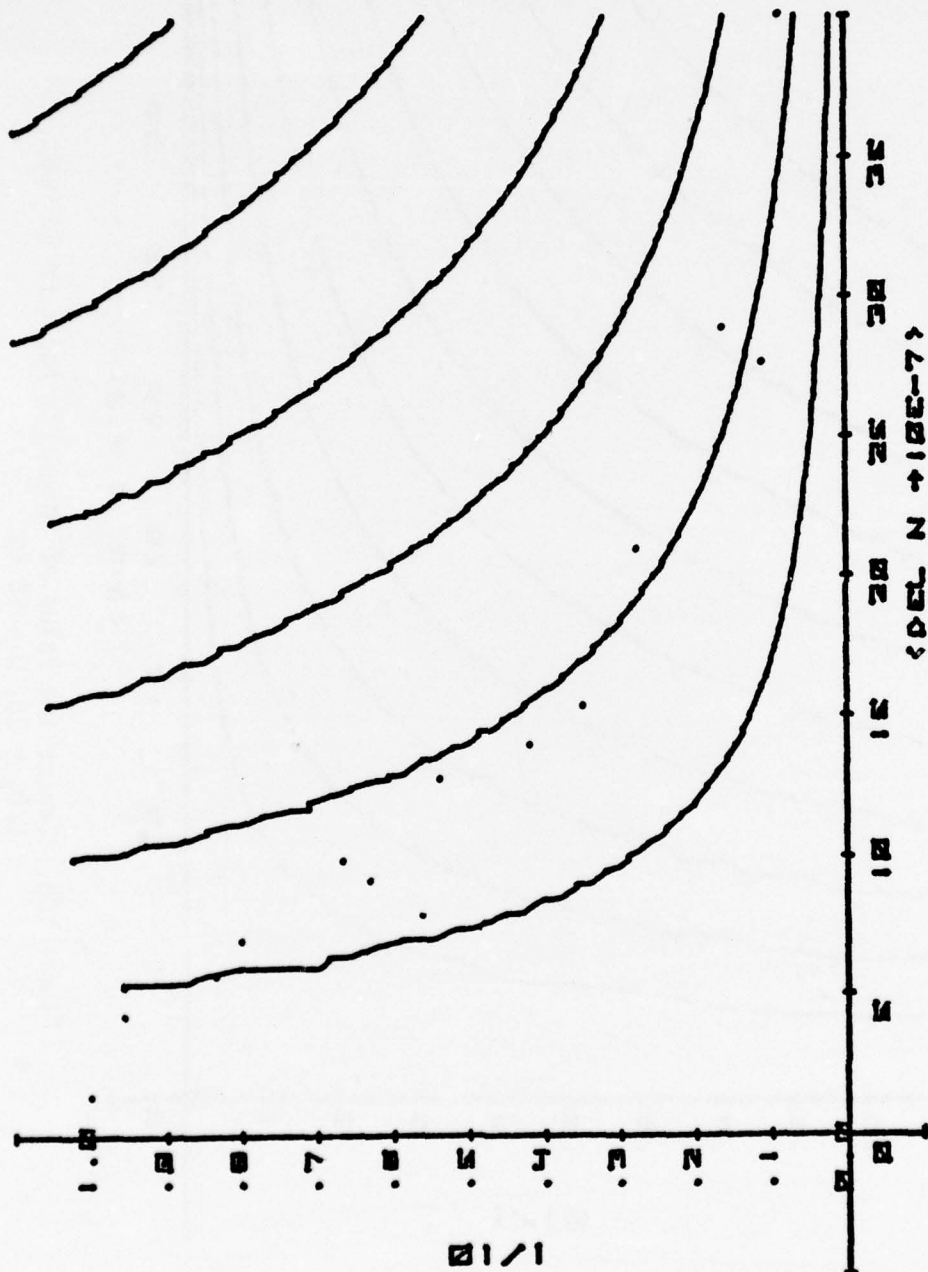


Figure 107. Centerline Value of Intensity for a He Cd Beam,
 $L/D_p = 28$, $D = 30.58$ mm

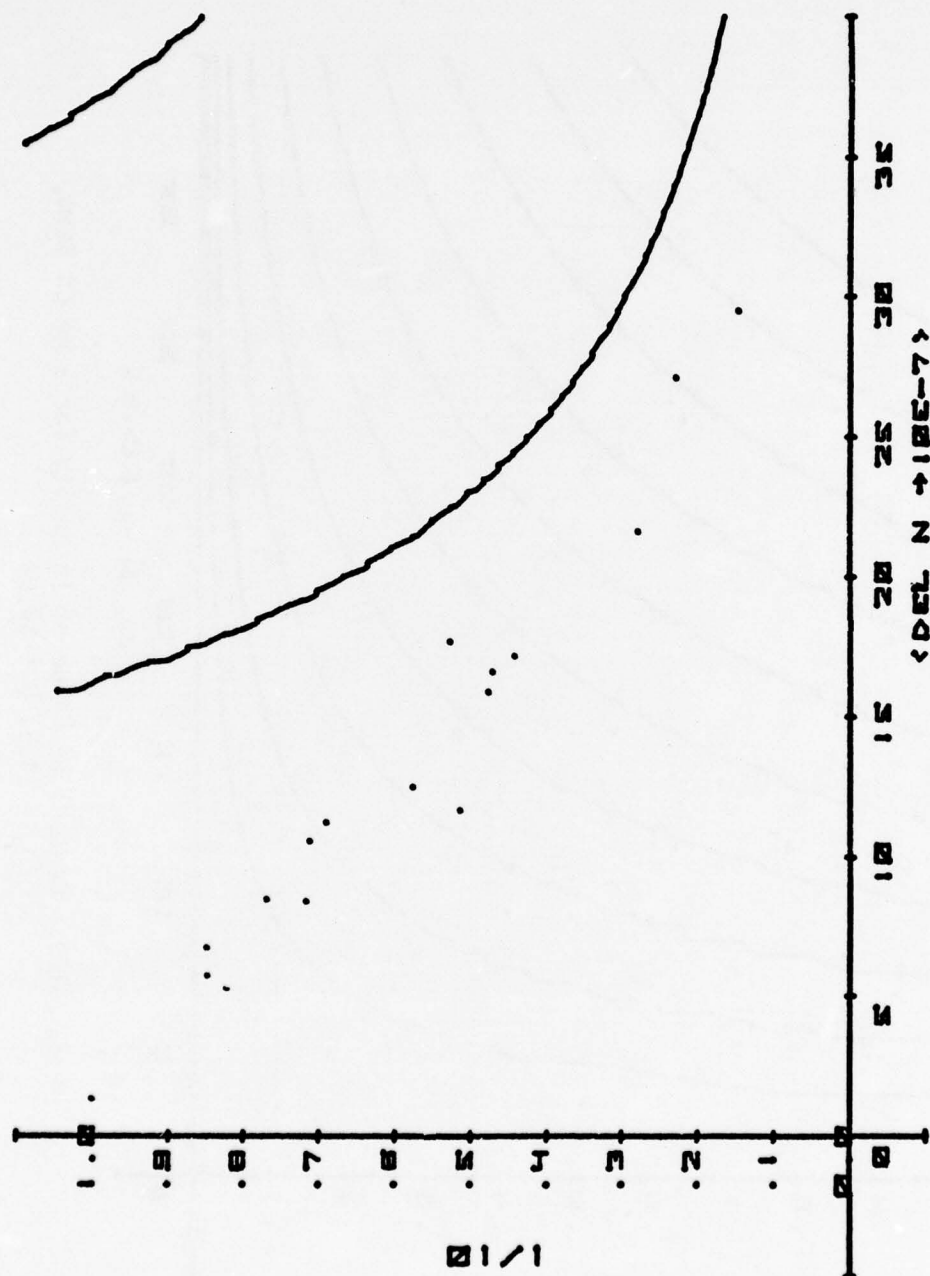


Figure 108. Centerline Value of Intensity for a He Cd Beam,
: $L/D_p = 28$, $D = 14.03$ mm

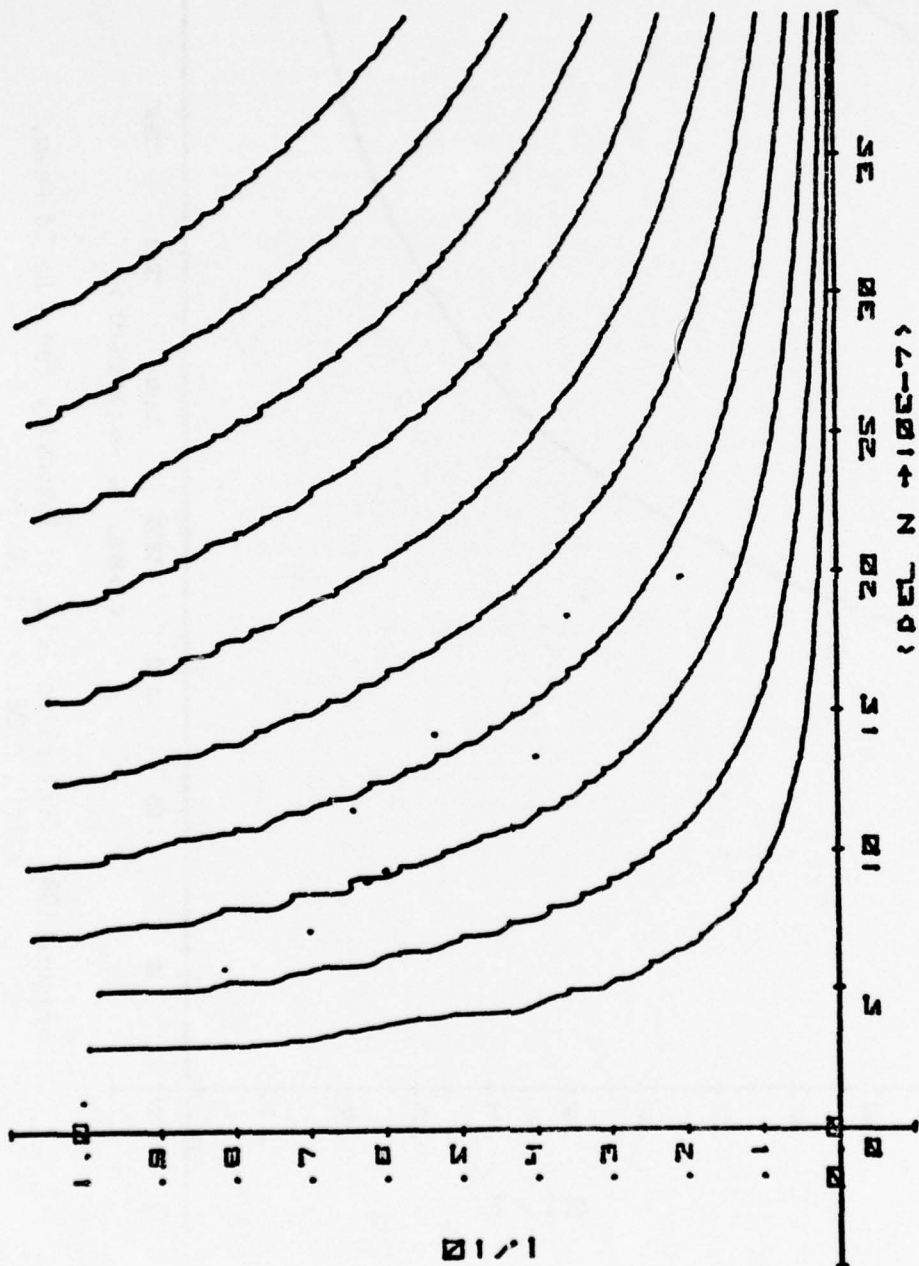


Figure 109. Centerline Value of Intensity for a He Cd Beam,
 $L/D_p = 34.5$, $D = 50$ mm

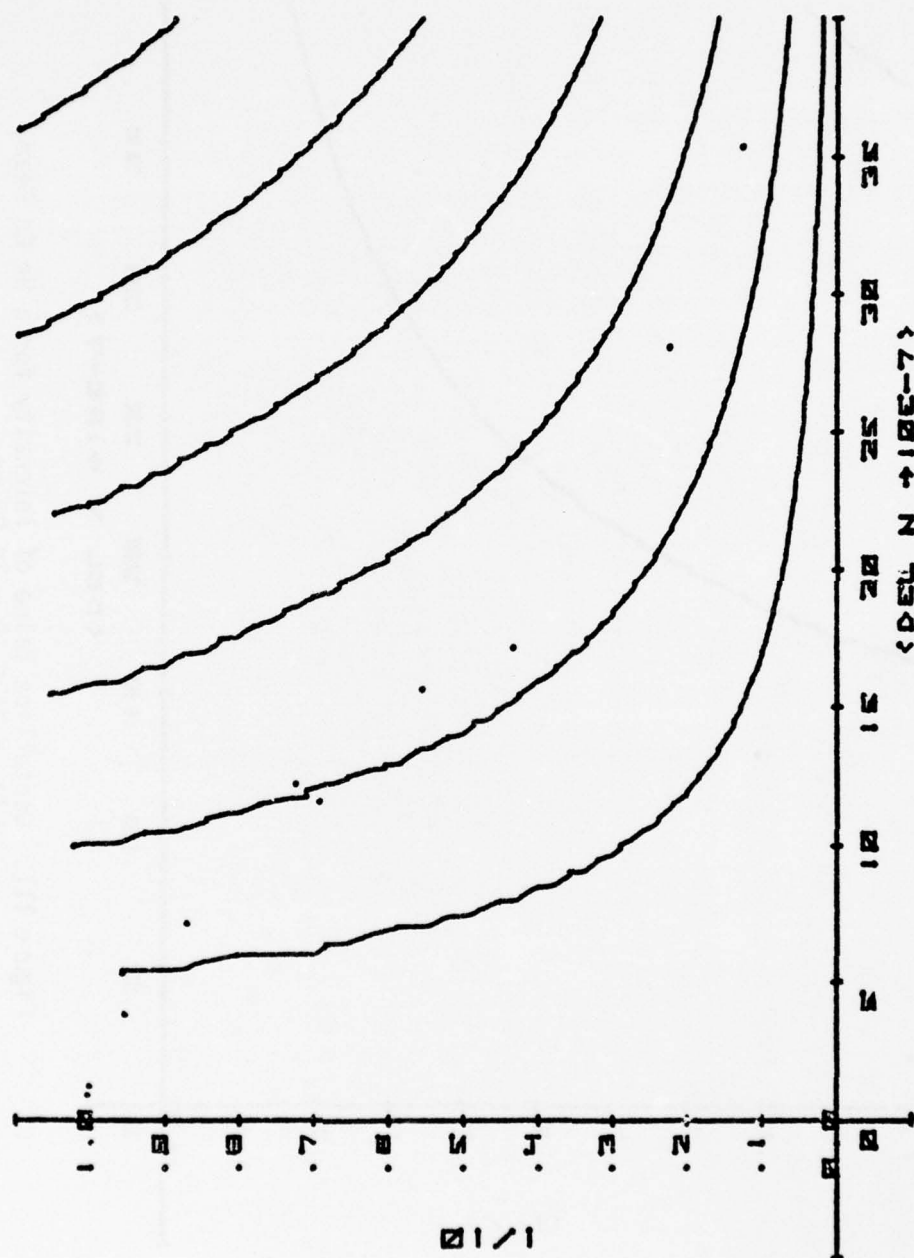


Figure 110. Centerline Value of Intensity for a He Cd Beam,
 $L/D_p = 34.5$, $D = 30.58 \text{ mm}$

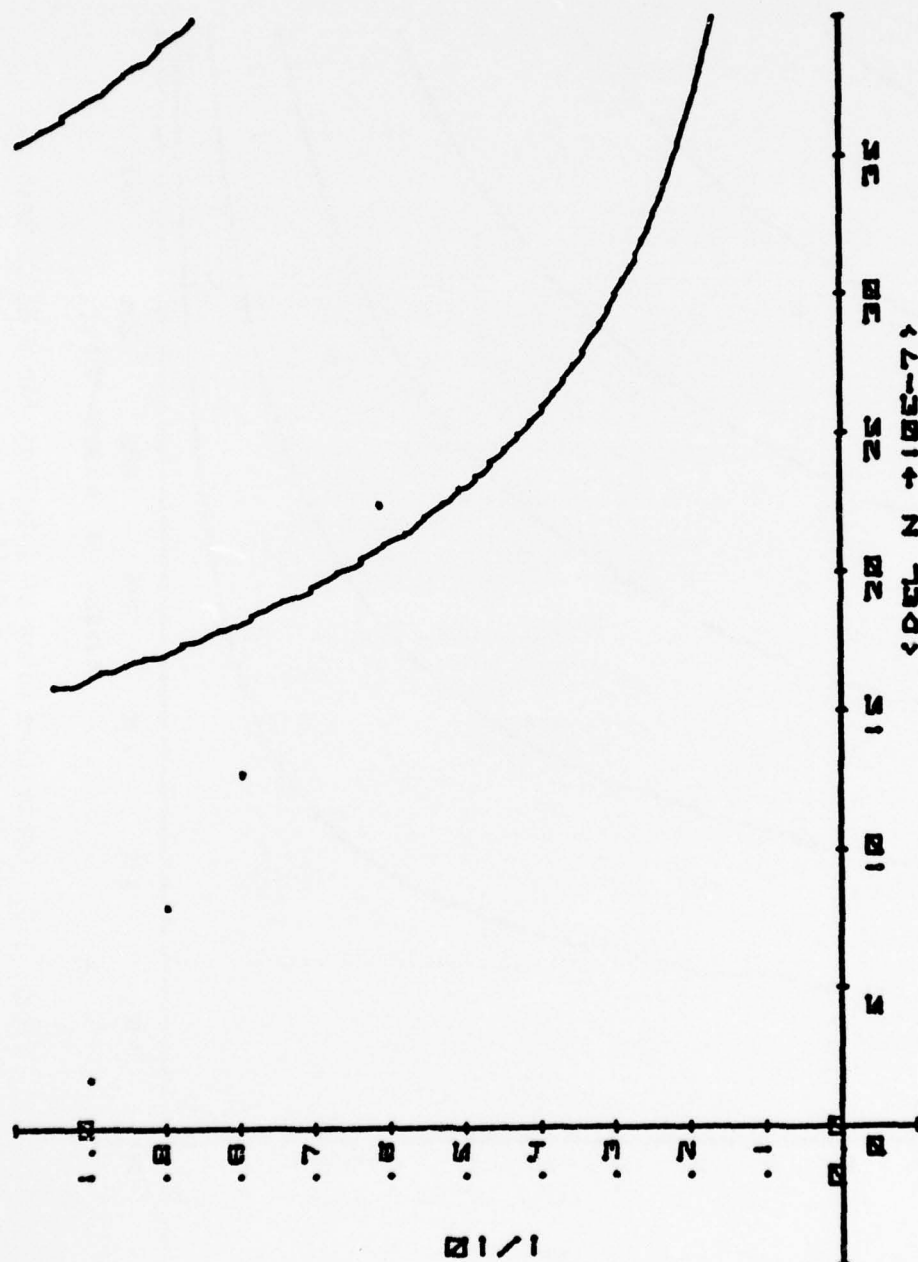


Figure 111. Centerline Value of Intensity for a He Cd Beam,
 $L/D_p = 34.5$, $D = 14.03$ mm

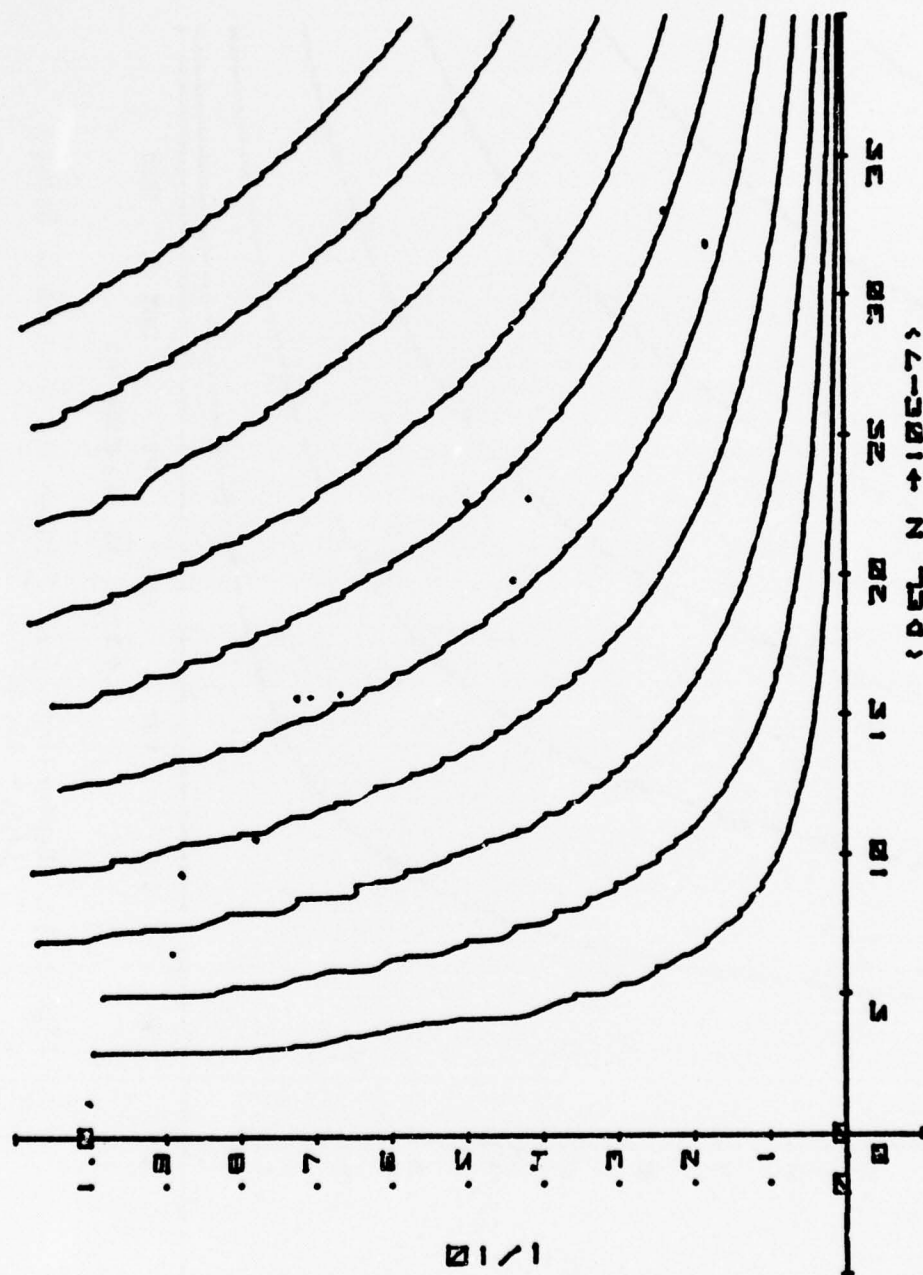


Figure 112. Centerline Value of Intensity for a He Cd Beam,
 $L/D_p = 45$, $D = 50$ mm

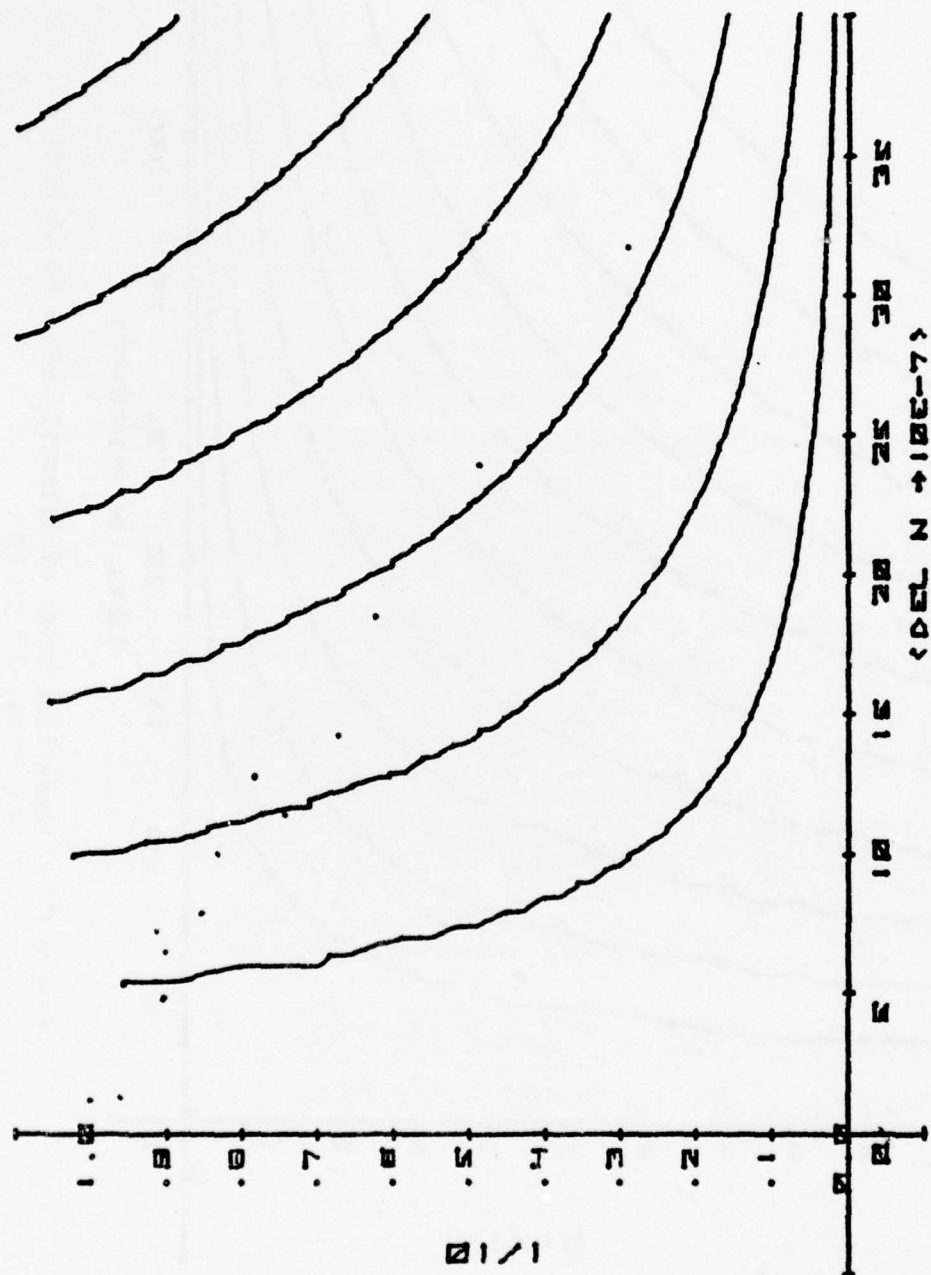


Figure 113. Centerline Value of Intensity for a He Cd Beam,
 $L/D_p = 45$, $D = 30.58 \text{ mm}$
 $\Delta N \times 10^{21} \text{ cm}^{-2}$

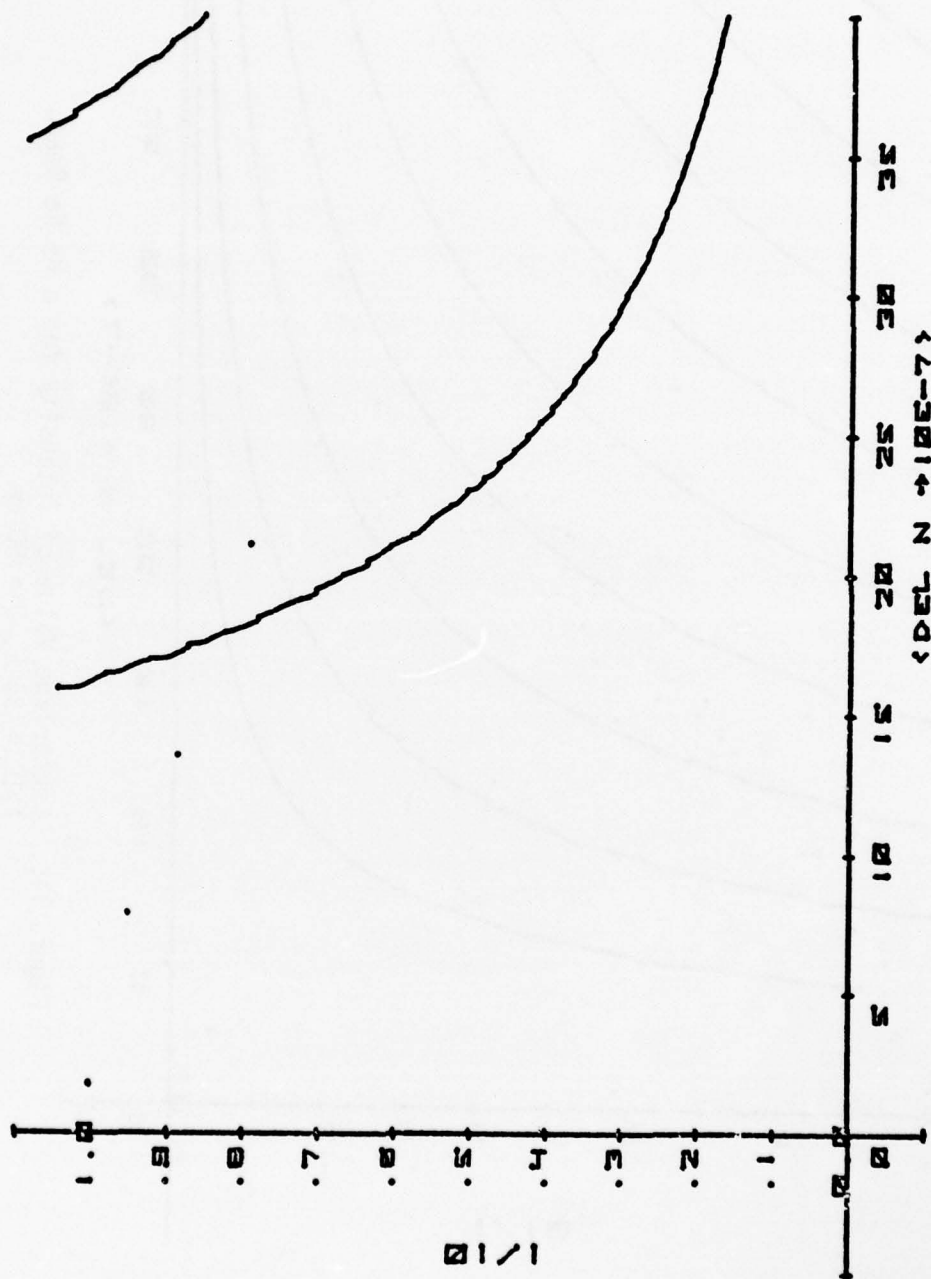


Figure 114. Centerline Value of Intensity for a He Cd Beam,
 $L/D_p = 45$, $D = 14.03$ mm

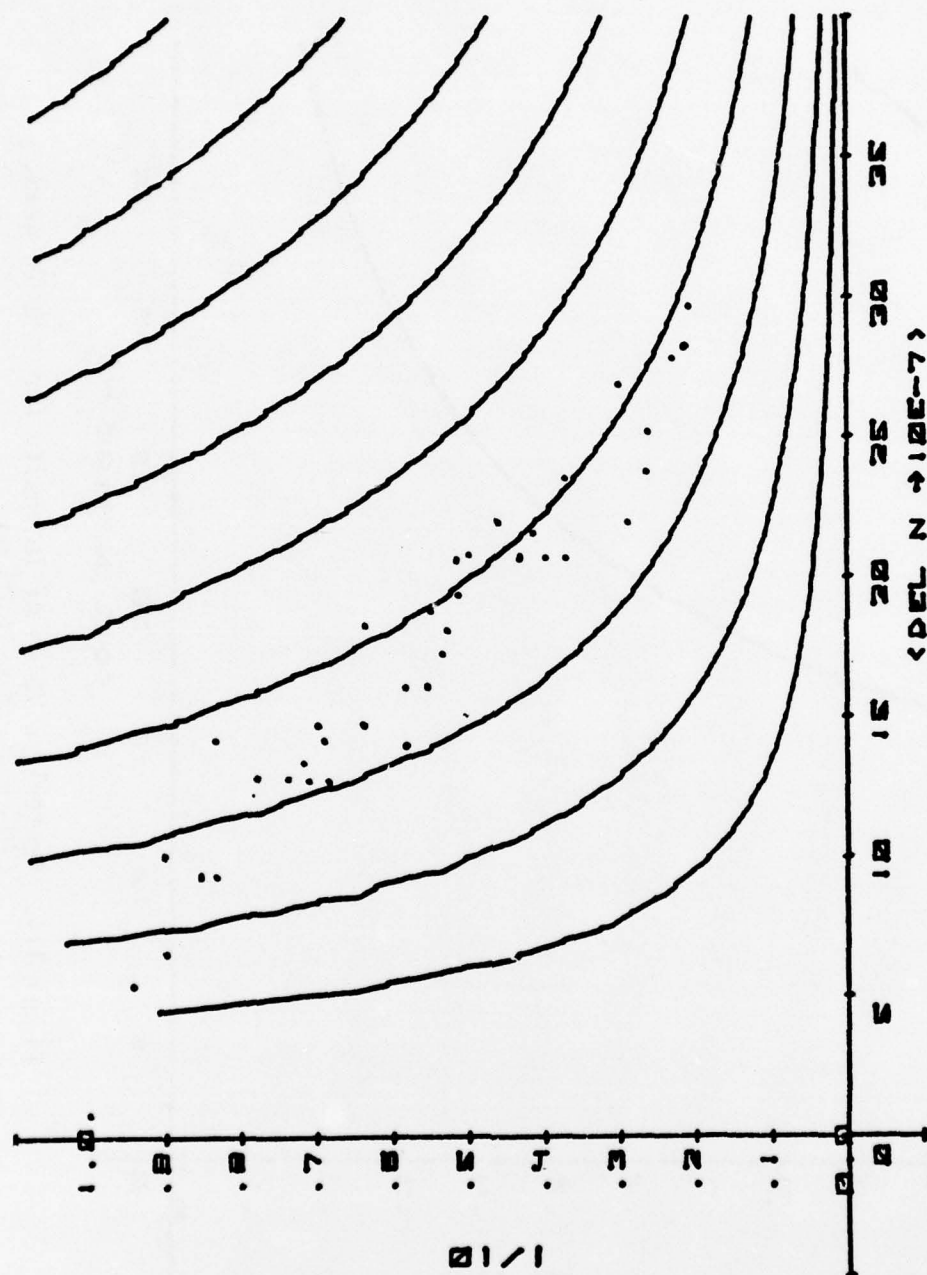


Figure 115. Centerline Value of Intensity for a He Ne Beam,
 $L/D_p = 34.5$, $D = 50$ mm

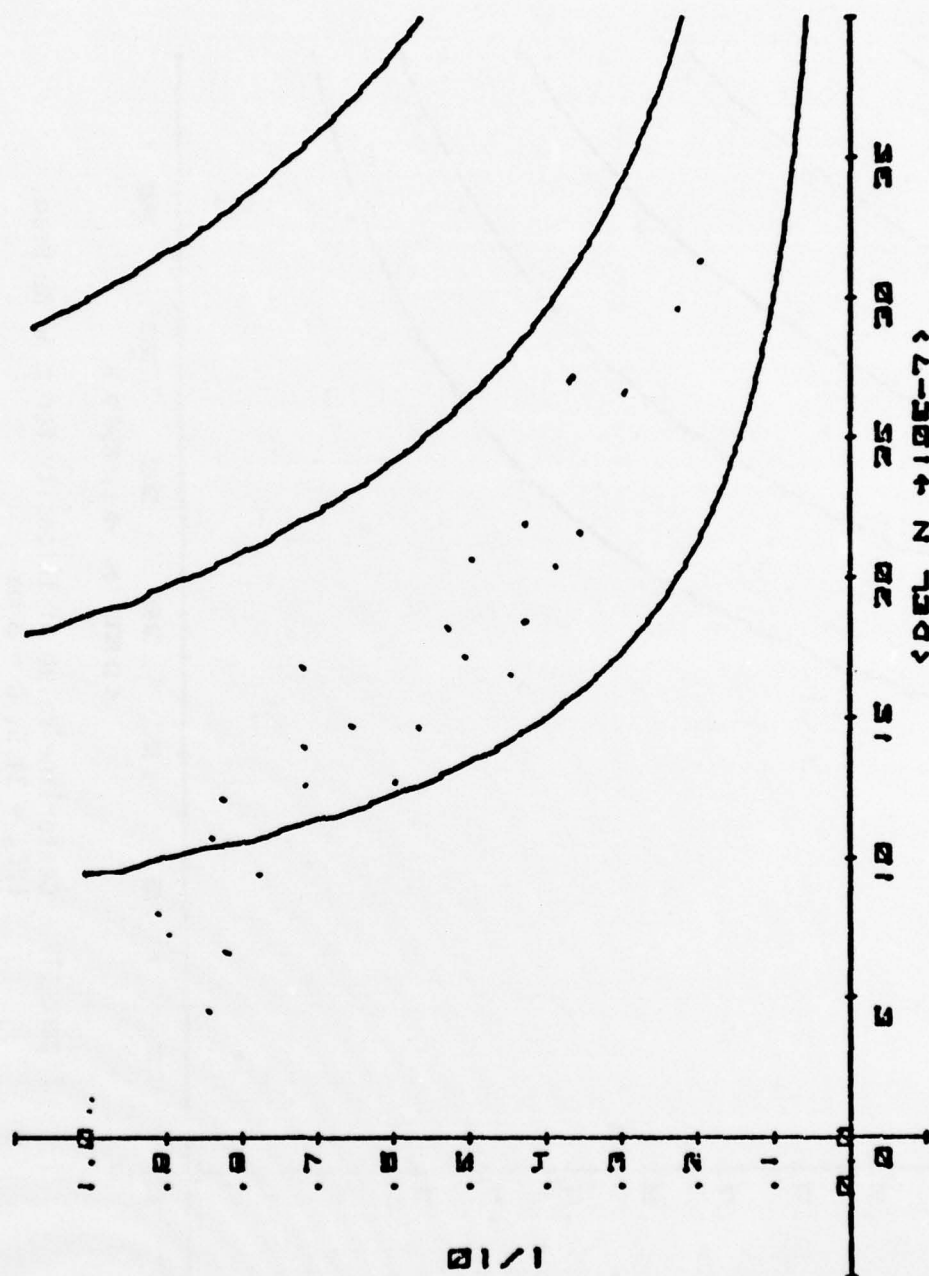


Figure 116. Centerline Value of Intensity for a He Ne Beam,
 $L/D_p = 34.5$, $D = 26 \text{ mm}$

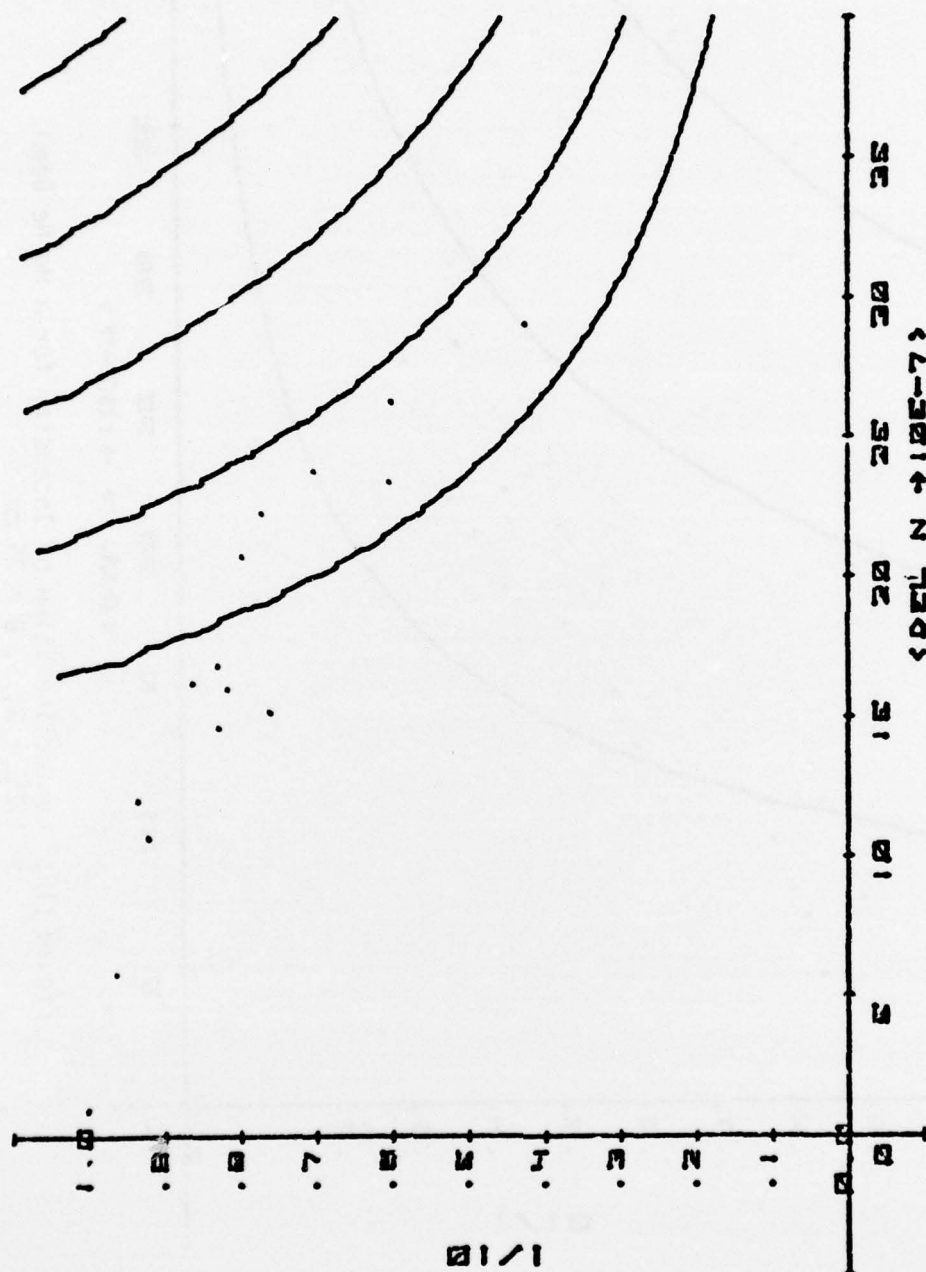


Figure 117. Centerline Value of Intensity for a He Ne Beam,
 $L/D_p = 34.5$, $D = 8$ mm

Figures 64 through 69. Figures 64 to 66 show that the smaller value of Λ_T given in the table occurs for the larger values of $K Q/U$ or $\langle \Delta \eta \rangle$. The 50mm diameter beams show very good agreement with the predicted integral scales of turbulence. Comparison of the 50mm He Ne data with the 50mm He Cd indicates excellent agreement with the wave length dependence of equation (110). As the ratio of beam diameter to turbulence scale approaches 1, the effective turbulence scale approaches the microscale of turbulence. The range of measured values of the temperature microscale are given in the last column of Table 7. The He Cd 14.03mm diameter beam at $L/D_p \approx 28$ and the 8mm diameter He Ne beams show values of turbulence scales very close to the minimum measured microscale and the L/D_p stations of 34.5 and 45 for the 14.03mm diameter He Cd beams indicate microscales near the maximum indicated values measured values. Replacement of the integral scale with the microscale, as D/Λ approaches 1, appears approximately correct. Sutton's expression for α is shown to give a good functional description of I/I_0 after I/I_0 is below 75 to 80%. Quantitatively, the predicted values are quite good below the I/I_0 's of .75 to .80%.

Table 7. Comparison of ΔT and λ_0 Scales from Centerline Laser Intensity Measurements with Their Measured Values

| Laser λ | L/Dp | Beam Diameter | ΔT from Fig. 106-117 | ΔT from Fig. 54 and 64-66 | λ_0 from Fig. 67-69 |
|--------------------|------|------------------|---------------------------------|--------------------------------------|--------------------------------|
| He Cd 441.6mm | 28 | 50mm | .64cm | .6 to 1.4cm | .12 to .5cm |
| | | 30.58 | .51 | | |
| | | 14.03 | .13 | | |
| | 34.5 | 50mm | 1.02cm | 1 to 1.6cm | .1 to .4cm |
| | | 30.58 | .64 | | |
| | | 14.03 | .31 | | |
| | 45 | 50mm | 1.52cm | 1 to 2cm | .12 to .57cm |
| | | 30.58 | .76 | | |
| | | 14.03 | .38 | | |
| He Ne 632.8mm | 34.5 | 50mm | 1.02cm | 1 to 1.6cm | .1 to .4cm |
| | | 26 | .38 | | |
| | | 8 | .09 | | |

CHAPTER VI

CONCLUSIONS

The objective of this dissertation was to determine whether the discrepancies between analytic and experimental results were caused by inaccuracies of the analytic models or by difficulties encountered in making precise experimental measurements for ranges of geometric conditions typical of laser cavities. The objective required the creation of controlled turbulence conditions which would produce beam spreads on the order of 1.5 to 2 times that of a diffraction limited beam diameter. In this dissertation, experimental beam spread measurements have been reported for the geometric range of conditions encountered in and around laser cavities with the ratio of the integral temperature scale of turbulence to the laser beam diameter, $\Delta T/D$, varied from <1 through >1 . The values of beam spread have been presented for the range of turbulence Reynolds numbers which are normally encountered in laser cavities. The attenuation or extinction coefficient, αL_0 , was varied from $\ll 1$ to >1 . The parameters required to predict laser beam spread are wave length, laser beam diameter, integral turbulence scale, micro turbulence scale, and the fluctuation of the index of refraction. The beam spread for variation of the important parameters was reported at the half power points and the centerline of the laser intensity distribution for wave lengths of 441.6nm and 632.8nm.

Chernov's beam spread and centerline intensity expressions for a rectangular aperture were used for comparison with the experimental data. Chernov's expression was found to apply to a circular aperture when the beam area, $\pi D^2/4$, replaces the rectangular aperture area, b_0^2 , and the three-dimensional integral scale, $\Lambda_T/.75$, is used instead of the energy scale, a .

The laser intensity distribution in a turbulent flow field was shown to be approximately gaussian. The normalized value of the focal spot radius, R/R_0 , at the half power and $1/e$ points of the power distribution curve is normally within 5 to 10% of the gaussian distribution when all distributions are normalized to the same normalized intensity value, I/I_0 .

The relationship between the fluctuation in index of refraction and the value of R/R_0 at the half power point with the rms fluctuation in index of refraction, $\langle \Delta n \rangle$, was found to be linear, within the measurement accuracy of individual parameters, and significantly better than previously reported in the literature. When the integral scale of turbulence, Λ_T , remained constant, deviations from linearity were within $\pm 1/2\%$. Although the extinction coefficient, αL_0 , ranged up to 4 for the reported data, the expression for $\alpha L_0 < 1$ was in excellent agreement with the experimental data for all αL_0 's with values of $I/I_0 < .8$.

The wave length dependence of beam spread was shown by taking the ratio of the values of R/R_0 for the half power point beams of helium neon and helium cadmium. The experimental beam wave length ratio of helium neon to helium cadmium, $\lambda_{He\ Ne}/\lambda_{He\ Cd}$, from the beam spread measurements

was compared in Table 3 to the actual wave length ratio. Table 3 indicated agreement of the experimental and actual values within -4%, -1%, +6%.

The beam diameter dependence of beam spread at the half power point obtained for Chernov's equation (95) is qualitatively correct, but does not predict the beam diameter effect on beam spread. Equation (95), when based upon beam spread measurements, tends to overestimate the diameter dependence by a +50% with the best value showing a +13% difference when a single scale of turbulence model is used.

When Chernov's equation (95) is modified by the substitution of the laser beam area, the α , and Λ_T values for a three-dimensional spectrum of turbulence, a significant improvement in the quantitative prediction of laser beam spread is obtained. The best previous prediction of beam spread compared to theory has been indicated to only be within a factor of 2 to 10. Given a value of $\langle \Delta \eta \rangle$, the factor of 2 uncertainty in the normalized R/R_0 value results in an uncertainty in Λ_T of the order of $+2\Lambda_T$, $-1/2\Lambda_T$. The largest differences from the predicted R/R_0 values, which were observed at the half power values of R/R_0 , were -20% to -30% for all beam diameters except the 8mm helium neon beam for which Λ_T/D ranges from 1 to 2. In this case, the value of the turbulence scale from the spread measurements is the same as the measured value of micro-scale, as was shown in Table 6. Table 6 also illustrates the excellent agreement by comparing the calculated Λ_T value obtained from beam spread measurements with the measured value of Λ_T .

Examination of the centerline intensity ratio, by means of Sutton's modified α in Chernov's expression, resulted in very good predictions of

$\Lambda_T/D < .01$ and $I/I_0 < 80\%$. The $\langle \Delta \eta \rangle^2$, Λ_T/D , and λ trends of beam spread were very good. The comparison of the experimental centerline intensities with parametric plots of equation (110) showed excellent agreement with $\langle \Delta \eta \rangle^2$. The comparison of the 50mm diameter He Ne and He Cd beam spreads at the L/D_p station of 34.5 showed excellent agreement for the wave length dependence of equation (110). Sutton's expression for the three-dimensional spectrum of turbulence gave excellent quantitative agreement with the actual measured integral scales of turbulence for the 50mm diameter beams. Integral scales of turbulence were derived from the beam spread measurements which were within 2 to 6% of the actual values at all stations except at $L/D_p = 45$. Experimental values shown in Figures 94 through 105 indicate excellent agreement with analytic values for these conditions. The quantitative agreement for $\Lambda_T/D < .01$ for centerline values was shown to be very good and better than any data reported previously.

As Λ_T/D approaches 2, it appears that the temperature microscale of turbulence may be used to replace the integral scale. The value of ℓ_{OT} obtained from beam spread measurements, as shown in Table 6, is within 11% of the measured value for the 8mm He Ne beam.

For intermediate values of Λ_T/D (approaching .3), equation (110) is found to be inadequate for the prediction of beam spreads. The discrepancy in temperature scale at Λ_T/D of .2 is 20%, and 34% at a Λ_T/D of .3 for the He Cd data.

Comparison of Tables 6 and 7, which summarizes the beam spread calculated and measured value of Λ_T , indicates that measurements of laser beam spread at the half power point of the laser power distribution are

more accurate in describing the Λ_T/D variation of laser beam spread by a ratio of nearly 2 to 1. The measurement of beam spread, for all values of $\Lambda_T/D \leq 1$ at the half power point, has been shown to agree with the predictions of equation (100).

The results of this dissertation have reduced the uncertainty in predicting laser beam spread by a factor greater than 2 for a wide range of turbulence conditions which are encountered in laser cavity flows. As a result of this improvement of the relationship between experiment and theory, the uncertainty in predicting losses and laser beam spread has likewise been reduced for all mediums and conditions for which diffraction effects may be neglected. The combination of Chernov's and Sutton's relations was shown to accurately predict the centerline intensity variation and accurately predict the half power point variation of beam spread.

The primary difficulty in predicting beam spread caused by turbulence, in the range of parameters investigated, consists in accurately measuring the turbulence parameters. As a result, the 2 to 10 fold discrepancies, which appear in the literature in predicting the beam focal spot size resulting from turbulence, may be attributed primarily to a lack of precise measurements.

CHAPTER VII

RECOMMENDATIONS

In and around laser cavities, the turbulent environment is much as was simulated in this experiment. Λ/D is of order 1 and ℓ_0 is not negligible compared to Λ . These conditions violate several of the analytical solutions available in the literature. It is recommended that the experimental data be compared quantitatively against available numerical solutions such as Lutomirski's (Lutomirski, 1970) or Sutton's, $D/\Lambda \sim 1$, (Sutton, 1969). A comparison of similar general conditions indicates that the specific agreement may be quite good.

It is recommended that a similar experiment be carried out for a longer wave length, such as CO_2 , under well controlled and measured turbulence conditions.

more accurate in describing the Λ_T/D variation of laser beam spread by a ratio of nearly 2 to 1. The measurement of beam spread, for all values of $\Lambda_T/D \leq 1$ at the half power point, has been shown to agree with the predictions of equation (100).

The results of this dissertation have reduced the uncertainty in predicting laser beam spread by a factor greater than 2 for a wide range of turbulence conditions which are encountered in laser cavity flows. As a result of this improvement of the relationship between experiment and theory, the uncertainty in predicting losses and laser beam spread has likewise been reduced for all mediums and conditions for which diffraction effects may be neglected. The combination of Chernov's and Sutton's relations was shown to accurately predict the centerline intensity variation and accurately predict the half power point variation of beam spread.

The primary difficulty in predicting beam spread caused by turbulence, in the range of parameters investigated, consists in accurately measuring the turbulence parameters. As a result, the 2 to 10 fold discrepancies, which appear in the literature in predicting the beam focal spot size resulting from turbulence, may be attributed primarily to a lack of precise measurements.

LIST OF REFERENCES

1. Barabanenkov, Y. U., Kravtsov, Y. A., Rytov, S. M., and Tamarskii, V. I., "Status of the Theory of Propagation of Waves in a Randomly Inhomogeneous Medium," Soviet Physics, Vol. 13, No. 5, 1971, 551.
2. Batchelor, G. K., "The Theory of Homogeneous Turbulence," University Press, Cambridge, 1953.
3. Bradshaw, P., "An Introduction to Turbulence and Its Measurement," Pergamon Press, 1971.
4. Chernov, L. A., "Wave Propagation in a Random Medium," Dover, 1967.
5. Collins, S. A., and Wortendyke, D. R., "A Study of the Interaction of Coherent Optical Radiation with Wind Tunnel Air Turbulence," The Ohio State University Research Foundation, 1935-14, 1965.
6. Collis, D. C., and Williams, M. J., "Two-Dimensional Convection from Heated Wires at Low Reynolds Numbers," J. Fluid Mechanics, 32, 1968, 357.
7. Corrsin, S., "Turbulence: Experimental Methods," Handbook der Physik, Vol. 8, Part 2, Springer, Berlin, 1963, 524.
8. Director, M. N., "Aerodynamic Parameters Affecting Practical Gas Dynamic Laser Design," AIAA Paper 73-626, 1973.
9. Freymuth, P., "Feedback Control Theory for Constant-Temperature Hot Wire Anemometers," The Review of Scientific Instruments, Vol. 38, No. 5, 1967, 677.
10. Freid, D. L., "Optical Resolution Through a Randomly Inhomogeneous Medium for Very Long and Very Short Exposures," Journal of the Optical Society of America, Vol. 56, No. 10, 1966, 1372.
11. Gebhardt, G. F., "The Log-Amplitude Mean Value for Laser Beam Propagation in the Atmosphere, with Applications for Optical Communications," The Ohio State University Electroscience Laboratory, Dissertation and TR 2156-8, 1968.
12. Gebhardt, G. F., and Collins, S. A., "Log-Amplitude Mean for a Laser-Beam Propagation in the Atmosphere," Journal of the Optical Society of America, Vol. 59, No. 9, 1969, 1139.

13. Goldstein, S., "Modern Developments in Fluid Dynamics," Vol. II, Dover, 1965.
14. Greenbaum, M., "How Well Can Laser Radiation be Focused Through the Atmosphere," Riverside Research Institute, TR T-1/174-1-00, 1971.
15. Hinze, J. O., "Turbulence," McGraw-Hill, 1959.
16. Huffnagel, R. E., and Stanley, N. R., "Modulation Transfer Function Associated with Image Transmission Through Turbulent Media," Journal of the Optical Society of America, Vol. 54, No. 1, 1964, 52.
17. Hyde, J. C., and Hosack, G. A., "An Investigation of Velocity Flow Fields in Chemical Laser Nozzles," AIAA Paper 73-641, 1973.
18. Lawrence, R. S., and Strohbehn, J. W., "A Survey of Clear-Air Propagation Effects Relevant to Optical Communications," Proceedings of IEEE, Vol. 58, No. 10, 1970, 1523.
19. Lutomirski, R. F., "Propagation of a Finite Optical Beam in an Inhomogeneous Medium," The Rand Corporation, RM-6055-ARPA, 1970.
20. Lutomirski, R. F., Huschke, R. E., Meerham, W. C. and Yura, H. T., "Degradation of Laser Systems by Atmospheric Turbulence," The Rand Corporation, R-1171-ARPA, 1973.
21. Meyer-Arendt, J. R., and Emmanuel, C. B., "Optical Scintillation: A Survey of the Literature," National Bureau of Standards, Technical Note 225, 1965.
22. Mills, R. R., Kistler, A. L., O'Brien, V. and Corrsin, S., John Hopkins University, NACA TN 4288, 1958.
23. Sandborn, V. A., "Resistance Temperature Transducers," Metrology Press, 1972.
24. Schmeltzer, R. A., "Means, Variances and Covariances for Laser Beam Propagation Through a Random Medium," Quarterly Applied Mathematics, Vol. 23, No. 4, 1967, 339.
25. Sutton, G. W., "Effect of Turbulent Fluctuations in an Optically Active Fluid Medium," AIAA Journal, Vol. 7, No. 9, 1969, 1737.
26. Tatarski, V. I., "Wave Propagation in a Turbulent Medium," Dover, 1961.
27. Townsend, A. A., "The Structure of Turbulent Shear Flow," University Press, Cambridge, 1956.